Preparation of Polyaniline Nanostructures for Energy and Charge-Transport Application

Thesis submitted for the Degree of Doctor of Philosophy (Science)
of Jadavpur University

2024

By

PUSPENDU DAS

School of Applied and Interdisciplinary Sciences

Indian Association for the Cultivation of Science

Jadavpur, Kolkata – 700032

India

Indian Association for the Cultivation of Science

2A & 2B Raja S. C. Mullick Road, Jadavpur

Kolkata-700032, India

Prof. Sudip Malik
Senior Professor
School of Applied and Interdisciplinary Sciences

Telephones: 2473-4971, 3372, 3073 (Ext. 1564)
Fax: (+91) (33) 2473-2805
E-mail: psusm2@iacs.res.in

CERTIFICATE FROM THE SUPERVISOR

This is to certify that the thesis entitled **“Preparation of Polyaniline Nanostructures for Energy and Charge-Transport Application”** submitted by Sri/~~Smt~~ **Puspendu Das** who got his/~~her~~ name registered on 12/09/2018 for the award of Ph. D (Science) degree of Jadavpur University, is absolutely based upon his own work under the supervision of **Prof. Sudip Malik** and that neither this thesis nor any part of it has been submitted for either any degree/~~diploma~~ or any other academic award anywhere before.

Malik 12/04/2024

Dr. Sudip Malik
Professor and Chairman
School of Applied & Interdisciplinary
Sciences (SAIS)
I.A.C.S, Jadavpur, Kolkata-700 032

Signature of the Supervisor

(date with official seal)

DECLARATION

I hereby declare that the research work presented in this thesis entitled **“Preparation of Polyaniline Nanostructures for Energy and Charge-Transport Application”** is the result of the thesis carried out by me under the supervision of Prof. Sudip Malik at School of applied and Interdisciplinary Sciences, Kolkata, and the same has not been submitted elsewhere for any degree or diploma.

Date: 12/04/2024

Puspendu Das.

PUSPENDU DAS

[Index No.: 165/18/Chem./26]

This Thesis is dedicated to

My Parents…..

Preface

The primary focus of this thesis is on preparation, characterisation and application of polyaniline nanostructures. The polyaniline nanostructures are synthesized by chemical oxidative polymerization method by using various organic carboxylic acid, especially Benzine tetracarboxylic acid (BTCA) and Guanosine mono phosphate (GMP) etc as dopant. The fibrous/tubular morphology of polyaniline nanostructures are controlled by aniline to dopant acid concentration and bulkiness of acid functionalized organic moity. The electrochemical energy storage property of polyaniline greatly depends upon morphology of nanostructures. Polyaniline nanostructures also have mild reducing property to form efficient metal nanoparticles on its surface. Polyaniline/metal composite are very useful for charge transport application and different kind of electrocatalysis. The all-thesis works has been carried out in School of Applied and Interdisciplinary Sciences of Indian Association for the Cultivation of Science, Jadavpur, Kolkata-32 under the supervision of Prof. Sudip Malik.

Thesis consists of six individual chapters. The Chapter-1 deals with a brief introduction on conducting polymer and polyaniline. Different morphological, optical, electrochemical properties of polyaniline nanostructures have been discussed. Several application points based on polyaniline nanostructures including supercapacitor, battery, electrocatalysis, memory device materials etc. have been introduced. Chapter-2 deals with details instrumentation and materials characterization in our research work. In Chapter-3 we have discussed the synthesis various organic acid doped polyaniline fibre for electrode materials of supercapacitor. In the Chapter-4 discuss about G-quadruplex dopped Polyaniline Hybrid Networks as Next-Generation Biocompatible Electrode Materials with Unprecedented Rheological Performance. The Chapter-5 is describing multiple resistive switching phenomena or charge transport in metal-nanoparticle embedded one-dimensional conducting polymer nanotubes. Finally in Chapter-6 has summarized the all-thesis work with the scope of future ambition.

Acknowledgement

I am deeply grateful to all those who have accompanied and supported me throughout my doctoral research journey. Their unwavering support, valuable suggestions, and assistance have been instrumental in helping me reach this milestone. I extend my heartfelt appreciation to each and every individual who has contributed to the success of this dissertation. Without their guidance and encouragement, this lengthy journey would not have been possible. It is with immense pleasure that I acknowledge their invaluable assistance and contributions.

First and foremost, my deepest gratitude goes to **Prof. Sudip Malik**, my esteemed research advisor, for his invaluable guidance, ideas, and constructive feedback throughout my research journey. I am immensely thankful to him for extending the opportunity to work under his mentorship and granting me the autonomy to pursue independent research encompassing materials synthesis, characterization, and application. Under his mentorship, I have cultivated the ability to meticulously plan my work, often strategizing late into the night before stepping into the lab the next day, and have developed resilience in navigating the most challenging situations. Prof. Malik’s ever-present smile and remarkable demeanour have been a source of inspiration, and his unwavering dedication to his family amidst his demanding schedule serves as a profound lesson in prioritization and balance. I am truly fortunate to have had the privilege of learning from him.

I extend my heartfelt gratitude to Prof. A. K. Nandi, Prof. T. K. Mondal, and Prof. S. Ghosh, esteemed faculty members, for their invaluable guidance and insightful suggestions provided during my JRF to SRF interview, as well as for engaging in fruitful scientific discussions during various seminars. Their expertise and encouragement have played a significant role in shaping my research journey, and I am sincerely thankful for their continued support.

I express my gratitude to Prof. J. Dash and Prof. M. Mondal from IACS, Jadavpur, Kolkata, India, for their invaluable scientific collaborations and insightful discussions throughout the course of this work. Their contributions and expertise have enriched my research endeavours, and I am deeply appreciative of their collaborative spirit and guidance.

I extend my sincere appreciation to DST-INSPIRE, New Delhi, India, for their generous financial support over the course of five years. Their funding has been instrumental in facilitating my research endeavours, and I am deeply grateful for their investment in my academic journey. Additionally, I would like to acknowledge my institute, IACS, for providing access to state-of-the-art laboratory facilities, extensive library resources, and advanced CSS instrumental facilities. These resources have contributed significantly to creating an exceptional research environment, for which I am truly thankful.

My special and heartful thanks to my lab senior Dr. Chanchal Chakraborty, Dr. Utpal Rana, Dr. Pradip K. Sukul, Dr Sanjoy Mondal, Dr. Manas K. Bera Dr. Dines Ch. Santra, Dr. Kausik Bag, Dr. Ketaki Samanta, Dr. Arkapal Roy and Ms. Shrabanti Basak, my lab mates Subhra and my lab Junior Prasanta, Ayan, Gopal, Saily, Lalmohan, Mustak, Runa, Praduman, Bankim, Antara, Agamoni and Samim for making a friendly atmosphere in our lab and their cooperation and invaluable help in lab. Especially I cannot forget Dr. Sanjoy Mondal who help me lot about lab related work, scientific discussion, paper writing etc. I will miss the group meeting discussion, evening tea, little jokes in lab time and many funny moments shared with them.

My special and sincere thanks to all my senior and colleagues of Prof. T. K. Mondal’s Lab, Prof A. K. Nandi’s Lab, Prof. S. Ghosh’s Lab for their inestimable cooperation, suggestions in that long journey.

Special thanks to all My Friends Debabrata Chakraborty, Madhuparna Roy, Subhamoy Jana, Gopal Rana, Arunabha Maity, Anik Sahoo, Soumyajit Hazra, and Ishita Pal for their support in my ups and down conditions. Debabrata, in particular, deserves special mention as he was not just a friend or roommate, but a brother-like figure who stood by me throughout my doctoral life. His constant support and companionship have been invaluable to me..

Many thanks to PSU stuff members Mr. Amit Chakraborty Mr. Panchu Gopal Chakraborty, Champadi, Sidharthada for help. I also would like to thank all instrumental operators, canteen, workshop, and cleaning, electrical, security stuff members of IACS.

My special thanks to my would-be wife Madhumita, for being with me in every time and every situation of my research carrier. My all frustration, depression, enjoyment had share with her during my PhD journey. Without her support I cannot complete PhD degree in a smooth way.

I am profoundly grateful to my parents, particularly my mother, for their unwavering moral support and everything they have bestowed upon me since my earliest memories. The support and love my mother showered upon me throughout the years were truly the greatest gifts I have ever received. Although I tragically lost my mother a year ago, her presence continues to guide and inspire me every day. Words cannot adequately express the depth of my love and gratitude to my parents, as well as to my sister Sangita and brother-in-law Ujjwal Da, who have always stood by my side and offered their unwavering support in every situation. Additionally, I extend my heartfelt thanks to my other family members for their continuous love, encouragement, and support.

I am deeply grateful for the unwavering support of my uncle, Mr. Manik K. Das, and my aunt, Sunandita Das, whose guidance and encouragement have been instrumental throughout my school and college years. Their presence and assistance have played a significant role in shaping my academic journey.

Finally, I extend my heartfelt gratitude to everyone who has contributed to the successful completion of this thesis. While I may not be able to mention each person individually, their support and contributions have been invaluable. Any errors or shortcomings that may exist within this thesis are solely my responsibility.

Finally, I would like to thank all who have made my stay at IACS, Kolkata so joyful and easy.

Puspendu Das.
12/04/2024

(Puspendu Das)

School of Applied and Interdisciplinary Sciences

Indian Association for the Cultivation of Science

Jadavpur, Kolkata, 700032, India

ABBREVIATION

APS	Ammonium Peroxydisulphate
BDP	Benzene tetra-carboxylic acid doped polyaniline
BTCA	Benzene tetra-carboxylic acid
CPs	Conducting Polymers
CV	Cyclic Voltammetry
GCD	Galvanostatic Charge Discharge
E	Energy Density
P	Power Density
EDLCS	Electric double-layer capacitors
EIS	Electrochemical Impedance Spectroscopy
FESEM	Field emission scanning electron microscopy
HCs	Hybrid capacitors
ITO	Indium Tin Oxide
MNPs	Metal nanoparticles
MOR	Methanol oxidation reaction
NPs	Nanoparticles
ORR	Oxygen reduction reaction
PANI	Polyaniline
PPy	Polypropylene
PVC	Polyvinyl Chloride
SC	Supercapacitor
SEM	Scanning electron microscopy.

SSSC	Solid state supercapacitor
TEM	Transmission electron microscopy
VPD	Vapour-Phase Deposition
AFM	Atomic Force Microscopy
XRD	X-Ray Diffraction
XPS	X-Ray Photoelectron Spectroscopy
FTIR	Fourier transforms infrared.
TGA	Thermal Gravimetric Analysis
UV-Vis	Ultraviolet-Visible
OA2	Benzene 1, 4-dicarboxylic
OA3	Benzene 1, 3, 5-tricarboxylic acid
OA4	Benzene 1, 2, 4, 5-tetracarboxylic acid
OPAN	Organic Acid Doped Polyaniline

TABLE OF CONTENTS

Chapter 1

Introduction **Page**

Chapter 2

Characterization & Instrumentation

Chapter 3

Fully organic polyaniline nanotubes as electrode material for durable supercapacitor

Chapter 4

Polyaniline/G-Quadruplex Hybrid Networks as Next-Generation Electrode Materials with Unprecedented Rheological Performance

Chapter 5

Charge transport in metal-nanoparticle embedded one-dimensional conducting polymer nanotubes: multiple resistive switching phenomena

Chapter 6

Summary & Conclusion

6.1 Summary & Conclusion

6.2 Scope of future work

CHAPTER 1

Introduction

1. Introduction

A polymer is really a large or macromolecule that is constructed from numerous tiny, repetitive, identical or distinct parts (monomer). Swedish eminent scientist Jöns Jacob Berzelius coined the term "polymer" in 1983. Polus (many) and meros (units) are two Greek words that are combined to form the word "polymer".[1]

Rubber, plastic, and other polymers are employed as insulating materials because of their high resistance to electrical conduction, which has allowed them to function as such for a long time. Polymers are thought of as nonconductors of electricity.[2] Polyethylene, which was accidentally created by German scientist Hans von Pechmann in 1898, is the most basic synthetic polymer. It is thought ludicrous that polymers or plastics might carry electricity, due to their widespread usage as insulating materials.

1.1. Conducting polymer

Organic polymers that transmit electricity across their chains via π -electron conjugations are known as conductive polymers. But in 1977, Alan G. MacDiarmid, Alan J. Heeger, Hideki Shirakawa, made a discovery that altered the conventional notion. When polyacetylene was doped with electrons, they discovered conductivity.[3] In 2000, the Nobel Prize was awarded in honour of such outstanding discovery. [4-6]

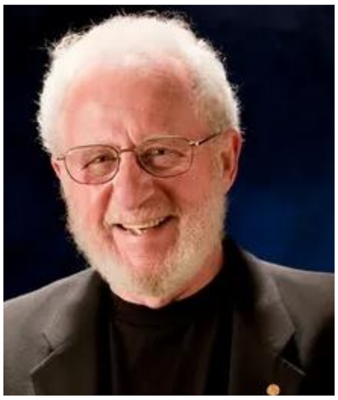

Alan J Heeger

Alan G. MacDiarmid

Hideki Shirakawa

Atoms are mostly covalently bound to one another in the polymer chain. Since there is no opportunity for valence electron delocalization when atoms are covalently bound together to form a saturated carbon compound and since neither charge carriers nor a conduit for their movement are accessible through the whole structure, the polymer acts like an insulator. However, when atoms are joined together in a polymer by unsaturated bonding, or by creating conjugated bonding, an electron delocalization may take place through the polymer's link. Conducting polymers are that type of polymer. The conducting polymers polyacetylene, polypyrrole, polyaniline, and polythiopene are a few examples. Conducting polymers or organic metals may eventually take the role of inorganic metal in a number of crucial applications.

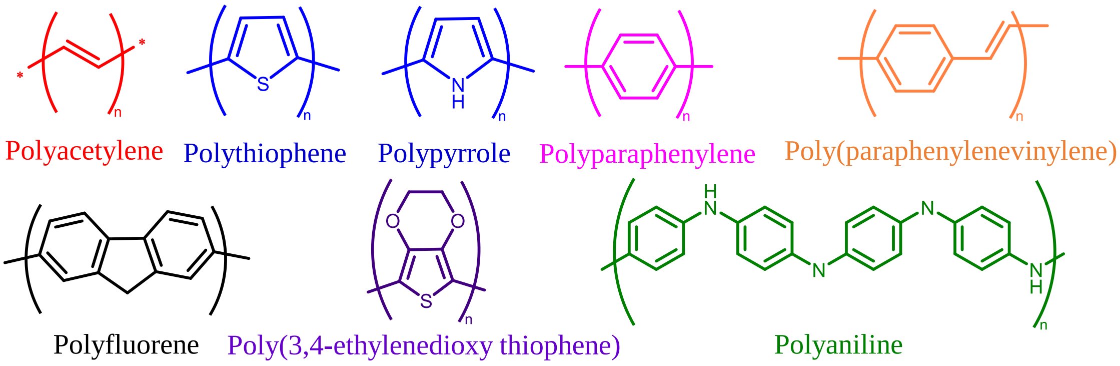

Figure 1.1 Some examples of chemical structures of conductive polymers

1.1.1 Historical background of conducting polymer.

Pohl, Katon, and their colleagues synthesised and described the first semiconducting polymers in the 1960s, which was marked the beginning of conducting polymer research.[6b] Conducting polymer research was advanced with the discovery of the high conductivity of polysulfurnitride (SN)x, a polymeric substance with intriguing electrical characteristics. Nearly half century ago, films of polyacetylene were discovered to have an electrical conductivity, which marked as the one of the milestones in polymer research.

1.1.2 Conduction mechanism and Band Gap of conducting polymer.

Since conducting polymers were discovered, a variety of applications have been investigated for their electrical characteristics. Researchers have more recently become interested in conducting polymers because of the possibility of using them in electronics. Conducting polymers and conductive polymeric composites are shown in an overview with a wide range of conductivity in **Figure 1.2**. By adjusting the dopant concentration, it is possible to change the conductivity of polymers over a broad range, begins from insulator to semiconductor and approaching metallic.

Understanding the band structure and charge carriers of such types of polymers are crucial in order to comprehend the conducting mechanism of polymers. The charge transfer that is carried out via a hopping process between the dopant molecules, which serve as hopping sites, is represented by molecularly doped polymers.[7] Depending on the band gap, scientists classify materials as insulator, semiconductor, or conductor (**Figure 1.3**). There are two primary bands in the energy profile diagram: (1) the valance band (lower energy), and (2) the conduction band (higher energy). [8] A substance with zero conductivity is referred to as an insulator when the gap between the conduction and valence bands is too great and makes it impossible for an electron to go from the valence to the conduction band. When the band gap is very small or almost zero, electrons may very readily hop from the valance to the conduction band, which is why these materials are known as conductors. Once more, if the band gap is neither large nor close to zero, the material is referred to as a semiconductor. [9]

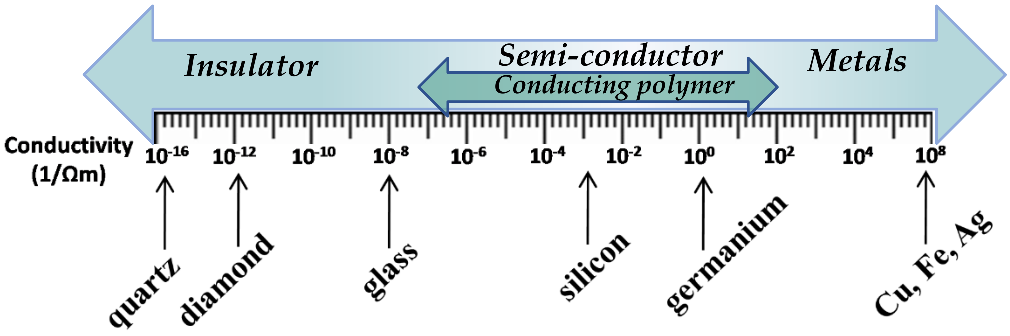

Figure 1.2 Conductivity range from insulator to metal via semiconductor and conducting Polymers

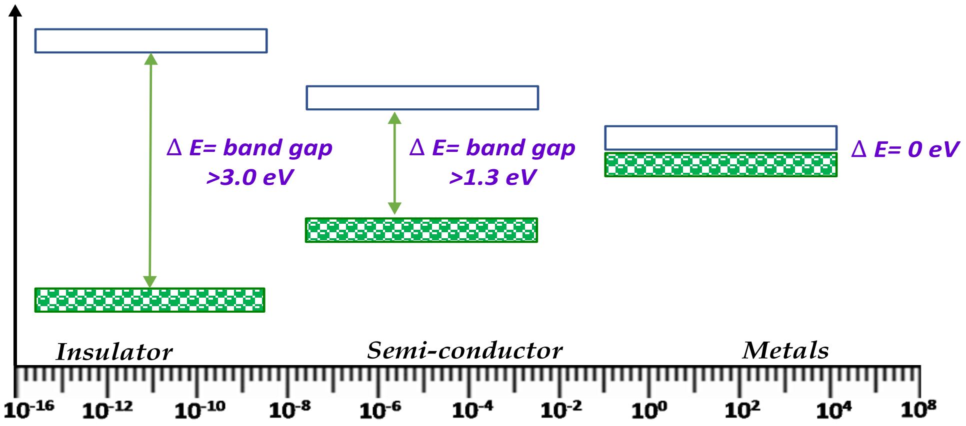

Figure 1.3 Energy profile band gap diagram of different materials

Excitonic state refers to the energy state that is located below the band edge (or polaronic state). The mobility of the electrons is connected, and the electrons (holes) are bonded in the excitonic state. Binding energy is the energy difference between the band edge and the excited state (E_{gap}). By absorbing energy, an electron moves from the valance band to the conductance band. A positive charge hole, also known as a positive-charge carrier, is produced when an electron departs from the fill electron side. An excitation with a single positive/negative electron charge is known as a positive/negative polaron. Exciton is a neutral excited state, whereas a bipolaron is a double-charged excited state. Exciton is often used to explain conveying a dipole in a simplification.[10] The idea of polarons and bipolarons has been used in **Figure 1.4**. to describe the process of conduction and the behaviour of charge carriers in CPs.

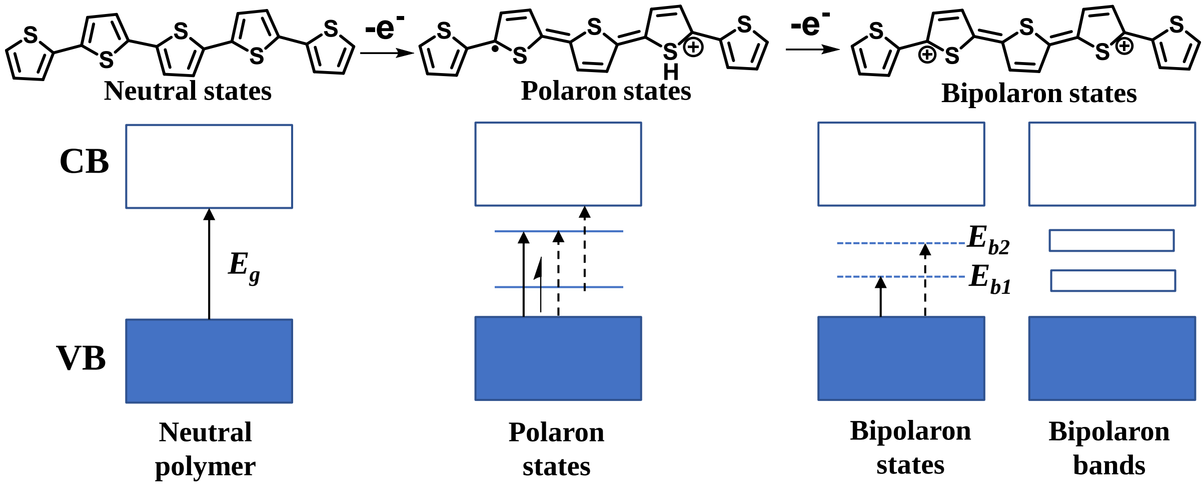

Figure 1.4 Energy levels diagram of neutral polymer, polaron, and bipolaron

The term “polaron” refers to a radical cation that is partially delocalized over a polymer segment. When an electron is withdrawn from the top of the valence band of a conjugated polymer but does not fully delocalize, a vacancy (hole or radical cation) is formed. Two things can happen when one electron is taken out of the polymer holding the polaron that has previously undergone oxidation: In order to form a “bipolaron”, this electron must first either create a second independent polaron or be removed from the first polaron level.

Polymers often produced polarons at low doping concentration but bipolarons at high doping concentration. Polarons are doubly charged although spin less than bipolarons. Additionally, structural distortion is connected to the bipolaron. The bipolaron's two positive charges work in tandem. Since resonance only happens in an electric field, polarons and bipolarons may both flow along the polymer chain. If multiple bipolarons are created, the band gap will be narrowed and the resulting narrow bipolaron bands will make the system's electron flow easier. CPs are peculiar system to conduct current without having a partially empty or partially filled band. Simple band theory cannot be explained their electrical conductivity.

1.1.3 Impact of doping and dopants on conductivity

A dopant, also known as a doping agent, is a very minute impurity that is added to a substance (in extremely low concentrations) to change its electrical or optical characteristics.[11]

Table-1.1 Stability and processing attributes of some conducting polymers.

POLYMER	CONDUCTIVITY (S/cm)	STABILITY (doped state)	PROCESSING POSSIBILITIES
Polyacetylene	10^3-10^5	Poor	Limited
Polyphenylene	1000	Poor	Limited
PPV	1000	Poor	Limited
PPS	100	Poor	Excellent
Polypyrrole	100	Good	Good
Polythiophene	100	Good	Excellent
Polyaniline	10	Good	Good

Conductivity of conducting polymer is influenced by the polymer's physical treatment, separation and purification methods, and synthesis process.[12] As the degree of crystallinity rises, electrical conductivity also increases. The degree of crystallinity in polymers may often be increased by mechanical stretching and heat treatment. The conductivity is significantly influenced by the dopant content. Impurity presence alters the conductivity of the doped polymer. [13]

Doping is the process of chemically oxidizing or reducing a polymer to yield it in its conductive state. The degree of a polymer's enhanced electric conductivity is mostly determined by the dopant's chemical compatibility with the polymer. Different polymers cannot benefit from the same dopant. The stability of conducting polymer is significantly influenced by the dopant's nature. The degree of doping has a direct impact on the conductivity of polymers. As the polymer is exposed to the dopant vapour for a longer period of time, the doping level rises. At times, a relatively slight increase in the dopant molar concentration is accompanied by a rapid increase in conductivity. [14] This sudden rise may be caused by the quick increase of charge carriers in mobility, which is brought on by interchain contact. In most cases, doping is quantitative, and the carrier concentration and dopant concentration are directly inversely correlated. Positive or negative charge carriers emerge in the polymers as a result of doping. [14-17]

Polymer + Dopant = $(\text{Doped polymer})^{+}$ + Dopant^{-}

Polymer + Dopant = (Doped polymer)$^-$ + Dopant$^+$

Doping causes the polymer chains to be rearranged, which creates new, ordered structures. Up to 50% of the mixture may include dopants. Additionally, adding dopant molecules causes a significant disruption in the chain order in quasi-one-dimensional polymer systems, which causes the polymer to reorganize.[18] Thus, the type and concentration of dopants, uniformity of doping, carrier mobility, crystallinity, and shape of polymers are only a few of the variables that affect the final conductivity in polymeric semiconductors. [14, 15]

1.1.4 Processability of conducting polymer.

CPs are usually insoluble and infusible and have a low processability. Low solubility is a result of the π -conjugated polymeric backbone's inherent rigidity. Because of this, large-scale processing is highly challenging and prohibitively expensive. By include flexible centers and links in the chain, chain flexibility may be increased, as can processability. Processability has improved when hard CPs are blended with processable polymers. In addition to improving processability, blending or mixing the CPs with their non-conducting processable counterparts also boosts the essential mechanical strength, adhesion, and environmental stability.[19, 20] By using the block copolymerization procedure, the conjugated chain's stiffness may be reduced and its processability increased.

1.1.5 Application of conducting polymer

Conductive polymers’ applicability is constrained by their low processability. However, there are some drawbacks because of the high manufacturing costs, material inconsistencies, toxicity, poor solubility in solvents, and impossibility of direct melting processes. They show promise in antistatic materials, [21] commercial displays,[22] and batteries, [23] but also have some limitations. Additionally, they show promise for organic solar cells,[24, 25] printable electronic circuits,[26, 27] organic light-emitting diodes,[28, 29] actuators, [30] electrochromism,[31, 32] supercapacitors,[33, 34] chemical sensors, [35, 39] and biosensors, [40, 41] transparent flexible displays, logic gates, and electromagnetic shielding [42] and possibly replacement for the popular transparent conductor indium tin oxide (ITO). [43, 44] CPs are rapidly ahead attraction in new applications with increasingly processable materials with better electrical and physical properties. The new nanostructured forms of conducting polymers provide a big platform in this field owing to their higher surface area and better dispersibility. With the availability of stable and reproducible dispersions conducting polymers have gained some large-scale applications shown in **Figure 1.5**.

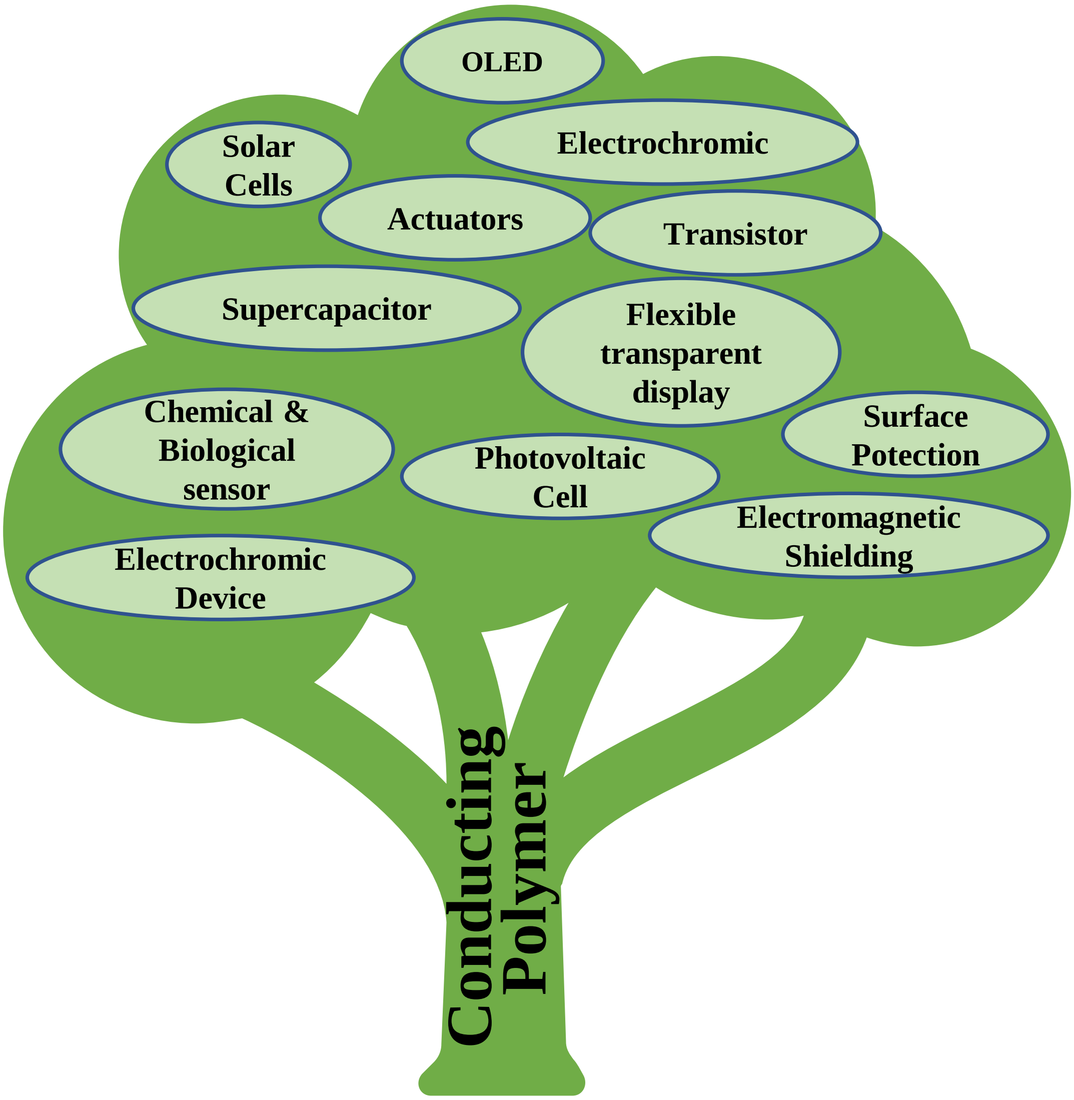

Figure 1.5 Diagram of the application of conducting polymer

1.2. Polyaniline

1.2.1 History and Background

Since it created well-formed crystalline salts with acids like sulfuric and phosphoric acid etc., the aniline monomer, also known as “Krystallin”, was initially synthesised by the pyrolytic distillation of indigo. A colourless oil in indigo was also discovered by Fritzsche in 1840. He named it aniline, presumably from the Spanish word for añil (indigo) and by oxidization it forms PANI. Although the first conclusive report of PANI did not appear until 1862, some experts still hold that it was the first occurrence of PANI.

The first article in 1862 reporting the synthesis of “Aniline Black” was made via an electrochemical process from aniline that had undergone anodic oxidation, and it was followed by a color shift when the voltage was changed, which was later referred to as electrochromic.[45, 46] The electrical qualities should have been tested at that time, though, which was regrettable. For the first time, MacDiarmid discovered in 1985 that aniline monomer in an acidic aqueous solution (for example, 1.0 mol/L HCI) could be chemically oxidized by ammonium peroxy-di-sulphate (APS) to obtain green powder of PANI with a conductivity of up to 3 S/cm, as measured by four probe method. This result was published in 1986 as the first instance proton doped conducting polymer, which was later referred to as "proton doping".[47] PANI has several advantages over other conducting polymers, including simple production, environmental stability, affordability, a unique proton doping process, and physical characteristics that may be altered by both the oxidation and protonation states. Due to these distinctive qualities, PANI is a significant player in the conducting polymer family still today.

1.2.2 Chemical Structure of Polyaniline

PANI can be found in several forms with various chemical and physical characteristics. Depending on the technique of synthesis, PANI can exist in three different states like fully oxidised (pernigraniline), partially reduced (emeraldine), and fully reduced (leucoemeraldine).

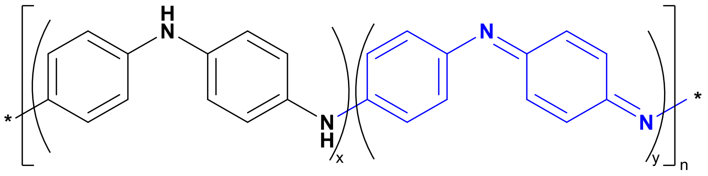

Figure 1.6 Basic chemical structure of polyaniline conducting polymer.

PANI was considered as a hybrid oxidized-reduced state polymer made up of oxidised quinoid and reduced benzoid units. [48] In addition, it was found that, in some experimental setups, PANI exhibited a behavior that could transform between that of a conductor and an insulator. Depending on x and y value from 0 to 1 (**Figure 1.6**), Polyaniline can be observed in one off its five predominant oxidation state.

a. **Leucoemeraldine:** Fully reduced state, x=1, y=0, Pale yellow or colorless.
b. **Protoemeraldine:** 75% reduced and 25 % oxidized form (amine content 75 % and imine content 25 %) of PANI, Light green color.
c. **Emeraldine:** Green or blue, the emeraldine (x=y=0.5) form of PANI, often referred to as emeraldine salt (ES) green in color and emeraldine base (EB) blue in color.
d. **Nigraniline:** Amine content 25% and imine content 75%, blue or dark blue in color.
e. **Pernigraniline:** Fully oxidized state (x=0, y=1) with imine links instead of amine links, violet in color.

The oxidation forms of the polymer at y=0, 0.5, and 1 are denoted by the states leucoemeraldine, emeraldine, and pernigraniline respectively, either in the form of protonated emeraldine salt or emeraldine base. According to literature, the three states or physical combinations of these elements are the most typical manifestations of PANI.

The most common and neutral form of PANI is emeraldine base (EB) (x=y=0.5), when it is protonated the imine nitrogen by any acid or doped, it becomes emeraldine salt (ES). The degree of protonation depends on its pH and oxidation state. Complete protonation of the imine nitrogen atoms in emeraldine base by aqueous acids results in the formation of a delocalized polysemiquinone radical cation and is accompanied by an increase in many times.[49]

Both perignaniline and emeraldine can create stable salts or bases. Due to its great room temperature stability, the emeraldine base form of PANI is thought to be the most useful form. PANI has recently awaken the interest of researchers because to its simple synthesis process, low production costs, strong electrical conductivity at ambient temperature, good environmental/thermal stability, and straightforward doping/dedoping chemistry, among other advantages. [47, 50, 51]

Polyaniline has an electrical conductivity of 10 S/cm, which is both lower than that of conventional metals (>104 S/cm) and greater than that of other popular conducting polymers (insulators, 10-9 S/cm). This range of conductivity (1–10 S/cm) is consistent with the polymer's semiconducting nature. [52, 53] It is instructive to quickly examine the chemical structure of polyaniline before moving on to distinct characteristics and morphology (**Figure 1.7**). The polymer made up of repetitive units that are simultaneously reduced and oxidized. The big three forms of PANI can change from one to the other by straightforward oxidation and reduction under suitable chemical or electrochemical conditions. [53]

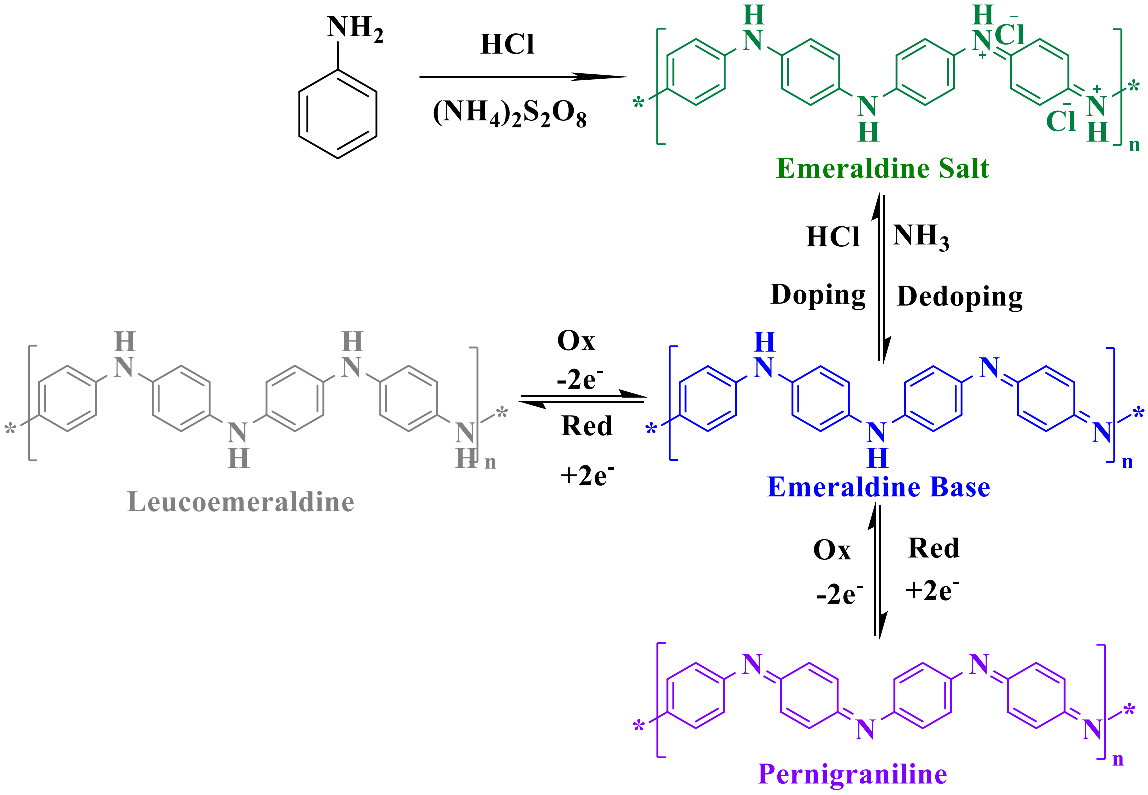

Figure 1.7 Red-ox reactions between the different forms of polyaniline.

1.2.3 Mechanism for Polymerization

Three crucial processes are involved in the formation of any polymer: (1) initiation (2) chain propagation and (3) termination. In the case of PANI, this is also true. The first step involves the interaction of two cation radicals to produce a dimer, p-aminodiphenyl amine, which can then undergo further oxidation to produce a PANI chain when aniline monomers are added. Aniline initially polymerizes slowly, but after oligomers are produced, they react with aniline much more quickly to make polymers. It anticipated that chain elongation would continue when aniline molecules are added in para-positions. It is generally known that the aniline constitutional units in PANI chains are connected in para-positions

Step 1: Initiation (Oxidation of Monomer)

Aniline is oxidized in the first step (**Scheme 1.1**) to produce a radical cation that has three resonance forms. Since it is the reaction's slowest stage, this one is known as the rate-determining step in aniline polymerization. A polymer chain is built from an active center that is established during initiation. One or two radicals are produced from the starting molecules in the first step.

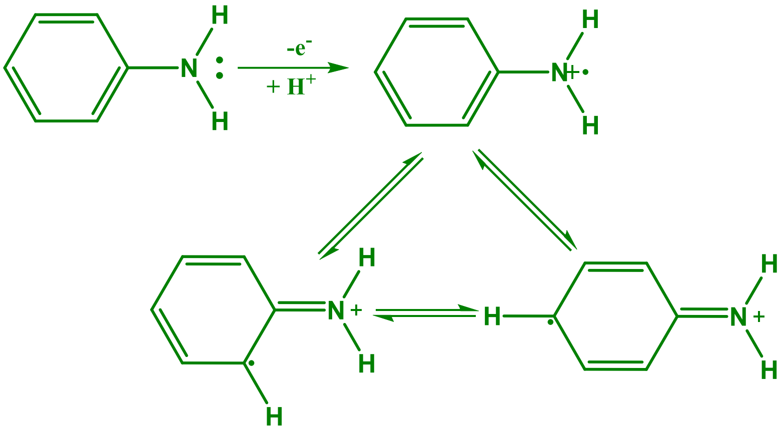

Scheme 1.1 Oxidation of aniline (monomer) during polymerization

Step 2: Radical coupling and re-aromatization

Radicals are transported from the initiator molecules to the existing monomer units in the second step. In this step N- and para- radical cations of aniline are couple with head to tail fashion, forming a dicationic dimer species (**Scheme 1.2**).

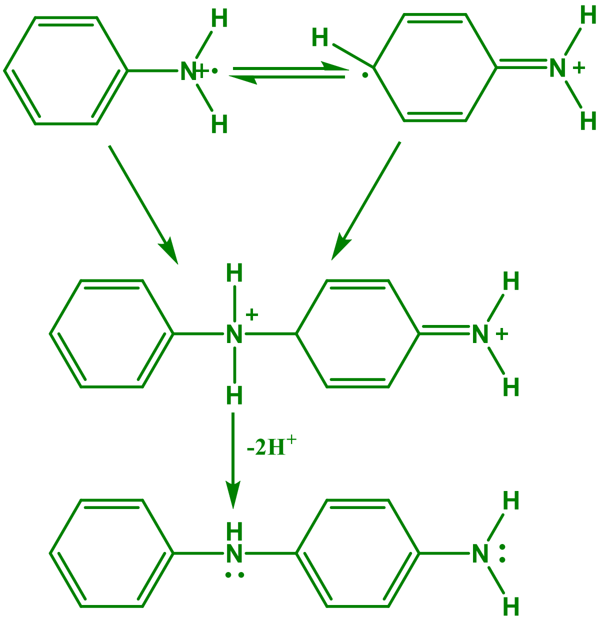

Scheme 1.2 Radical coupling and re-aromatization during polymerisation of aniline.

This dimer further undergoes the process of re-aromatization by losses of proton come to neutral state, yielding a dimer of aniline.

An aniline molecule is then added to a nucleate trimer to produce a tetramer that contains the phenazine component (**Scheme 1.2**). As an initiating center, the protonated tetramer phenazine structure functions. This piece initiates the growth of polyaniline chain at pH<2.5, in this stage anilinium cations as monomers are added in the propagation step.

Step 3: Chain propagation

In propagation step of polymerization PANI chains grow up in the protonated pernigraniline form (**Scheme 1.3**). Pernigraniline must be protonated at a pH of 2.5 in order for polymerization to take place.

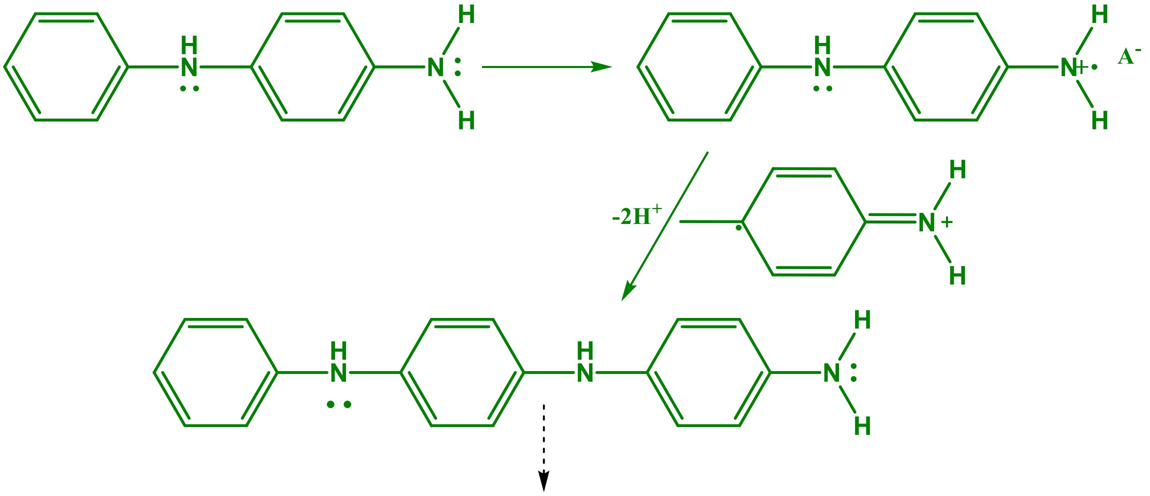

Scheme 1.3 Chain propagation of aniline during polymerization

Due to the polaronic charge delocalization along PANI chains, growth through the para position of the PANI chain is energetically more advantageous. As a result, only para locations are used to add anilinium molecules to expanding chains. Once chain growth has begun, the system's oxidation potential decreases and favours the growth of polymer chains over the emergence of new nucleates. The chains are made up of hundreds of aniline units joined in para locations because the rate of propagation is larger than the rate of initiation (**Scheme 1.3**).

Step 3: Termination

The chains are terminated by either hydrolyzing the amino group at the end or by reacting with certain process intermediates or finished chains. According to certain research, with the addition of a new monomer and an oxidant, the terminal aniline units may still become active even after the polymerization and encourage further chain elongation.

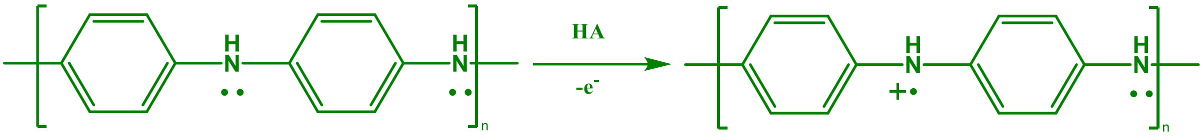

Scheme 1.4 Termination of Polyaniline chain

1.2.4. Synthesis methods of Polyaniline

There are numerous techniques used to produce polyanilines, including

A. Chemical synthesis[47, 54-56]
B. Electrochemical synthesis[57-59]
C. Vapor-phase deposition (VDP) processes[60]
D. Enzyme catalyzed polymerization method[61-63]
E. Mechano-Chemical method[64]
F. Plasma polymerization[65] *etc*.

However, chemical and electrochemical techniques are the most widely used and prevalent approach for polymer production. In other cases, rare processes including enzyme-catalysed polymerization, photochemical polymerization, and mechanochemical polymerization are also used. In the process of chemical synthesis, oxidants (including $FeCl_3$, H_2O_2, ammonium persulfate $(NH_4)_2S_2O_8$, $KMnO_4$, $HAuCl_4$ *etc*.) are used at low temperatures to oxidise aniline. Once more, aniline is oxidised for polymerization in the case of electrochemical polymerization by providing a potential voltage also, and then it is electrodeposited onto the substrate. These two well-liked techniques are often utilized to fabricate PANI in large quantities and with high stability.

1.2.4. (A) Chemical synthesis of PANI

In general, aniline is oxidatively polymerized in an acidic media to create the conducting form of PANI, also known as the emeraldine salt form of PANI. [44, 55, 56, 66] **Figure 1.8** describes the schematic illustration for aniline's chemical polymerization. This common chemical polymerization procedure involves adding aniline while stirring continuously to an ice-cold acidic solution (1M HCl, H2SO4, or any other organic carboxylic acid, such as sulphonic acid).

$$\text{Aniline + Dopant Acid} \xrightarrow[0\text{-}25^0\ C]{\text{Oxidant}} \text{Polyaniline (Emeraldine salt)} \xrightarrow[NH_3]{NH_4OH} \text{Polyaniline (Emeraldine Base)}$$

At a temperature between 0 and 5^0 C, an aqueous solution of an oxidant (such as ammonium peroxydisulfate, $FeCl_3$, etc.) is added with continuous stirring for 30 minutes. The resultant solution is maintained at a low temperature for 24 hours after being well mixed. The deep green precipitate is filtered, followed by numerous washes with water and methanol to remove oligomers, unreacted aniline, and APS.

The resultant green product has spent the night being dried in a vacuum oven at 60^0 C. The final product has a conductivity of ~$10\text{-}10^{-3}$ S/cm and is in the form of emeraldine salt.

The conductivity of the produced materials has changed depending on the size of the PANI fibers and the dopant structure.

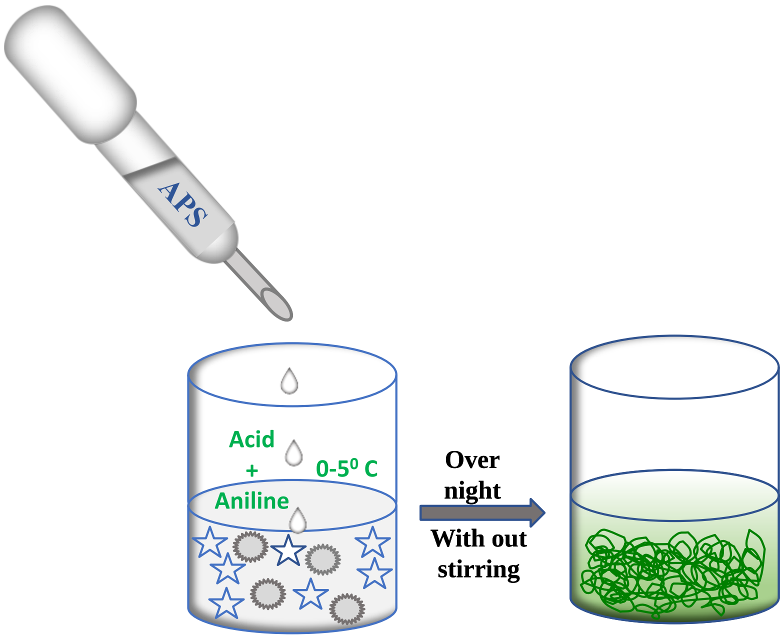

Figure 1.8 Schematic presentation of chemical synthesis procedure for polyaniline

By treating the resultant deep green emeraldine salt form with diluted NH_4OH, the emeraldine base form can be changed to its blue/violet color.

1.2.4.(A).1 Influential Factors for the Chemical Oxidation of Aniline

There are many factors that are affecting the conductivity, yield, morphology and reaction rate of the chemical synthesis of polyaniline. Four major parameters that have impact on the reaction and nature of final product are:

a. **Duration of the reaction:**

The characteristics of the polymer have not been considerably impacted by the polymerization time. When the oxidant [APS]/[Aniline] molar ratio **r>1.15**, the percentage yield of the PANI increases with time (0–2h). Following that, the length of the reaction has no impact on the yield, conductivity, and elemental makeup of the polymer. Longer polymerization times result in a modest increase in the polymer's intrinsic viscosity.[67]

b. **Effect of temperature:**

In contrast to oxidation-reduction reagents, which shorten the induction time, chemical oxidation consists of two steps: a fast exothermic step that is temperature-dependent and varies with the concentration of the oxidant. The slow endothermic step depends on the pH, temperature, and concentration of the reactants while the dissolved oxygen in the solvent has no effect. It is extremely exothermic to add aqueous solutions of the oxidant (APS) to the reaction medium that contains the aniline monomer. Therefore, cooling the polymer reaction medium before oxidant addition is required to prevent local heating and potential crosslinking of the lengthening PANI chains. The ideal range for low-temperature polymerization is 0 to 5° C. With a drop in polymerization temperature, the PANI's intrinsic viscosity rises.[67g]

c. Concentration of the oxidant:

In addition to dopant, oxidant is crucial for the chemical procedure of polymerization reaction of PANI. Due to its high oxidational potential (E=2.05V), ammonium persulphate was the most commonly employed oxidant. The electrical conductivity of the generated PANI is only slightly influenced by the oxidant [APS]/[Aniline] molar ratio. However, it was discovered that the ratio had a significant impact on the yield and viscosity of the polymer. The [APS]/[Aniline] ratio grows linearly with the polymer yield. When the aforementioned mole ratio (**r**) is less than 1.15, the yield, elemental composition, conductivity, and degree of oxidation of the resultant polymer are mostly independent of **r**. However, when **r>1.15** occurs, the PANI is overoxidized, which causes a reduction in the conductivity and yield of the polymer as well as a noticeable change in morphology.

d. pH of the medium:

Aniline or anilinium salts, such as aniline hydrochloride or aniline sulphate, are generally chemically oxidised to produce PANI in an acidic aqueous media in the presence of an oxidant. When aniline (**Scheme 1.2**) molecules are coupled to oligomeric and polymeric structures, hydrogen atoms are extracted from the molecules and released as protons, creating acid as a byproduct. As a result, pH always drops as aniline oxidation proceeds.[68]

The ratio of neutral aniline molecules to anilinium cations varies with the acidity of the reaction media. At pH 4.6, two species - neutral molecules and anilinium ions - coexist in equal numbers. At increasing pH levels, neutral aniline molecules will prevail. Aniline molecules have a lower oxidation potential than anilinium cations. Therefore, oxidizing neutral aniline molecules advances without difficulty, whereas oxidizing anilinium cations is challenging.

Distinct forms of oxidations show up in real-world oxidation tests as different acidity profiles, or the time-dependence of pH.[68, 69]

1.2.4. (B) Electrochemical synthesis of PANI

The electrochemical polymerization (ECP) technique for polymerizing aniline to PANI has recently attracted a lot of scientific attention. [57-59] This is primarily because ECP offers better control over the beginning and ending stages of polymerization. Second, in ECP it was anticipated that the product would be produced in a reasonably pure form (no extra chemicals, such as surfactants or oxidants, are utilized in this process).

$$\begin{array}{c}\textbf{Aniline + Dopant}\\ \textbf{Acid}\end{array} \xrightarrow{\textbf{Voltage}} \begin{array}{c}\textbf{Polyaniline}\\ \textbf{(Emeraldine salt)}\end{array}$$

The electrochemical polymerization is frequently accomplished by using one of three approaches to an aqueous solution of aniline: (i) a constant voltage (potentiostatic), (ii) a variable current and voltage (potentiodynamic), and (iii) a constant current (galvanostatic).

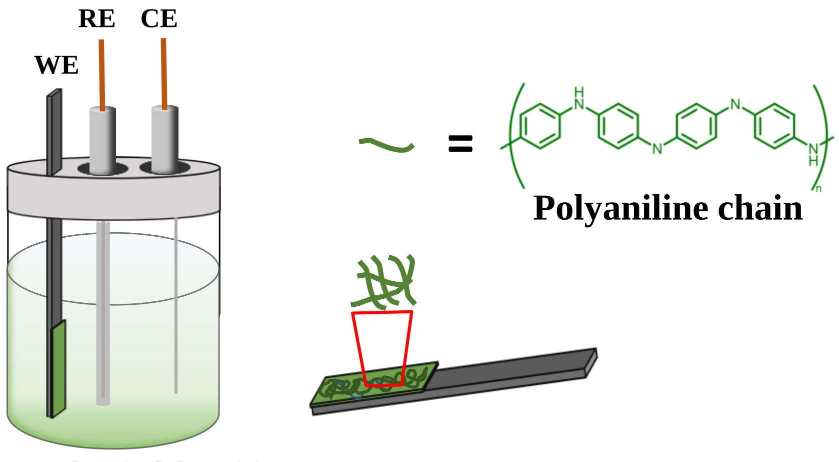

Figure 1.9 Schematic presentations for electro-chemical synthesis of polyaniline

In the ECP technique, three electrodes, a counter electrode (Pt wire), a reference electrode (Ag/AgCl), and a working electrode are dipped into an electrolyte solution, such as an acid (HA).

1.2.4. (C)Vapor-phase deposition (VDP) processes

Vapor-phase deposition (VDP) technologies are used to directly build the PANI thin films (in the form of emeraldine salt) on substrates without the need of any extra doping procedures shown in **Figure 1.10**.

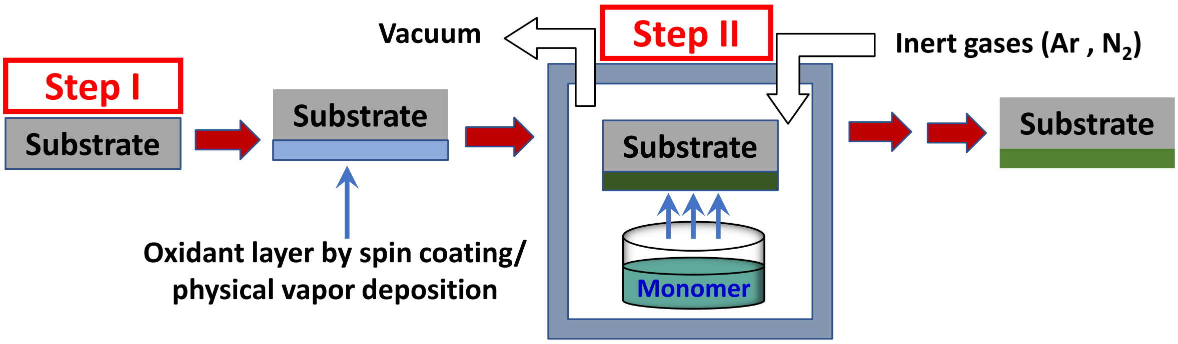

Figure 1.10 Schematic presentations of Vapor-phase deposition for synthesis of polyaniline

Aniline monomer is polymerized in vapour phase to produce PANI thin films, which are then grown directly on substrates for polymeric films. The oxidants are prepared and coated on a clean substrate in this procedure first (like PET, PVC, PS etc.). In a reaction chamber at various temperatures, dried oxidant substrate sheets are exposed to aniline vapour. In order to eliminate unreacted oxidant, aniline monomer, and by-products from the grown films of conductive PANI after polymerization, the films are washed with water/methanol many times and dried to get thin films of PANI. [60]

1.2.4. (D) Enzyme catalyzed polymerization method

In aqueous organic conditions with neutral pH, the enzyme-catalyzed reactions are typically conducted at room temperature. Aniline is converted to PANI when an oxidoreductase enzyme, such as horseradish peroxidase (HRP) or soybean peroxidase (SBP), is present. [61] Using polyelectrolyte templates including sulfonated polystyrene,[62] poly (vinyl phosphonic acid)[63b], and deoxyribonucleic acid (DNA), among others, the majority of enzymatic polymerization of aniline was conducted. Enzymatic oxidation of aniline to PANI also produces no by-products, preventing salt contamination of the reaction medium. However, PANI fibres have been spun from an enzymatically created, water-soluble version of PANI.

1.2.4. (E) Mechano-Chemical method

A solid anilinium salt can be used as the starting moiety in solid state polymerization of aniline, which is achievable at room temperature. Because aniline is basic in nature, it produces solid salts with doping acids (such as HCl, H_3PO_4, CSA, etc.) through an acid base reaction. [70] The reaction is caused by ball-milling an aniline salt and an oxidant under ambiguous circumstances, according to a recent study by Kaner et al. The reaction of CSA and aniline in water, followed by the evaporation of the solvent, produces the salt of aniline-acid. In a grinding bowl made of stainless steel, the solid precursor is added and then sealed. The substance was put into a beaker once the spinning stopped. The yield can be achieved upto 65 % by utilising a 1:1 molar ratio of anilinium salt to oxidant after many rounds of washing with water/methanol. The preparation of a significant amount of the conducting PANI is now made straightforward and solvent-free by this process.

1.3. Properties of Polyaniline

1.3.1. Optical Properties

Figure 1.11 displays the UV-Vis spectroscopy investigation of polyaniline. The relative oxidation state of PANI may be determined using the spectroscopic technique extremely effectively. The PANI samples generate a deep green product known as “emerald salt” when doped with acid.

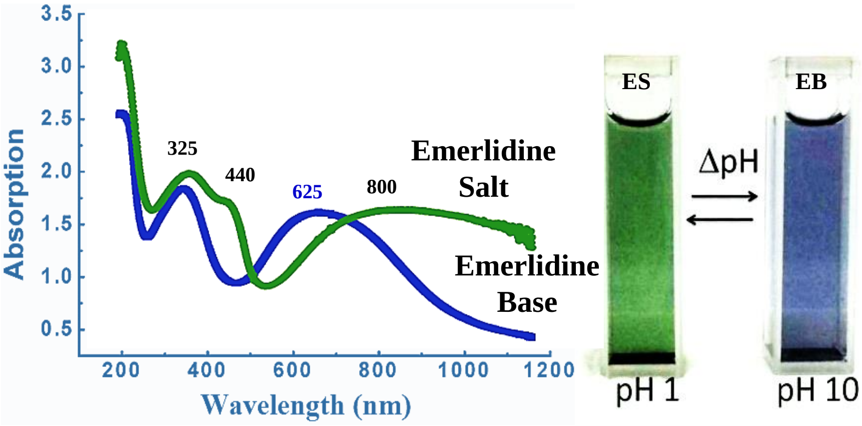

Figure 1.11 (a) Digital photograph (b) UV-vis spectra of emerlidine base and emerlidine salt form of PANI at pH 10 and pH 1 respectively.

This product is easily transformed into a violet/blue colour emeraldine base state by simple base treatment (**Scheme 1.4**). Three distinctive absorption peaks, with their centres at 325, 435, and 820–900 nm, are seen in the emeraldine salt form of PANI. The peak for the π–π* transition in the benzenoid rings, polaron–π* transition and the π–polaron transition, respectively. [71-73] UV-visible spectra of the emeraldine base form of PANI show two peaks at 325 and 630 nm, which are assigned to the amine and imine segment of PANI. In emeraldine salt form of PANI the peak 630 nm disappeared and a new peak at ~820 nm is appeared but the position of the 325 nm peak is not changes although the intensity of the peak decreases. These indicate that the protonation process only takes place on the imine segment of the emeraldine PANI chain.

The presence of these peak at 630 nm and 820 nm are strongly implies the PANI emeraldine base (EB) and emeraldine salt (ES) form of PANI respectively.

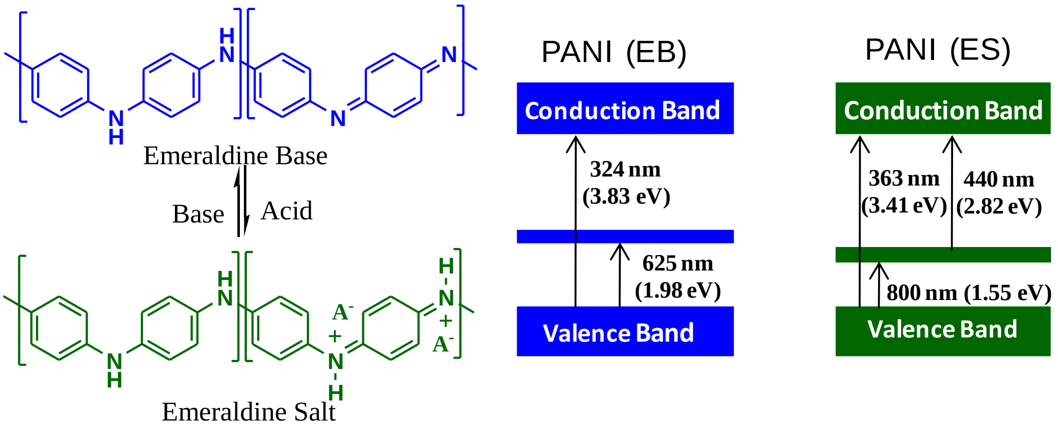

Figure 1.12 Band gap and conduction mechanism of emeraldine base and salt form.

This peak intensity greatly depends on the pH of the medium and polymerization time. The peak intensity as well as peak sharpness of π→polaron transition depends solvent polarity also.[72, 74]

1.3.2. Structural Properties

1.3.2.1 FTIR Study

Infrared (IR) spectroscopy is a powerful analytical tool used to determine the structural characteristics of PANI nanostructures as shown in **Figure 1.13**. The presence of characteristic stretching bands at approximately 3430 cm^{-1}, 1566 cm^{-1}, 1490 cm^{-1}, 1300 cm^{-1}, 1125 cm^{-1}, 1037 cm^{-1}, and 795 cm^{-1} signifies the successful formation of polyaniline. Specifically, the stretching bands at ~3430 cm^{-1}, 1566 cm^{-1}, and 1490 cm^{-1} correspond to γ N-H, highly hydrogen bonded γ C=C of quinoid rings, and γ C=C of benzenoid rings, respectively.

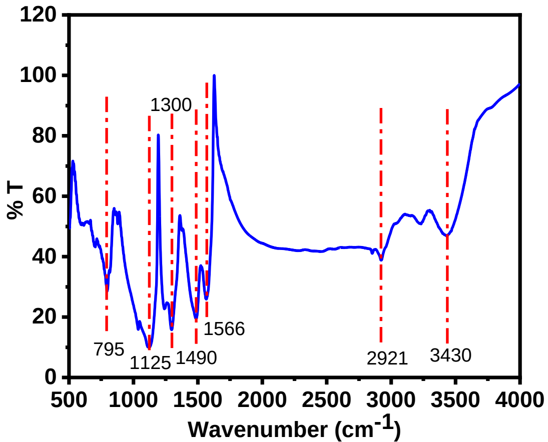

Figure 1.13 characteristic FTIR spectra of emerlidine salt (ES) form of polyaniline.

Additionally, the bands at 1300 cm^{-1}, 1125 cm^{-1}, and 795 cm^{-1} represent γ C-N of the secondary aromatic amine, aromatic in-plane deformation of the 1,4-disubstituted benzene, and out-of-plane deformation of the same benzene, respectively [71-73]. The $I_{benzenoid}/I_{quinoid}$ (I_B/I_Q) ratio plays a crucial role in determining the form of polyaniline present. It provides insights into the percentage of imine and amine units within the polymer chain. An I_B/I_Q ratio of 1 suggests the presence of emeraldine form, $I_B/I_Q \geq 1$ indicates leucoemeraldine form, and $I_B/I_Q \leq 1$ implies pernigraniline form of polyaniline. Furthermore, the concentration of the dopant significantly influences the structural properties of polyaniline, which is reflected in the IR spectra. For instance, Wan et al. demonstrated that with increasing concentration of HCl dopant from 0.2 M to 2.0 M, the band at 1125 cm^{-1} (at 0.2 M) shifts to 1180 cm^{-1} (at 2.0 M). This shift indicates a greater localization of electrons in the PANI chain due to the variation in dopant concentration. [75]

Table 1.2 Absorption frequency (cm^{-1}) of various Functional group

Functional Groups	**Absorption frequency (cm^{-1})**	**Functional Groups**	**Absorption frequency (cm^{-1})**
γC–H aromatic out of plane deformation for 1,4 disubstituted benzene	795	hydrogen bonded γ C=C of benzenoid rings	1490
γC–H aromatic in plane	1125	hydrogen bonded γ C=C of quinoid rings	1566
γC–N of secondary aromatic amine	1300	γ C–H of phenyl rings	2921
γ N-H	3430		

1.3.2.2 X-ray Powder Diffraction

In our investigation, we utilized XRD analysis to examine the orientation of the conducting polymer, specifically PANI. The XRD spectrum displayed three prominent diffraction peaks at 2θ = 14°, 20°, and 26.0°, as shown in **Figure 1.14**. These sharp scattering peaks strongly indicate the robust crystalline nature of PANI.[71] The diffraction peak centred at 2θ = 20° signifies the periodicity in the direction parallel to the polymer chain, while the peak at 2θ = 26.0° is attributed to the periodicity in the direction perpendicular to the polymer chain.[71, 73] The intensity of the diffraction peaks is directly related to the d-spacing, which is associated with the packing and arrangement of polymer chains.

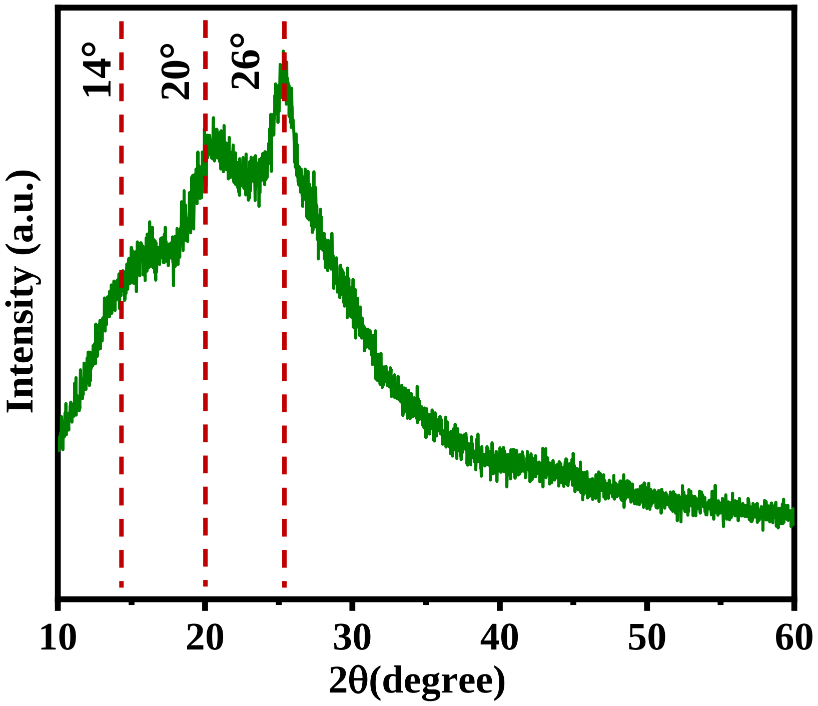

Figure 1.14 Powdered XRD pattern for HCl doped pure PANI.

Notably, an increase in the intensity of the peak at 2θ = 25° suggests improved π-π* inter-chain stacking within PANI. This indicates a more planar chain conformation, leading to the elongation of the effective conjugation length of PANI.[76] This extended conjugation is critical in enhancing the electrical conductivity and charge transport properties of the material.

1.3.2.3 XPS Study

X-Ray Photoelectron Spectroscopy (XPS) of PANI nanotube was performed on a glass surface coated solid sample in the region of 200-800 eV. Strong signals at 284, 399, and 531 eV are due to C1s, N1s and O1s respectively. The deconvoluted spectrum of C1s (region 281-294 eV) was composed of three peaks, position at 284.1 eV (C=C/C-C), 285.3 eV (C-O/C-N) and 287 eV (C=O). Similarly, N1s peak consist of three peaks at 399.1eV (-N=), 401 eV (-NH-) and 402.9 eV (-N^+-). And the O1s peak was combine of two peaks at the peak position of 530.9 eV (C=O) and 532.4 eV (C-O/C-OH)

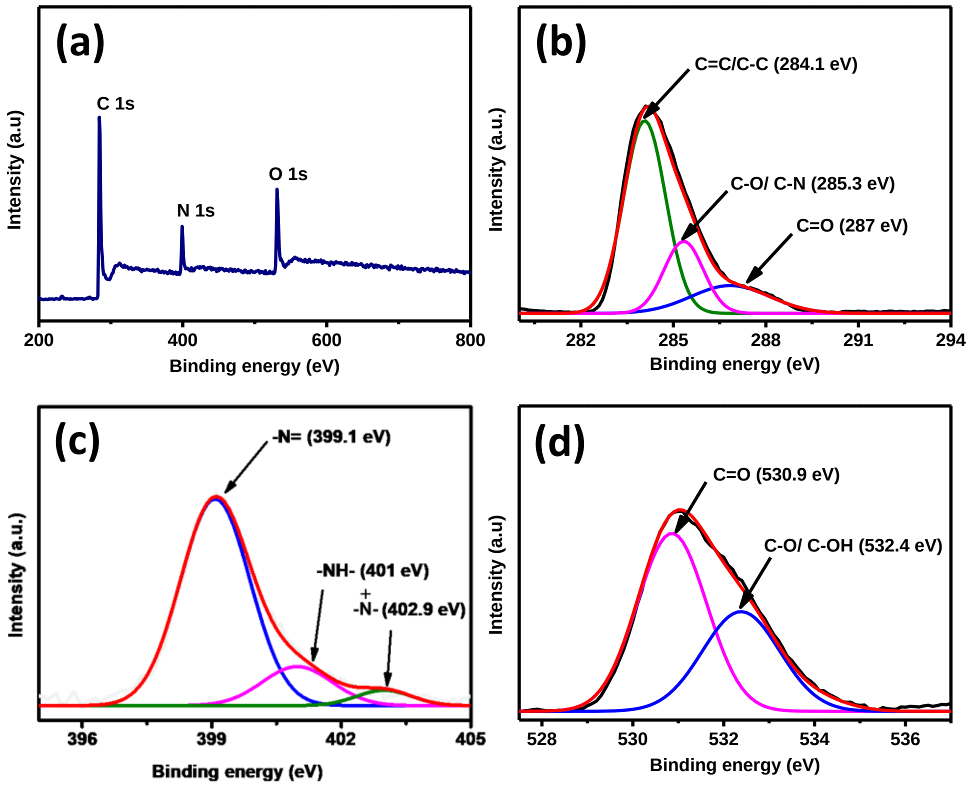

Figure 1.15 XPS results of PANI nanotubes perform on the surface of glass.

1.3.3 Morphological Properties

Intrinsically conducting polymers, such as polyaniline (PANI), have proven to be highly versatile and valuable materials in various research fields. These polymers find applications in sensors, electroluminescent devices, polymer-based electronics, and organic photovoltaic cells, among others, with their functionality depending on their morphology. Numerous factors significantly influence the morphology of PANI, including the nature of the dopant, concentration of the dopant, reaction temperature, solvent, oxidant, and monomer used in the synthesis process. Researchers have dedicated efforts to study the structural effects on device preparation, leading to the development of several methods for fabricating PANI nanostructures. In recent years, substantial progress has been made in the synthesis of PANI micro/nanostructures, and their characteristics have been systematically studied. By carefully adjusting these synthesis parameters, a wide range of PANI micro-/nanostructures, from one-dimensional (1D) to three-dimensional (3D) architectures, have been successfully synthesized. These include single crystalline nanoneedles,[77] aligned arrays,[78] nanotubes,[71-74, 79] nanofibers,[80] nanosheets,[81] and hollow spheres.[82] The "template" polymerization approach is a common procedure used in PANI synthesis, wherein the monomer units are organized in a template-like manner. Various synthesis methods have been reported, including those involving soft templates or without templates. Hard templates, such as nearly monodisperse inorganic oxide nanoparticles and polymer nanoparticles, are often used to control the morphology and structure of PANI during synthesis. This continuous exploration and development of PANI micro/nanostructures hold tremendous promise for advancing the capabilities of these materials in numerous applications. The ability to tailor PANI morphology through controlled synthesis methods enables researchers to optimize its properties for specific applications, leading to the design of high-performance devices and innovative technologies in fields ranging from electronics to energy conversion. As a result, intrinsically conducting polymers like PANI continue to be at the forefront of cutting-edge research, driving advancements in materials science and enhancing the potential for future technological breakthroughs.

1.3.3.1 Hard template based PANI nanostructures

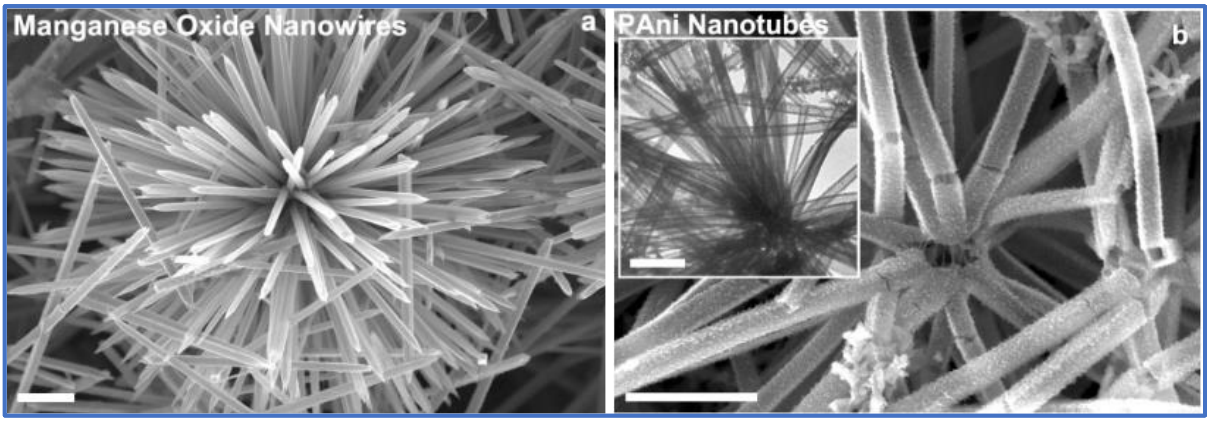

Figure 1.16 Scanning electron microscopy (SEM) images of a) the crypto-melane-phase manganese oxide template and b) the resultant PANI nanotubes. The inset of (b) is the transmission electron microscopy (TEM) image of the PANI nanotubes. The scale bar is 1 µm.

L. Pan et al presented a noteworthy investigation involving the utilization of MnO2 hard templates for the synthesis of fibrous morphologies coated with polyaniline, as depicted in **Figure 1.16** [83]. In their study, they elucidated the intricate interplay between manganese oxide nanowires of varying diameters and the subsequent formation of PANI nanotubes. The researchers systematically explored the impact of template rod dimensions on the resultant PANI structures. Notably, the team successfully generated PANI sphere-brush structures characterized by tube diameters of 76, 192, and 211 nm. These dimensions were achieved by employing template rods with corresponding diameters of 45, 108, and 120 nm.

Through meticulous statistical analyses, it was revealed that the PANI tubes exhibited a substantially larger outer diameter while maintaining a marginally smaller inner diameter compared to the manganese oxide wires used as templates. This discrepancy suggested a distinctive growth pattern, where PANI exhibited a preferential outward expansion.

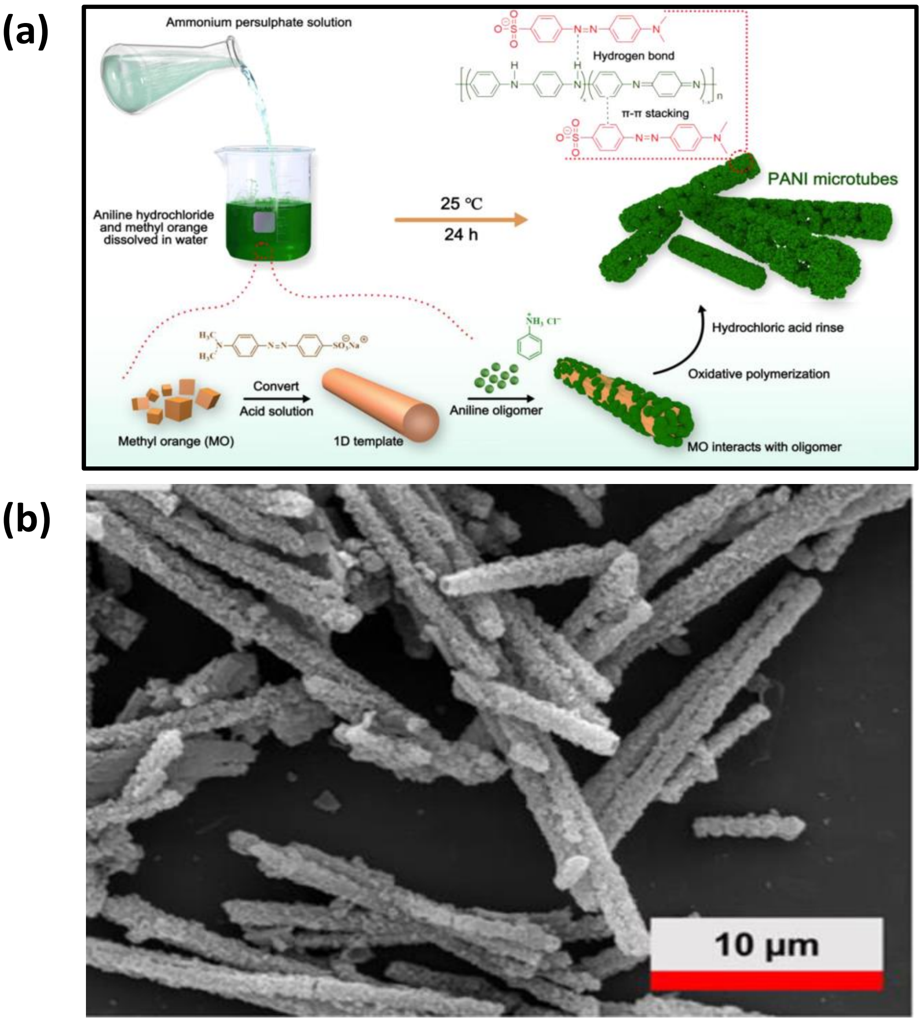

Figure 1.17 (a) Synthesis process and mechanism of the PANI microtubes, (b) SEM micrographs of PANI microtubes prepared in the presence of Methyl Orange as template.

G. Cao et al conducted a comprehensive study, yielding valuable insights into the synthesis of polyaniline (PANI) nanostructures, as depicted in **Figure 1.17**.[84] The researchers embarked on elucidating the impact of the presence of MO (Methyl Orange) on the resultant morphologies of PANI particles. Notably, the conventional PANI nanoparticles synthesized in the absence of

MO exhibited the anticipated aggregated morphology, a characteristic feature observed in their study. Seeking to enhance the synthesis process, G. Cao et al introduced a novel approach resulting in the fabrication of PANI microtubes with varying lengths. By systematically altering the molar ratio of the aniline monomer to MO, the researchers managed to tailor the morphology of the PANI structures. Specifically, when the molar ratio stood at 20, the PANIs manifested short rod-like structures interspersed with amorphous components. Remarkably, by lowering the molar ratio to 15 while concurrently increasing the concentration of MO within the mixture, the PANIs exhibited consistent and uniform tubular structures. This optimization led to the generation of PANI microtubes boasting lengths reaching up to 20 μm, marking a significant achievement in their study.

The findings further revealed that this specific aniline hydrochloride-to-MO ratio represented the optimal condition for synthesizing PANI microtubes with the desired attributes. Notably, even as the concentration of MO continued to increase, the morphology of the PANI microtubes remained relatively unaffected, indicating a threshold beyond which further alterations were minimal.

S. Pang's shows their noteworthy study highlights the surprising effect of different urea/aniline ratios on the shape of polyaniline (PANI) nanostructures, providing important insights into their design and features (**Figure 1.18**) [85].SEM images presented in their study depict distinct PANI nanostructures resulting from different experimental conditions. In the absence of urea, the PANI sample showcases well-defined and densely packed rod-like structures, exhibiting a diameter ranging from 100 to 150 nm. Contrastingly, when urea is introduced, a transformative effect on PANI morphology is observed. The PANI sample synthesized with urea manifests itself as regular and uniform nanotubes, characterized by an inner square aperture. These nanotubes possess average inner and outer diameters spanning approximately 60 to 120 nm and 140 nm, respectively. Remarkably, the side length of the square capillary is around 70 nm, in alignment with SEM observations. An insightful analysis of these findings reveals the significance of these structural variations. The incorporation of urea into the synthesis process imparts the unique feature of nanotube formation in PANI structures.

The presence of larger capillary channels within these nanotubes offer a pivotal advantage, facilitating effective electrolyte infiltration. This, in turn, engenders a higher number of active sites available for electrode reactions, thereby contributing to enhanced electrochemical performance.

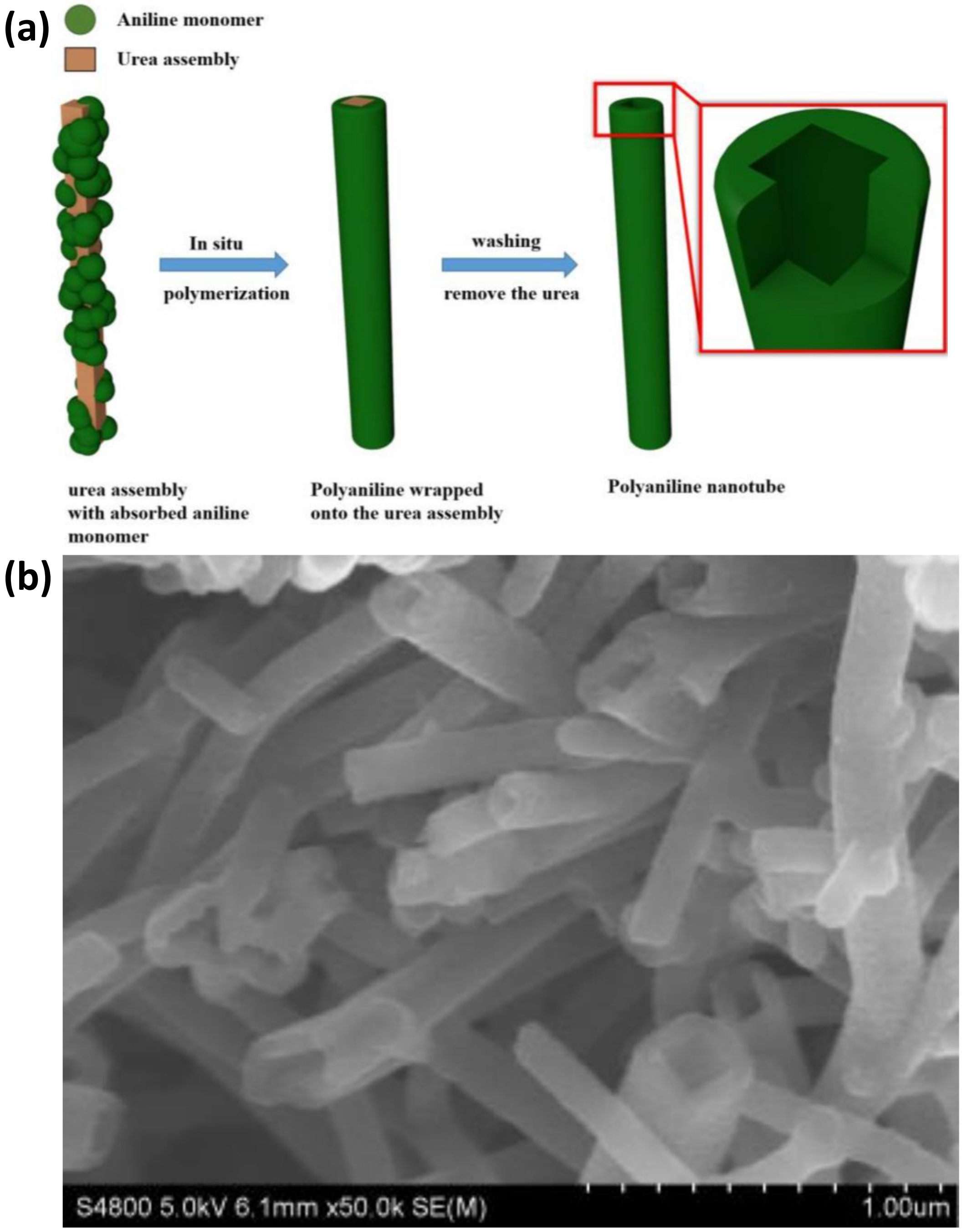

Figure 1.18 (a) Schematic illustration of the synthesis of polyaniline nanotube (b) SEM images of PANI nanostructures at urea/aniline ratios: 3:1.

Moreover, the thinner walls of the PANI nanotubes significantly shorten the charge diffusion distance, leading to accelerated electrode reactions. This dual benefit - comprising larger capillary channels and thinner nanotube walls - favorably influences electrode kinetics by promoting faster charge transfer. The combination of these factors effectively contributes to achieving swift electrode reactions, underscoring the practical utility of these PANI nanostructures in various applications, such as energy storage and advanced electronics.

1.3.3.2. Soft template based PANI nanostructures

In recent years, significant strides have been taken in the realm of polyaniline nanotube synthesis, with a growing focus on adopting "soft templates" or even eschewing templates altogether. The concept of a soft template centers around the integration of surfactants that guide the growth of the polymer within or around self-assembled micelles. This approach has been referred to using various terms in the literature, such as the "template-free" method or the self-assembly method, each highlighting the essence of this innovative strategy [86]. Notably, the term "template-free" denotes the fabrication of these distinctive nanotube structures without the traditional reliance on "hard templates" (**Figure 1.19**). This progressive approach encompasses a straightforward process that leverages a diverse array of soft templates and surfactants.

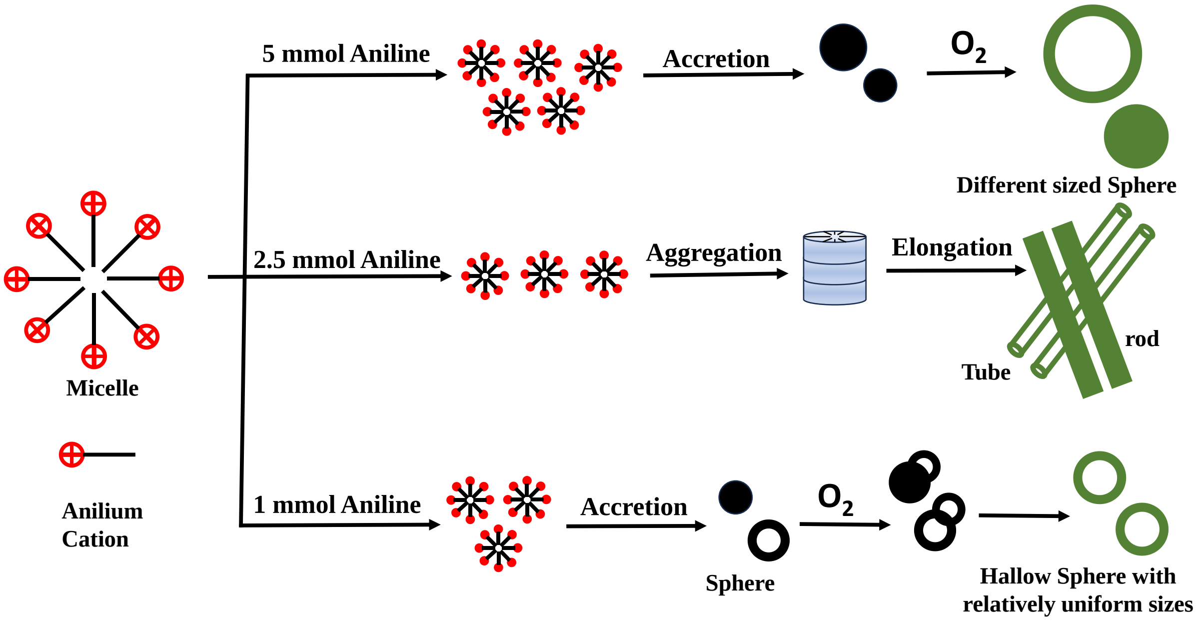

Figure 1.19 Schematic illustration of the synthesis of polyaniline by soft template method.

These dynamic tools play a pivotal role in generating polyaniline nanofibers, capitalizing on their ability to induce controlled growth and organization of the polymer. One hallmark of this strategy is the versatility it affords, with a broad spectrum of soft templates and surfactants being harnessed to orchestrate the creation of polyaniline nanotubes. In particular, acids endowed with bulky organic side groups have been harnessed as effective surfactants in this context. Their strategic incorporation not only facilitates the synthesis of nanotubes but also influences their morphology and properties, rendering them amenable to customization for specific applications. The shift towards soft-template methodologies signifies a departure from conventional approaches that employ rigid templates, unlocking a realm of possibilities for tailored nanotube synthesis. This innovative trajectory underscores the multidisciplinary nature of materials science, bridging chemistry and engineering to engineer intricate nanostructures with enhanced functionalities. As researchers explore the nuances of soft templates, a rich landscape of opportunities emerges for designing advanced materials that hold great promise for various technological frontiers.

Wan et al. introduced a noteworthy contribution in the field by presenting a method for synthesizing highly crystalline polyaniline (PANI) nanotubes and nanofibers with diameters ranging from 80 to 170 nm (**Figure 1.20**). This innovative approach, referred to as the "micelle soft-template" method, involves the utilization of dicarboxylic acids as dopants, each varying in the number (n) of –CH2– groups (n = 0–4). Their study revealed a significant correlation between the number of –CH2– groups in the dicarboxylic acids and the resulting diameter of the nanostructures. It was intriguingly observed that as the number of –CH2– groups in the dicarboxylic acids increased, the diameter of the nanostructures was also increases [87]. This finding underscores the intricate interplay between the molecular structure of the dopants and the resultant morphology of the synthesized PANI nanotubes and nanofibers. Furthermore, a noteworthy relationship emerged between the diameters of these nanostructures and their electrical conductivity. As the diameter decreased, the conductivity of the nanostructures exhibited an increase, highlighting the consequential impact of size on the conductivity properties.

To comprehensively understand the underlying factors governing these outcomes, the research delved into the influence of the length of –CH2– groups within the dicarboxylic acids. This investigation encompassed a thorough SEM study, which provided visual insights into the relationship between the length of –CH2– groups and various aspects of the nanostructures, including their conductivity, crystallinity, morphology, and size.

Malik et al. contributed significantly to the field through their innovative approach, involving the "soft template" synthesis of polyaniline at low temperatures. In their experimental study, they harnessed the potential of benzene tetracarboxylic acid (BTCA) as a dual-functional agent, acting as both a soft template and a dopant [56].

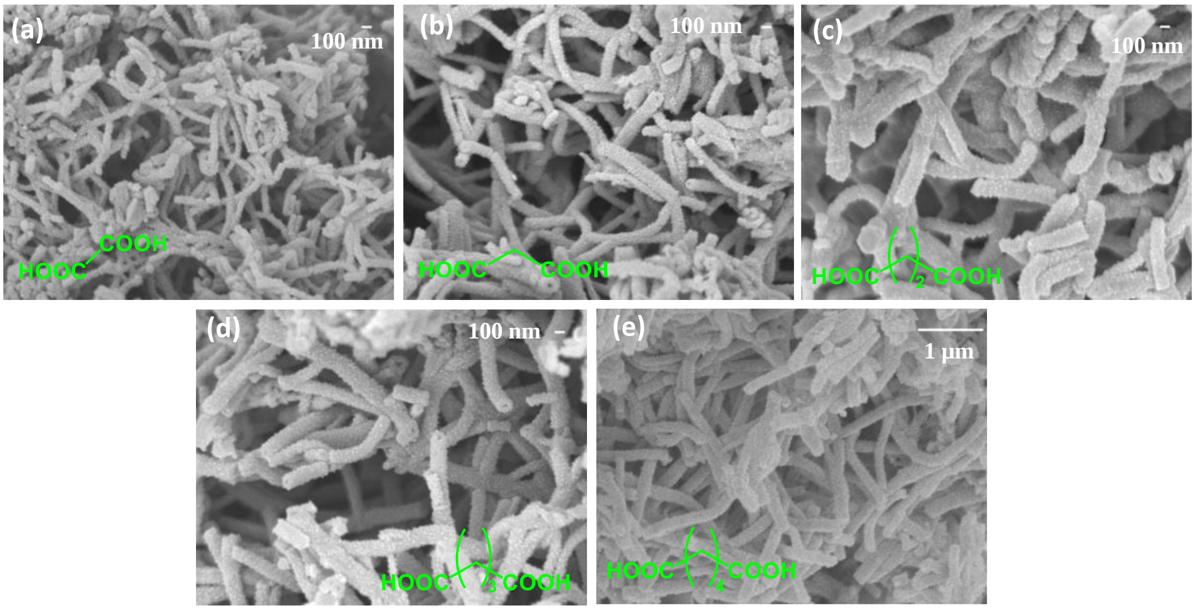

Figure 1.20 SEM images of PANI nanostructures doped with different dicarboxylic acids: (a) OA-PANI, (b) MA-PANI, (c) SA-PANI, (d) GA-PANI, and (e) AA-PANI. Synthetic conditions: [dopant]/[An] = 0.25; 0-4 °C

Table 1.3 Different dicarboxylic acid doped PANI nanostructures and fiber diameter

Name of nanostructures	Dopant acid (- CH_2 group, n)	Diameter of PANI fiber
OA-PANI	Oxalic acid (n=0, OA)	80 nm
MA-PANI	Malonic acid (n=1, MA)	100 nm
SA-PANI	Succinic acid (n=2, SA)	110 nm
GA-PANI	Glutaric acid (n=3, GA)	130 nm
AA-PANI	Adipic acid (n=4, AA)	170 nm

Their work showcased the remarkable capability of this approach to yield unique nanostructures under mild conditions, marking a notable advancement in the realm of polyaniline synthesis. Under carefully controlled conditions of low temperature, a transformative process unfolded over a span of 24 hours. During this period, the collaboration between aniline and BTCA initiated the formation of tube-like morphologies, characterized by their elegant structure, extended lengths exceeding 300 µm, and a finely tuned diameter of approximately 200 nm. This intricate assembly represented a substantial departure from conventional approaches and highlighted the potential of the "soft template" strategy to yield tailored nanostructures with impressive dimensions and characteristics.

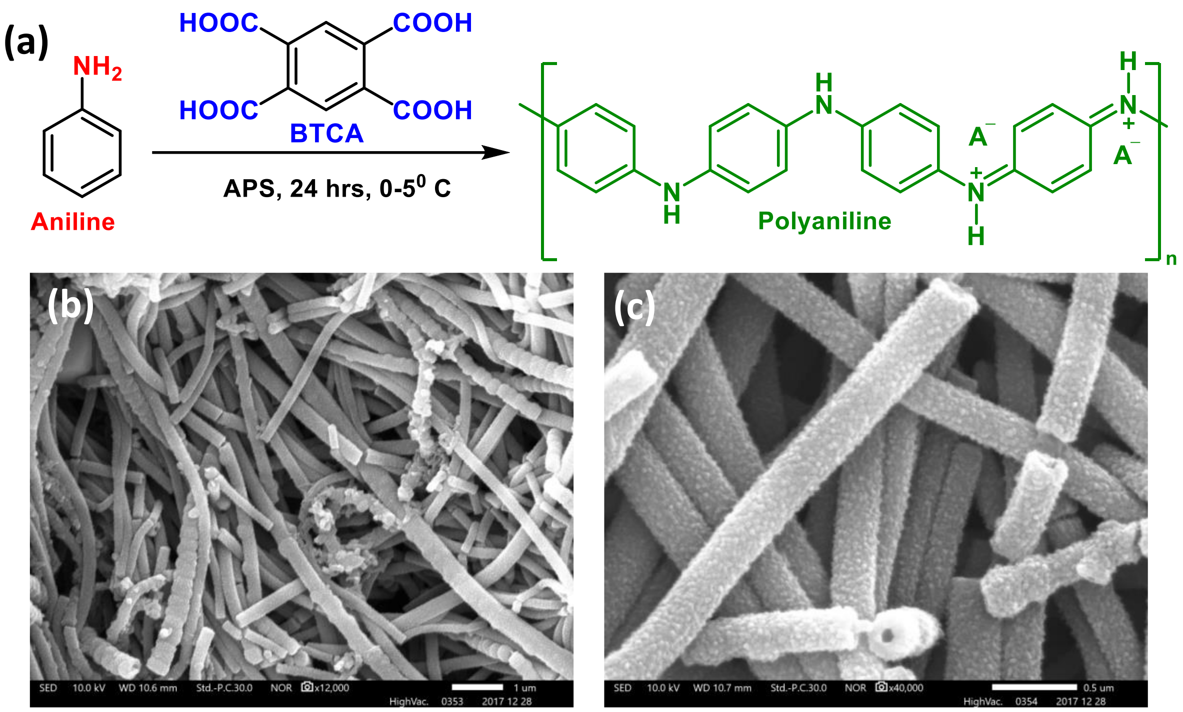

Figure 1.21 (a) Schematic presentations for polyaniline formation by soft template method, (b) FESEM image of BTCA-PANI fiber, (c) High resolution FESEM image.

The remarkable outcome achieved by Malik et al. can be attributed to the judicious optimization of the aniline-to-BTCA molar ratio, which played a pivotal role in influencing the resulting fiber lengths. Through meticulous experimentation and thoughtful parameter adjustments, they managed to achieve an optimal balance that led to the formation of elongated nanotube structures at low temperatures, underscoring the finesse of their approach. The results, depicted in **Figure 1.21,** serve as visual evidence of the success of this innovative endeavor. The synthesized polyaniline nanotubes, with their well-defined tubular morphology and notable dimensions, provide a testament to the effectiveness of the "soft template" methodology proposed by Malik et al. Their work not only expands the repertoire of polyaniline synthesis techniques but also underscores the potential of harnessing soft templates to achieve controlled and sophisticated nanostructures, paving the way for further advancements in materials science and nanoengineering.

Malik's research group continued to delve deeper into the intricate factors influencing the synthesis of polyaniline nanotubes, specifically exploring the impact of the number of carboxylic groups within the benzene aromatic core. In their quest to unravel this complex phenomenon, they employed 1,4-benzene dicarboxylic acid (BDA-1) with C2-symmetry, 1,3,5-benzene tricarboxylic acid (BTA-1) with C3-symmetry, and 1,2,4,5-benzene tetracarboxylic acid (BTCA) with C_{2i}-symmetry. These distinct acids possessed varying quantities of –COOH groups symmetrically positioned on the same aromatic core, a pivotal parameter under investigation [88].

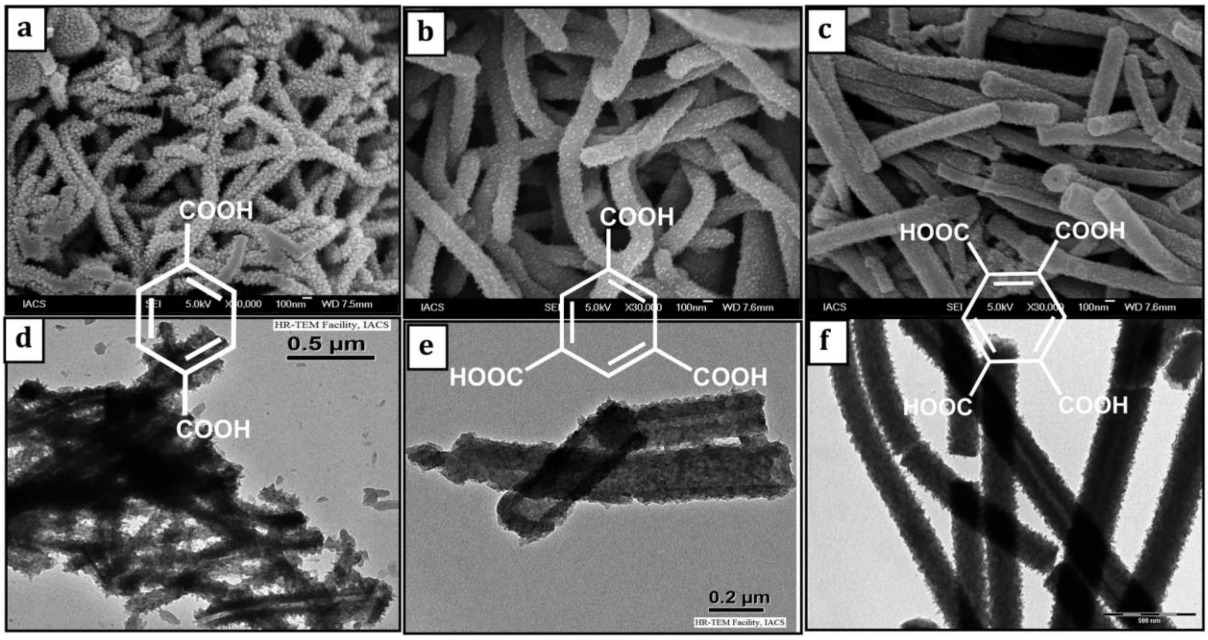

Figure 1.22 Different number of carboxylic acid group benzene core and FESEM images of corresponding acid doped PANI nanostructures (a) Terephthalic acid, (BDA) (b) Benzene tri carboxylic acid (BTA) and (c) Benzene tetra carboxylic acid (BTCA)

To their astonishment, the research unveiled a fascinating revelation: all three symmetric aromatic acids acted as potent dopants, catalyzing the formation of micro-meter sized nanotubes characterized by high aspect ratios (length/diameter ratios). The reported values were approximately 55 for BDA/PANI, 65 for BTA/PANI, and an impressive 300 for BTCA/PANI. These findings underscore the versatile nature of these acids as effective inducers of nanotube structures, each with its unique geometry and surface characteristics. Further insights emerged from the analysis of the nanotube surfaces. The research showcased a distinct progression in surface smoothness across the spectrum of nanotube products. Notably, BDA/PANI nanotubes displayed a notably rough surface, attributed to the inherent limited solubility of BDA in water. This surface roughness provided an interesting perspective into the influence of solubility dynamics on the resultant nanotube morphology.

Equally compelling were the trends in nanotube diameters, which correlated directly with the number of -COOH groups present in the dopant. The research demonstrated a clear pattern: as the number of -COOH groups increased, the diameter of the nanotubes followed suit. This was reflected in measured diameters of 148 nm for BDA/PANI, 156 nm for BTA/PANI, and 164 nm for BTCA/PANI [88]. This observed relationship between dopant structure and nanotube dimensions offered novel insights into the mechanistic interplay driving nanotube formation. The intriguing findings reported by Malik's group, as illustrated in **Figure 1.22**, underscore the intricate interplay between dopant characteristics and resulting nanotube properties. The study not only expands our understanding of polyaniline nanotube synthesis but also exemplifies the potential of systematically exploring dopant chemistry to achieve tailored nanostructures with unique attributes.

1.4. Metal nanoparticles (MNPs)-polyaniline composite

Noble metal nanoparticles (MNPs) like Au, Ag, Pd, and Pt have garnered widespread attention due to their extensive applications spanning medical devices to electronic energy systems. The distinct properties of MNPs are heavily influenced by factors such as shape, size, composition, crystallinity, and surface structure. Consequently, a range of techniques, including physical, chemical, and even biological methods, have been developed to synthesize and precisely modulate the size and morphology of MNPs. However, the prevalent chemical routes for MNP synthesis rely on environmentally detrimental organic solvents and polymer capping agents (as depicted in **Figure 1.23**). Additionally, this conventional chemical synthesis approach lacks the flexibility required for controlling MNP size and morphology, often leading to inherent limitations. To address the environmental concerns posed by traditional methods, researchers have turned to electrochemical deposition and electro polymerization as alternatives to fabricate MNPs nanocomposites. Despite these efforts, these techniques haven't entirely resolved the challenge of achieving comprehensive control over factors like loading density and MNP size. However, amidst this critical situation, conducting polymers, particularly polyaniline (PANI), emerge as a crucial solution to this dilemma [89].

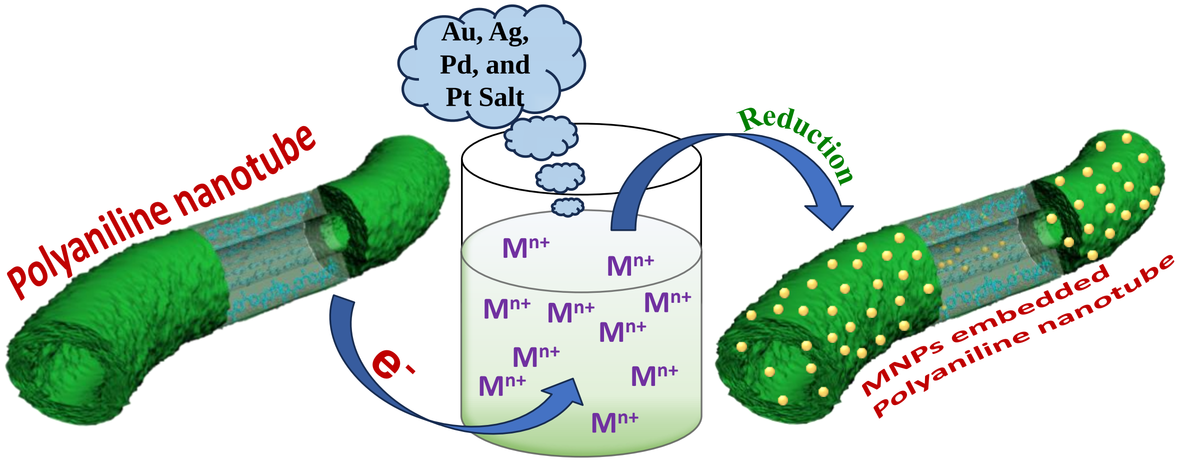

Figure 1.23 Schematic view of MNPs formation pathways on PANI nanotubes via a direct chemical reduction technique (a) chemical reduction of metal ions by PANI tubes.

The distinguishing aspect of PANI lies in its capacity to enable controlled loading densities, sizes, and environmentally friendly formation of MNPs. This is achieved through a remarkable interplay between PANI and metal ions. When the reduction potential of metal ions exceeds that of PANI, the spontaneous reduction of metal ions to form zero-valent MNPs occurs upon interaction [90]. PANI, known for its cost-effective synthesis, ease of production, and environmental stability, emerges as an ideal candidate for this role. In this innovative PANI-mediated approach, electron transfer occurs from PANI to metal ions, leading to the oxidation of PANI to a higher oxidation state. By leveraging PANI as both a template and a reducing agent in a water-based solvent, the need for environmentally harmful organic solvents and reducing agents is circumvented [91, 92]. This methodology extends to the synthesis of zero-valent Au, Ag, Pd, and Pt NPs. However, it faces limitations in reducing metal ions like Cu^{2+}, Ni^{2+}, and Zn^{2+} due to their lower reduction potential compared to PANI [90, 92, 93]. The synthesis of PANI-MNPs composites encompasses two primary routes. One involves the direct reduction of metal ions (e.g., Au^{3+}, Ag^{+}, Pd^{2+}, Pt^{2+}) through PANI powder, films, or solutions (**Figure 1.23**). The other entails chemical oxidation of monomers to polymerize PANI using metal salts, accompanied by simultaneous reduction of metal ions to form zero-valent MNPs.

Table 1.4 Standard electrode potential of metal and PANI

Materials	**E^0 (V)**	**ΔE^a (V)**	**MNPs formation**
PANI	**0.7-0.75**	**----**	
Au^{3+}/Au	**1.50**	**0.75**	**Yes**
Ag^{+}/Ag	**0.8**	**0.05**	**Yes**
Pd^{2+}/Pd	**0.83**	**0.08**	**Yes**
Pt^{2+}/Pt	**0.755**	**0.005**	**Yes**
Ni2+/Ni	**-0.25**	**-1.0**	**No**
Co2+/Co	**-0.28**	**-1.03**	**No**

ΔE^a = The reduction potrential difference between the metal ions and PANI

The advantages of this PANI-mediated synthetic platform are multifaceted:

Cost-effectiveness and Environmental Friendliness: This method eliminates the need for organic solvents, reducing agents, capping agents, or surfactants, resulting in an environmentally friendly process in comparison to conventional techniques.

Controlled Attributes: The approach enables facile control over the size, morphology, and loading density of MNPs on PANI surfaces.

One-Step Reaction: The synthesis procedure involves a single step, streamlining the process and contributing to its efficiency.

The PANI-MNPs composites exhibit a range of potential applications, including:

Highly Efficient Heterogeneous Catalysts: The composites can act as catalysts for various reactions, whether through chemical or electrochemical routes, due to their enhanced catalytic properties.

Effective SERS Substrates: These composites can serve as Surface-Enhanced Raman Scattering (SERS) substrates, enhancing the sensitivity of spectroscopic techniques.

Diverse Applications: The versatile nature of PANI-MNPs composites opens doors to a variety of essential applications beyond those mentioned.

In summary, this innovative approach offers a green and versatile synthetic platform for creating PANI-MNPs composites with controlled properties, presenting a significant stride towards environmentally friendly and efficient materials for numerous technological applications.

1.5 Electrical Conductivity of conducting polymer

The electrical and transport properties of conducting polymers hold crucial significance. The electrical conductivity of conjugated polymers is strongly influenced by several factors: **(a)** *molecular structure*, **(b)** *material morphology*, **(c)** *temperature variations*, and **(d)** *the type of dopant acid used*. Within the field of conducting polymers, polyaniline (PANI) is recognized as a semiconducting material. To comprehend the conductivity of semiconductors, it is valuable to consider the energy band model. This model elucidates the electrical behaviour and conduction mechanisms. Conductivity in conducting polymers adheres to Ohm's law, establishing a linear relationship between current, voltage, and resistance. This fundamental law governs the flow of electrical current through materials. However, the unique properties of conducting polymers, particularly PANI, introduce complexities that necessitate a deeper exploration of their electrical behaviour. Molecular structure profoundly influences the electrical properties of PANI. The arrangement of conjugated molecular units plays a pivotal role in determining the material's conductivity. Additionally, the morphology of the material, including factors like crystallinity and alignment, significantly impacts its ability to transport charges. Temperature variations exert a critical influence on PANI's conductivity. The thermal energy affects the movement of charge carriers, leading to changes in electrical properties. PANI's conductivity generally increases with higher temperatures due to enhanced charge mobility. The role of dopant acids in conducting polymers is paramount. Dopants introduce charge carriers into the polymer matrix, influencing its conductivity. In the case of PANI, different dopant acids can alter the electronic structure and charge carrier concentration, resulting in varying conductive behaviours.

1.5.1. Ohm's Law

A fundamental electrical property of solid materials is their ability to facilitate the flow of electric current. Ohm's law establishes a direct relationship between the potential difference (V) across a material, its electrical resistance (R), and the electric current (I) passing through it. This relationship is expressed by the equation:

$$V = I \times R$$

$$R = \rho \times \frac{l}{A}$$

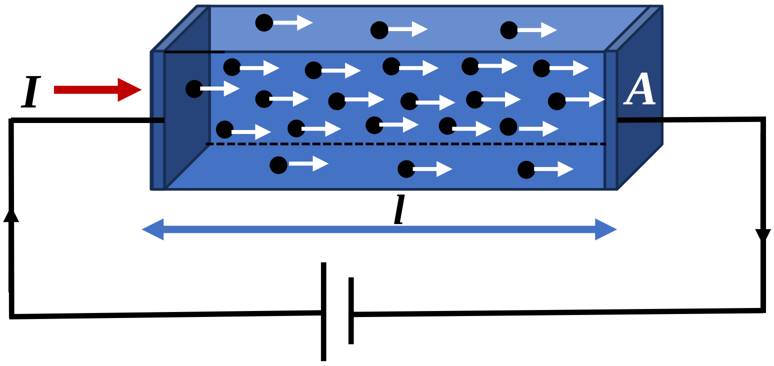

Figure 1.24 Schematics representation of ohm's law

Here, the resistance (R) denotes the hindrance a material presents to the flow of electric current. In this context, 'ρ' represents the specific resistivity of the material, measured in ohm-centimetres (ohm cm). The parameters 'A' and 'l' respectively represent the surface area of the electrode and the distance between the two electrodes, as illustrated in **Figure 1.24**. Another parameter commonly employed to characterize a material's electrical behaviour is its electrical conductivity.

Sometimes, electrical conductivity is used to specify the electrical character of a material. In this case Ohm's law is expresses in terms of current density, conductivity and applied electric field as:

$$\sigma = n \times q \ \times \mu$$

Where, 'σ' signify the electrical conductivity 'n' is charge carriers, 'q' charge of each carrier and 'μ' is the mobility of each carrier.

The electrical conductivity of a material indicates its capacity to facilitate the passage of electric current under the influence of an applied electric field. This parameter is crucial for characterizing a material's ability to conduct electricity and its performance in various electrical applications.

1.5.2. Electrochemical property

For the mechanistic analysis of red-ox systems, cyclic voltammetry (CV) is the most efficient and adaptable electro-analytical method currently available. Because of its high information content and relative simplicity, CV is well-liked. The most common application is as a diagnostic tool to clarify the electrode processes of a red-ox pair. The cathodic and anodic peaks are used to track the oxidation and reduction process. Anodic current, for instance, is produced in the Fe^{3+}/Fe^{2+} system when Fe^{2+} is electrochemically oxidised to Fe^{3+}. The cathodic current shows that during the reverse scan, Fe^{3+} is reduced back to Fe^{2+}. Therefore, during the forward and backward scan, CV has the ability to quickly produce a new species. The Randle-Sevcik relationship below governs the peak current, Ip.

$$I_p = k\, n^{3/2} A\, D^{1/2} C\, \gamma^{1/2}$$

To determine the normal electrochemical behavior and redox states of polyaniline, the cyclic voltammetry (CV) approach is quite helpful. **Figure 1.25** of the CV research illustrates the two oxidation and reduction peaks at various voltage potentials. [94, 95] The application of potential, the material and surface area of the electrodes, the temperature, the composition of the electrolyte, and other factors all affect how polyaniline behaves electrochemically.

The CV curve (**Figure 1.25**) showcases three distinct sets of redox peaks, each manifesting through anodic and cathodic current peaks. The first set (peaks A_1 and C_1) emerges within the 0 to 0.25 V vs. (Ag/AgCl) range, signifying the conversion of fully reduced leucoemeraldine base into partially oxidized emeraldine. The second set (peaks A_2 and C_2) occurs between 0.35 V and 0.5 V vs Ag/AgCl, corresponding to the Benzenoid to Quinoid transformation.

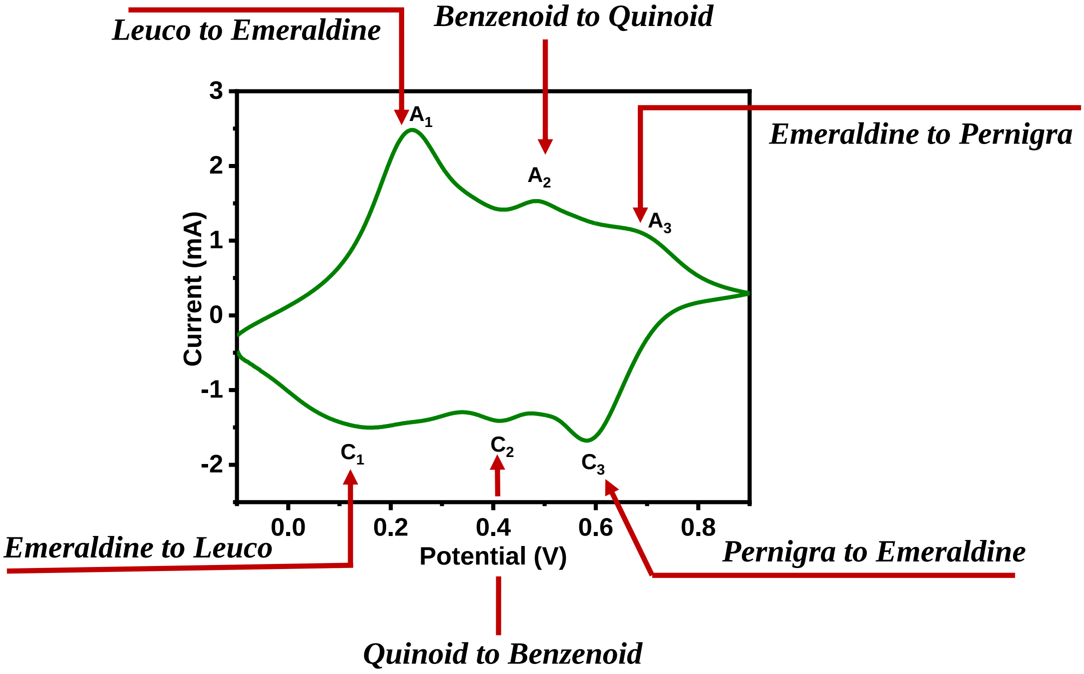

Figure 1.25 A typical cyclic voltammetry curves for PANI in 1M H_2SO_4 solution at scan speed 50 mV with different oxidation reduction state.

The third set (peaks A_3 and C_3) materializes within the 0.6 to 0.8 V vs. Ag/AgCl range, indicating the conversion of emeraldine to the fully oxidized pernigraniline form. It's noteworthy that potential peaks A_1 and C_1 remain pH-independent, whereas peaks A_3 and C_3 exhibit a pronounced pH dependence.

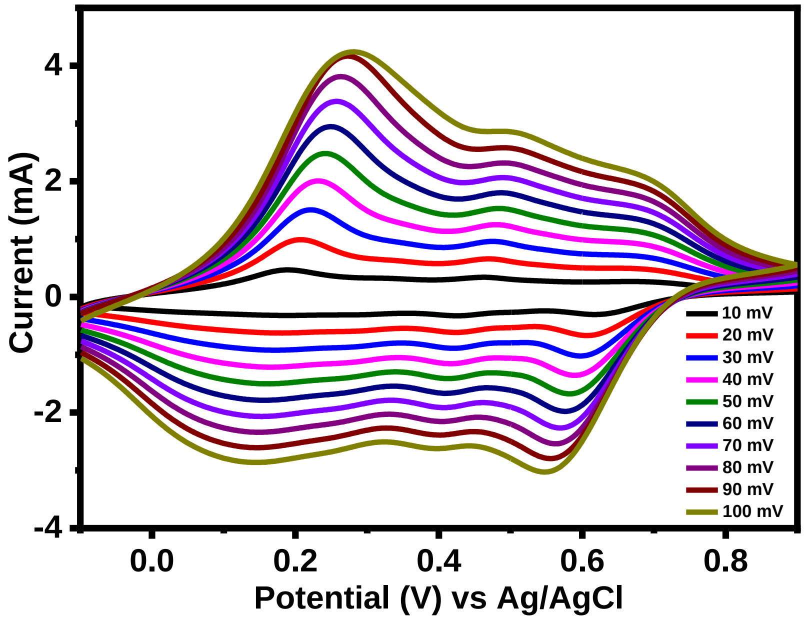

Figure 1.26 Room temperature cyclic voltammetry study of PANI film in 1M H_2SO_4 solution with different scan rate (10-100 mV/s)

This pH study indirectly confirms proton exchange during the A_3 and C_3 steps. Additionally, observations reveal that polyaniline is more susceptible to oxidation in mildly acidic solutions. This phenomenon is evident as peaks A_3 and C_3 shift towards the left with increasing pH. The influence of scan rate on current peaks (both anodic and cathodic) is apparent from the linear relationship illustrated in **Figure 1.26**. This observation underscores the interplay between scan rate and current, shedding light on the kinetics of the redox processes involved in polyaniline's electrochemical behavior. [73, 96] In the case of proton doping, radical cations are generated at the imine nitrogen atoms. These charge carriers are deemed responsible for facilitating electronic conduction within the polyaniline structure [97]. This distinctive doping mechanism further contributes to polyaniline's remarkable electrical properties and its suitability for various applications in the field of conducting polymers.

1.6. Application of PANI and PANI-MNPs composites

1.6.1. Rechargeable batteries

In recent years, significant attention has been directed towards the development of PANI-metal batteries. Polyaniline (PANI) stands out due to its various advantages compared to other conducting polymers. Its straightforward and rapid preparation through chemical or electrochemical methods, coupled with its resistance to aerial oxidation and moisture, contributes to its appeal. Additionally, PANI's capacity to store a substantial charge through redox processes has spurred interest in both non-aqueous [98] and aqueous battery [99] systems. In non-aqueous environments, rechargeable batteries often incorporate lithium as the anode material (**Figure 1.27**).

However, using non-aqueous solvents in PANI-lithium batteries presents a challenge. During charging, lithium plating onto lithium electrodes can lead to dendrite formation, particularly at high charging rates. These dendrites can grow extensively and potentially create internal short-circuits within the cell. Moreover, the elevated cathodic potential of the Li/Li^+ couple frequently results in solvent decomposition, the exact mechanism of which remains partially understood [99 (a)]. Despite these challenges, the pursuit of PANI-metal batteries continues due to PANI's promising characteristics, including its charge storage capabilities, chemical durability, and suitability for diverse battery applications. Efforts to address the issues associated with non-aqueous systems, such as dendrite formation and solvent decomposition, are ongoing to realize the potential of PANI in energy storage technologies.

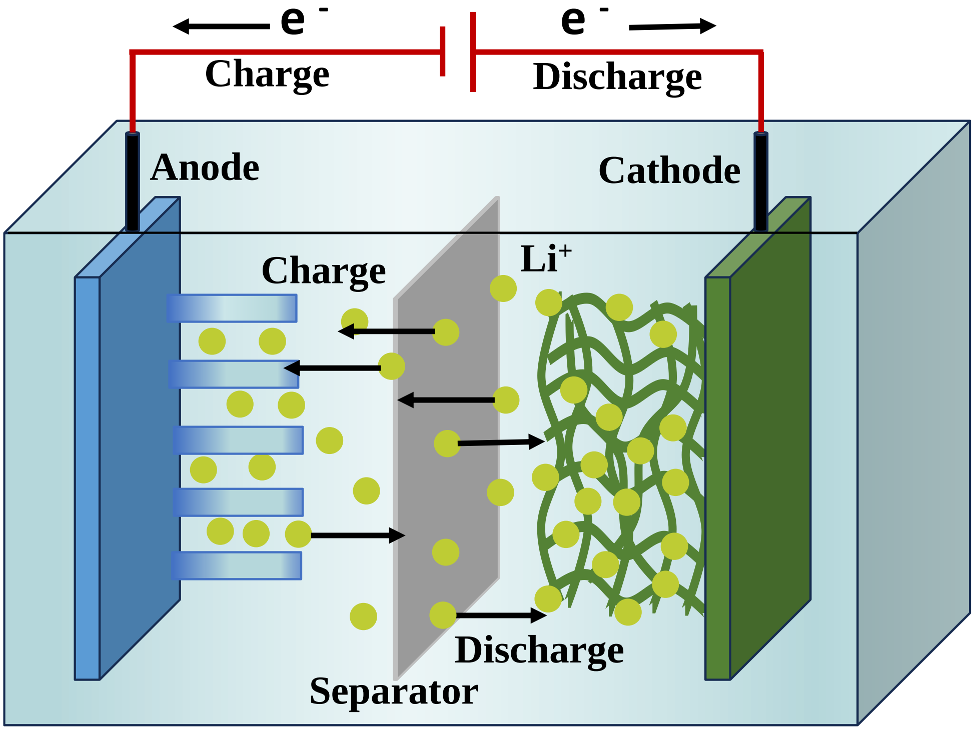

Figure 1.27 Schematics representation of Polyaniline Li-ion Battery

Utilizing PANI as the cathode material, coupled with lithium-doped aluminum as the anode material, in a propylene carbonate electrolyte containing 1M lithium perchlorate, yields an open circuit voltage of 3.7 V. This combination offers a massic capacity of 145 Ah/kg and a relatively low self-discharge rate of approximately 8% after a 90-day period, enhancing the appeal of the PANI-lithium battery for diverse technological applications. In a recent communication, it was demonstrated that this battery configuration can achieve a maximum discharge capacity of 164 Ah/kg, boasting not only a low self-discharge rate but also a prolonged lifespan when employed as a positive active material in a secondary lithium battery [98 (a)]. The elevated massic capacity of PANI can be attributed to its fibrous structure, which is fabricated through galvanostatic deposition in an aqueous solution containing 1M perchloric acid and 0.5M aniline at room temperature, utilizing a current density of 5mA/cm². This remarkable capacity and structural advantage hold significant promise for advancing energy storage solutions.

1.6.2. Supercapacitor

In recent times, the global energy crisis has emerged as a significant concern, prompting researchers worldwide to seek innovative solutions. The rapid growth of the global economy coupled with escalating environmental issues has underscored the urgent need for efficient, clean, and sustainable energy sources. In response, emerging technologies in the realm of energy conversion and storage have gained paramount importance. Among the various energy storage devices available, electrochemical capacitors stand out as an effective and efficient solution. Among these, the supercapacitor (also known as ultracapacitor or electrochemical capacitor) has garnered significant attention. It is hailed as a highly promising energy storage system due to its distinctive capabilities. Functioning as a bridge between conventional batteries and capacitors, supercapacitors exhibit a unique hybrid property that offers remarkable advantages in energy storage and utilization. Supercapacitors, as depicted in **Figure 1.28**, represent a breakthrough in energy storage technology.

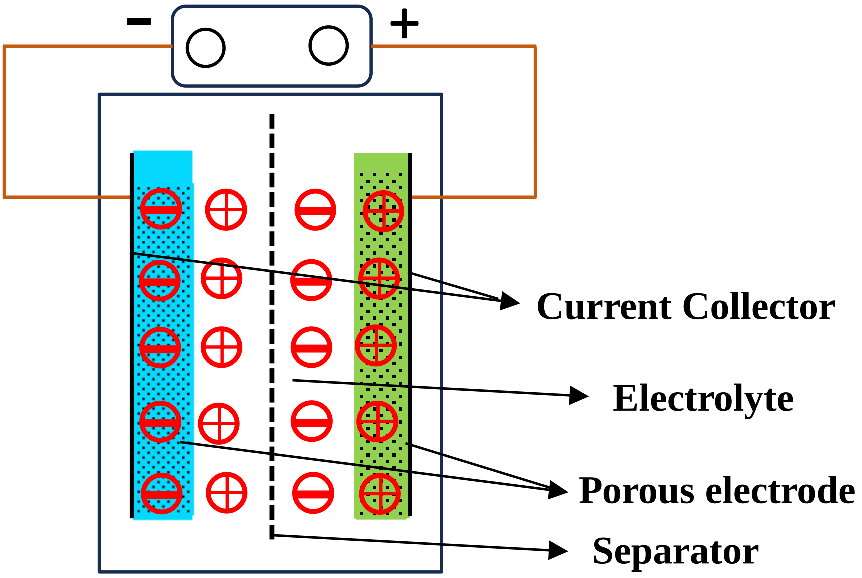

Figure 1.28 Working principles of a supercapacitor

They possess the ability to store and deliver energy rapidly, thanks to their high-power density. This makes them well-suited for applications requiring immediate and intense energy release. Simultaneously, supercapacitors demonstrate a prolonged cycle life, capable of withstanding numerous charge-discharge cycles without experiencing significant degradation. The hybrid nature of supercapacitors encompasses the best of both worlds. Like conventional capacitors, they can rapidly store and release energy, while resembling batteries in terms of their energy storage capacity. This combination of features positions supercapacitors as a versatile solution for addressing the increasing energy demands of modern society. Supercapacitors find diverse applications across various industries. They are instrumental in renewable energy integration, enabling efficient storage of surplus energy generated by sources such as solar and wind power.

In the transportation sector, supercapacitors are employed in regenerative braking systems for hybrid and electric vehicles. Additionally, they play a critical role in consumer electronics, industrial processes, and backup power solutions. As the world continues to search for sustainable energy solutions, supercapacitors have emerged as a beacon of hope. Their ability to balance rapid energy delivery, prolonged cycle life, and versatile applications makes them a cornerstone technology in the journey towards a cleaner and more sustainable energy landscape. Ongoing research and development in this field hold the promise of further enhancing the performance and applications of supercapacitors, contributing significantly to addressing the global energy challenge.

Supercapacitor devices are distinguished by their utilization of specialized materials that capitalize on high surface area electrode materials and thin electrolytic dielectrics. This strategic approach enables these devices to achieve capacitances that are several orders of magnitude greater than those achievable with conventional capacitors. Conventional batteries are known for their high energy density, which enables them to store significant amounts of energy. However, they tend to offer lower power density and cyclic stability due to the inherent degradation of materials during electrochemical reactions. This drawback limits the practicality of conventional batteries in situations demanding high-power outputs and extended cycling capabilities. On the other hand, conventional capacitors deliver high power density but fall short in terms of energy density. Moreover, they lack chemical reactions during the charge-discharge process, leading to constraints in overall energy storage capacity. Amid this intricate scenario, supercapacitors emerge as a pivotal solution, serving as a bridge that effectively combines the strengths of both conventional batteries and capacitors. By striking this balance, supercapacitors can achieve exceptional power density, energy density, and significantly enhanced cycle life [97, 100]. The distinctive chemistry and structure of supercapacitors contribute to their exceptional performance.

The use of high surface area electrode materials maximizes the surface available for charge accumulation, boosting their energy storage capabilities. Meanwhile, the utilization of thin electrolytic dielectrics facilitates rapid ion transport, resulting in quick charge and discharge rates. Supercapacitors prove indispensable in various applications where the demand for both high-power bursts and prolonged operational life is paramount. They are particularly well-suited for tasks such as rapid energy delivery, regenerative braking in electric vehicles, and supporting intermittent renewable energy sources.

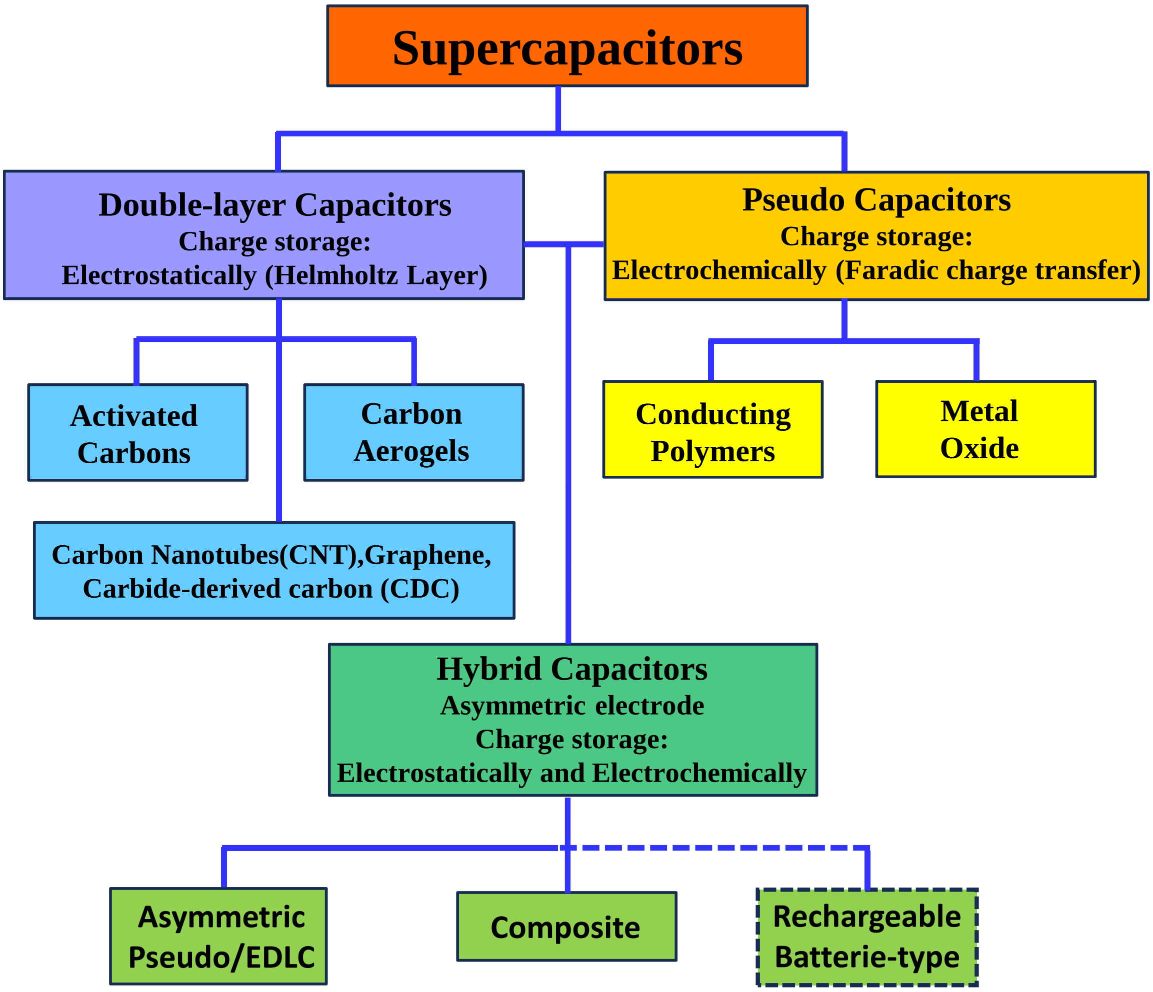

The charge storage mechanism of a supercapacitor closely resembles that of a traditional capacitor. This mechanism primarily involves the accumulation of electrical charges on the surfaces of the electrodes. Depending on the specific charge storage mechanism employed, supercapacitors can be categorized into three distinct types: double-layer capacitors, pseudocapacitors, and hybrid capacitors.

Double-Layer Capacitors (EDLCs):

Double-layer capacitors operate by storing charges through the electrostatic absorption of ions at the electrode-electrolyte interface **Figure 1.29**. This phenomenon leads to the formation of a double-layer region where ions are separated by a dielectric material, resulting in charge storage.[101] However, the energy density of double-layer capacitors is limited due to their sole reliance on the electrostatic mechanism for charge storage.

This limitation makes them more suitable for applications requiring high power outputs and rapid charge-discharge cycles. The total charge stored in the EDLCs is proportional to amount of double layer formation i.e., exposed surface area of the solid current collector to the electrolyte. The materials (charcoal, activated carbon, CNTs, graphene etc.) have high surface area result high capacitor vale are used in these devices.

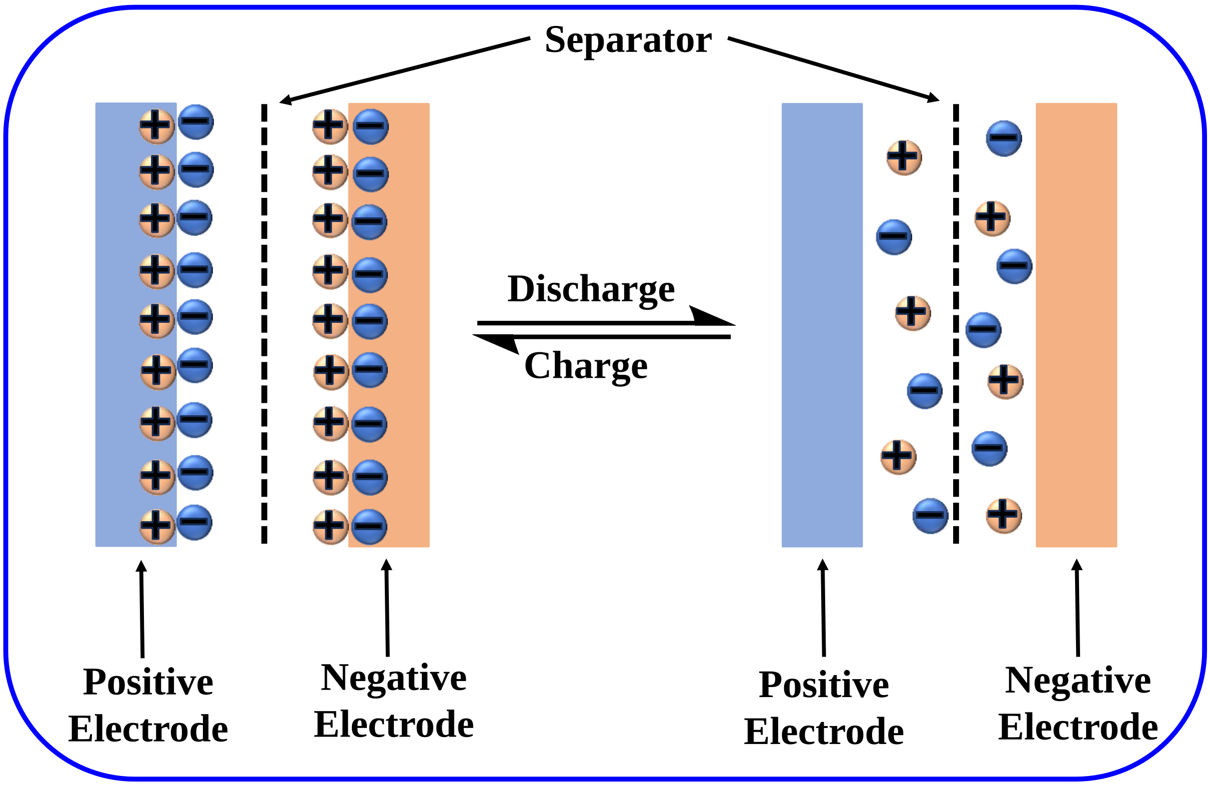

Figure 1.29 Charging-discharging mechanism of a EDLCs capacitor.

The advantages of EDLCs are as follows:

a. There is no chemical reaction happened during charge/discharge time.
b. Overcharging does not affect the life cycle compare to batteries.
c. The total amount of charge stored is many times higher (F/g) than conventional capacitor.
d. Quick charge/discharge gives high power density compare to batteries.
e. Device charge/discharge mechanism is very simple and no special circuit is required for device charging.

Apart from many advantages EDLCs have some disadvantages are as follows:

a. High internal resistance compares to conventional capacitor and unable to work at AC voltage.
b. Low capacitance results low energy density.

Pseudocapacitors:

Pseudocapacitors exhibit a distinct charge storage mechanism involving reversible redox reactions occurring at the electrode surfaces. This enables them to store a larger number of charges compared to double-layer capacitors, consequently leading to higher energy densities. The electrochemical processes involved in pseudocapacitors are more dynamic and involve faradaic reactions, which contribute significantly to their improved energy storage capabilities. Pseudocapacitors are thus capable of delivering both high power and enhanced energy storage, making them valuable in applications requiring a balance between the two. Mainly two types of materials are used to store charge in pseudocapacitors, conducting polymer and metal oxide. [102-104]

Advantages of Pseudocapacitor:

a. Pseudocapacitor has very high specific capacitance compare to EDLCs and battery.
b. Pseudocapacitor device is highly charge/discharge reversible.

Disadvantages of Pseudocapacitor:

a. Low cell voltage.
b. High production cost of electrode materials.
c. Low cyclic stability compares to EDLCs.

Hybrid Capacitors:

Hybrid capacitors combine the charge storage mechanisms of both double-layer capacitors and pseudocapacitors. By leveraging both electrostatic ion absorption and reversible redox reactions, hybrid capacitors aim to optimize energy density while maintaining high power output. This hybridization results in improved overall performance, making them well-suited for a broader range of applications that demand versatile energy storage capabilities. The selection of the appropriate type of supercapacitor depends on the specific requirements of the intended application. Double-layer capacitors are preferred when high power and rapid charge-discharge cycles are crucial. Pseudocapacitors excel in applications requiring a higher energy density without compromising power performance. Hybrid capacitors, on the other hand, strike a balance between energy density and power output, making them suitable for scenarios that demand both attributes. As researchers continue to explore novel electrode materials, electrolytes, and designs, supercapacitors are poised to evolve further, enhancing their charge storage mechanisms and overall performance. This ongoing innovation holds the potential to unlock new applications and contribute to the advancement of energy storage technologies, addressing the diverse energy needs of modern society.

Flexible Solid-State Supercapacitors

With the proliferation of portable and flexible electronics in our daily lives, there is an escalating need for energy storage solutions that offer lightweight, flexibility, and high efficiency. [105, 106] This demand has driven the exploration of energy storage technologies that can align with the requirements of modern consumer electronics. As environmental concerns and sustainable energy initiatives gain momentum, research in this field has become paramount.

Solid-state supercapacitors (SCs) present (**Figure 1.30**) [107] a compelling alternative to liquid electrolyte-based counterparts, offering distinct advantages such as portability, environmental friendliness, stability, and flexibility, thus expanding the potential application spectrum of SCs. [108, 109]

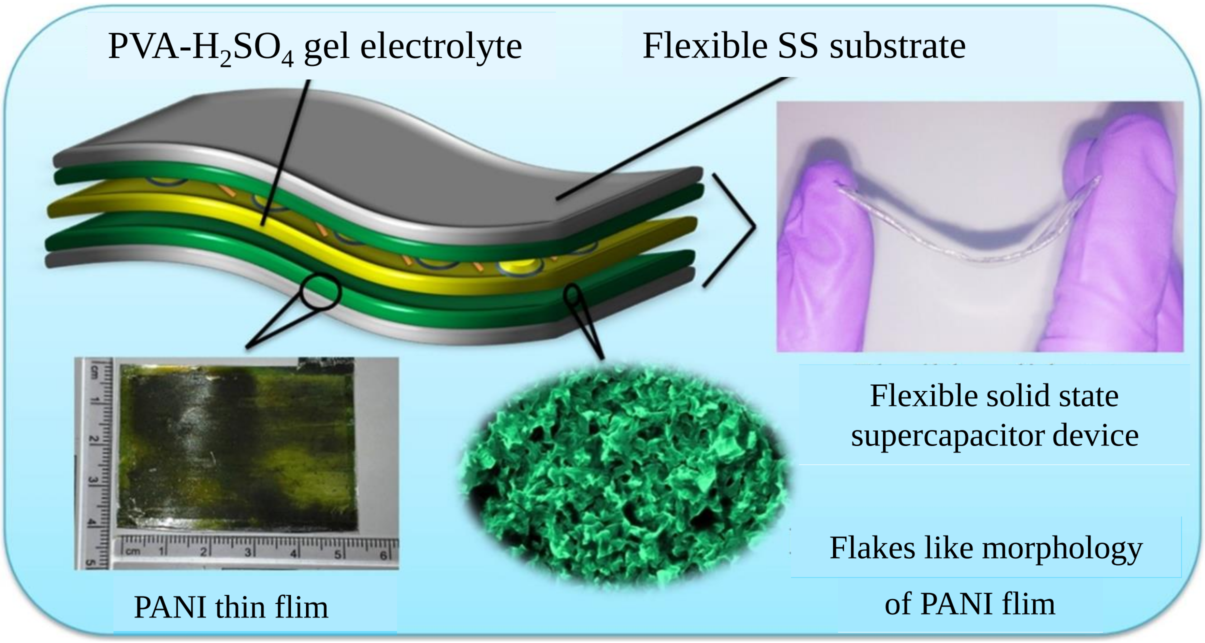

Figure 1.30 Solid state flexible supercapacitor devices

To further enhance the flexibility and compactness of flexible supercapacitors, innovation is essential in optimizing their structural design. The emergence of planar supercapacitors introduces a novel approach, enabling thinner and more flexible device configurations. In this context, polyaniline nanostructures have gained prominence as efficient electrode materials for high-performance supercapacitors due to their large-scale synthesis feasibility, environmental stability, and cost-effectiveness.

The morphology of polyaniline plays a pivotal role in the charge storage activity of supercapacitor devices. Notably, flexible graphene–polyaniline paper holds significant promise, offering advantages such as affordability, easy scalability for various device sizes, simplified large-scale production, and impressive energy storage performance. This underscores its potential for practical applications in portable energy devices.

1.6.3. Memory device based on PANI nanostructures

Memory devices have revolutionized modern electronics by providing efficient means to store and retrieve information. Polyaniline (PANI), a conductive polymer, has emerged as a promising candidate for memory devices due to its tunable electrical properties, ease of synthesis, and compatibility with flexible electronics. Memory devices based on PANI nanostructures hold potential for various applications, including resistive switching memory and capacitive memory.

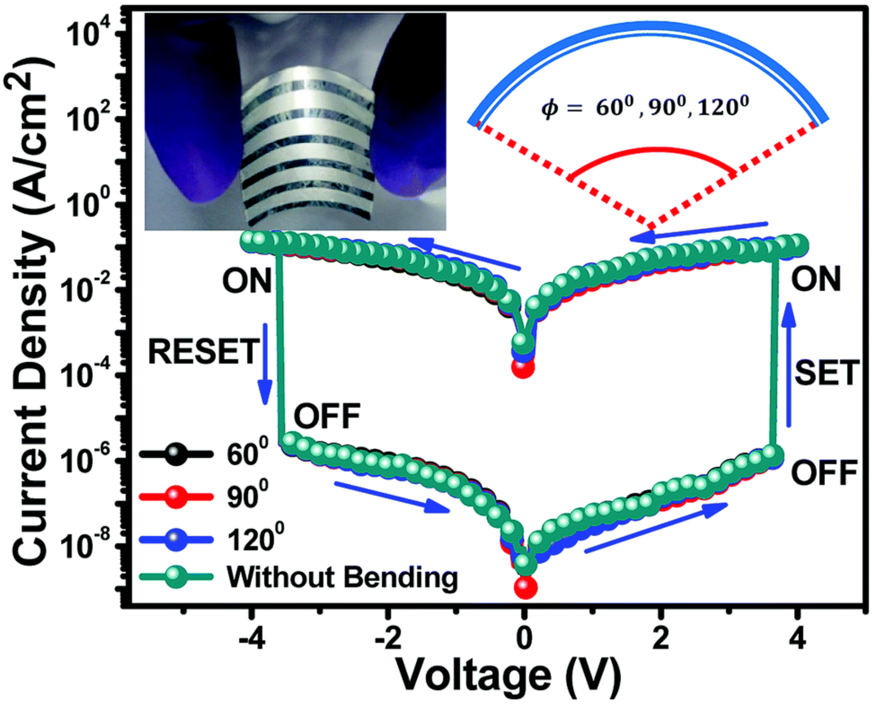

Figure 1.31 Current–voltage (I–V) switching characteristic of Al/ZnO–PVA/PEDOT: PSS/Al/flexible PET substrate [110]

The fundamental objective of a memory device revolves around facilitating the storage and retrieval of binary digital data sequences consisting of “1’s” and “0’s”. This function serves as a cornerstone of modern computing systems, acting as the primary storage mechanism. Electronic memory devices, designed as forms of semiconductor storage, offer rapid response times, compact sizes, and the capability to both read and write data when connected to a central processing unit (CPU) or processor. Unlike conventional silicon-based electronic memory, where data storage relies on the quantity of charge retained within memory cells, organic/polymer electronic memory operates on an entirely distinct principle. Specifically, it employs different states of electrical conductivity, namely ON and OFF states, in response to an applied electric field, to store data (**Figure 1.31**) [110]. This innovative approach to data storage through organic/polymer electronic memory presents an alternative or supplementary technology to the established semiconductor-based electronic memory. With the potential to redefine memory storage paradigms, organic/polymer electronic memory holds promise as a versatile solution for addressing the evolving demands of digital data storage and manipulation.

Electronic memory devices can be classified into two main categories based on the type of storage they offer: volatile and non-volatile memory. Volatile memory refers to memory that loses its stored data once power supply is cut off or if it's not refreshed periodically with an electrical pulse. Currently, the most prevalent form of primary storage relies on volatile memory. The electronic memory can be further segmented into sub-categories, including read-only memory (ROM), hybrid memory, and random-access memory (RAM). Among these memory types, write-once read-many-times (WORM) memory has gained significant popularity, as depicted in **Figure 1.31**. WORM memory enables data to be written to the memory once, but read many times afterward, making it a valuable choice for applications that require secure, unalterable data storage. This intricate landscape of electronic memory types underscores the diverse range of options available for various applications, each tailored to specific needs and priorities, be it speed, durability, or data retention.

Kaner et al. shows the device performance scans produced with nanoparticles in four different solutions and four different size ranges (1, 2, 6, and >20 nm) are shown in (**Figure 1.32**). [111]

The turn-on voltages of the devices made from solutions containing 1, 2, and 6 nm gold nanoparticles were determined to be 1.5, 3, and 4.5 V, respectively, from these characteristic scans, while the on/off ratio, or the difference between the low conductivity state and high conductivity state measured at 1 V, was found to be 4, 3, and 1.5 orders of magnitude, respectively.

11

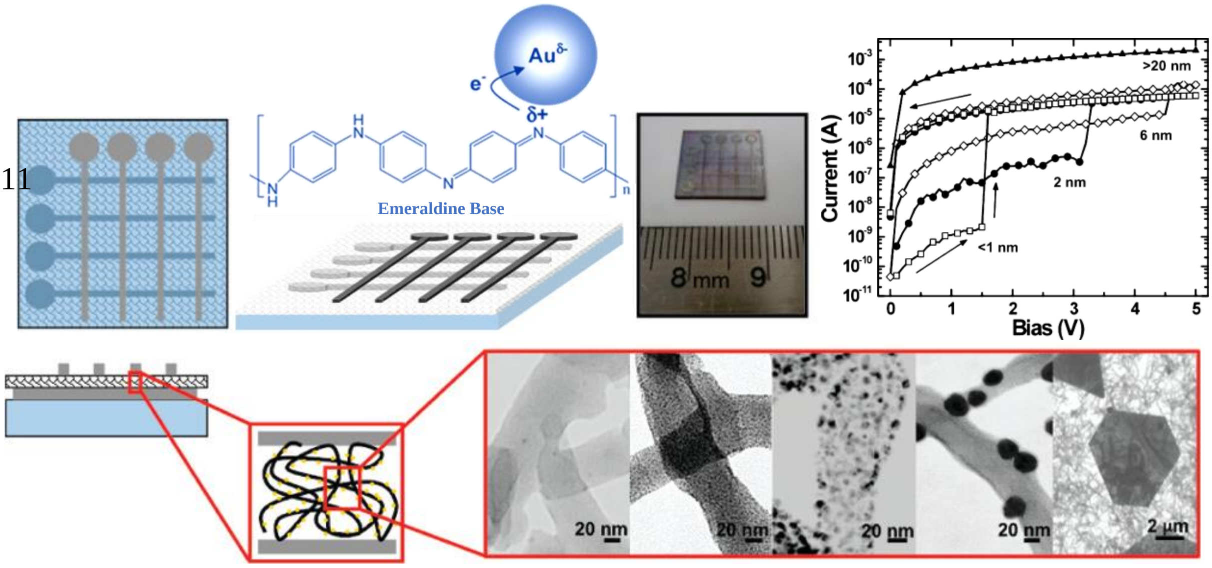

Figure 1.32 Characteristic I–V scans for autoreduced gold nanoparticle–polyaniline nanofiber composite memory devices. [111]

The data depict typical I-V scan results; the initial scan may occasionally be abnormal due to residual charge that accumulated in the device during manufacture.

The performance curve may show jumps in the initial scan, but after a few cycles, it stabilises and becomes repeatable. During the initial scan, the >20 nm gold nanoparticle device did switch on once before staying in the high conductivity state with a turn-on voltage of 6 V. This device's high conductivity status persisted after the initial scan and it was unable to be removed. This may indicate that the device will short due to filament development or gold particles that are relatively big (>20 nm) clumping together. An examination of all these trials reveals two main trends: the on/off current ratio drops and the turn-on voltage required to enter the high-conductivity on-state rises as the particle size grows. A higher on/off ratio for the optimum device increases stability, while a lower turn-on voltage uses less power.

Due to their poor cycling and high turn-on voltages, the bigger gold nanoparticles are obviously not the best choice for bistable memory systems. The capacity for charge storage on the gold particle, however, increases with particle size.[112] Because of the increased off-state current and increased residual charge as a result, the device's on/off ratio decreases. Due to near proximity of the gold nanoparticles, there is a tendency for lower turn-on voltages with smaller nanoparticles, which is probably related to a lowered barrier. As a result, it would seem that smaller nanoparticles improve device performance, as seen by the smaller on/off ratios and lower voltages required to switch on devices. The low turn-on voltage, high on/off ratio, and best exhibited cycling, with hundreds of write-read-erase cycles, were observed with the 2 nm nanoparticle composite among the devices examined here, leading to the greatest performance.

1.6.4. Various sensing application of PANI nanostructures

Polyaniline (PANI) has gained significant attention as a sensing material due to its unique electrical, chemical, and structural properties. Its versatile nature allows for the development of sensors capable of detecting a wide range of analytes. Here are some detailed applications of polyaniline as a sensor:

Gas Sensors:

Polyaniline-based gas sensors are widely used to detect toxic and flammable gases in industrial and environmental settings. When exposed to target gases, PANI undergoes changes in its electrical conductivity, making it an effective sensing material. For instance, in ammonia detection, PANI can adsorb ammonia molecules, causing a decrease in conductivity. [113] Such sensors are vital for air quality monitoring, leak detection, and safety in industries.

Chemical Sensors:

Polyaniline can be functionalized with specific receptors or responsive groups to create chemical sensors. These sensors detect changes in pH,[114] acidity, or specific ions in solutions. PANI’s conductivity responds to changes in the chemical environment, allowing for real-time monitoring of chemical processes and detecting harmful substances in liquids.

Biosensors:

By immobilizing biomolecules like enzymes, antibodies, or DNA on PANI surfaces, biosensors can detect biological molecules.[115] When the target molecule binds to the immobilized biomolecule, it triggers changes in PANI’s conductivity. This technique is used in medical diagnostics, drug screening, and monitoring biological interactions.

Humidity Sensors:

Polyaniline-based humidity sensors measure changes in humidity levels by absorbing or desorbing water vapor. PANI's electrical conductivity is affected by water absorption, enabling the sensor to provide real-time humidity measurements.[116] These sensors find applications in climate control systems, weather stations, and food storage.

Strain and Pressure Sensors:

Polyaniline’s conductivity changes when subjected to mechanical strain or pressure. By integrating PANI into flexible or stretchable materials, sensors can detect physical deformation.[117] These sensors are used in wearable devices, robotics, and structural health monitoring.

Optical Sensors:

Functionalizing PANI with dyes or nanoparticles allows it to respond to changes in light absorption or emission. PANI-based optical sensors are used to detect analytes by monitoring shifts in optical properties, making them suitable for chemical analysis, environmental monitoring, and medical diagnostics.[118]

Electrochemical Sensors:

PANI can serve as a transducing material in electrochemical sensors.[119] Changes in PANI’s conductivity are measured as changes in current or potential during electrochemical reactions. Electrochemical sensors are employed for detecting heavy metals, environmental pollutants, and biomolecules in various samples.

Temperature Sensors:

The electrical conductivity of PANI is influenced by temperature changes. By calibrating PANI's conductivity response to temperature variations, it can be utilized as a temperature sensor. These sensors are applied in temperature monitoring and control systems.[120]

Electronic Skin (E-skin):

Flexible and stretchable PANI-based sensors can mimic human skin by detecting pressure, temperature, and humidity changes. E-skin finds applications in prosthetics, robotics, and wearable health devices, enhancing human-machine interactions.[121]

Polyaniline's versatile characteristics, ease of synthesis, and responsiveness to different stimuli make it an attractive material for sensor applications across various fields. Researchers continue to explore innovative ways to optimize its properties and tailor PANI-based sensors for specific detection requirements.

1.6.5. Electro-catalysis

Electrocatalysis is a dynamic process in which the driving force for a chemical reaction arises from an applied voltage, leading to reaction initiation in the presence of an electrocatalyst. These specialized catalysts play a pivotal role at the interface between the electrode and the electrolyte, facilitating and enhancing electrochemical reactions. Electrocatalysts exist in two main forms: heterogeneous and homogeneous. Heterogeneous electrocatalysts encompass various materials, such as platinum surfaces or nanoparticles, which catalyze reactions occurring at the electrode-electrolyte interface. On the other hand, homogeneous electrocatalysts can include coordination complexes or enzymes that actively participate in electron transfer processes and intermediate chemical transformations.

Mainly electrocatalysis lies on the concept of electron transfer. Electrocatalysts, often with well-defined structures and properties, mediate the exchange of electrons between the electrode and reactants, thus influencing the rate and selectivity of electrochemical reactions. Through this mediation, electrocatalysts enable complex chemical reactions to occur efficiently and under controllable conditions. Moreover, they can modify the activation energy barrier, allowing reactions that might otherwise be sluggish to proceed at a much faster pace.

The significance of electrocatalysis transcends various fields, spanning from energy conversion and storage in fuel cells and batteries to environmental applications like water purification and air pollution control. The design and development of efficient electrocatalysts are essential for improving the performance and efficiency of electrochemical devices and processes. An electrochemical catalyst participates in a multifaceted reaction that encompasses a sequence of elementary processes, each contributing to the overall electrochemical transformation. These processes involve:

Adsorption/Desorption: At the outset, reactants from the electrolyte adsorb onto the surface of the electrode, a crucial step that governs the availability of reactants for subsequent reactions. Following the reaction, products desorb from the electrode surface back into the electrolyte.

Bond Breaking and Reorganization: The electrochemical reaction may involve breaking existing chemical bonds within reactant molecules and their subsequent reorganization to form new products. This step is vital for the rearrangement of atoms and bonds as reactants transform into desired products.

Electron Transfer: Central to electrochemistry, electron transfer is pivotal in mediating the exchange of electrons between the electrode and the reactants. This step often involves the movement of charges, leading to the generation of electrical current and the conversion of chemical energy into electrical energy.

While electron transfer and bond cleavage steps usually dictate the overall reaction rate, the strength of adsorption and the spatial arrangement of reactants on the electrode surface significantly influence the dominant reaction pathway. The affinity of reactant molecules to the electrode surface and their preferred orientations play pivotal roles in shaping the reaction mechanism. Adsorption strengths determine whether certain reactions proceed via associative or dissociative pathways, thereby impacting the selectivity of the reaction products.

In the context of green energy production and energy conversion, several crucial electrochemical reactions hold great importance. These include the methanol oxidation reaction (MOR), the oxygen reduction reaction (ORR) and the hydrogen evolution reaction (HER), which are central to fuel cell technologies. Similarly, reactions involving the electrocatalytic conversion of carbon dioxide (CO2) to valuable chemicals or renewable fuels contribute to efforts in carbon capture and utilization, addressing both energy and environmental challenges. The intricate understanding of these electrochemical reactions allows scientists and engineers to design efficient electrocatalysts, optimize reaction conditions, and drive advancements in sustainable energy technologies.

1.6.5.1. Electro-catalytic methanol oxidation reaction (MOR)

Direct alcohol fuel cells (DAFCs) have attracted considerable attention as promising power sources suitable for portable applications, presenting distinctive advantages in comparison to hydrogen-based systems. Alcohols such as methanol, ethanol, ethylene glycol, and glycerol offer several notable benefits, particularly their high volumetric energy density. This characteristic simplifies the storage and transportation of fuels, setting them apart from the challenges associated with handling hydrogen. A fuel cell operates as a sophisticated electrochemical device, orchestrating the conversion of the chemical energy inherent in the chosen fuel into usable electrical energy through intricate electrochemical reactions that transpire at the electrode-electrolyte interface.

At its core, a fuel cell comprises two key electrodes: the anode and the cathode. Within the anode, fuel oxidation reactions take place, while the cathode is the site of oxygen reduction reactions. These two complementary reactions are pivotal to the entire energy conversion process within a fuel cell.[122, 123] As fuel is oxidized at the anode, it releases electrons, and these electrons then travel through an external circuit, generating an electric current that can power various devices. Simultaneously, oxygen is reduced at the cathode, and the ions produced during fuel oxidation combine with oxygen to form water as the main byproduct. This harmonious interplay between the anode and cathode reactions culminates in the efficient generation of electricity while minimizing emissions and promoting cleaner energy utilization.

DAFCs, with their efficient utilization of alcohols and inherent advantages, hold immense potential for various applications ranging from portable electronic devices to automotive systems.

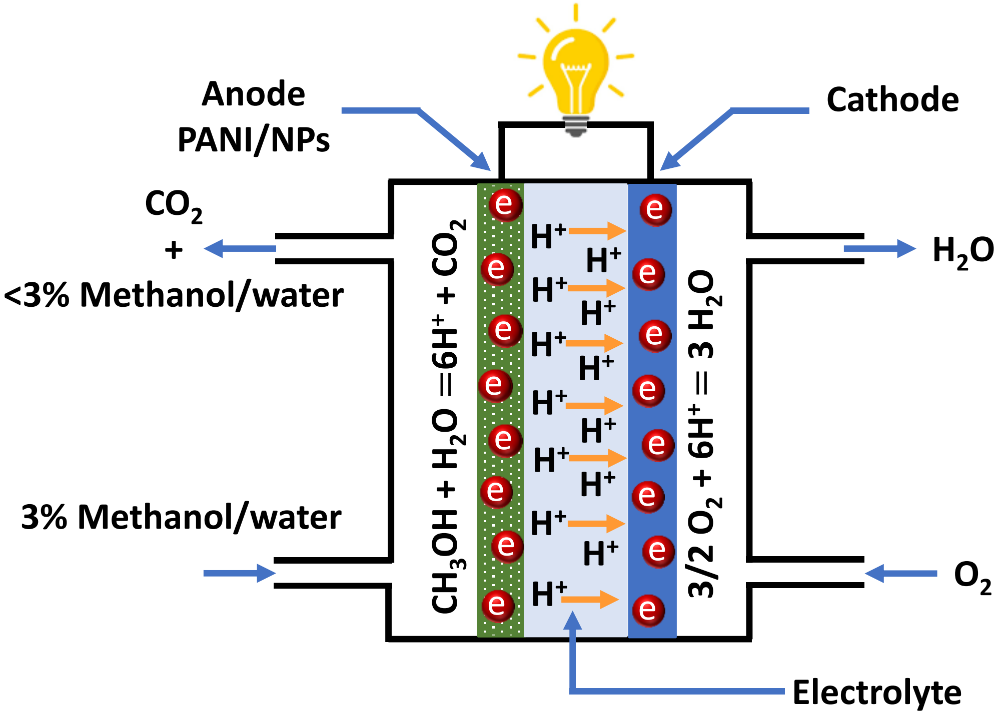

Figure 1.33 Design and working principle of methanol fuel cell

Their compatibility with a variety of alcohols contributes to their versatility, while their capacity to provide electrical power through electrochemical means positions them at the forefront of sustainable energy solutions. As the drive for cleaner and more efficient energy sources intensifies, DAFCs emerge as a significant player in the quest for a greener and more sustainable future.

In the Direct Methanol Fuel Cells (DMFCs), achieving optimal performance hinges on two critical factors, catalyst loading and the preparation of the membrane-electrode assembly (MEA). The operation of a methanol fuel cell is outlined in **Figure 1.33**, where the anode chamber's activity assumes a pivotal role in determining fuel cell performance. To enhance device activity, researchers are actively exploring various strategies to modify the anode chamber. These approaches involve incorporating different composites such as polymers, polymer@ metal nanoparticles, and metal oxide nanoparticles. Particularly, tailoring the catalyst loading on the anode chamber has emerged as a crucial avenue for improving DMFC performance.

Numerous catalysts loading processes have been developed to optimize the anode chamber's catalytic activity. These techniques encompass methods like spraying, sputtering, screen printing, decaling, and electro-deposition. In the quest for enhanced fuel cell efficiency, scientists are investigating innovative ways to introduce catalyst materials onto the anode surface. This includes using precise deposition techniques such as sputtering and electro-deposition, which enable controlled and uniform distribution of catalyst materials. Additionally, techniques like screen printing and decaling offer versatility in creating patterned catalyst layers, tailored to specific electrode designs.

The choice of catalyst loading technique depends on factors such as the desired catalyst material, the substrate's composition, and the overall fuel cell architecture. Researchers aim to strike a balance between achieving high catalytic activity, even catalyst distribution, and efficient utilization of materials. By optimizing catalyst loading methods, DMFCs can be engineered to exhibit superior performance, increased efficiency, and enhanced methanol oxidation, ultimately contributing to the advancement of sustainable energy technologies.

1.6.5.2. Oxygen reduction reaction (ORR)

The field of energy conversion technology is currently experiencing a surge in research and development activities due to its remarkable attributes, which include exceptional energy conversion efficiency, minimal environmental pollution, and the potential for widespread applications. Among the numerous areas of investigation within this domain, the oxygen reduction reaction (ORR) stands out as a focal point of extensive study in the realms of electrochemistry and catalysis. This attention stems from the critical role that ORR plays in facilitating electrochemical energy conversion and storage devices. Essentially, ORR involves the intricate chemical processes occurring at the oxygen electrode within electrochemical systems, making it a fundamental component in various energy conversion technologies.

The significance of ORR stems from its pivotal contribution to key electrochemical processes, particularly in applications such as fuel cells and metal-air batteries. These devices rely on efficient oxygen reduction to enable the conversion of chemical energy into electrical energy. Moreover, the catalytic enhancement of ORR can significantly impact the overall performance and efficiency of energy conversion systems. As a result, scientists are extensively investigating catalyst materials and reaction mechanisms to improve the kinetics and efficiency of ORR.

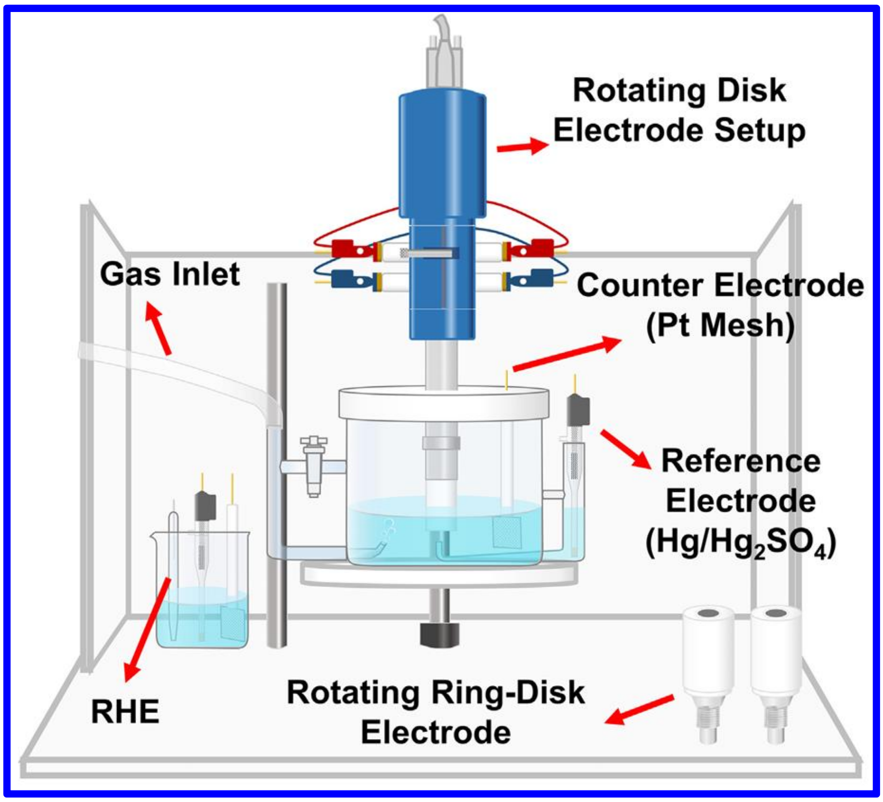

Figure 1.34 Schematic diagram of typical rotating-disk electrode (RDE) testing setup in three electrode configurations. Catalysts are loaded on an embedded glassy carbon disc of RDE. CE and RE are acronyms of counter electrode and reference electrode, respectively.

The study of ORR encompasses a wide range of approaches, including experimental investigations, theoretical modelling, and advanced characterization techniques. Researchers are striving to uncover novel catalysts, explore reaction pathways, and understand the underlying principles that govern ORR. By enhancing our comprehension of ORR mechanisms and optimizing catalytic materials, scientists are poised to drive advancements in energy conversion technologies, leading to more sustainable and efficient energy solutions for the future.

The oxygen reduction reaction (ORR) can proceed through either a two-step, two-electron pathway involving the formation of H_2O_2 (in acidic medium) or HO_2^- (in alkaline medium) as intermediate species, or a more efficient four-electron process that directly reduces O_2 to form

H_2O (in acidic medium) or OH^- (in alkaline medium), subsequently combining with a proton to yield water.[124] This dual pathway nature of the ORR is crucial in determining the overall efficiency of energy conversion processes, particularly in fuel cells. Fuel cells function by electrochemically oxidizing fuel and reducing oxygen, resulting in the production of water as the sole byproduct. This offers numerous advantages, including high energy conversion efficiency, minimal emissions, and environmental friendliness.

Traditional fuel cell technology relies on precious platinum (Pt) as a catalyst for facilitating the ORR at the cathode (**Figure 1.34**). In aqueous solutions, the Pt catalyst serves as an active site for effective adsorption and reduction of molecular O_2, following either the two-electron or four-electron pathway.[125] Despite its efficacy, the use of Pt presents challenges due to its exorbitant cost, susceptibility to time-dependent drift, susceptibility to fuel cross-over effects, and vulnerability to CO deactivation. To overcome these limitations, there is a pressing need to identify alternative catalyst materials that are cost-effective, readily available, and capable of matching or even surpassing the catalytic activity of Pt for the cathodic ORR in fuel cells. This pursuit aims to enhance the overall performance and feasibility of fuel cell systems, making them more accessible and viable for widespread energy applications. Through innovative research and development, scientists aim to develop catalysts that not only offer comparable performance but also overcome the drawbacks associated with precious metal catalysts, thus driving advancements in fuel cell technology.

1.6.6. PANI/MNPs composite as a catalyst in Organic synthesis

Both polyaniline (PANI) and PANI modified with metal nanoparticles (MNPs) have demonstrated noteworthy catalytic activity. The synthesis of metal nanoparticles typically involves a metal salt, a reducing agent, and a stabilizer, and these nanoparticles can be supported on various substrates such as oxides, charcoal, or zeolites. When PANI is employed as a support material, it not only serves as a substrate but also plays the roles of reducing agent and stabilizer also. This dual functionality offers distinct advantages, leading to simplified and reproducible synthesis processes. The integration of metal nanoparticles onto a PANI support holds great potential for applications in organic catalysis due to the combined benefits of catalytic activity, ease of preparation, and controllable synthesis.

Utilizing PANI as a support material for metal nanoparticles offers several advantages, including reducing the complexity of the synthesis process. In conventional methods, the need for separate reducing agents and stabilizers is eliminated as PANI serves both functions, streamlining the production of metal nanoparticles supported on PANI. This simplification results in enhanced reproducibility and greater ease in obtaining consistent catalytic materials.

Furthermore, the synergistic interaction between PANI and metal nanoparticles contributes to the catalytic performance of the composite material. PANI's electronic properties and surface characteristics can influence the adsorption of reactants and intermediates, ultimately impacting the catalytic activity. This unique interplay between PANI and MNPs leads to improved catalytic efficiency and selectivity, making PANI-supported metal nanoparticles promising candidates for diverse organic catalysis applications.[126, 127]

The exceptional versatility and potential of PANI and MNPs modified PANI in organic catalysis underscore the significance of this composite material in advancing catalytic processes. As researchers continue to explore and optimize the interaction between PANI and metal nanoparticles, new opportunities for designing efficient and tailored catalysts for various applications are anticipated.

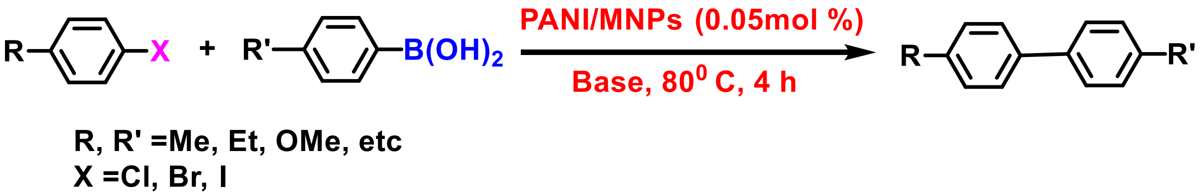

Scheme 1.35 MNPs decorated PANI as a catalysis Suzuki-Miyaura coupling reaction.

1.7 Aim and Motivation

Polyaniline (PANI) and polyaniline/metal nanoparticles (PANI - MNPs) have received considerable attention across a diverse array of application fields, as highlighted in the earlier introduction. This thesis work is centred around the synthesis of polyaniline nanostructures and an in-depth exploration of their inherent properties, and their potential applications. The versatility of these applications is intricately linked to various factors, each of which plays a crucial role in determining the feasibility and effectiveness of employing polyaniline-based materials. The demand for specific applications utilizing polyaniline hinges on a range of factors, foremost among them being the cost of materials production. An economically viable synthesis procedure is of paramount importance to ensure that the resulting products are both practical and commercially feasible for widespread adoption. Additionally, the shape, size, and density of particles within the polyaniline nanostructures significantly impact their behaviour and performance across different applications.

The thesis work mainly focuses on the synthesis of various kind of PANI nanotube and their potential application. The synthesis process itself holds considerable dominant over the applicability of polyaniline nanostructures. The ability to control and fine-tune the synthesis parameters enables the production of nanostructures with optimized properties for targeted applications mainly for energy and memory storage application.

1.7.1. Literature survey for Project 1

In past few decades electrochemical capacitors or supercapacitors were the most attractive device due to its high value of specific power, fast charging - discharging capability, lightweight, clean, flexible portable energy storage properties and also long durability.

Chen *et al*.[128] reported the use of PANI conducting nanotubes electrode materials in ionic liquid as the electrolyte, full-cell pseudo capacitors attained astounding energy densities of 84 W h /kg and power densities of 182 kW /kg. MnO_2 nanotubes were used as sacrificed templates in a one-step in situ chemical polymerization procedure that produced the PANI nanotubes. Importantly, the energy storage capacity of the PANI-nanotube pseudo capacitors was significantly increased by a factor of almost five times as compared to that of the PANI-nanotube pseudo capacitors in the acidic aqueous electrolyte.

Also, Miao *et al*.[129] reported use of the electro spun poly (amic acid) fibre membrane as a template, hollow polyaniline (PANI) nanofibers with adjustable wall thickness was created and showed the hollow PANI nanofibers as electrode materials of specific capacitance of 601 F /g at 1 A /g.

Based on that literature survey, I have designed **Project 1** that deals with fine-tuned PANI nanotube for energy storage application discussed in **Chapter 3**.

Project 1

In that Project, as a metal-free electrode material, an organic acid doped polyaniline nanotubes were prepared and utilized for the construction of supercapacitor devices. The morphology of the polymer nanostructure was tuned by using organic acids with various numbers of functionalized carboxylic groups, such as benzene dicarboxylic acids (OA2), benzene tricarboxylic acids (OA3), and benzene tetracarboxylic acids, greatly influences how much energy it can store (OA4). UV-Vis, XRD, FTIR, FESEM, and HRTEM were used to characterize the produced nanostructures. Cyclic voltammetry (CV), galvanic charge discharge (GCD), and electrochemical impedance spectroscopy were crucial tools for determining the charge storage characteristics of nanostructure (EIS). The best nanostructure, with a specific capacitance of 400 F/g at 0.5 A/g in the three-electrode setup, has been found to be benzene tetracarboxylic acids (OA4) doped polyaniline (OA4PAN).

1.7.2. Literature survey for Project 2

A variety of synthesis techniques for conducting polymer hydrogels were demonstrated in recent years. Normally, conducting polymer hybrid networks are created by either directly combining conducting polymer and the hydrogel component or polymerizing the appropriate monomer within the hydrogel network precursor.

Recently, Dai *et al*.[130] reported interfacial polymerization has been used to create conducting polymer hydrogels made of polyacrylamide (PAAm) and polyaniline (PAn). Because the PAn produced at the water/organic-solvent interface only spontaneously assembles into the PAAm hydrogel, the interfacial polymerization is far more inexpensive and effective than the standard preparation techniques. The resultant PAAm/PAn composite hydrogel, in contrast to typical materials, has exceptional attributes such as homogenous structure, improved mechanical toughness, high electrical conductivity, and the capacity to reversibly interconvert between the doped and dedoped states. Interfacial polymerization as described does not require a particular class of organic solvents or acid dopants to produce conducting polymer hydrogels.

Wu *et al.*[131] developed a unique and extremely flexible solid-state supercapacitor that is based on a graphene/polypyrrole hydrogel (PGH) with extended cycle performance that was created using a straightforward heating method. In particular, the PGH-based pore architectures bring more electrochemically active surfaces for the absorption and desorption of electrolyte ions as well as higher mechanical flexibility. With a high specific capacitance of 363 F cm-3 at a current density of 1.0 mA cm-3 and outstanding cycle stability with capacitance retention of 98.6% after 12000 charge/discharge cycles in bending, folded, and twisted states, flexible supercapacitors have a special structural design. Compared to comparable polypyrrole (PPy)-based materials, the PGH produced in this work has outstanding electrochemical and flexible capabilities.

Based on this literature survey, I have designed Polyaniline with G-quadruplex - hybrid network for energy storage application discussed in **Chapter 4**.

Project 2

In-situ preparation of polyaniline into G-quadruplex assembled through chemical oxidation of aniline in presence of APS to make a hybrid network that had been investigated with the help of FTIR, XRD, absorption studies to know about the formation hybrid network of G-quadruplex assembled and polyaniline (PANI) in aqueous medium. Overall changes of micro-structural morphology of G-quadruplex assembly network before / after the polymerization had been investigated with FESEM and HRTEM and the strength /stiffness of the said hybrid network had been explored through by rheological studies. Subsequently, this hybrid network had been utilized as electrode material for the electrochemical energy storage studied by Cyclic voltammetry (CV), galvanic charge discharge (GCD) and electrochemical impedance spectroscopy (EIS). It had been noticed that the hybrid network made of PANI / G-quadruplex is providing specific capacitance ~ 405 F/g at 0.5 A/g in the three-electrode system. A symmetrical solid-state device (2 × 2 cm2) made of bioconjugate network which had been fabricated and it had revealed the specific capacitance of 118 F/g at a 1 A/g in wide potential window with high cyclic stability up to 20000 cycles at 7 A/g (~ 87 % retention of specific capacitance). This hybrid network may be eligible to use for various energy storage system in near future.

1.7.3. Literature survey for Project 3

Recently, nanoparticles are effectively very useful way in the field of catalysis, surface property measurement, biology, electronic device preparation *etc*. Cost effective, easy, size and loading/population tunable preparation of nanoparticles are demanding in new research area.[132-135] By considering the oxidation-reduction behavior of polyaniline, metal nanoparticles (Ag, Au, Pd and Pt) coated PANI have been synthesized at room temperature, easily.[132]

In my **Project 3,** Ag-nanoparticles decorated PANI nanotube was decorated without using external reducing agent for the purpose of Memory storage application in **Chapter 5.**

Project 3

In this work one-dimensional conducting functional polymer nanotubes with embedded metal nanoparticles had been carefully chosen for RS memory applications in this work. Chemical polymerization had been used to create pure benzene tetracarboxylic acid-doped polyaniline (BDP) and silver (Ag) metal-doped BDP (MBDP). All the samples had been extensively characterized by FTIR, UV-Vis, XRD, FESEM, TEM, etc. before looking at RS performances. Pure BDP samples did not create any RS, according to an electrical transport investigation, while MBDP samples containing tailored Ag NPs produced both a low resistive state (LRS) and a high resistive state (HRS). The Ag NP loading concentration had a significant impact on the ON/OFF resistance ratio. At a high applied current, the sample with a 36.7 percent loaded Ag content (MBDP 10) demonstrated a clear second resistive transition in addition to reaching the best RS properties. These materials were particularly attractive options for plastic-based RS device applications due to a significant increase of RS properties, such as retention time (104 s), durability (250 cycles), and restricted dispersion of RS. Furthermore, the usage of MBDP 10 in logic operation was made possible by its many resistive states (for example, OR gate). Temperature-dependent transport measurement and low-frequency 1/f conductance noise spectroscopy had been used to examine the detailed charge transport in pure BDP and MBDP 10 samples (with the ideal concentration of Ag NPs) in order to comprehend the physics behind the RS occurrences.

1.8. References

1. Jöns Jacob Berzelius". Encyclopædia Britannica Online. Retrieved 3 August **2008**.
2. M. Amin and M. Salman, *Rev. Adv Mater. Sci*., 2006, **13**, 93.
3. H. Shirakawa, E. J. Louis, A. G. MacDiarmid, C. K. Chiang and A. J. Heeger, *Chem. Comm*. 1977, 578.
4. J. Stejskal, Dendrimers, Assemblies, Nanocomposites, MML Series, 5 Ed. By R. Arshady and A. Guyot. Citus *Books*, London, 2002, **195**.
5. A. G. MacDiarmid, *Rev. Mod. Phys*., 2001 **73**, 3.
6. (a) www.nobel.se/chemistry/laureaters/2000/index.html; (b) J. D Stenger-Smith *Progress in Polymer Science*, 1998, **23**, 57.
7. M. H. Ram, N. S. Sunaresan and B. D. Malhotra. *J. Mat. Sci. Lett*., 1994, **13**, 1490.
8. Y. Cheng, S. H. Yang and C. Hsu, *Chem. Rev*., 2009, **109**, 5868.
9. D. Jiles, Introduction to the electronic properties of materials, Chapman & Hall, London, 1994.
10. J. L. Bredas and G. B. Street, *Acc. Chem. Res*., 1985, **18,** 309.
11. K. Y. Jen, M. V. Lakshmikantan, M. Albeck, M. P. Cava, W. S. Huang and A. G. MacDiarmid. *J. Polym. Sci.Polym. Lett.* 1983, **21**, 441.
12. G. Tourillon and F.Garnier. *J. Phys. Chem*., 1983, **87**, 2289.
13. G. M. Golob and P. Ehrlich, *J. Polym. Sci. Polym. Phys*., 1977, **15**, 627.
14. J. C. W. Chein, *Polyacetylene: Chemistry, Physics and Material science*, (Academic press, New York), 1984.
15. S. Maiti., J. Sci. Ind. Res., 1986, **12**, 179.
16. J. E. Frommer and R. R. Chance., Encyclopedia of polymer science and engineering edited by J. I. Kroschwitz (Wiley, New York) 1986, 462.
17. T. J. Lewis., *Faraday Discuss. Chem. Soc*., 1989, **88**, 189.

18. A. A. Pud., Synth. Met., 1994, **68**, 1.

19. G. Dandreaux, E.Galvin and G. E. Wnek, Appl. Polym. Sci., 1983, **48**, 541.

20. H. Naarmann. "Polymers, Electrically Conducting". Ullmann's Encyclopedie of Industrial Chemistry. DOI: 10.1002/14356007.

21. R. H. Friend, R. W. Gymer, A. B. Holmes, J. H. Burroughes, R. N. Marks, C Taliani, D. D. C. Bradley, D. A. Dos Santos, J. L. Brédas, M. Lögdlund and W. R. Salaneck, *Nature*, 1999, **397**, 121.

22. B.G. Levi, New Printing Technologies Raise Hopes for Cheap Plastic Electronics, Physics Today, Feb. 2001, 20-22.

23. W. U. Huynh, J. J. Dittmer and A. P. Alivisatos, *Science*, 2002, **295**, 2425.

24. S. Gunes, H. Neugebauer and N. S. Sariciftci, *Chem. Rev.*, 2007, **107**, 1324.

25. H. Sirringhaus, T. Kawase, R. H. Friend, T. Shimoda, M. Inbasekaran, W. Wu and E. P. Woo, *Science*, 2000, **290**, 2123.

26. W. Clemens, W. Fix, J. Ficker, A. Knobloch and A. Ullmann, *J. Mater. Res.*, 2004, **19**, 1963.

27. J. H. Burroughes, D. D. C. Bradley, A. R. Brown, R. N. Marks, K. Mackay, R. H. Friend, P. L. Burns and A. B. Holmes, *Nature*, 1990, **347**, 539.

28. J.C. Scott, S.A. Carter, S. Karg and M. Angelopoulos, *Synth. Met.*, 1997, **85**, 1197.

29. J. Ding, L. Liu, G. M. Spinks, D. Zhou, G. G. Wallace and J. Gillespie, *Synth. Met*, 2003, **138**, 391.

30. P. Chandrasekhar, B. J. Zay, G. C. Birur, S. Rawal, E. A. Pierson, L. Kauder and T. Swanson, *Adv. Funct. Mater.*, 2002, **12**, 95.

31. S. A. Sapp, G. A. Sotzing, J. L. Reddinger and J. R. Reynolds, Adv. Mater., 1996, **8**,808.

32. Q. Wu, Y. Xu, Z. Yao, A. Liu and G. Shi, *ACS Nano*, 2010, **4**, 1963.

33. K. Zhang, L. L Zhang, X. S. Zhao and J. Wu, *Chem. Mater.*, 2010, **22**, 1392.

34. X. Ma, G. Li, M. Wang, Y. Cheng, R. Bai and H. Chen., *Chem. Eur. J.*, 2006, **12**, 3254.

35. S.Virji, J. Huang, R. B. Kaner and B. H. Weiller, *Nano Lett.*, 2004,**4**,491.

36. J. Huang, S. Virji, B. H. Weiller and R. B. Kaner, *J. Am. Chem. Soc.*, 2003, **125**, 314.

37. J. D. Fowler, S. Virji, R. B. Kaner and B. H. Weiller, *J. Phys. Chem. C*, 2009, **113**, 6444.

38. M. D. Shirsat, M. A. Bangar, M. A. Deshusses, N. V. Myung and A. Mulchandani, *Appl. Phys. Lett.*, 2009, **94**, 083502.

39. H. Chang, Y. Yuan, N. Shi and Y. Guan, *Anal. Chem.*, 2007, **79**, 5111.

40. Z. M. Tahir, E. C. Alocilj and D. L. Grooms, *Biosens. Bioelectron.*, 2005, **20**, 1690.

41. P. Saini, V. Choudhary and S. K. Dhawan, *Polym. Adv. Technol.*, 2009, **20**, 355.

42. S. 1. Na, S. S. Kim, J. Jo and D.Y. Kim, *Adv. Mater.*, 2008, **20**, 4061.

43. P. C. Hsu, H. Wu, T. J. Carney, M. T. McDowell, Y. Yang, E. C. Garnett, M. Li, L. Hu and Y. Cui, *ACS Nano*, 2012, **6**, 5150.

44. H. Letheby, *J. Chem. Soc.*, 1862, **15**, 161.

45. M. F. Goppelsroder. *Compt. Rend.*, 1876, **82**, 331.

46. J. C. Chiang and A. G. MacDiarmid, *Synth. Met.*, 1986, **13**,193.

47. A. G. MacDiarmid and A. J. Epstein, *J. Faraday Discuss. Chem. Soc.*, 1989, **88**, 317.

48. J. Y. Shimano and A.G. MacDiarmid, *Synth. Met.*, 2001, **123**, 251.

49. Y. Wei and K. F. Hsueh, *J. Polym Sci A Polym Chem.*, 1989, **27**, 4351.

50. E. M. Genies, A. Boyle, M. Lapkowski and C. Tsintavis, *Synth. Met.*, 1990, **36**, 139.

51. A. G. MacDiarmid, J. C. Chiang, A. F. Richter and A. J. Epstein *Synth. Met.*, 1987, **18**, 285.

52. J. Stejskal, P. Kratochvil and A. D. Jenkins, *Polymer*, 1996, **37**, 367.

53. J. C. Chiang and A. J. Macdiarmid, *Synth. Met.*, 1986, **13**, 193.

54. H. Letheby, *J. Chem. Soc.*, 1862**, 15**, 161.

55. Y. Sun, Alan G. MacDiarmid and J. Epstein, *J. Chem. Soc., Chem. Commun.*, 1990, 529

56. U. Rana, K. Chakrabarti and S. Malik *J. Mater. Chem.*, 2012, **22**, 15665.

57. E. W. Paul, A. J. Ricco and M. S. Wrighton, *J Phys. Chem.*, 1985, **89**, 1441.

58. T. A. Skotheim, R.L. Elsenbaumer and J. Reynold, Handbook of conducting polymers, Marcel Dekker, New York, 1998.

59. G. G. Wallace, G. M. Spinks and P. R. Teasdale, Conductive Electroactive Polymers, CRC Press,London, 2002.

60. J. Li, L. H. Zhu, W. Luo, Y. Liu and H. Q. Tang, *J. Phys Chem C*, 2007, **111**, 8383.

61. R. Nagarajan, S. K. Trypathy, J. Kumar, F. F. Bruno and L. A. Samuelson, *Macromolecule*s, 2000, **33,** 9542

62. W. Liu, A. L. Cholli, R. Nagarajan, J. Kumar, S. K. Trypathy and F. F.Bruno, *J. Am. Chem. Soc.*, 1999, **121**, 11345.

63. (a) H. Zemel and J. F. Quinn. *U S Patent*, 1995, **420**, 237; (b) R. Cruz-Silva, R. Romero-Garcıa, J. L. Angulo-Sanchez, E. Flores-Loyola, M. H. Farıas and F. F. Castillon, *Polymer*, 2004, **14**, 4711;

64. (a) R. L. Hand and R. F. Nelson, *J. Am. Chem. Soc.*, 1974, **96**, 1133; (b) J. Huang, J. A. Moore, J. H. Acquaye and R. B. Kaner, *Macromolecule*, 2005, **38**, 317.

65. (a) W. Liu, J. Kumar, K. J. Senecal and L. A. Samuelson, *J Am Chem Soc.*, 1999, **121**, 71. (b) N. V. Bhat, and N. V. Joshi, *Plasma Chem. Plasma Process.*, 1994, **4**, 151; (c) L. A. Samuelson, A. Anagnostopoulos, K.S. Alva, J. Kumar and S.K. Tripathy, *Macromolecules*, 1998, **31**,4376. (d) R. M. Nabid and A. A. Entezami, *Eur Polym. J*, 2003, **39**, 1169.

66. A. G. MacDiarmid and A. J. Epstein *Chem. Soc.*, 1989, **88**, 317.

67. (a) E. N. Konyushenko, J. Stejskal, I. Sedenkova, M. Trchova, I. Sapurina, M. Cieslar and J. Prokes, *Polym Int.*, 2006, **55**, 31, (b) 1. Stejskal, 1. Sapurina, M. Trchova, E. N.

Konyushenko and P. Holler, *Polymer*, 2006, **47**, 8253, (c) 1. Stejskal, I. Sapurina, M. Trchova and E. N. Konyushenko, *Macromolecules*, 2008, **41**, 3530; (d) H. J. Ding, J. Y. Shen, M. X. Wan and Z. J. Chen, *Macromol Chem Phys.*, 2008, **209**, 864; (e) L. J. Zhang, Z. D. Zujovic, H. Peng, G. A. Bowmaker, P. A. Kilmartin and J. Travas-Sejdic, *Macromolecules*, 2008, **41**, 8877; (C. Laslau, Z. D. Zujovic, L. J. Zhang, G. A. Bowmaker and J. Travas- Sejdic, *Chem Mater*, 2009, **21**, 954; (g) 1.-E. Osterholm, Y. Cao, F. Klavetter and P. Smith, *Polymer*, 1994, **35**, 2902.

68. G. Ciric-Marjanovic, E. N. Konyushenko, M. Trchova and J. Stejskal. *Synth Met.*, 2008, **158**, 200.

69. (a) J. Stejskal, A. Riede, D. Hlavata, J. Prokes, M. Helmstedt and P. Holler, *Synth Met.*, 1998, **96**, 55; (b) D. Yang, W. Lu, R. Goering and B. R. Mattes, *Synth Met.*, 2009, **159**, 666.

70. (a) R. L. Hand and R. F. Nelson, *J. Am. Chem. Soc.*, 1974, **96**, 1133; (b) J. Huang, J. A. Moore, J. H. Acquaye and R. B. Kaner, *Macromolecule*, 2005, **38**, 317.

71. U. Rana and S. Malik, *Chem. Commun*., 2012, **48**, 10862.

72. J. Huang, S. Virji, B. H. Weiller and R. B. Kaner, *J. Am. Chem. Soc.*, 2003, **125**, 314.

73. M. Mitra, C. Kulsi, K. Chatterjee, K. Kargupta, S. Ganguly, D. Banerjee and S. Goswam, *RSC Adv*., 2015, **5**, 31039.

74. S. Virji, J. Huang, R. B. Kaner and B. H. Weiller, *Nano Lett*., 2004, **4**, 491.

75. (a) K. Huang and M. X. Wan, *Chem. Mater*., 2002, **14**, 3486; (b) U. Rana, K. Chakrabarti and S. Malik, *J. Mater. Chem*., 2011, **21**, 11098.

76. K. Lee1, S. Cho, S. H. Park, A. J. Heeger, C.-W. Lee and S.-H. Lee, *Nature*, 2006, **441**, 65.

77. N. Nuraje, K. Su, N. Yang and H. Matsui, *ACS Nano*, 2008, **2**, 502.

78. Q. W.Tang, J. H. Wu, X. M. Sun, Q. H. Li, J. M. Lin and M. L. Huang, *Chem. Commun*., 2009, 2166.

79. (a) P. Anilkumar and M. Jayakannan, *Macromolecules*, **2007**, 40, 7311 (b) K. Huang and M. Wan, *Chem. Mater*., 2002, **14**, 3486.

80. (a) D. Li and R. B. Kaner, *J. Am. Chem. Soc*., 2006**, 128**, 968 (b) S. Mondal, U. Rana, R. R. Bhattacharjee and S. Malik, *RSC Adv*., 2014, **4**, 57282.

81. H. B. Zhang, J. X. Wang, Z. Wang, F. B. Zhang and S. C. Wang, *Macromol. Rapid Commun*., 2009, **30**, 1577.

82. (a) Z. Wei and M. Wan, *Adv. Mater*., 2002, **14,** 1314; (b) X. Shi, A. J. Briseno, R. J. Sanedrin and F. Zhou, *Macromolecules*, 2003, **36**, 4093.

83. L. Pan, L. Pu, Y. Shi, S. Song, Z. Xu, R. Zhang, and Y. Zheng, *Adv. Mater*., 2007, **19**, 461 – 464.

84. G. Cao, J. Xu, S. Cai, Y. Chen, D. Zhou, H. Zhang, C. Jiang, G. Zhang, and Y. Tian, *ACS Appl. Polym. Mater*. 2023, **5**, 593 – 601.

85. S. Pang, W. Chen, Z. Yang, Z. Liu, X. Fan, D. Fang, *Polymers* 2017,**9(10)**, 510

86. W. Chen, R. B. Rakhi and H. N. Alshareef, *J. Mater. Chem. A*, 2013, **1**, 3315.

87. Z. Zhang, M. Wan and Y. Wei, *Adv. Funct. Mater*. 2006, **16**, 1100.

88. U. Rana, S. Mondal, J. Sannigrahi, P. K. Sukul, Md. A. Amin, S. Majumdar and S. Malik, *J. Mater. Chem. C*, 2014, **2**, 3382.

89. V. Armel, O. Winther-Jensen, R. Kerr, D. R. MacFarlane and B. Winther-Jensen, *J. Mater. Chem.*, 2012, **22,** 19767.

90. P. Xu, X. Han, B. Zhang, Y. Dua and H.-L. Wang, *Chem. Soc. Rev*., 2014, **43**, 1349.

91. D. Li, J. X. Huang and R. B. Kaner, *Acc. Chem. Res*., 2009, **42**, 135.

92. W. M. Lemke, R. B. Kaner and P. L. Diaconescu, *Inorg. Chem. Front*., 2015, **2**, 35.

93. W. G. Li, Q. X. Jia and H. L. Wang, *Polymer*, 2006, **47,** 23.

94. (a) W.-S. Huang, B. D Humphrey and A. G MacDiarmid, *J. Chem. Soc. Faraday Trans*., 1986, **82**, 2385; (b) E. M. Geniès, M. Lapkowski and J. F. Penneau, *J. Electroanal. Chem. Interfacial Electrochem*., 1988, **249**, 97.

95. (a) E. Song and J.-W. Choi, *Nanomaterials*, 2013, **3**, 498; (b) R. S. Diggikar, D. J. Late and B. B. Kale, *RSC Adv*., 2014, **4**, 22551.

96. W. W. Focke and G. E. Wnek, *J. Electroanal. Chem. Interfacial Electrochem*, 1988, **256**, 343.

97. (a) J. R. Miller and P. Simon, *Science*, 2008, **321**, 651; (b) J. M. Tarascon and M. Armand, *Nature*, 2001, **414**, 359.

98. (a) A. Z. Sadek, C. O. Baker, D. A. Powell, W. Wlodarski, R. B. Kaner, K. Kalantarzadeh, *IEEE Sens. J.*, 2007, **7**, 213; (b) A. Z. Sadek, W. Wlodarski, K. Shin, R. B. Kaner and K. Kalantar-zadeh, *Nanotechnology*, 2006, **17**, 4488

99. a) F. Goto, K. Abe, K. Okabayashi, T. Yoshida and H. Morimoto, *J. Power Sources*, 1987, **20**, 243; (b) S. Taguchi and T. Tanaka, *J. Power Sources*, 1987, **20**, 249; (c) E. M. Genies, A. A. Syed and C. Tsintavis, *Mol. Cryst. Liq. Cryst.*, 1985, **121**, 181

100. M. Winter and R. J. Brodd, *Cgem. Rev.*, 2004, **104**, 4245

101. J. K. Pandey, H. Takagi, A. N. Nakagaito, Handbook of Polymer Nanocomposites. Processing, Performance and Application, ISBN 978-3-64245229-1, DOI; 10.1007/978-3-64245229-1.

102. J. K. Pandey, H. Takagi, A. N. Nakagaito, Handbook of Polymer Nanocomposites Processing, Performance and Application, ISBN 978-3-64245229-1, DOI 10.1007/978-3-64245229-1.

103. G. Wang, L. Zhang and J. Zhang, Chem. *Soc. Rev.*, 2012, **41**, 797-828.

104. https://en.wikipedia.org/wiki/Pseudocapacitance.

105. (a) Q. Cao, H.-S Kim, N. Pimparkar, J. P Kulkarni, C. Wang, M. Shim, K. Roy, M. A. Alam and J. A. Rogers, *Nature*, 2008, **454**, 495. (b) D. H. Kim, N. Lu, R. Ma, Y. S. Kim, R. H. Kim, S. Wang, J. Wu, S. M. Won and H. Tao, A. Islam, *Science*, 2011, **333**, 838.

106. H. Nishide and K. Oyaizu, *Science*, 2008, **319**, 737

107. B. Pandit, D. P. Dubal, B. R. Sankapal, *Electrochim. Acta*, 2017, **242**, 382-389.

108. X. Lu, M. Yu, G. Wang, Y. Tong and Y. Li, *Energy Environ. Sci.*, 2014, **7**, 2160.

109. (a) Y. He, W. Chen, C. Gao, J. Zhou, X. Li and E. Xie, *Nanoscale*, 2013, **5**, 8799; (b) Y. Xu, Z. Lin, X. Huang, Y. Liu, Y. Huang and X. Duan, *ACS Nano*, 2013, **7**, 4042.

110. J. J. L. Hmar, *RSC Adv.*, 2018,**8**, 20423-20433.

111. C. O. Baker, B. Shedd, R. J. Tseng, A. A. M. Morales, C. S. Ozkan, M. Ozkan, Y. Yang, and R. B. Kaner, *ACS Nano*, 2011, **5**, 3469–3474.

112. Tseng, C.-W.; Tao, Y.-T, *J. Am. Chem. Soc.* 2009, **131**, 12441– 12450

113. J. Cai, C. Zhang, A. Khan, C. Liang and Wen-Di Li, *RSC Adv.*, 2018,**8**, 5312-5320.

114. Y. Li, Y. Mao, C. Xiao, X. Xu and X. Li, *RSC Adv.*, 2020,**10**, 21-28

115. C. Dhand, M Das, M. Datta, B.D. Malhotra, *Biosensors and Bioelectronics*, 2011, **26**, 2811-2821.

116. I. A. Anisimov, R. W. Evitts, D. E. Cree and L. D. Wilson, *ACS Appl. Polym. Mater.*, 2022, **4**, 7204–7216.

117. S. Sharma, A. Chhetry, P. Maharjan, S. Zhang, K. Shrestha, Md. Sharifuzzaman, T. Bhatta, Y. Shin, D. Kim, S. Lee, J. Y. Park, *Nano Energy*, 2022, **95**, 106970.

118. C. Luo, Y. Wang, X. Li, X Jiang, P Gao, K. Sun, J. Zhou, Z. Zhang, and Q. Jiang, Nanomaterials, 2017, 7(3) 67.

119. M. A. Hussein, A. Khan and K. A. Alamry, RSC Adv., 2022, 12, 31506-31517.

120. J. Pan, S. Liu, H. Zhang, and J. Lu, Sensors, 2019 19(19) 4105.

121. S. Y. Hong, Y. H. Lee, H. Park, S. W Jin, Y. R. Jeong, J. Yun, I. You, G. Zi, J. S. Ha, 2016, 28 (5), 930-935.

122. N. Kakati, J. Maiti, S. H. Lee, S. H. Jee, B. Viswanathan and Y. S. Yoon, *Chem. Rev.*, 2014, **114**, 12397.

123. X. Ge, A. Sumboja, D. Wuu, T. An, B. Li, F. W. T. Goh, T. S. A. Hor, Y. Zong and Z. Liu, *ACS Catal.*, 2015, **5**, 4643

124. M.-H. Shao, P. Liu and R. R. Adzic, *J. Am. Chem. Soc.*, 2006, **128**, 7408.

125. X. Wang, L. Zou, H. Fu, Y. Xiong, Z. Tao, J. Zheng and X. Li, *ACS Appl. Mater. Interfaces*, 2016, **8**, 8436.

126. (a) B. J. Gallon, R. W. Kojima, R. B. Kaner and P. L. Diaconescu, *Angew. Chem., Int. Ed.*, 2007, **46**, 7251; (b) J. Han, Y. Liu and R. Guo, *J. Am. Chem. Soc.*, 2009, **131**, 2060.

127. B. J. Gallon, R. W. Kojima, R. B. Kaner and P. L. Diaconescu, *Angew. Chem.*, 2007, **119**, 7389.

128. W. Chen, R.B. Rakhi, H.N. Alshareef, *J. Mater. Chem. A*, 2013, **1**, 3315–3324.

129. Y.-. E. Miao, W. Fan, D. Chen, T. Liu, *ACS Appl. Mater. Interfaces*, 2013, **5** 4423–4428

130. Dai, T.; Qing, X.; Wang, J.; Shen, C.; Lu, Y., *Compos. Sci. Technol.*, 2010, **70**, 498–503.

131. Wu, X.; Lian, M., *J. Power Sources*., 2017, **362**, 184–191.

132. C. Ban, X. Wang, Z. Zhou, H. Mao, S. Cheng, Z. Zhang, Z. Liu, H. Li, J. Liu and Wei Huang, *Sci. Reports*, 2019, **9**, 10337.

133. E. W. Lim and R. Ismail *Electronics*, 2015, **4**, 586-613.

134. K. T. Patil, K. A. Nirmal, S. A. Jadhav, S. R. Patil, T. D. Dongale, D-K. Kim, P. S. Patil, *Materialia*, 2021, **15**, 101026.

135. J. T. Holgate, M. Coppins and J. E. Allen, *Appl. Phys. Lett*, 2018, **112**, 043302.

CHAPTER 2

Characterization & Instrumentation

2. Characterization

Conducting polymers (such as polyaniline, polypyrrole, polythiophene) and conducting polymer composites have been occupied a frontier area in the recent research fields. Along with their synthesis as well as potential application, it is also very much essential to analyse their physical and chemical properties. For exploration of their structural properties and the various potential application, it is mandatory to study their synthetic mechanism. To know the above-mentioned mechanism and properties, several types of characterization techniques were applied to establish their inherent properties e. g. chemical composition, thermal stability, morphology, binding energy, photoluminescence etc. However, the basic working principles of those characterization techniques which were frequently used in my thesis work were discussed. The characterization techniques included UV-Vis spectroscopy, Fourier transform infrared (FTIR) spectroscopy, X-Ray Diffraction (XRD), Field-emission Scanning Electron Microscopy (FESEM), Transmission Electron Microscopy (TEM), Atomic Force Microscopy (AFM), Electrochemical study, X-Ray Photoelectron Spectroscopy (XPS), Current (I)-Voltage (V) Measurement *etc*.

2.1 Ultraviolet-visible (UV-vis) spectroscopy

In the modern laboratory, ultraviolet-visible (UV-vis) spectroscopy is the most essential analytical method. Because of its ease of use, adaptability, speed, accuracy, and affordability, UV-Visible spectrometry is commonly used to understand a) absorption property b) the band gap and c) nature of polymer chain, perticularly for conducting polymer.

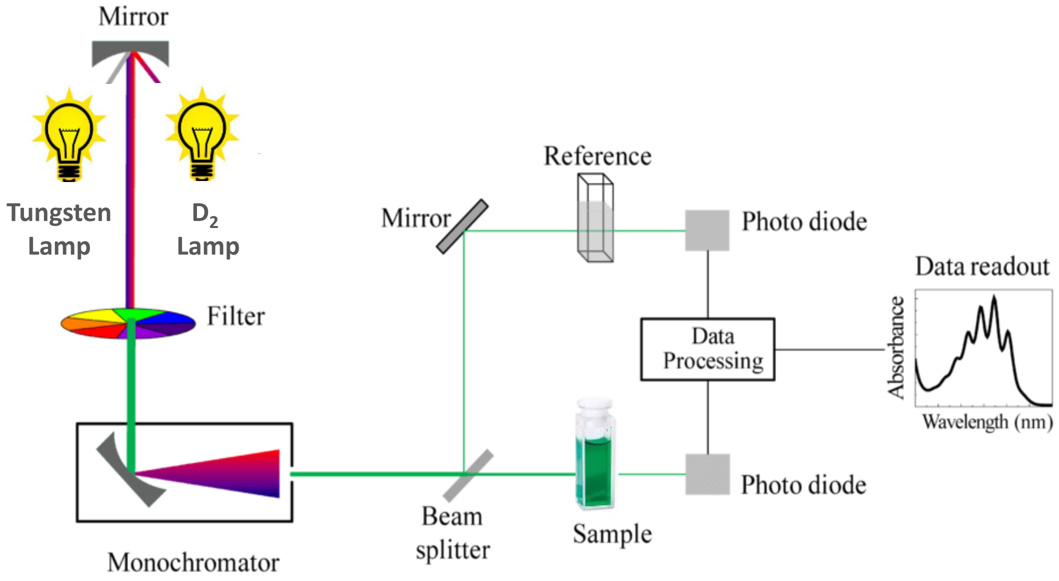

Figure 2.1 Schematic representation of working principle of UV-Vis spectroscopy

In general, absorbance and transmittance spectroscopy are the two main modes used to record ultraviolet-visible (UV-Visible) spectroscopy. In UV-Visible spectroscopy, there are primarily two wavelength regions: the ultraviolet area, or 200-400 nm, and the visible range, or 400-800 nm. When UV light is irradiated on the samples, the outermost electronic transitions take place from a lower to a higher energy level. The absorption of the light occurs and an absorbance spectrum is obtained if the wavelength of the incoming light matches the energy gap of the electronic transition. These electronic transitions are typically referred to as $\pi \rightarrow \pi^*$ and/or $n \rightarrow \pi^*$ transitions.

When UV-visible light passes through the sample solution some of the light is absorbed by the sample and rest part of the light transmit through the solution (**Figure 2.1**)

In UV-Visible spectroscopy Lambert-Beer's law is used to measure the absorbance of the light absorbing sample solution. According to this law absorbance is represented as:

$$A = \epsilon.\ c.\ l. \quad \ldots\ldots\ldots\ldots\ldots\ldots\ldots\ldots\ldots\ldots \quad (2.1)$$

Where, “A” is the absorbance (-log I/I_0), “ϵ” is molar extinction coefficient (L mol^{-1} cm^{-1}), “c” is concentration of samples (mol/L), “l” is the path length of UV cell (cm)

The spectrophotometer may also be used to measure the amount of transmittance following the interaction between light and matter. After the light has been absorbed, its intensity has changed from I_0 to I. The percentage of transmittance is the intensity ratio of the transmittance light to the incoming light, or ($100*I/I_0$). To get the absorbance from the percent transmittance, use the equation $A = -\log (T/100)$, where A is the absorbance and T is the percent transmittance. UV-vis spectra have been used to determine if an organic chromophore, metal ion, inorganic complex, or ionic species are present in the given item also we can we can determine concentration and the absorbance band pattern of the sample can also provide sample nature.

2.2 Fourier transform infrared (FTIR) spectroscopy

To identify the functional groups contained in materials, FTIR spectroscopy has been utilised. The FTIR apparatus is made up of one beam splitter, one fixed mirror, one moveable mirror, and one infrared (IR) light source, as illustrated in **Figure 2.2**. When exposed to electromagnetic radiation, a molecule’s IR-active bonds can alter the molecules' dipole moment.

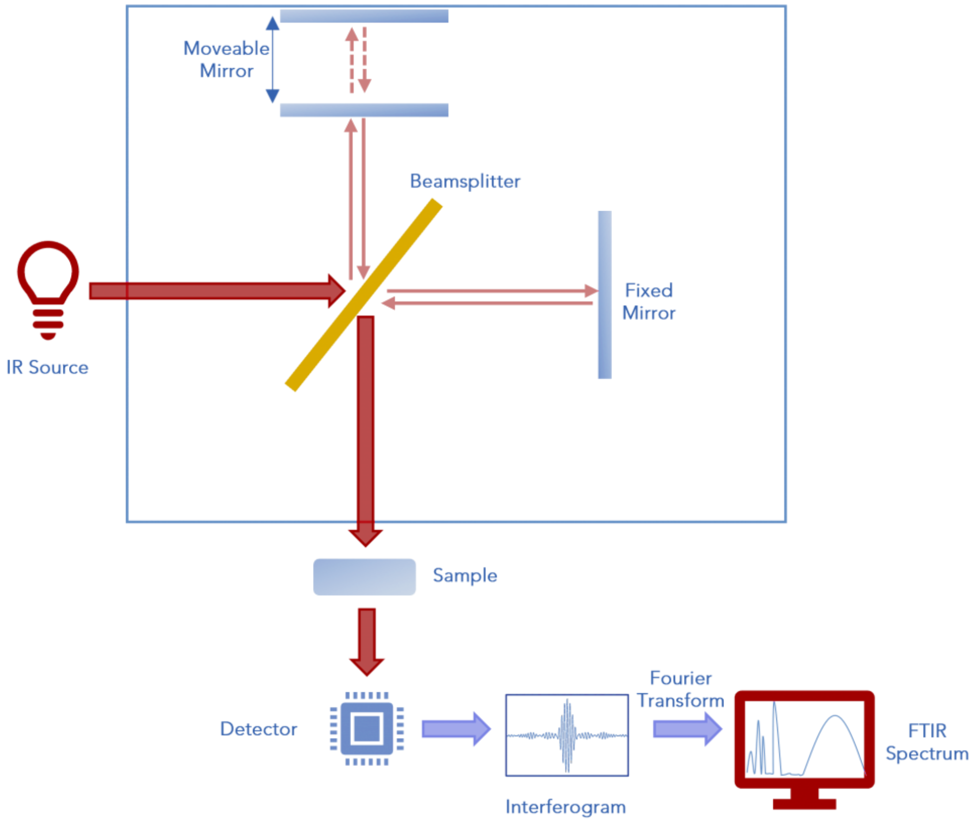

Figure 2.2 Schematic presentation of instrumentation for FTIR spectroscopy

Infrared absorption spectra result from the molecules moving from a lower to a higher vibration level when they are stimulated by infrared light. Because there are several rotational levels and a number of vibrational levels, both of them are affected by infrared absorption. When describing the absorption of infrared radiation, the words wavelength or wave number can be employed, while transmittance (T) or absorbance are used to describe the strength of the band seen in the FTIR spectrum (A). To dilute the samples with KBr, pellets with a range of 400-4000 cm^{-1} were made using the FTIR-8400S instrument (Shimadzu) in this thesis study.

2.3 X-Ray Diffraction (XRD) study

The characterisation of crystalline materials, such as metals, ceramics, polymers, plastics, or other inorganic or organic substances, is best accomplished using X-ray diffraction (XRD) methods. X-rays, an electromagnetic radiation, interact with materials in XRD research (**Figure 2.3**). Either absorption-where energy from the X-ray photon is transferred to the absorbing material-or scattering-where the X-ray photon is “redirected” by interaction with the scattering material-occurs as a result of that interaction. Bruker AXS diffractometer (D8 advance) XRD equipment with Cu K_α radiation (λ = 1.542Å), 40 kV generator voltage, and 40 mA current has been employed in our research.

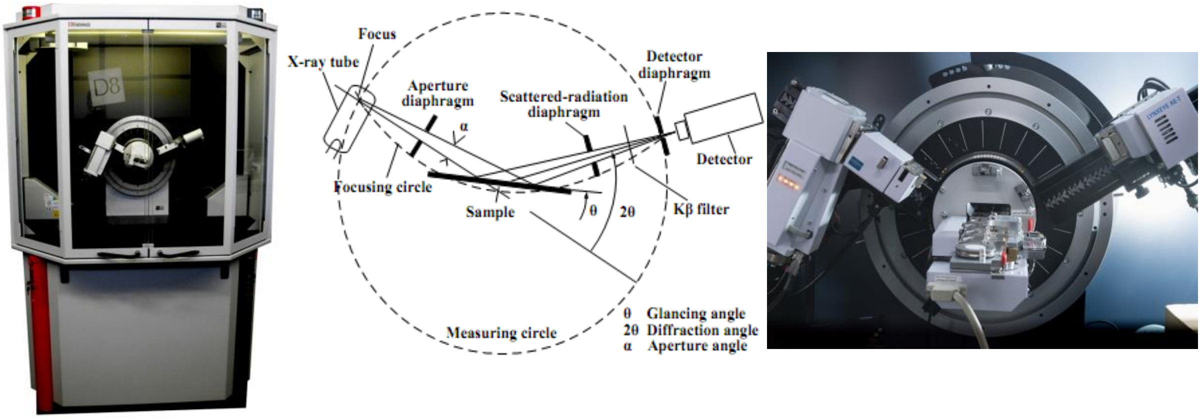

Figure 2.3 Representation of working principle for XRD and XRD Bruker AXS diffractometer instrument

According to “Bragg’s Law”, secondary “diffracted” beams of X-rays linked to interplanar spacing in the crystalline powder are produced as a result of the interaction of X-rays with sample: $n\lambda = 2d \sin\theta$.................................(2.2).

Where “n” is an integer, “λ” is the X-ray wavelength, “d” is the interplanar distance that causes diffraction, and “θ” is the diffraction angle.

2.4 Optical Microscope

An optical microscope is a type of microscope made consisting of a few lenses and using visible light to generate a magnified picture of a tiny object that can be seen with the unaided eye. Typically, the objective lens is positioned near to the sample and has a short focal length. When a sample is exposed to visible light, an objective lens gathers any light that is passed through the sample or reflected back, creating a true picture of the sample that is then magnified by an eyepiece. This eyepiece or ocular lens gives the viewer a magnified view of the thing.

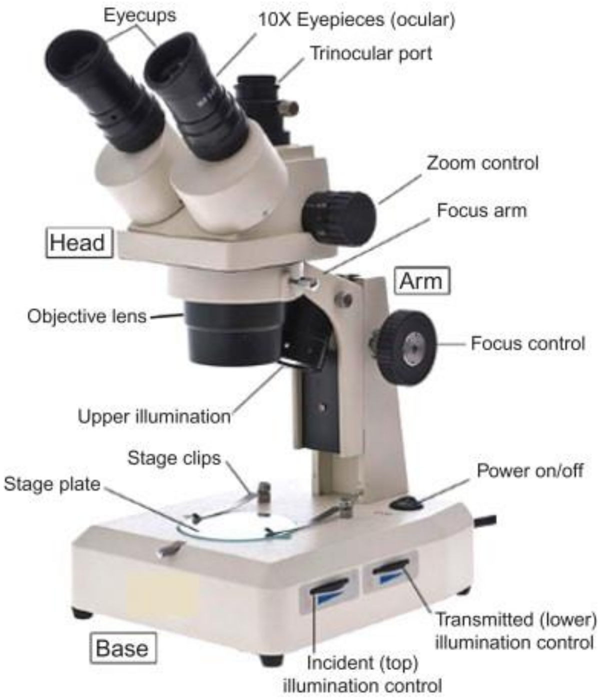

Figure 2.4 Olympus BX53M Optical Microscope equipped with DP23 Camera

2.5 Electron Microscope

Unlike light on optical microscopes, where light waves are used to form the image and magnification is acquired by a set of optical lenses, an electron microscope employs a "electron beam" to make the picture of the item and magnifies it using electromagnetic fields. The electron microscope offers a number of benefits over optical microscopes, including (i) having a better resolving power and the ability to see the structure of tiny objects. (ii) Other than using an optical microscope, it is feasible to see an object's three-dimensional exterior form.

The ultra-structure of a variety of biological, nanomaterials, cells, big molecules, metals, and crystals is studied using electron microscopes. The electron microscope is frequently used in industry for failure analysis and quality control. The transmission electron microscope (TEM), scanning electron microscope (SEM), reflection electron microscope (REM), scanning transmission electron microscope (STEM), and other forms of electronic microscopy are helpful in the modern world. However, SEM and TEM were mostly employed in this study.

2.5.1 Field-emission Scanning Electron Microscope (FESEM)

A high vacuum instrument, the SEM operates at less than $1x10^{-7}$ Pa in the gun zone. The vacuum contributes in preventing discharges inside the gun zone and permits electron flow along the column without scattering. The electron gun delivers a big, steady current in a little beam. Thermionic emitter and field emitter are the two different types of emission sources. According on the emitter the instrument is classified into various categories like scanning electron microscope (SEM) and field emission scanning electron microscope (FESEM) with a functioning thermionic emitter. The most popular filaments used by thermionic emitters are tungsten (W) and lanthanum hexaboride. Thermionic sources operate with relatively low brightness, cathode material evaporation, and thermal drift. One method of producing electrons that gets around these issues is field emission. A cold cathode field emitter, commonly known as a field emission gun (FEG), produces electrons as well. FESEM use a field emission pistol to provide a clearer picture with spatial resolution of less than 2 nm electrostatic distortions (that implies better than SEM).

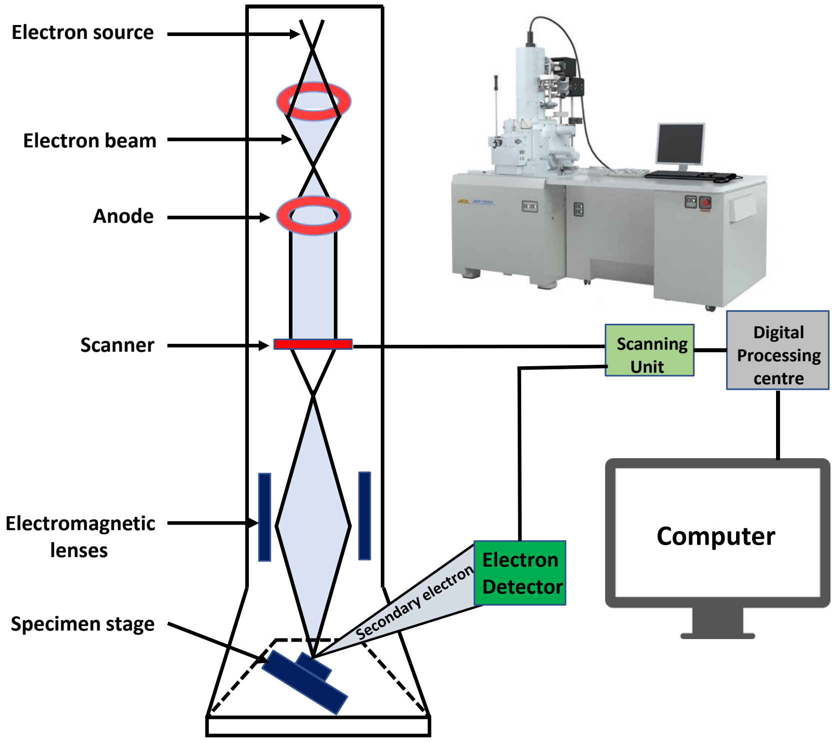

Figure 2.5 Working principle of FESEM instrument (Inset image is for FESEM instrument)

Recent advances in electron microscopy have been greatly influenced by nanotechnology, which places demands on the technology for both higher resolution and more information from the sample. Utilize a stream of extremely intense electrons in an electron microscope to examine things at extremely tiny scales. Most electrons in conventional electron microscopes are produced by "heating" a tungsten filament (electron gun). However, a "cool" source is used in a field emission (FE) electron microscope. The release of electrons from a conductor's surface as a result of an intense electric field is known as field emission. The cathode is a very tiny and pointed tungsten needle (tip diameter 10-100 nm). The development of scanning electron microscopes (SEMs), which has been aided by improvements in secondary electron detector technology, is compatible with the FE source. The setup requires an extreme vacuum (10-6 Pa) in the microscope's column, and the acceleration voltage between the cathode and anode is typically in the range of 0.5 to 30 kV. (**Figure 2.5**). As a result, in the study of nanomaterials, the FE scanning electron microscope (FE-SEM) is a particularly valuable instrument for high resolution surface imaging.

A FESEM device (JEOL, JSM 6700F) operating at 5 kV in secondary electron mode was used to examine the surface morphology of prepared materials. The sample was prepared by drying a drop of diluted solution or dispersion on a thin cover glass or, occasionally, a solid sample spread on carbon tape at room temperature before being kept in vacuum. Platinum was applied to the surface before the experiment to lower the surface potential caused by the buildup of electrostatic charge.

2.5.2 Transmission Electron Microscopy (TEM)

An essential technique for characterising materials in the nanometre (nm) range is transmission electron microscopy (TEM). The interaction of the high energy electron beam with the specimen is the foundation of TEM. The electron source for the TEM is mounted on top of the microscope, and the electron is released there and goes through the vacuum column (**Figure 2.6**). The electron is focused into a very tiny beam using an electromagnetic lens. At this point, the beam has passed through the specimen and is being dispersed by it. The density of the material in the area affects how the electron beam scatters. The denser materials show greater dispersion.

Finally, the unscattered or scattered electrons strike the fluorescent screen or photographic film mounted on the bottom of the microscope, producing a shadow picture of the object (bright field image) or scattered electrons (dark field image). The sample's size, shape, crystalline phase, and hollow or tube-like character were all revealed by the TEM in the picture data. Since the electron scattering in the TEM is dependent on the density of the materials, sample preparation is crucial. For the best possible pictures, a thin coating of the sample should be applied to the TEM grid. In my thesis, a diluted sample that had been well purified was dropped onto a copper grid that had been coated with carbon. The images were captured using a 200 kV electron source-equipped JEOL-JEM 2010 electron.

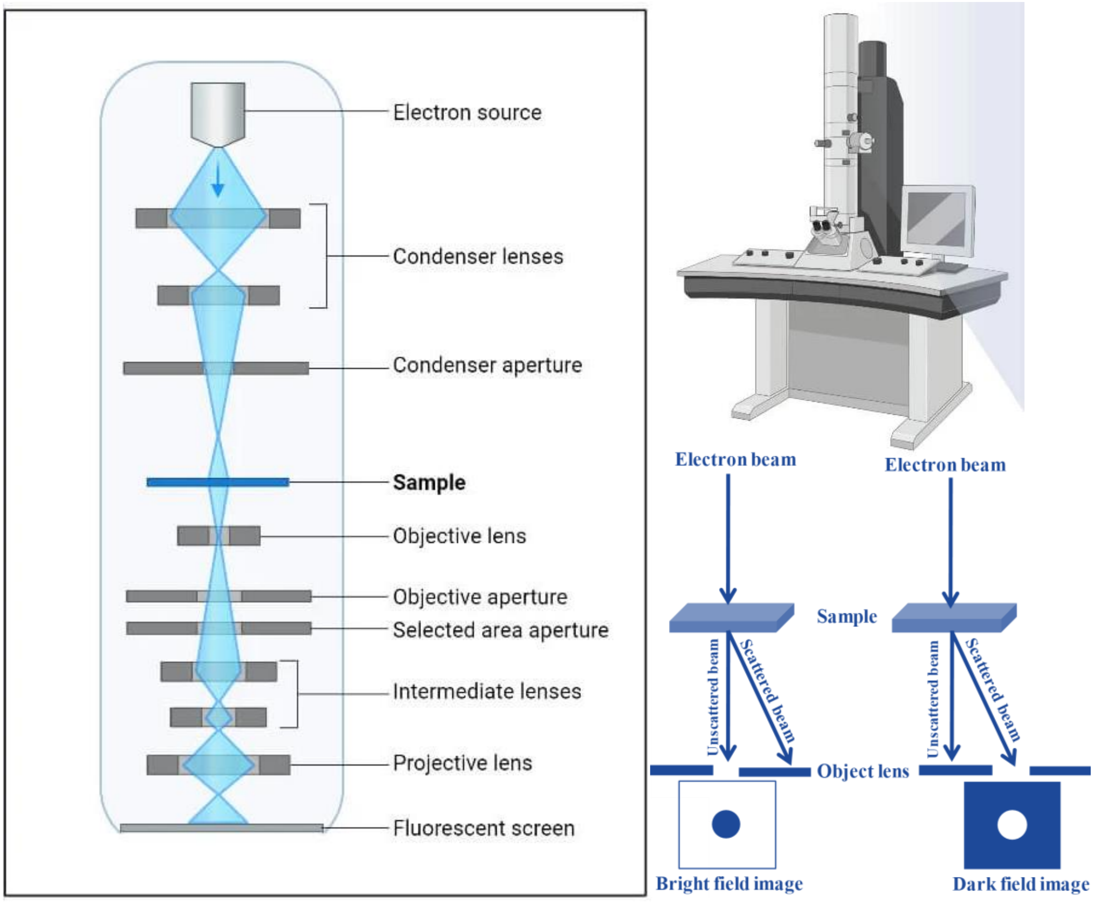

Figure 2.6 Schematic presentation and working principle of the TEM instrument and the bright field and dark field imaging principle

2.6 Atomic force microscopy (AFM) study

A extremely high-resolution kind of scanning probe microscopy is atomic force microscopy (AFM). An atomic force microscope was used to examine the topology of the dried material (Veeco, model AP 0100). AFM offers 3D morphology profiles of materials. The non-contact mode of the AFM instrument was used with a resonance frequency of about 250 KHz for the tip end. Sample solution was drop-cast on an atomically flat mica surface prior to instrumenting the diluted analyte. The samples were then dried in vacuum and at room temperature for the following two nights.

2.7 Electrochemical study

In the recent research era, electrochemical measuring has gained popularity as a method for investigating electrochemical reactions. The exchange of chemical to electrical and electrical to chemical energy is the main focus of this study. Chemical processes known as electrochemical reactions occur when electrons are moved from one electrode to another.

Electron(s) are transferred from one species to another during a reduction-oxidation process; this electrochemical relationship notion is used in cyclic voltammetry (CV) studies.

2.7.1 Cyclic voltammetry (CV)

Three electrodes are used in the CV technique: the working electrode (WE), the reference electrode (RE), and the counter or auxiliary electrode (**Figure 2.7**). A method of electrochemical measurement known as cyclic voltammetry ramps the working electrode potential linearly against time.

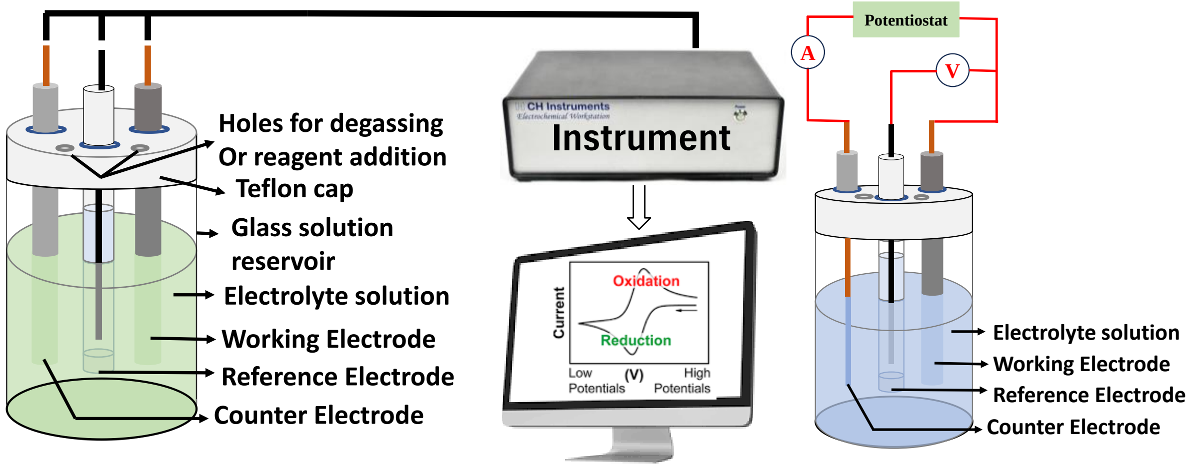

Figure 2.7 Schematic instrument set up and three electrodes cell set up of electrochemical workstation

In a CV experiment, the potential of the electrode of interest and the current flowing between two electrodes (the working and counter electrodes) are shown on the y-axis. On the x-axis, a reference electrode potential is displayed. A cyclic voltammogram, which is frequently referred to as an electrochemical spectrum, is the name of the ensuing plot (X-axis vs. Y axis). The concentration of the analyte solution is frequently directly proportional to the current that flows, especially during current peaks.

The CV method is frequently employed to get qualitative data on electrochemical processes. The thermodynamics of redox processes and the kinetics of heterogeneous electron-transfer reactions may both be learned a lot from cyclic voltammetry.

$$\mathbf{M^{+} + e^{-} \rightleftharpoons M}$$

A typical red-ox reaction is a reversible single electron process in which one molecule (M+) is reduced to generate another species (M). Figure 2.5 shows the cyclic voltagram of a single, reversible electron transfer process. The possibility is evaluated adversely to result in a reduction in this area.

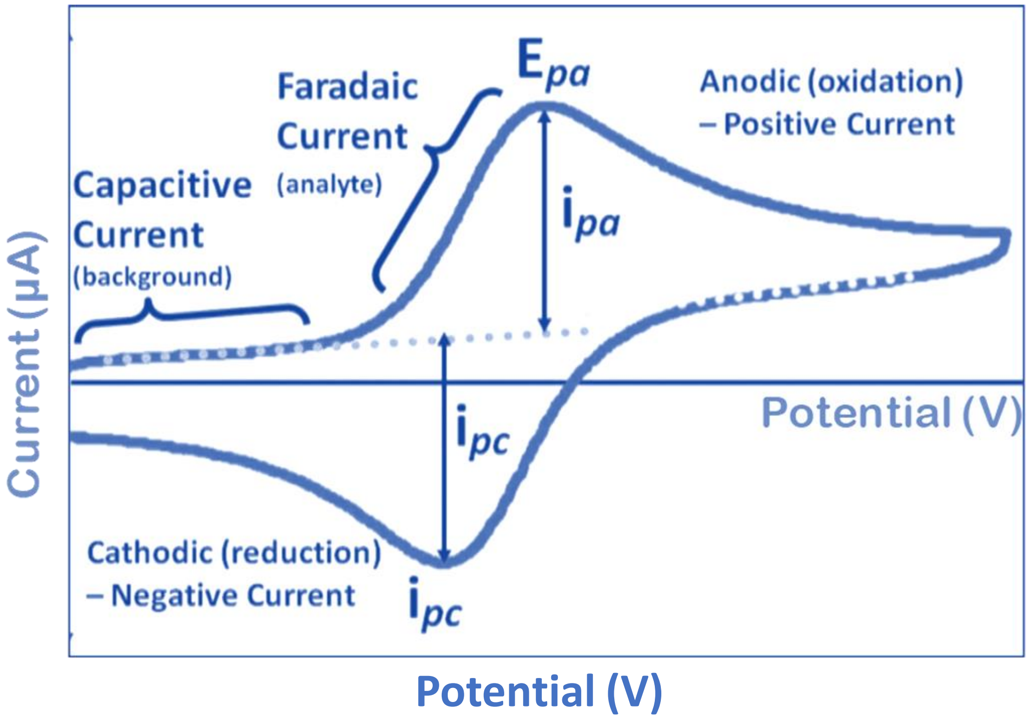

Figure 2.8 Cycle voltammogram of a single electron oxidation reduction reaction.

It is possible to read straight from the programme that the anodic sweep's peak potential is E_{pa} and its corresponding peak current is i_{pa}, and the cathodic sweep's peak potential is E_{pc} and its corresponding peak current is i_{pc}. If two peaks have different potentials (E_{peak}), the connection between them may be calculated:

$$\Delta E_{peak} = E_{pa}-E_{pc} = 0.059V/n \text{..............................} (2.3)$$

The formal reduction potential E^o for such a reversible couple is the mean of E_{pa} and E_{pc} and the i_{pa} and i_{pc} are very close in magnitude ($i_{pa}/i_{pc}=1$). 'V' is Potential and 'n' for number of redox reactions electrons

$$E^o = (E_{pa} + E_{pc})/2 \text{ ....} (2.4)$$

The peak current for a reversible system is described by the Randles-Sevcik equation:

$$I_p = 2.69 \times 105\, n^{3/2} A\, D^{1/2}\, C\, s^{1/2} \text{ ....} (2.5)$$

Where 'I_p' stands for peak current (amps), 'n' for number of redox reaction electrons, 'A' for electrode area (cm^2), 'D' for analyte diffusion coefficient (cm^2/s), 'C' for analyte concentration (mol/cm^3), and ‘s’ for sweep rate (V/s). The analytically most relevant property of equation is that I_p is linearly dependent on the analyte concentration.

2.7.2 Galvanostatic Charge Discharge (GCD)

GCD technique is mainly used for measurement of the energy storage capacity of a material (**Figure 2.9**). In GCD technique, the potential of one electrode is monitored as a function of time with respect to a suitable reference electrode through a constant current flow between two electrodes. GCD test help to understand the nature of electrode materials with rest to linear and nonlinear GCD curve nature. Linear GCD curve indicated ideal behaviour and nonlinear curve indicates some red-ox phenomenon occurring within the electrode materials.

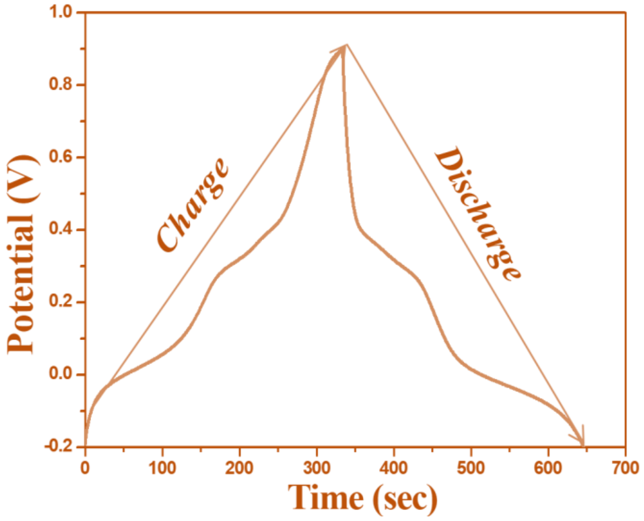

Figure 2.9 Typical of galvanostatic charge discharge curve showing nonlinear charge-discharge pattern

By using the following equations to calculate specific capacity (C_S), areal capacitance (C_A), energy density (E), and power density (P), GCD study aids in understanding the energy/charge storage capacity of electrode materials.

$$\text{Specific capacity } (\mathbf{C_S}) = (i \times \Delta t) / (\Delta V \times m) \text{ .... } (2.6)$$

$$\text{Areal capacity } (\mathbf{C_A}) = (i \times \Delta t) / (\Delta V \times A) \text{ .... } (2.7)$$

Where, ‘i’ is current, ‘Δt’ is discharge time, ‘ΔV’ is potential windows and ‘m’ is active mass of electrode materials where ‘A’ is the area of active electrode

$$\text{Energy density } (\mathbf{E}) = 1/7.2 \times C_s \times (\Delta V)^2 \text{ and Power density } (\mathbf{P}) = E/\Delta t \text{ .... } (2.8)$$

2.7.3 Electrochemical Impedance Spectroscopy (EIS)

EIS, or electrochemical impedance spectroscopy, is a potent diagnostic technique for identifying the different resistive effects that the electrode material experiences throughout the electrochemical reaction. EIS is helpful for the investigation and creation of novel materials and electrode architectures, as well as for the product verification and quality control in manufacturing processes.

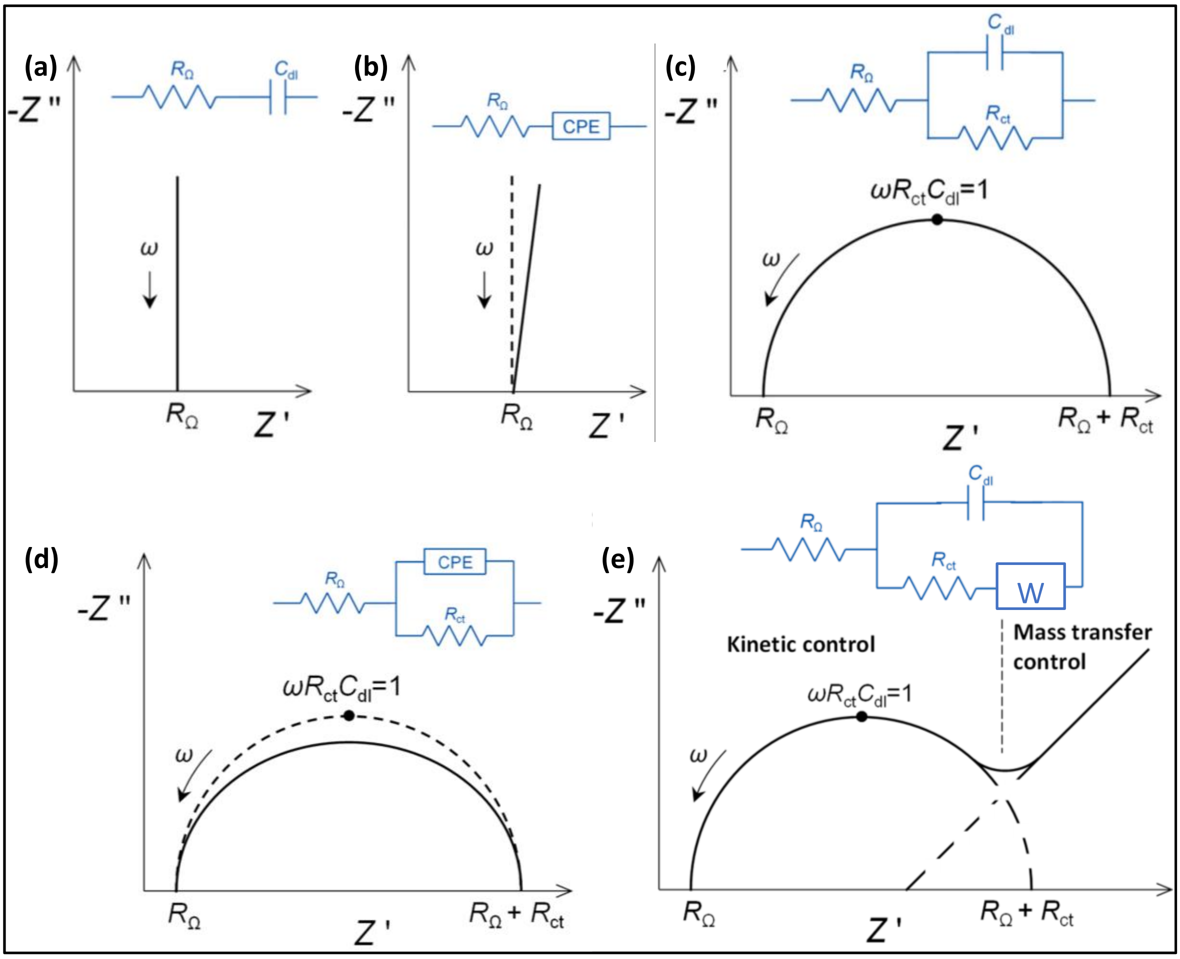

Figure 2.10 The circuit diagram and the Nyquist plot of electrochemical impedance spectroscopy (ESI) study.

On a complex plane, also known as a Nyquist plot, the real impedance of the cell is compared with the fictitious impedance, which stands in for the capacitive and inductive characteristics of the cell. The electrochemical impedance spectroscopy (EIS) circuit architecture is shown in **Figure 2.10 (a–e)**. It is composed of the Warburg impedance (W), the charge-transfer resistance (R_{ct}), the solution resistance (R_{Ω}), the electron transfer resistance (Ret), the double-layer capacitance (C_{dl}), and the constant phase element (CPE). All current passes via the uncompensated solution, hence R_s is added to the EC as a series element. The total current passing through the electrodes, in contrast, is the sum of the individual contributions from the double-layer charging and the faradic process.

The R_Ω and 'W' represent bulk properties of the electrolyte and diffusion of the redox probe, while C_{dl} and R_{ct} depend on dielectric and insulating features at the electrode/electrolyte interface.

The frequency dependent specific capacitance can be calculated from the Nyquist plot using the following equation

$$\text{Specific capacitance} = (-)1/(m \times 2\pi \times f \times Z_{img}) \quad ....(2.9)$$

Where, 'f' indicates the frequency, 'm' implies mass of electrode materials and 'Z_{img}' imaginary impedance.

2.8 X-Ray Photoelectron Spectroscopy (XPS)

A popular method for determining the quantitative chemical composition of a surface is X-ray photoelectron spectroscopy (XPS), which is based on the photoelectric effect (**Figure 2.11**) The elemental composition is measured at parts per thousand levels by the XPS spectroscopic method. Core electrons with the distinctive binding energy exist in every atom. The expelled electron was detected using the XPS method when an X-ray beam (Al K_α or Mg K_α ray) directly struck the sample surface.

In XPS, a unique type of photoemission-the ejection of an electron from a core level by an X-ray photon with energy hv-is what we are interested in. The electron spectrometer then analyses the energy of the released photoelectrons, and the information is shown as a graph of intensity (counts/s) versus electron energy (the X-ray induced photoelectron spectrum). The experimental quantity that the spectrometer measures is the electron's kinetic energy (E_k), which is not an inherent attribute of the material because it depends on the photon energy of the X-rays used. The quantity that uniquely identifies an electron in terms of its parent element and atomic energy level is called the binding energy of the electron (E_b). The binding energy of the core electron is given by the Einstein relationship:

$$E_b = h\nu - E_k - W_f \quad .... (2.10)$$

Where '*hv'* is the photon energy, 'E_k' is the kinetic energy of the electron and 'W' is the spectrometer work function.

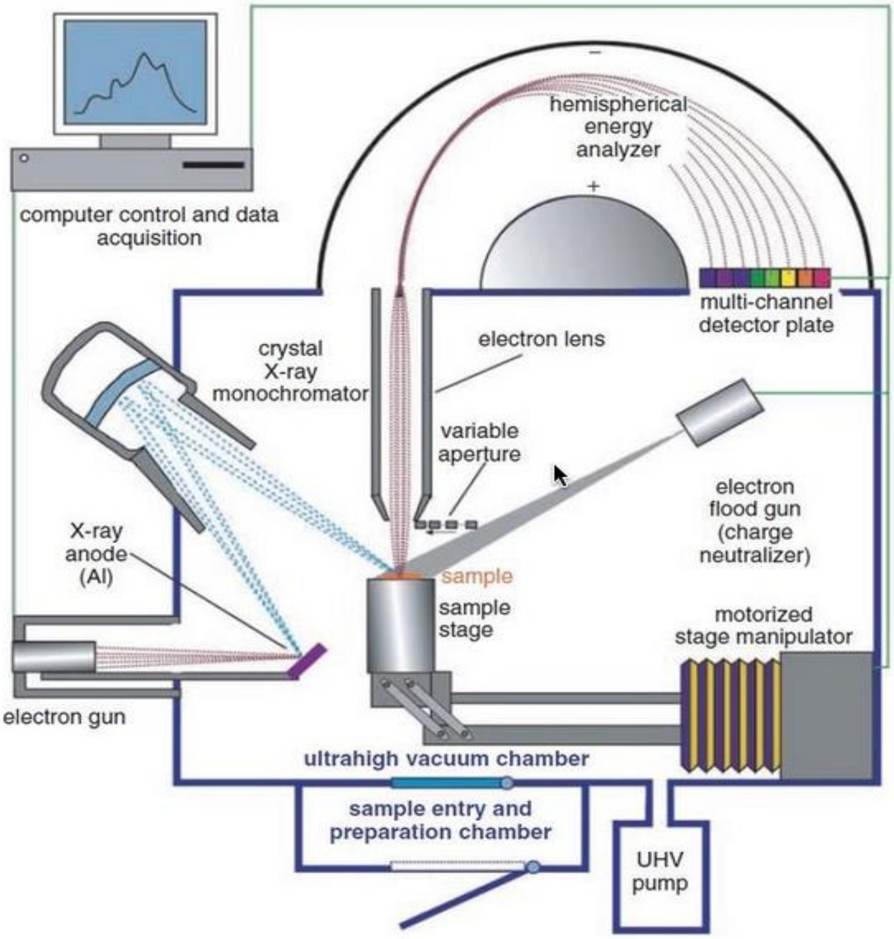

Figure 2.11 Presentation of working principal diagram of XPS study with spectrum (inset image for XPS instrument)

An electron from the K shell is released from the atom during the photoemission process, which is schematically depicted in **Figure 2.12**. (1s photoelectron). Due to the fact that any electrons with a binding energy lower than the photon energy will be included in the spectrum, the photoelectron spectrum will rather faithfully recreate the electronic structure of an element. **Figure 2.12**, which overlays a picture of the electron's orbital with the lead XPS spectrum, serves as an illustration of this. The ionised atom must relax in some way after releasing a photoelectron. This is possible by X-ray fluorescence, which is the emission of an X-ray photon.

The process of photoemission is shown schematically in **Figure 2.12**, where an electron from the K shell is ejected from the atom (1s photoelectron). The photoelectron spectrum will reproduce the electronic structure of an element quite accurately since all electrons with a binding energy less than the photon energy will feature in the spectrum. This is illustrated in **Figure 2.12** where the XPS spectrum of lead is superimposed on a representation of the electron's orbital. Once a photoelectron has been emitted, the ionized atom must relax in some way. This can be achieved by the emission of an X-ray photon, known as X-ray fluorescence.

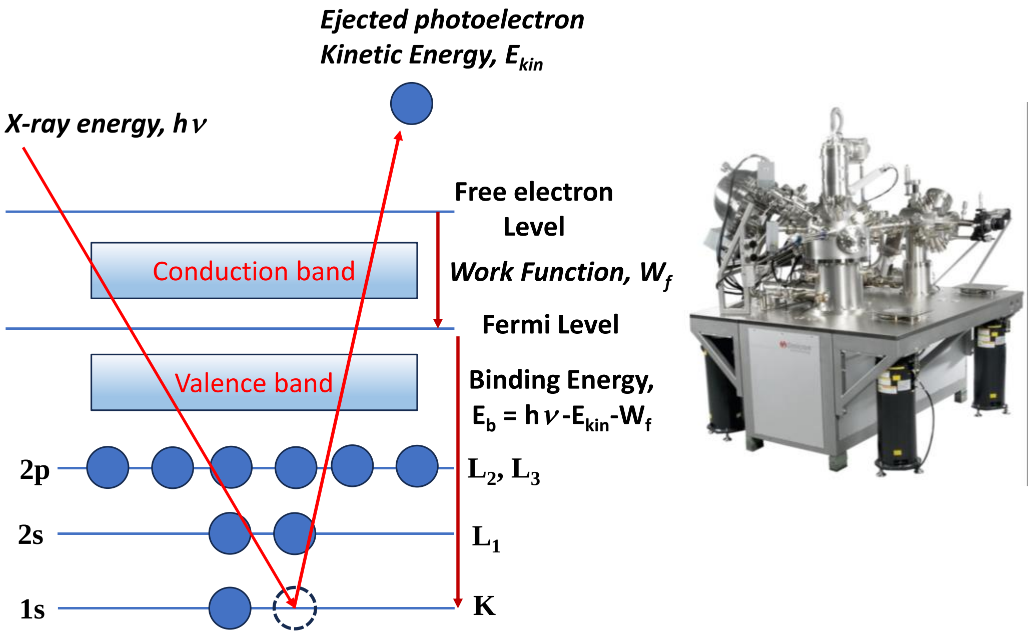

Figure 2.12 Schematic diagram of the XPS process, showing photo-ionization of an atom by the ejection of a 1s electron

Ejection of an Auger electron is the alternate scenario. In light of this, the XPS procedure, also known as X-AES, results in the production of Auger electrons (X-ray induced Auger electron spectroscopy). X-AES can provide useful chemical information on an atom even if it is not commonly used.

2.9 Thermo Gravimetric Analysis (TGA)

The thermal and environmental stability of the sample was measured using the Thermo Gravimetric Analysis (TGA) method. The temperature at which synthesised samples degraded was determined using the TA thermal analysis equipment. Under an environment of N2, samples were heated at a rate of 10 °C/min from 25 to 800 °C. The TGA sample pan, which was connected to a delicate microbalance assembly, was filled with a sample. The TGA balance assembly's sample holding part was then put into a high-temperature furnace. The balance assembly assessed the initial sample weight at room temperature and then continually monitored changes in sample weight (losses of weight) while heat was given to the sample. At a certain ultimate temperature, the amount or percentage of non-combusted residue was examined in typical weight loss profiles.

2.10 Inductively coupled plasma atomic emission spectroscopy (ICP-AES)

The analytical method known as inductively coupled plasma atomic emission spectroscopy (ICP-AES) is used to find trace metals. ICP-AES is made up of two components: the optical spectrometer and the ICP. ICP-AES is a form of emission spectroscopy that creates excited atoms and ions that emit electromagnetic radiation at wavelengths specific to a particular element using an inductively coupled plasma. The process uses a flame with a flame temperature between 6000 and 10000 K. The concentration of the element in the sample may be inferred from the intensity of this emission.

2.11 Current (I)-Voltage (V) Measurement

At room temperature, a computer interfaced with a dc source electrometer (Keithley model 617) to measure the Current-Voltage (I-V) properties of the samples. By using the pressed pellet technique or drop-casting the sample between two electrodes of Al and ITO coated glass (Al/Sample/ITO), the sample was prepared for I-V measurements. Generally, IV measurement is done in two probe and four probe method.

Four-probe testing involves using four probes connected to a voltage source and a current meter. The four probes are placed on a material in a specific configuration. Two probes are used to pass a current through the material, while the other two are used to measure the voltage drop across the material. The voltage and current values are then used to calculate the electrical resistance or conductivity of the material.

The four-probe technique is preferred over the two-probe technique because it eliminates the effects of contact resistance, which can cause errors in the measurement of electrical properties. The four probes are placed so that the current passes through the material without passing through the contact resistance, which is measured separately. This allows for more accurate measurements of the material's electrical properties.

Four-probe testing is used in various applications, including measuring the electrical properties of semiconductors, metals, and insulators. It is commonly used to fabricate and test electronic devices like transistors and solar cells. Four-probe testing is also used to characterise various applications, such as developing new materials for batteries, sensors, and other electronic devices.

In addition, four-probe testing is used to study the electrical properties of biological tissues and cells. This technique is used to measure the electrical properties of biological tissues, such as the conductivity of the skin, and to study the electrical behaviour of cells in response to different stimuli.

Beyond the basic four-probe technique, several advanced techniques can be used to measure the electrical properties of materials. One such technique is the frequency-dependent four-probe technique, which measures the electrical properties of materials over a range of frequencies. This technique is instrumental in studying materials that exhibit frequency-dependent electrical properties, such as biological tissues and cells.

Four-probe testing is a powerful technique for measuring the electrical properties of various materials, from semiconductors and metals to biological tissues and cells. By eliminating the effects of contact resistance, four-probe testing allows for more accurate measurements of electrical properties, which are critical for developing and testing electronic devices and materials. With advanced techniques such as frequency-dependent and scanning four-probe testing, researchers can gain a deeper understanding of the electrical properties of materials and their behaviour in various applications.

2.12 Rheological studies

Rheological experiment for the viscoelastic studies of GMP gel network and various GMP-PANI hybrid networks were performed by advanced rheometer (AR 2000, TA Instruments) using a cone plate geometry on a peltier plate. The diameter of the plate is 40 mm, the cone angle 4^0 and the plate gap is 121 µm.

2.13 Surface area analysis

The specific surface area and the porosity measurement of the nano-porous materials are the most precious tools. These measurements are carried out by absorbing the inert gas molecules such as N_2, Ar, and Kr into the solid surface. Sometimes CO_2, NH_3 and water vapour are also used in this measurement. When a gas or vapour molecules come into the contact with any solid surface, some of them are absorbed. The absorbed molecules are termed as adsorbate and the solid surface in where the absorption takes placed, called as adsorbent. The porosity of a material is determined from the volumetric nitrogen gas in the adsorption-desorption isotherm at 77 K. This study also confirms the presence of void space into the matters from which we can say either the materials are porous or non-porous.

N_2 adsorption/desorption isotherm of Polyaniline samples were performed by using iSorp HP1-100, (Anton Paar, USA) at 77 K.

2.14 Compressive studies

Compression test of gel samples are done by computer controlled MCR 702e DMA (Anton Paar, Austria). The working axle force of the liner drive in between 0.001 N - 40 N. The compression test of gels was carried out between two parallel plates with the diameter of 25 and 50 mm, respectively. In the compressing strain sweep experiment, the original gap between the plates is set to 5 mm as the height of hydrogel composites, then the lower plates move with fixed moving speed of 12 cycles min^{-1}. The compressive stress of gel samples was measured in the compressive strain (e %) range of 0.001 to 100. All compression experiments have been done at room temperature 25^{o} C.

CHAPTER 3

Fully organic polyaniline nanotubes as electrode material for durable supercapacitor

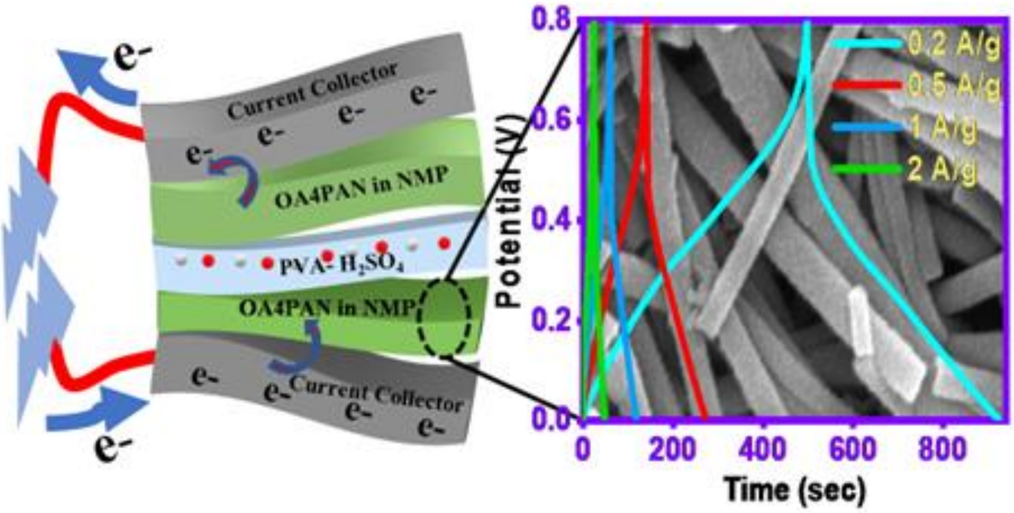

3.1. Introduction

With the ever-growing global demand for clean energy sources and the crisis of non-renewable energy sources,[1-3] in past few decades electrochemical capacitors or supercapacitors are the most attractive device due to its high power density, fast charging- discharging capability, lightweight, clean, flexible portable energy storage properties and also long durability.[4-7] Several attempts have taken by researchers or technologists to improve the electrochemical parameters such as power density charge-discharge cycle, stability, flexibility and environmental stability of electrochemical capacitors in which one may think of the optimization of three components (electrodes or electrode materials, electrolyte and separator).[8-12] Among the different electrode materials like carboneous materials (CNT / graphene/ graphene oxides),[13] metal oxides (including MnO_2, RuO_2, Co_3O_4 and IrO_2),[14-16] and composite materials, conducting polymers have drawn considerable substantial attention.[17] According to the charge storage mechanism, electrochemical capacitors are broadly classified as three categories: a) electrochemical double layer capacitors (EDCLs) where charges stored based on adsorption on the electrode surface, b) pseudocapacitors where charges are stored via faradic process or redox process and c) hybrid capacitors in which both previous two mechanisms are operating. Mainly, carboneous materials are used for EDCL capacitors.[8,9,17,18] Though the specific capacitance of carboneous material is relatively low, however, cycle stability is much higher than that of other materials.[17] Metal oxides or conducting polymers which are commonly considered to enhance the capacitive values, are providing the enormous possibility to refine / retune the structure-property to generate optimum behaviours for commercialization or technological applications.[18,19] Therefore, conducting polymer is easy choice to prepare the most promising electrode materials in the supercapacitors owing to the structural variations. An ideal electrochemical electrode material should have following properties: i) *wide range of working potential* (large amount of charge will be stored), ii) *high-rate performance* (i.e., retention of capacitance at high current rate). And to achieve it, ion transport from electrode to electrolyte and charge transfer at interface of electrode should be higher (mesoporous structure may offer ion –buffering place and minimize ion-diffusion path) and iii) *high retention of capacitance*, iv) *low leakage current*.

Among different conducting polymers, polyaniline (PANI) is the most vital and useful polymer because of its facile synthesis, cost effective starting or raw materials, good thermal and environmental stability, multiple redox states, high range electrical conductivity and good cycle stability etc[20,21]. Because of these advantages, bulk PANI is also used in supercapacitor electrode materials and recent development of facile as well as effective methods of synthesis of PANI nanotubes with high aspect ratio and enhanced surface area have created enormous interest as capacitors.[22] Owing to their exciting properties such as high electrical conductivity, high surface area, tunable photoluminescence and excellent dispersion in various solvents plays also an important role in their electrochemical performances. Few reports of PANI nanostructures on the electrochemical properties are noticed in the literature,[23] whereas, plethora of PANI based nanocomposites (either with carboneous or metal oxides) are already replete with the literature. PANI nanotubes with MnO_2 were utilized as supercapacitor electrode materials,[24] having specific capacitance of 528 F/g at 1 A/g current density in 1 M H_2SO_4 electrolyte. PANI nanofibers prepared by electro-spinning method were exhibited the specific capacitance of 601 F/g at 1 A/g and retaining 62 % of capacitance after 500 cycles.[25] PANI nanowire arrays using hard host were revealed relatively high specific capacitance of 950 F/g and it retained 88 % of the original capacitance after 500 cycles.[26] It is known that the pseudo capacitance of PANI is coming from the redox reaction relating counter-ion influx and out flux from the polymer chains. The advantage of vertically aligned nanowire lies into the ion diffusion from a bulky solution to the surface of PANI nanowires. The counterions hereby can attain or depart the surface of PANI nanowires fast, even at very high charge–discharge rate. Alternatively, PANI nanowires having less than 50 nm in diameter may reduce the charge transport distance in the PANI materials. Therefore, the counter ions effortlessly penetrate the inner layer of the PANI, which makes almost full utilization of the electrode materials. Optimized ionic diffusion path as well as narrow diameter may diminish the ionic diffuse resistance along with charge transfer resistance.

3.2. Experimental Section

3.2.1 Materials

Aniline monomer (Merck Chemicals) was purified by vacuum distillation procedure and stored at low temperature in dark place before using. Benzene 1, 2, 4, 5-tetracarboxylic acid (OA4), Benzene 1, 3, 5-tricarboxylic acid (OA3), Benzene 1, 4-dicarboxylic acid (OA2), were purchased from Sigma-Aldrich and used without further purification. Ammonium persulphate ($(NH_4)_2S_2O_8$, APS), Hydrochloric acid (HCl), were purchased from Merck Chemicals. All aqueous solutions were prepared in 18 MΩ water obtained from a Millipore Milli-Q system.

3.2.2. Preparation of OAnPAN, Nanostructures (n=2, 3, 4)

The synthetic technique of PANI nanotube was followed by our previously reported work.[23-24] In the present procedure, desired amount of organic dopant acids (like OA2, OA3 and OA4) were dissolved in 15 mL of double distilled water with continuous stirring for 1 hour at room temperature. Distilled aniline 100 µL (1.02 g/cm^3, 1.1 mmol) was added to the acid solutions with extra 1h rapid stirring at low temperature. After cooling the reaction temperature to 0 °C-5 °C, an aqueous solution of APS was added dropwise to the reaction mixture at stirring condition. Immediately, colour of the solution was changed from light yellow to brown and the mixture was allowed to stand in 0-5 °C temperature for 24 hours without any disturbance. Resulting deep green coloured precipitate was washed with double distilled water and methanol, to removed excess amount of APS and oligomers from reaction mixture. At last, the product was dried under vacuum oven at 60 °C temperature to get OPAN nanostructures in powdered form.

3.2.3. Making of (1:1) PVA – H_2SO_4 gel Matrix

Approximately 1 gm PVA was taken in 10 mL deionize water to prepare 10 wt. % PVA solution. The mixture was heated for 2-3 hrs. at 85^o C until a cleared solution was obtained. Then cooled to room temperature. Then 546 µL H_2SO_4 was added to it and stirred for 30 min. to get homogenize solution. [25]

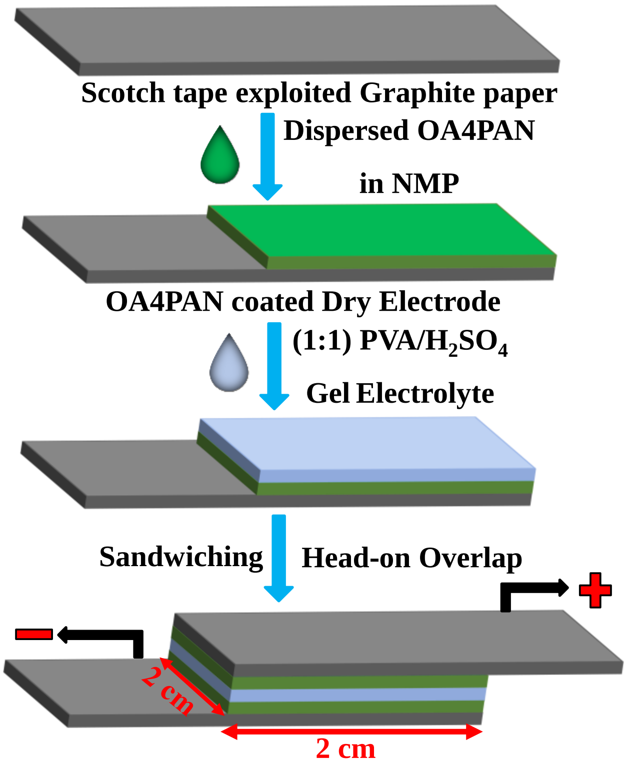

Scheme 3.1: Preparation of solid-state device using OA4PAN composite with gel electrolyte.

3.2.4. Making of solid-state flexible devices

To check the performance and stability in real application of the OA4PAN composite, three symmetric devices having area 2 x 2 cm^2 with mass loading 2 mg, 5 mg, and 10 mg were prepared with gel matrix. A high concentrate solution of OA4PAN was prepared in N-Methyl-2- pyrrolidine (NMP) solvent at room temperature with constant stirring for 2 hrs. Device fabrication was done by drop casting the mentioned amount of OA4PAN in a scotch tape exploited graphite paper. After drying the electrode material each electrode was sandwich by (1:1) PVA – H_2SO_4 (Scheme 1) which acts as well as electrolyte and separator.

3.3. Results and discussion

3.3.1. Morphological study

FESEM images of different organic acids doped OAPAN nanostructures and representative HRTEM image of OA4PAN are shown in **Figure 3.1** and **Figure 3.2** respectively. The tubular shaped morphology has been observed for OA4, OA3 and OA2 composites and all OAPAN fibres show tube-like in nature.

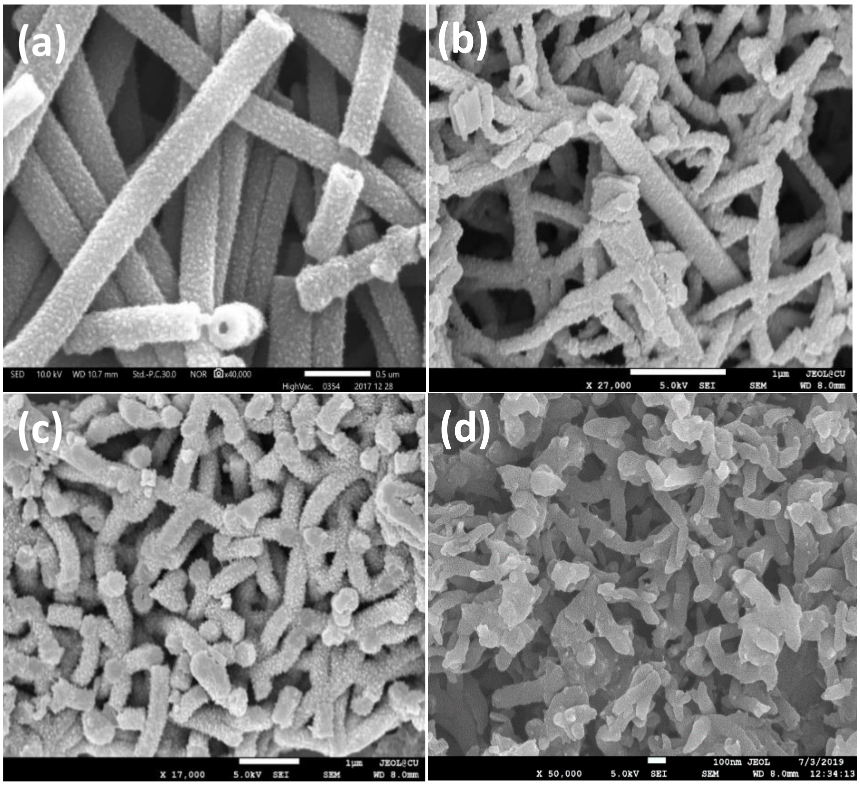

Figure 3.1 FESEM images of PANI nanostructures: (a) OA4PAN, (b) OA3PAN, (c) OA2PAN and (d) HCl doped polyaniline (HPAN)

For comparison, polyaniline prepared with HCl (HPAN) that has been synthesized in similar condition, reveals random agglomerate morphology. A close inspection of each composite of OPAN indicates the information about fibres diameter, length as well as nature of the fibre. Highest aspect ratio (length/diameter) is ~125 for OA4PAN nanostructures. The same ratio for OA3PAN and OA2PAN are ~40 and ~25 respectively indicating that these fibres are also tube-like hollow pattern morphology as OA4PAN. The fibres pattern of OA4PAN are very uniform, hollow tube and high aspect ratio that may facilitate the high charge accumulation capability on its surface.

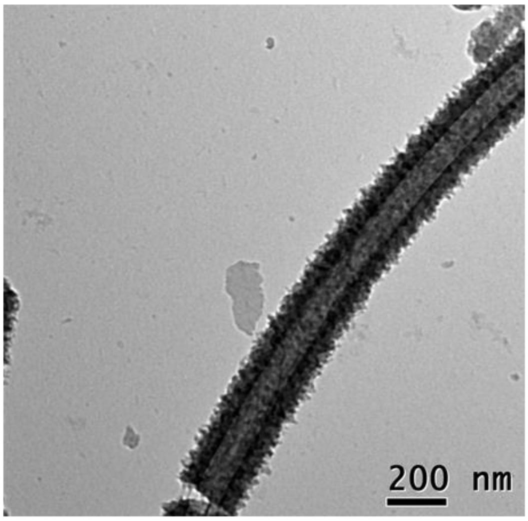

Figure 3.2 Representative HRTEM images of synthesized OPAN nanostructures.

3.3.2. Spectroscopic study

UV-Vis spectra of the PAN nanostructures were done from well disperse aqueous solution (**Figure 3.3a**). It shows that the three absorption peaks arise at ~350, 435 and 900 nm. Two peaks at ~350 and 435 nm are due to π-π^* transition and polaron-π^* transition of benzenoid rings, respectively. Another peak at ~900 nm with free tail extended to IR region for π-polaron transition.[27,28,30] These three characteristic PANs peaks are present in three OA4PAN, OA3PAN and OA2PAN nanostructures. These results indicate that PAN chains remain in emeraldine salt state in all nanostructures and are conducting in nature. The absorption intensity of the π-polaron (peak at ~880-900 nm) is sharp for OA4PAN compared to others, revealing the decrease of conjugation length of PANI chains in OA3PAN and OA2PAN nanostructures.

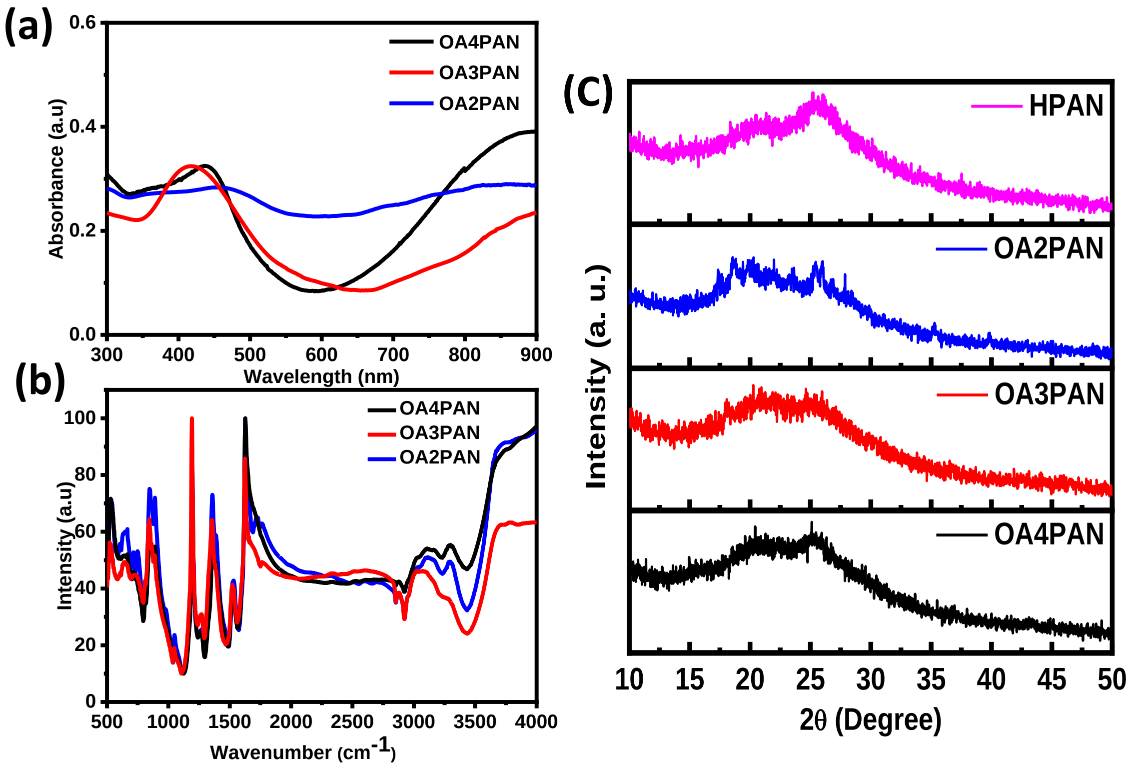

Figure 3.3 (a) UV-vis study; (b) FTIR spectra; and (c) XRD of organic acid doped PAN (OPAN).

3.3.3. FTIR study

To confirm the PANI formation in all nanostructures, FTIR study was performed for OA4PAN, OA3PAN and OA2PAN composites in **Figure 3.3b**. The presence of stretching vibration band at ~3441, 2925, 1581, 1480, 1302, 1236, 1103 and 792 cm^{-1} reveals the PAN formation. The characteristic stretching bands at 3441 cm^{-1} for γN-H of PAN chain, 2925 cm^{-1} for γC-H of phenyl rings, 1581 cm^{-1} for γC=C of quinoid rings, 1480 cm^{-1} for γC=C of benzenoid rings, 1302 cm^{-1} for γC-N of secondary aromatic amine, 1103 cm^{-1} for γC-H aromatic in plane and 792 cm^{-1} γC-H aromatic out of plane deformation for 1,4 disubstituted benzene are proved PANI formation in the nanostructures.[27,28,30-32]

3.3.4. XRD study

Powder X-ray diffraction (XRD) pattern of OA4PAN, OA3PAN and OA2PAN samples are shown in **Figure 3.3c**. XRD patterns show peaks at $2\theta \approx 15°$, 20.3° and 25.6° for (011), (100) and (110) plane, revealing little crystalline nature of PAN composites. The peaks appear at $2\theta = 20.3°$ and 25.6° are for regularity in parallel and perpendicular direction of the PAN chain respectively.[27,33-35] Peak at 25.6° corresponds to d-spacing ~3.48Å for the face-to-face interaction of phenyl rings of PAN chains.[36] Highest intensity peak at 25.6° is observed for OA4PAN, suggesting greater extent of π-π staking of polymer chain in B4CAP than that of other three nanostructure.

3.3.5. BET study

N2-adsorption studies have been performed for all three nanostructures and from BET surface area analysis, it has been observed that OA4PAN has high surface area than the other three nanostructures (**Figure 3.4**).[31] Hence, from the morphological studies and BET surface area analysis, OA4PAN should considered as good electrode materials among four PANI nanostructures.

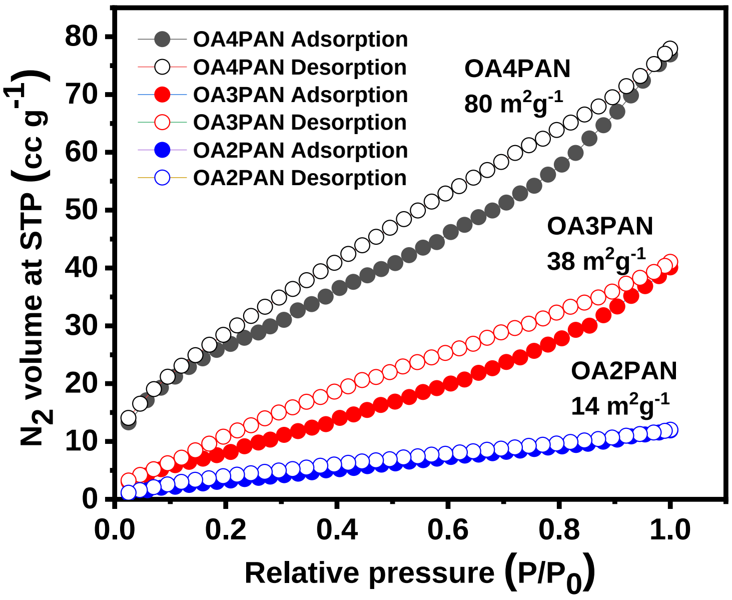

Figure 3.4 BET surface area study of organic acid doped PAN (OPAN).

3.3.6. Electrochemical study

Capacitive performances of four polymer composites have been evaluated by cyclic voltammetry (CV) and galvanostatic charge-discharge (GCD) methods with three electrode systems, where glassy carbon electrode was used as working electrode, Pt as counter electrode and Ag/AgCl as reference electrode. The specific capacitance (C_S), Power density (P) and energy density (E) were calculated by using the following equation,

$$\text{Specific Capacitance, } C_S = \frac{i \times \Delta t}{\Delta V \times m} \quad \text{(F/g)} \qquad \ldots\ldots\ (3.1)$$

$$\text{Energy Density, } E = \frac{C_S \times \Delta V^2}{7.2} \quad \text{(Wh/Kg)} \qquad \ldots\ldots\ (3.2)$$

$$\text{Power Density, } P = \frac{E\times 3600}{\Delta t} \quad \text{(W/Kg)} \qquad \text{........ (3.3)}$$

Where, 'i' is current, 'Δt' is discharge time, 'ΔV' is potential windows and 'm' is active mass of electrode materials.

The larger area under the CV curve for OA4PAN represents the good capacitance value than other nanostructures. Highest CV currents with three pairs of redox peaks of OA4PAN indicate the high conductivity or low internal resistance of this composite than other three polymer composites, as the electrode material. In **Figure 4 (a)** the peaks A1/C1 are due to the transformation of emeraldine from leucoemeraldine, the small peaks A2/C2 are attribute for the conversion of benzenoid to quinoid and the peaks A3/C3 are for emeraldine to pernigraniline.[37-40]

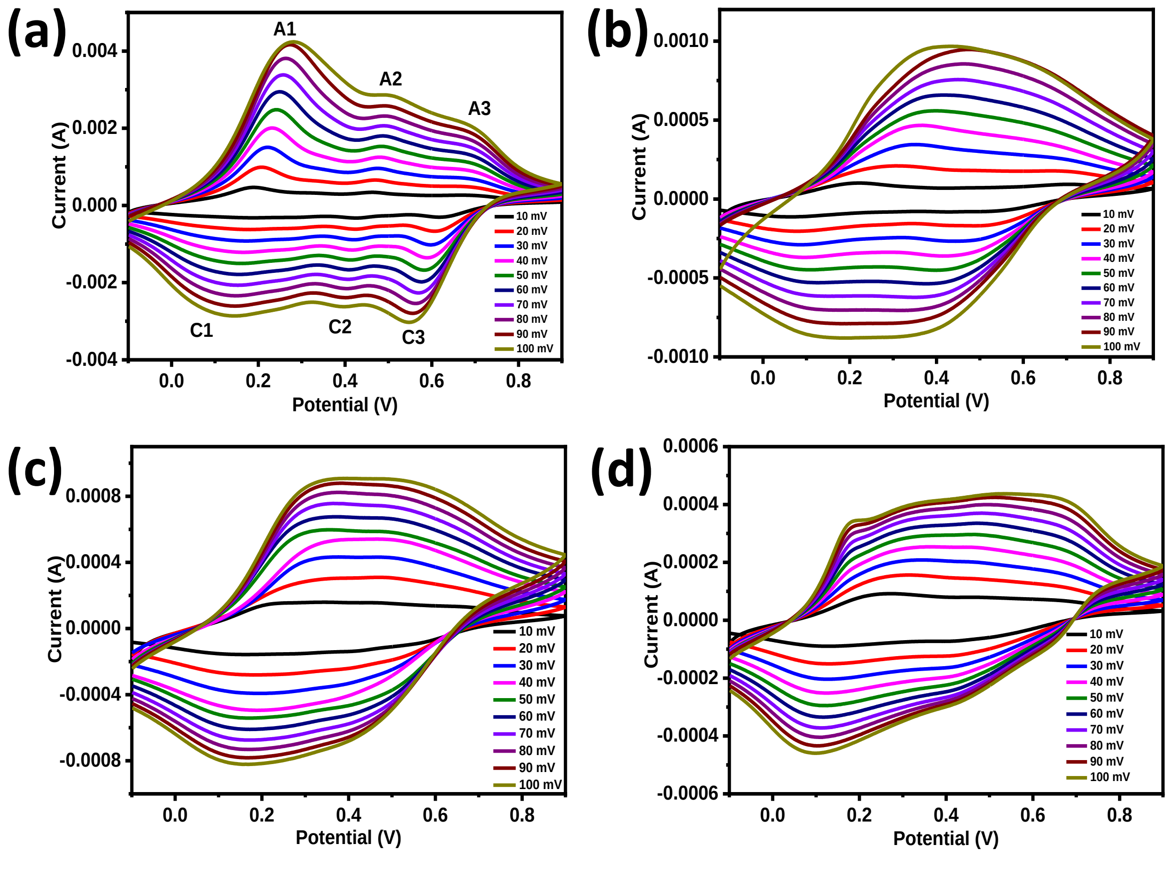

Figure 3.5 Cyclic Voltammetry of (a) OA4PAN, (b) OA3PAN, (c) OA2PAN, (d) HPAN;

CV curves of OA4PAN at different scan rates (**Figure 3.5**) exhibit well-resolved as well as reversible redox peaks at lower scan rate. With increasing scan speed, peak current increases with broadening of CV peaks, signifying the pseudocapacitance feature of the various acid doped PAN. The asymmetric nature of the CV curve suggests the combined double-layer and pseudocapacitive contributions to the total capacitance. Electrochemical capacitance properties of the PANI composites have been further tested by the GCD method at different current densities 0.5 – 10 A/g. The calculated specific capacitance values of OA4PAN, OA3PAN, OA2PAN and HPAN composites are 395, 305, 215 and 156 F/g at 0.5 A/g current density respectively shown in **Figure 3.6**. The relative higher value of specific capacitance (395 F/g) is achieved for the OA4PAN composite and it is possibly due to the presence of higher surface areas OA4PAN samples and it provides better conductive paths for fast electron transport.[27,31]

3.3.7. Specific capacitance and Cyclic stability

The maximum energy density (E) and power density (P) estimated for the OA4PAN composite are 35.05 Wh/kg and 200.32 W/kg, respectively at 0.5 A/g. The cyclic stability is also an imperative parameter from the application point of view. Long term cyclic life stability has been tested by 3000 continuous GCD for OA4PAN composite. After the 3000th cycle, 76.8% retention of total specific capacitance (i.e., ~ 23.2% of total specific capacitance loss) at current density 7 A/g in 0.5 M H_2SO_4 electrolyte solution (**Figure 3.7c**) has been observed. This decrease of specific capacitance after 3000 cycles may be explained by the loss of active material in the current collector (due to swelling or contraction) which causes the partial

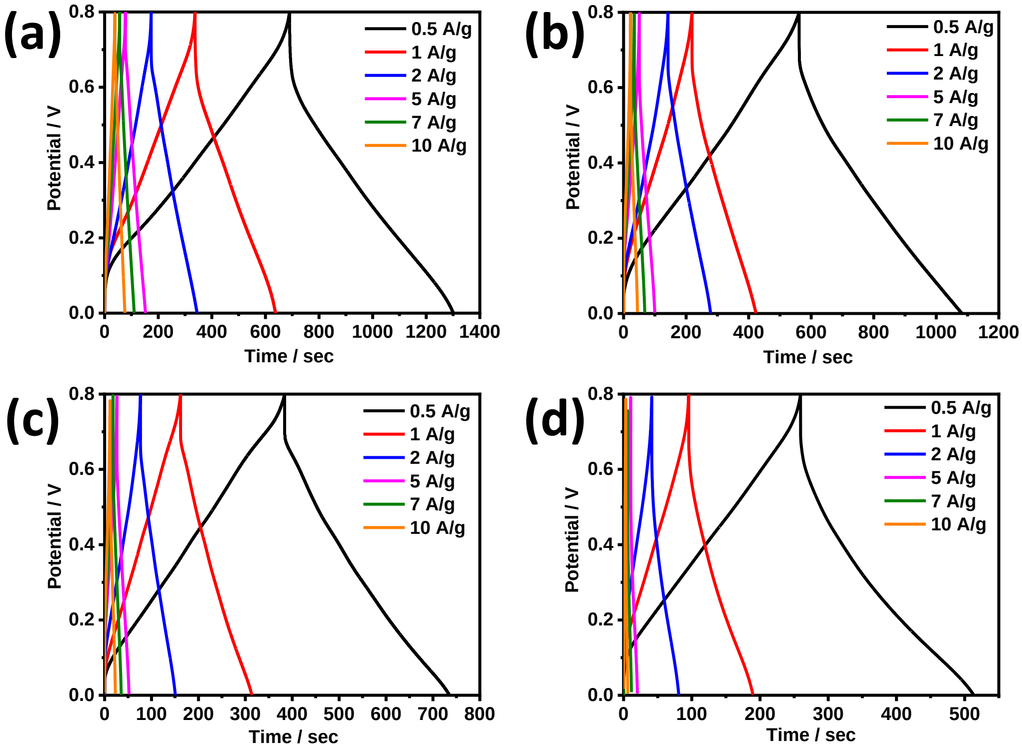

Figure 3.6 Galvanic charge discharge of (a) OA4PAN, (b) OA3PAN, (c) OA2PAN, (d) HPAN in three electrode system.

blockage of the regular structure. The stabilities of OA4PAN after long cycles (3000 cycles) have been checked with Uv-Vis and morphological studies. As shown in the **Figure 3.8**, there

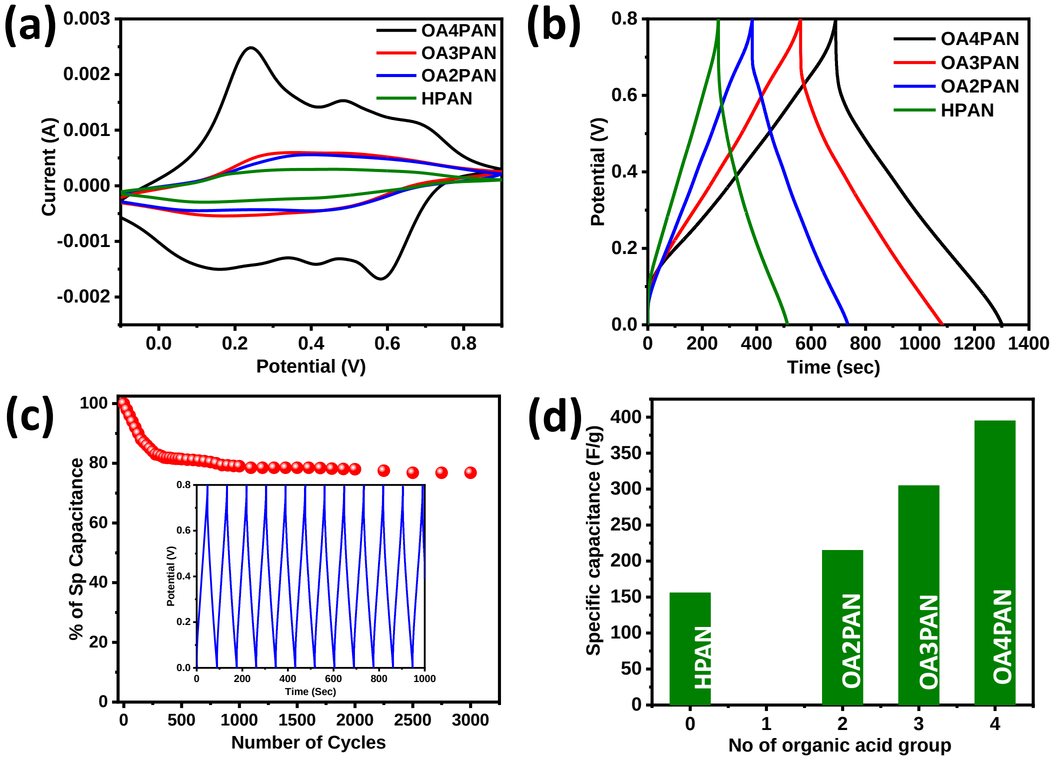

Figure 3.7 Comparative study of (a) Cyclic Voltammetry (b) galvanic charge discharge of polymers; (c) cyclic stability of OA4PAN; (d) Representative bar diagram of four specific capacitance value.

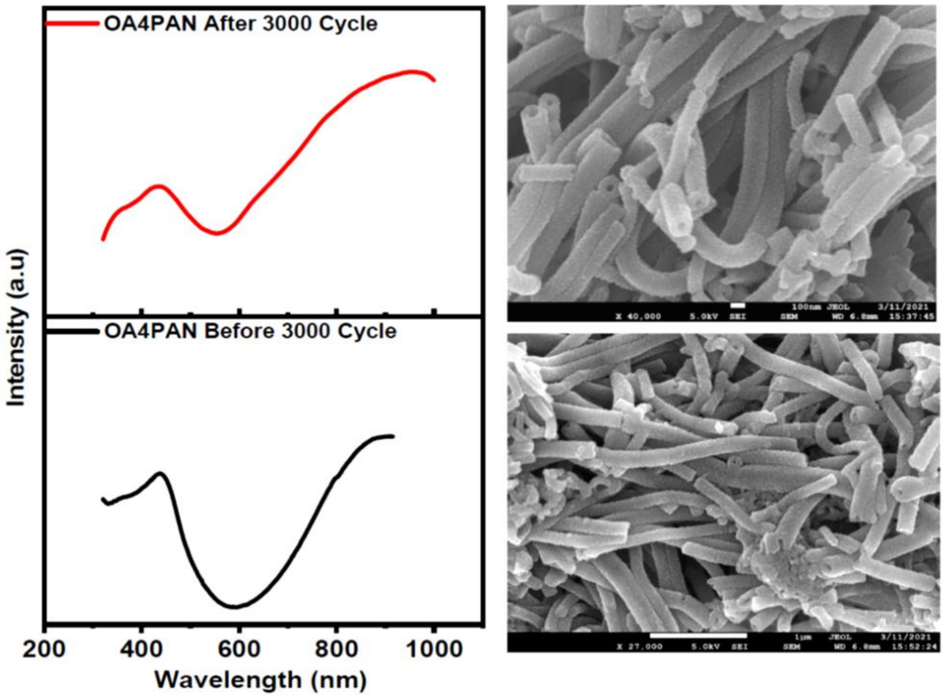

Figure 3.8 UV-Vis spectra before and after 3000 charge-discharge cycle and FESEM images after 3000 charge-discharge cycle for OA4PAN composite.

are no significant change of shape of i) absorption spectra, revealing PANI chains are in emeraldine state and ii) tubular shape of OA4PAN composites after long cycle of charging and discharging.

3.3.8. Electrochemical study of symmetric Devices

The capacitive behaviour of the synthesized OA4PAN was calculated by classical two electrode method.[29,41,42] To check the performance and stability, three symmetric devices (2x2 cm^2) made of OA4PAN were fabricated on scotch tape exploited graphite paper by casting dropwise high concentrated solution of OA4PAN in N-Methyl-2- pyrrolidine (NMP) solvent at room temperature.

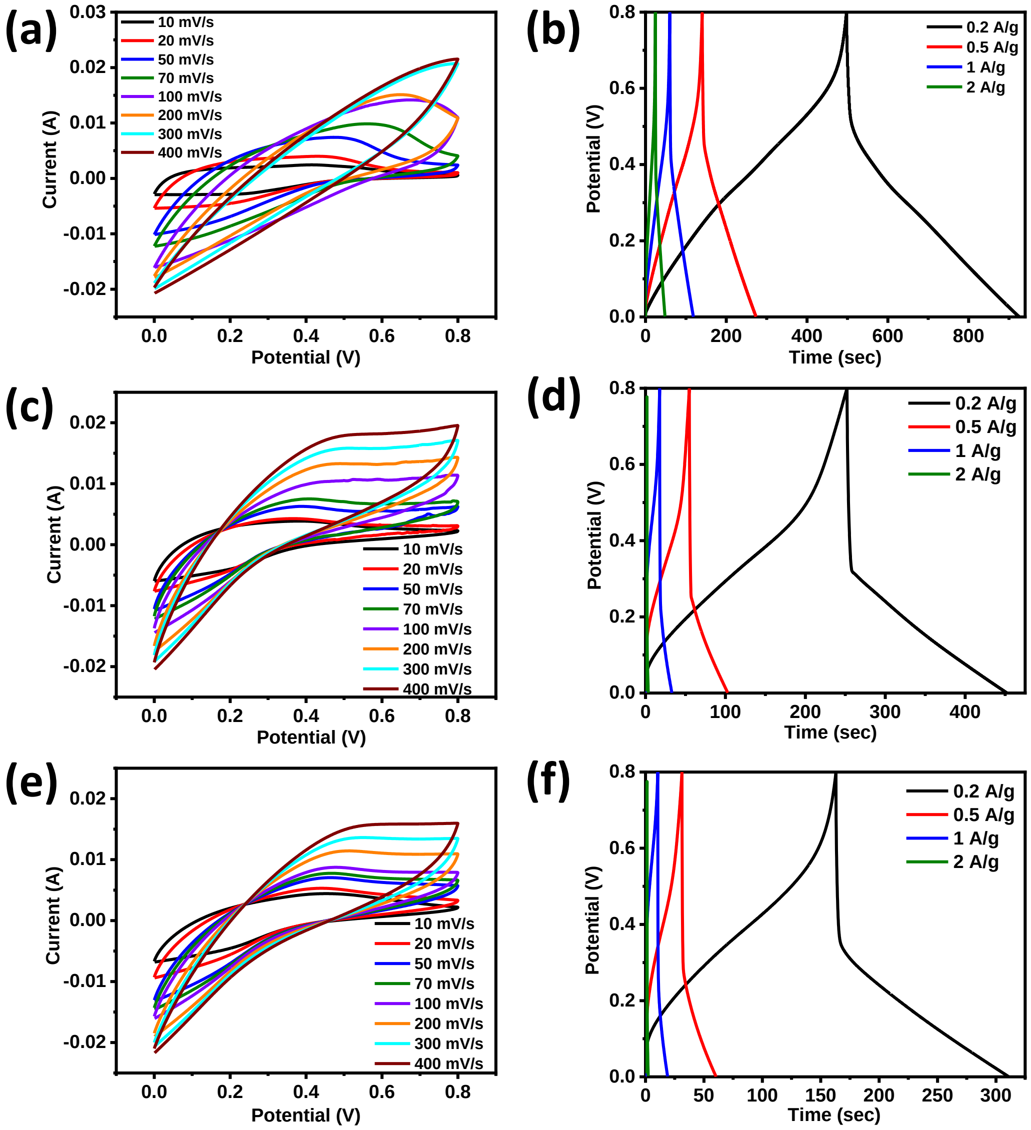

Figure 3.9 CV plots and Galvanic charge-discharge plots devices made of OA4PAN on graphite paper having area 2 x 2 cm^2 with mass loading (a, b) 2 mg, (c,d) 5 mg, and (e,f) 10 mg

After drying the electrode material each electrode was sandwiched by gel of (1:1) PVA–H_2SO_4. CV studies of all devices (**Figure 3.9**) were performed at various scan rate such as at 10, 20, 50, 70, 100, 200, 300, and 400 mV/s, respectively. The potential window of 0 V to 0.8 V was taken for the CV as well as GCD analysis. A couple of redox peaks are noticed from the CV curve, revealing the redox behaviour of polyaniline chains present in solid-state flexible device. The integrated area of the CV curves gradually enhances with scan rate, implying the improved specific capacitance value. GCD curves (**Figure 3.9**) of solid-state flexible device at various current densities of 0.2, 0.5, 1.0, and 2.0 A/g, are quasi-triangular in shape and the specific capacitance value of the device has been evaluated from the GCD curve using the **Equation 3.1**.[43,44].

It has observed that at variable scan rate 2 mg mass loading device reveal the best result of capacitance value. At 0.2 A/g, 0.5 A/g, 1 A/g and 2 A/g scan rate, values of specific capacitance (C_S) are of 107 F/g and 83.44 F/g, 72.88 F/g and 59.5 F/g respectively.

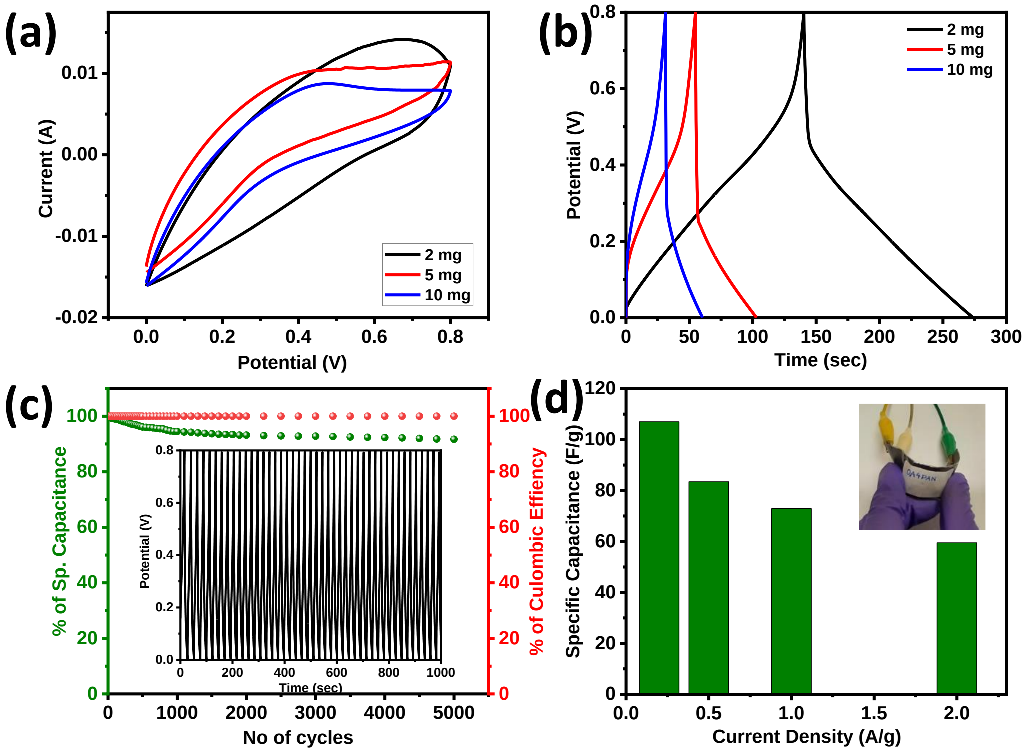

Figure 3.10 Comparative Studies of three devices of area 2x2 cm^2 (a) cyclic voltammetry at 100 mV/s; (b) Galvanic Charge Discharge at 0.5 A/g; (c) Cycle Stability and the retention of columbic efficiency up to 5000 cycles at 2A/g current density and (d) bar diagram of Sp. Cap. vs current density of the symmetric device with mass loading 2mg.

Energy density (E) values are 9.5 Wh/Kg, 7.42 Wh/Kg,6.48 Wh/Kg and 5.29 Wh/Kg, Power Density (P) values are 80 W/Kg, 200 W/Kg, 400 W/Kg and 800 W/Kg respectively at the said scan rate. **Figure 3.10** is the comparative study of CV and GCD of three devices of area 2x2 cm^2. In **Figure 3.10** the area under the curve is maximum 2 mg mass loading that means the capacitive behaviour is relatively high for that device.

This conclusion reflects the result in the **Figure 3.10b**, which shows the specific capacitance value 83.44 F/g at 0.5 A/g current density. 2 mg mass loading device shows 90.9% retention of specific capacitance value up to 5000 cycles at 2A/g current density in **Figure 3.10c**. and the coulombic efficiency of the device does not alter even after 5000 cycles. **Figure 3.10d** is the bar diagram of sp. capacitance vs current density.

3.3.9 Flexibility studies

For the flexibility and stability test of the device, the CV and GCD have been measured in deferent bending angle (**Figure 3.11a-b**). Apparently, there is no change of shape of CV and GCD curves upon bending. In **Figure 3.11c-d** the CV and GCD have been checked in different voltage windows like 0-0.4, 0-0.6, and 0-0.8 V at 50 mV/s scan rate and 0.5 A/g current density. Nature of GCD plot is unaltered even at higher operating voltage of 0 V to 0.8 V ranges, revealing the stability of the solid-state flexible device made of OA4PAN. Discharge time is also increasing with the enhancement of the potential window, as a result, the capacitance values have increased. We have again estimated the power density and energy density from the available results, it has been observed that this device made of OA4PAN has achieved the energy density of 9.5, 7.4, 6.5, 5.3 Wh/Kg and power density of 80, 200, 400, 800 W/kg at current density of 0.2, 0.5, 1, 2 A/g respectively as seen from Ragone plot (**Figure 3.11e**).

Electrochemical impedance responses have been measured in an open-circuit potential and in the frequency range of $0.01-10^5$ Hz for the solid-state flexible device (**Figure 3.11 f**). For this solid-state device a solution resistance value of 8.998 Ω is obtained. From the graph it is quite evident that the flexible device behaves like an ideal supercapacitor.[24,45,46]

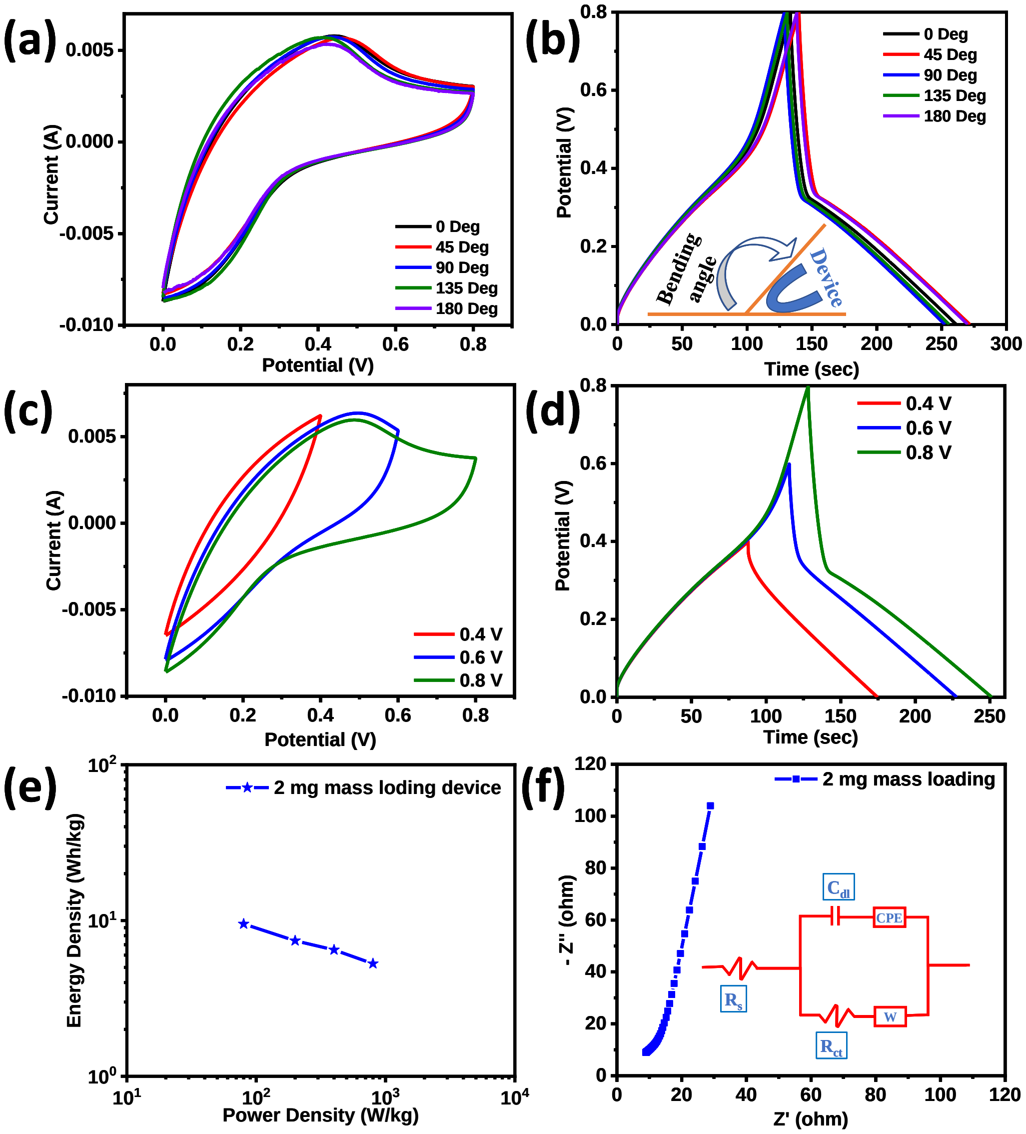

Figure 3.11 Flexibility test of the 2 mg mass loading and area 2x2 cm^2 of solid-state device at different bending situation (a) CV plot at 50 mV/s scan rate and (b) GCD plot at 0.5 A/g scan rate, (c) CV plot in different voltage window at 50 mV/s scan rate and (b) GCD plot in different voltage window at 0.5 A/g scan rate. (e) Ragon plot (f) electrochemical impedance studies.

3.4. Conclusions

Herein in the manuscript, organic acid doped polyaniline nanotubes have been employed as an electrode material for the development of electrochemical capacitor. Organic acids used as dopant in the chemical oxidation of aniline are benzene dicarboxylic acids (OA2), benzene tricarboxylic acids (OA3) and benzene tetracarboxylic acids (OA4) to make polyaniline nanostructures. Morphological studies with the help of FESEM and HRTEM reveal the formation of nanotubes with organic acids on contrary to HCl doped PAN. After characterization of OPAN with UV-Vis, XRD, XPS and FTIR, these OPAN are subjected to electrochemical studies and subsequently to galvanostatic charge-discharge studies to have the idea about the suitability of these as electrode materials. It has been noticed that OA4PAN is the optimum nanostructures among four OPAN having specific capacitance 394 F/g with 76.8% retention of total specific capacitance after 3000 cycles. The OA4PAN solid-state flexible device has showed the specific capacitance of 84 F/g at a 0.5 A/g, energy density of 7.42 Wh/kg at a 0.5 A/g, power density of 200 W/kg at a 0.5 A/g and also retains 90.9% of its specific capacitance after 5000 charge-discharge cycles. Albeit low as comparative to nanocomposites with carboneous analogue but significant electrochemical performances with simple organic acid doped polyaniline nanotube provides its potential for prospective application as electrode materials for flexible supercapacitor device.

3.5. References

1. H. Nishide, K. Oyaizu, *Science*, 2008, **319** 737- 738.

2. P. Simon, Y. Gogotsi, *Nat. Mater.*, 2008, **7** 845-854.
3. H. Guan, L-Z. Fan, H. Zhang, X. Qu, *Electrochim. Acta*, 2010, **56** 964-968.
4. Z. Yang, J. Zhang, M. C. W. Kintner-Meyer, X. Lu, D. Choi, J. P. Lemmon, J. Liu, *Chem. Rev.*, 2011, **111** 3577- 3613.

5. C. Arbizzani, M. Mastragostino, F. Soavi, New trends in electrochemical supercapacitors. *J. Power Source*, 2001, **100** 164-170.
6. J. Yan, T. Wei, B. Shao, Z. Fan, W. Qian, M. Zhang, F. Wei, *Carbon*, 2010 **48** 487-493.
7. H. Baughman, A. A. Zakhidov, W. A. de. Heer. *Science*, 2002, 297 787-792.
8. M. Winter, R. J. Brodd, *Chem. Rev.*, 2004, **104** 4245-4270.
9. G. Wang, L. Zhang, J. Zhang, *Chem. Soc. Rev.*, 2012, **41** 797-828.
10. P. Simon, Y. Gogotsi, B. Dunn, *Science*, 2014, **343** 1210−1211.
11. Z. Yu, L. Tetard, L. Zhai, J. Thomas, *Energy Environ. Sci.*, 2015, **8** 702−730.
12. F. Wang, X. Wu, X. Yuan, Z. Liu, Y. Zhang, L. Fu, Y. Zhu, Q. Zhou, Y. Wu, W. Huang, *Chem. Soc. Rev.*, 2017, **46** 6816-6854.
13. M. Kaempgen, C. K. Chan, J. Ma, Y. Cui, G. Gruner, *Nano Lett.*, 2009, **9** 1872-1876.
14. Z-S. Wu, D. W. Wang, W. Ren, J. Zhao, G. Zhou, F. Li, H. M. Cheng, *Adv. Funct. Mater.*, 2010, **20** 3595-3602.
15. X. H. Cao, Y. M. Shi, W. H. Shi, G. Lu, X. Huang, Q. Y. Yan, Q. C. Zhang, H. Zhang, *Small*, 2011, **7** 3163-3168.

16. Y. W. Cheng, H. B. Zhang, S. T. Lu, C. V. Varanasiad, J. Liu, *Nanoscale*, 2013, **5** 1067-1073.

17. L. L. Zhang, X. S. Zhao, *Chem. Soc. Rev.*, 2009, **38** 2520-2531.

18. Z. Wu, L. Li, J-M. Yan, X-B. Zhang, *Adv. Sci.*, 2017, **4** 1600382.

19. J. Kim, J. Lee, J. You, M-S. Park, M. S. A. Hossain, Y. Yamauchi, J. H. Kim, *Mater. Horiz.*, 2016 **3** 517-535.

20. C. Peng, S. Zhang, D. Jewell, G. Z. Chen. *Prog. Nat. Sci.*, 2008, **18** 777-788.

21. A. Burke, *Electrochim. Acta*, 2007, **53** 1083-1091.

22. A. M. Bryan, L. M. Santino, Y. Lu, S. Acharya, J. M. D'Arcy, *Chem. Mater.*, 2016, **28** 5989-5998.

23. A. Eftekhari, L. Li, Y. Yang, *J. Power Sources*, **2017**, 347 86-107.

24. W. Chen, R. B. Rakhi, H. N. Alshareef, *J. Mater. Chem. A*, 2013, **1** 3315-3324.

25. Y-E. Miao, W. Fan, D. Chen, T. Liu, *ACS Appl. Mater. Interfaces*, 2013, **5** 4423-4428.

26. K. Wang, J. Huang, Z. Wei, *J. Phys. Chem. C*, 2010, **114** 8062-8067.

27. U. Rana, K. Chakrabarti, S. Malik, *J. Mater. Chem.*, 2012, **22** 15665-15671.

28. U. Rana, S. Mondal, J. Sannigrahi, P. K. Sukul, M. A. Amin, S. Majumdar, S. Malik, *J. Mater. Chem. C*, 2014, **2** 3382-3389.

29. B. Anothumakkool, A. T. Arun Torris, S. N. Bhange, S. M. Unni, M. V. Badiger, S. Kurungot, *ACS Appl. Mater. Interfaces*, 2013, **5** 13397-13404.

30. S. Mondal, U. Rana, S. Malik, *ACS Appl. Mater. Interfaces*, 2015 **7** 10457-10465

31. S. Mondal, U. Rana, P. Das, S. Malik, *ACS Appl. Polym. Mater.*, 2019, **1** 1624-1633.

32. L. Wang, X. -L. Wu, W. -H. Xu, X.-J. Huang, J.-H. Liu, A.-W. Xu, *ACS Appl. Mater. Interfaces*, 2012, **4** 2686-2692.

33. Y. Wang, H. D. Tran, L. Liao, X. Duan, R. B. Kaner, *J. Am. Chem. Soc.*, 2010, **132** 10365-10373.

34. Y. Yan, R. Wang, X. Qiu, Z. Wei, *J. Am. Chem. Soc.*, 2010, **132** 12006-12012.

35. Y. Ma, C. Hou, H. Zhang, M. Qiao, Y. Chen, H. Zhang, Q. Zhang, Z. Guo, *J. Mater. Chem. A*, 2017, **5** 14041-14052

36. K. Lee, S. Cho, S. H. Park, A. Heeger, C. -W. Lee, S.-H. Lee, *Nature*, 2006, **441**, 65-68.

37. S. Mondal, U. Rana, S. Malik, *J. Phys. Chem. C*, 2017, **121** 7573-7583.

38. S. B. Yoon, E. H. Yoon, K. B. Kim, *J. Power Sources*, 2011, **196** 10791-10797.

39. E. Song, J. W. Choi, *Nanomaterials*, 2013, **3** 498-523.

40. M. S. Kumar, P. Das, K. Y. Yasoda, N. K. Kothurkara, S. Malik, S. K. Batabyal, *J. Energy Storage*, 2020, **31**, 101700.

41. X. Lu, M. Yu, G. Wang, Y. Tong, Y. Li, *Energy Environ. Sci.*, 2014, **7**, 2160-2181.

42. Z. Weng, Y. Su, D. W. Wang, F. Li, J. Du, H. M. Cheng, *Adv. Energy Mater.*,2011, **1** 917-922.

43. Y. Xie, Y. Liu, Y. Zhao, Y. H. Tsang, S. P. Lau, H. Huang, Y. Chai, *J. Mater. Chem. A*, 2014, **2** 9142-9149.

44. D. Ghosh, S. Giri, C. K. Das, *Nanoscale*, 2013, **5** 10428-10437.

45. W. Zhou, X. Liu, Y. Sang, Z. Zhao, K. Zhou, H. Liu, S. Chen, *ACS Appl. Mater. Interfaces*, 2014 **6** 4578-4586.

46. S. Zhu, M. Wu, M. H. Ge, H. Zhang, S. K. Li, C. H. Li, *J. Power Sources*, 2016, **306** 593-601.

CHAPTER 4

Polyaniline/G-Quadruplex Hybrid Networks as Next-Generation Electrode Materials with Unprecedented Rheological Performance

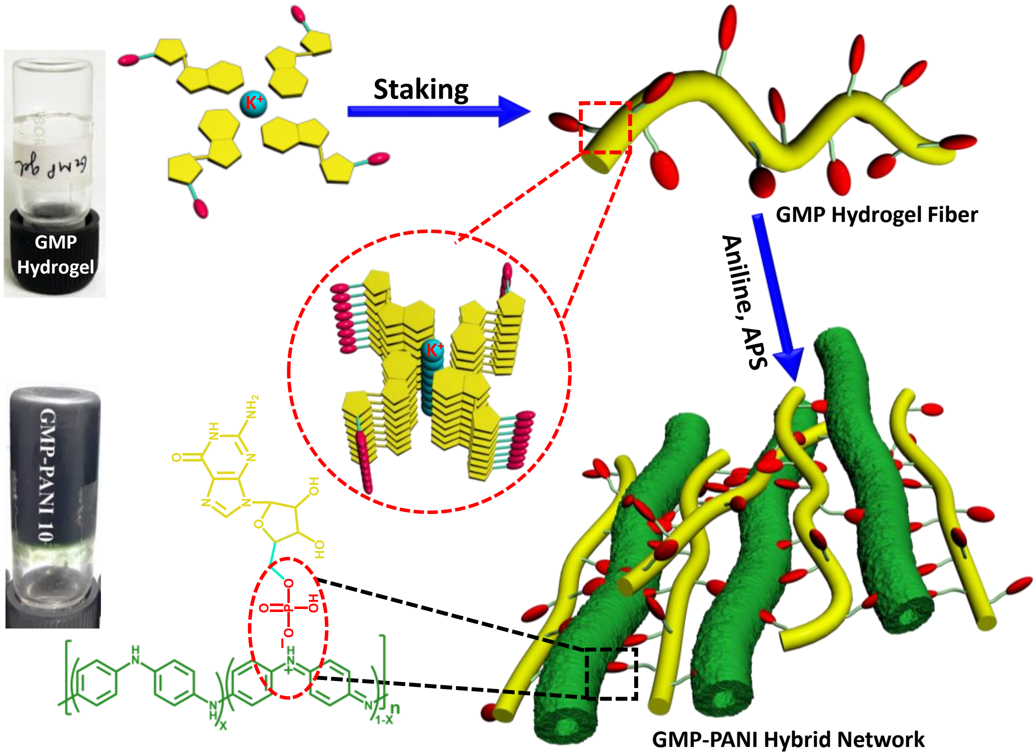

4.1 Introduction

Lightweight, flexible, and highly efficient energy storage devices are becoming more and more prevalent in our daily lives due to portable and flexible electronics.[1-4] Because they can offer a high-power density, a long cycle life, and the potential to achieve a reasonably high energy density close to typical batteries, supercapacitors are widely acknowledged as a significant class of energy storage devices.[5-7] High performance flexible solid-state supercapacitors based on several carbon nanomaterials, metal composite, and conducting polymer composites have received a lot of attention.[8-17] Owing to the simple synthesis, low cost, superior stability, customizable electric and electrochemical properties, conducting polymers have received a lot of attention in the fields of electrical devices, biosensors, super-capacitors,[18,19] actuators, and drug administration.[20-23] However, the application of this material is severely constrained by its poor processability in the form of insoluble granular powder or intractable brittle thin film. It is well known that the polymer hydrogels preserve the distinctive three-dimensional hybrid network with significant water content. Due to their excellent solid-liquid interface, strong electric characteristics, simplicity of processing, conducting polymer hybrid networks often provide inherent conducting frameworks and facilitate the transfer of charges, ions, or molecules in the three-dimensional porous network.[24–30] Typically, conducting polymer hybrid networks are created by either directly combining conducting polymer and the hydrogel component or polymerizing the appropriate monomer within the hydrogel network precursor.[31-36] However, it is challenging for conducting polymer to distribute uniformly throughout the hydrogel network in a non-continuous phase, otherwise, stability or mechanical properties of the hybrid network will be hampered by the presence of second component. The most prevalent 3D macroscopic architecture is found in polyaniline (PANI) hydrogel network having large specific surface area, high porosity, high electrical conductivity, and easy to prepared and printed with ease using an inkjet printer to create micropatterns for huge arrays of devices.[37-42] G-rich DNA and RNA sequences adopt four-stranded G-quadruplex structures and these natural DNA and RNA secondary structures have emerged as potential anticancer targets owing to their functional role in gene expression and telomerase maintenance. Small molecules have been designed to bind and stabilize DNA and RNA G-quadruplexes for developing alternative anticancer strategies. They contain a macrocyclic guanine quartet (G-quartet) as the basic structural unit. The G-quartet contains square planar arrangement of four guanine moieties interconnected via hydrogen bonding between Watson-Crick and Hoogsteen edges of the neighbouring guanines (**Scheme 1**). G-quartet is further stabilized by central cations (Na^+, K^+,

NH^{4+} etc.). Owing to its distinctive self-assembly properties, the natural nucleotide guanosine monophosphate and its derivatives have the propensity to form G-quartet structures via H-bonding. Subsequent aggregation of these G-quartets into columnar aggregates by π–π stacking leads to synthetic G-quadruplex assemblies generating tuneable three-dimensional cross-linking fibrillar hydrogel networks. The properties of hydrogels can be modulated by external stimuli such as pH, temperature, constituents and ions. Though, methods to prepare stable hydrogels of guanine derivatives have been reported, their applications and utility have not been traversed extensively.[43-44] A G4 hydrogel fabric composed of guanosine 5'-monophosphate disodium salt, potassium chloride with the pH being tuned by utilizing small volume of HCl has been used as soft-matrix into which conducting polymers are embedded to generate the organic hybrid network having high specific surface area, high electrical conductivity and fast ion diffusion processes which are of particular interest to achieve high capacitor performance and device applications.

In this context, it has been attempted to i) develop novel hybrid network composed of hydrophilic conducting polymer, particularly with polyaniline and G4 (**Scheme 4.1**), ii) investigate the structure-property relation and iii) the application of hybrid network as electrode materials.[45-47] To the best of our knowledge, novel hybrid network made of conducting polymers and G-quadruplex like assemblies have not been studied yet as electrode material and may lead to unique biomaterials based on conducting polymers.

4.2 Experimental Section

4.2.1 Materials: Prior to usage, aniline monomer (Merck Chemicals) was vacuum distilled to remove impurities before being kept at a low temperature in a dark location. Ammonium persulphate (APS) ((NH4)2S2O8), PVA, N-Methyl-2-pyrrolidine (NMP) were purchased from Merck Chemicals. Millipore Milli-Q 18 MΩ cm water was used to produce all aqueous solutions. Guanosine 5'-monophosphate disodium salt [Na2(5'-GMP)], potassium chloride (KCl), were procured from Sigma Aldrich and used without further purification. In all the experiment we used Milli-Q water (pH ~7.4).

4.2.2 Preparation of GMP and GMP-PANI hydrogel networks

a) A mixture of Na2(5'-GMP) (33 mg, 0.08 mmol, 1 equiv.) and KCl (17 mg, 0.23 mmol, 2.8 equiv.) was dissolved in 1.0 mL Milli-Q water. This suspension was then heated to obtain a clear solution. The pH of this hot solution was then adjusted to 6.8-7.0 using HCl. The resulting mixture was then cooled to room temperature. Gelation occurred on standing (until gelation was observed) to give a clear reversible gel (pH ~6.8-7.0).

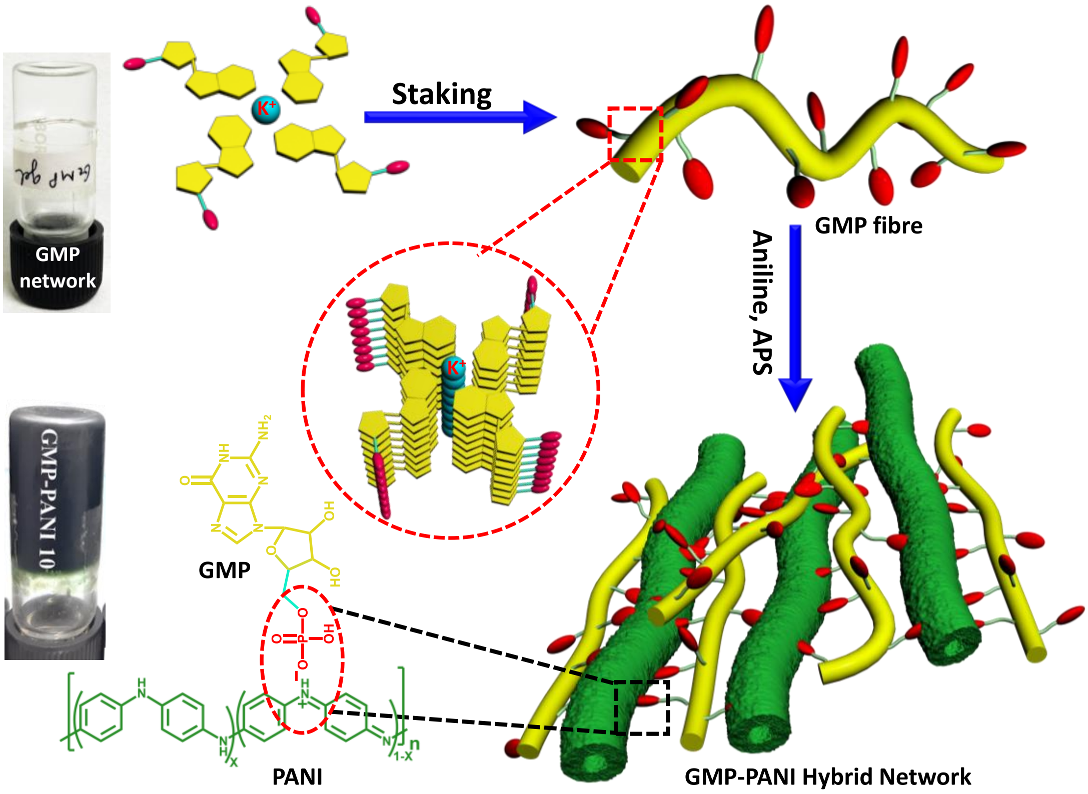

Scheme 4.1 Schematic representation of synthesis procedure of guanosine 5'-monophosphate ($Na_2$5'-GMP) and GMP-PANI hybrid networks.

Table 4.1 Preparation of different GMP-PANI hybrid networks.

Sample	Amount of GMP hydrogel taken (mL)	Aniline taken (µL)	APS taken (mg)
GMP-PANI 5	3.00	15.00	37.00
GMP-PANI 10	3.00	30.00	75.00
GMP-PANI 25	3.00	75.00	186.00
GMP-PANI 50	3.00	150.00	370.00

b) In 2.5 mL GMP hydrogel, required amount of aniline (15, 30, 75, and 150 µL) was dispersed by heating and continuous stirring for 20 min at 75 - 80°C. After that required amount of APS

(37 mg, 75 mg, 186 mg, 370 mg) was dissolved in 0.5 ml GMP hydrogel in similar way previous procedure. Two reaction mixture was mixed and kept in room temperature to become a hydrogel again. Then the composites were washed with ice cold water and methanol to remove the excess APS and oligomer.

4.2.3 Preparation of PVA-H_2SO_4 (1:1) gel electrolyte

To prepare a 10 wt.% polyvinyl alcohol (PVA) solution, approximately 1.00 g of PVA was mixed with 10 mL of Milli-Q water. The mixture was heated at 85°C for 2-3 hours until a transparent solution was achieved. After cooling it to room temperature, 546 µL of H_2SO_4 was added to the solution and stirred for 30 min to ensure uniformity. [49]

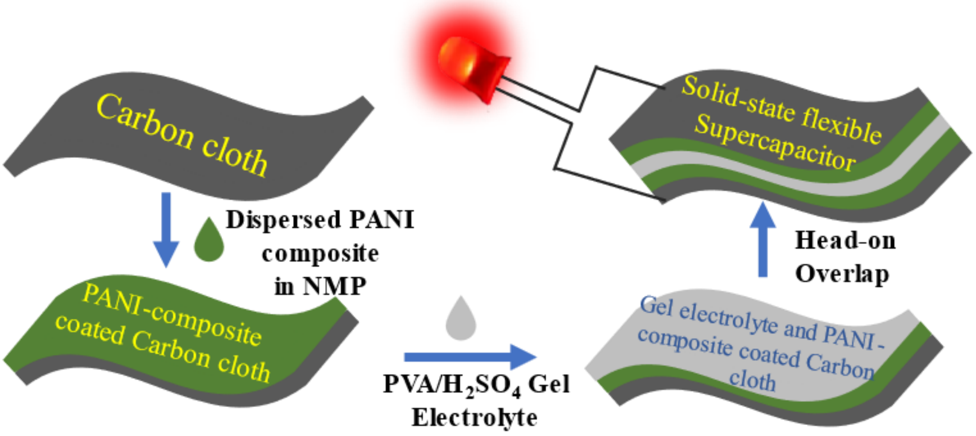

Scheme 4.2 Schematic illustration of the all-solid-state flexible supercapacitor.

4.2.4 Fabrication of all solid-state flexible device

To thoroughly assess the performance and stability of the GMP-PANI 10 hybrid network in practical applications, we fabricated symmetric devices with an area of 2 × 2 cm2 and a mass loading of 2 mg using GMP-PANI hybrid network. To achieve this, we prepared a concentrated GMP-PANI 10 solution in N-Methyl-2-pyrrolidine (NMP) solvent at room temperature, ensuring uniformity by continuously stirring the solution for 2 hours. The device fabrication process was meticulously carried out, involving precise drop casting of the specified amount of GMP-PANI 10 onto a carbon cloth substrate. This step ensured the formation of a well-adhered and homogenous electrode material. Afterward, the electrode material was allowed to dry, and each individual electrode was skilfully sandwiched between layers of PVA-H2SO4 in a 1:1 ratio. This PVA-H2SO4 combination not only served as an efficient electrolyte but also acted as a separator, ensuring the effective isolation of the two electrodes and preventing any undesirable short circuits. The incorporation of PVA-H2SO4 as both the electrolyte and separator (as depicted in Scheme 2) further simplified the device structure, enhancing its overall stability and performance.

4.2.5 Cell culture: U2OS cells, derived from human osteosarcoma epithelial cells, were cultured in a mixture of DMEM and F12K in a 1:1 ratio. HCT116 cells, originating from human colorectal carcinoma, and WI-38 cells, derived from human fetal lung fibroblast cells, were separately cultured in DMEM with high glucose (5.5 mM) and in EMEM with NEAA, respectively. Those culture media were supplemented with 10% FBS and maintained at a pH of 7.4. The cells were incubated at 37°C in an atmosphere containing 5% carbon dioxide (CO_2) and 95% air.

4.2.6 XTT assay: The XTT cell proliferation assay was conducted to assess the capacity of viable cells to convert a slightly yellow tetrazole, known as (2,3-bis-(2-methoxy-4-nitro-5-sulfophenyl)-2H-tetrazolium-5-carboxanilide), into a vivid orange formazan product. To enhance the reduction reaction, a solution of PMS (N-methyl dibenzopyrazine methyl sulfate) was introduced. This bioreduction process was linked to the production of NAD(P)H through glycolysis, which exclusively occurred in viable cells. In the typical assay, specific cell lines (U2OS, HCT116, WI-38) were seeded into 96-well plates and exposed to varying concentrations of GMP-PANI 10 for a duration of 24 hours. Following that incubation period with the compound, a mixture containing 4 mL of XTT (1mg/mL) and 10 μL of PMS (3 mg/mL) was added to 100 μL of the cell culture medium in each well. The absorbance (A) of the formazan dye was then measured at 450 nm using a microplate reader. The percentage of viable cells was calculated using the following formula,

$$\text{Viable cells (\%)} = [(A_{\text{Treated cells}} / (A_{\text{Untreated cells}}) \; X \; 100]$$

and the half maximal inhibitory concentration (IC50) was estimated by plotting cell viability (%) vs concentration.

4.3 Results and discussion

Required amount of aniline was dispersed within Guanosine 5'-monophosphate (GMP) hydrogel matrix by warming and continuous stirring for 20 min. After cooling the mixture, required amount of APS solution was added and two reaction mixture were mixed and kept in room temperature to become a hydrogel. The change of colour of the mixture from colourless to brownish to greenish and finally deep green colour have primarily revealed the formation of PANI chains within the GMP hydrogel matrix. It is important to mention that the addition of external dopant acids which are prerequisite to initiate the oxidation of aniline during chemical polymerization, does not require in the present system. It is possibly owing to the presence of acidic functional group (phosphate group) within GMP hydrogel. PANI itself does not produce gels with any dopant acids, and significantly, the formation of PANI chains within hybrid network does not disturb / break GMP hydrogel network as evidenced from the inversion of gel tubes. To know strength or weakness of the hybrid network with respect to pristine GMP network, rheological studies have been performed.

4.3.1 Rheological studies

Soft matters like gels, colloids, paste, *etc.* are viscoelastic substances that combine both the characteristics of viscous (liquid) and elastic (solid) components. When the soft matter is subjected to a shear strain (g) during a sinusoidal oscillation:

$$\gamma(t) = \gamma_0 \sin \omega t$$

The stress (σ) response is given by the equation:

$$\sigma(t) = \sigma_0 \sin\ (\omega t + \delta)$$

where ω is the angular frequency and δ is the phase difference between the strain and the stress. The stress and strain waves are in phase for a material that is completely elastic, meaning that the full applied energy is stored in the system, and δ = 0°. However, in a perfectly viscous system, δ = 90°, meaning that the stress and strain waves are 90° out of phase, and all input energy is converted to heat. A phase angle of 0° to 90° can be observed in viscoelastic materials.[48] The parameters storage modulus (G′) and loss modulus (G″), which are given as,

$$G' = \left(\frac{\sigma_0}{\gamma_0}\right) \cos(\delta) \text{ and } G'' = \left(\frac{\sigma_0}{\gamma_0}\right) \sin(\delta)$$

G' and $G''$are used to gauge the mechanical characteristics of hydrogels. The storage modulus (G′) represents the deformation energy stored during the shear process of a viscoelastic material (i. e. solid-like nature), the loss modulus (G″) is a representation of the energy dissipated during the shear process (flow or liquid-like nature), and in the gel state, G′ > G″ and G′(ω) should be invariant throughout angular frequency.

Frequency sweep and strain sweep experiments have been carried out on the **GMP, GMP-PANI 5, GMP-PANI 10, GMP-PANI 25, and GMP-PANI 50** hybrid networks and the results are displayed in **Figure 1a-b**. Results make it clear that G′ > G″ across a broad frequency band supports the viscoelastic properties of hybrid networks. [47] It is quite interesting to observe that the value of G′, which is considered as a gauge of network strength, rises with an increase in PANI content until a certain point in the networks before decreasing in **Figure 1c**. The G″ value likewise follows the same arrangement. This rise in modulus value may be attributed to the growth as well as the presence of PANI chains and the branching of GMP nanofibers makes it simpler to store and release energy. As compared to the GMP network or physical mixture of GMP and PANI (Figure. S2), the enhancements of G′ (1062 times) and G″ (161 times) show a remarkable improvement for **GMP PANI 10** hybrid network. The rheological data are used to determine the percent enhancement moduli of the networks, and **Table 2** lists all the characteristics. With the increase of PANI chains to a certain proportion inside the network, it is obvious that moduli values of hybrid networks also increase and the dissipation factor (tan δ) of the network, as determined by the ratio of loss to storage modulus, likewise decreases. In comparison to the GMP and other **GMP-PANI** networks, **GMP-PANI 10** network has an enormous increase of the storage modulus, possibly owing to the optimum ionic interactions between phosphate group of GMP network and amine/imine nitrogen of PANI chains (**Scheme 1**). Therefore, it is obvious that the polymerization of aniline does not produce the macroscopic phase separation that is detrimental effect to properties of hybrid systems, rather the presence of PANI imparts excellent rheological properties than the parent GMP network.

Table 4.2. Comparison of the rheological properties of GMP network, GMP-PANI 5, GMP-PANI 10, GMP-PANI 25 and GMP-PANI 50 hybrid networks.

Sample	Storage modulus G′ (Pa)	Loss modulus G″ (Pa)	Complex modulus G* (Pa)	% Increase in G′	% Increase in G″	tan δ
GMP	8	4.3	9	-	-	0.54
GMP-PANI 5	179	24	180	2138	458	0.13
GMP-PANI 10	8500	693	8528	106150	16016	0.08
GMP-PANI 25	3150	1036	3316	39275	24086	0.33
GMP-PANI 50	2031	240	2045	25288	5481	0.12

4.3.2 Dynamic Mechanical studies

After getting the enhanced values of moduli, the hybrid gel networks have been kept under the dynamic compression mode (**Figure 1d**) to check the compressive strength (the ability of a hybrid network to withstand stress without failure, i.e., the maximum stress) and toughness (the amount of energy stored within network before failure, i.e., the area under the curve upto the maximum stress) of networks.

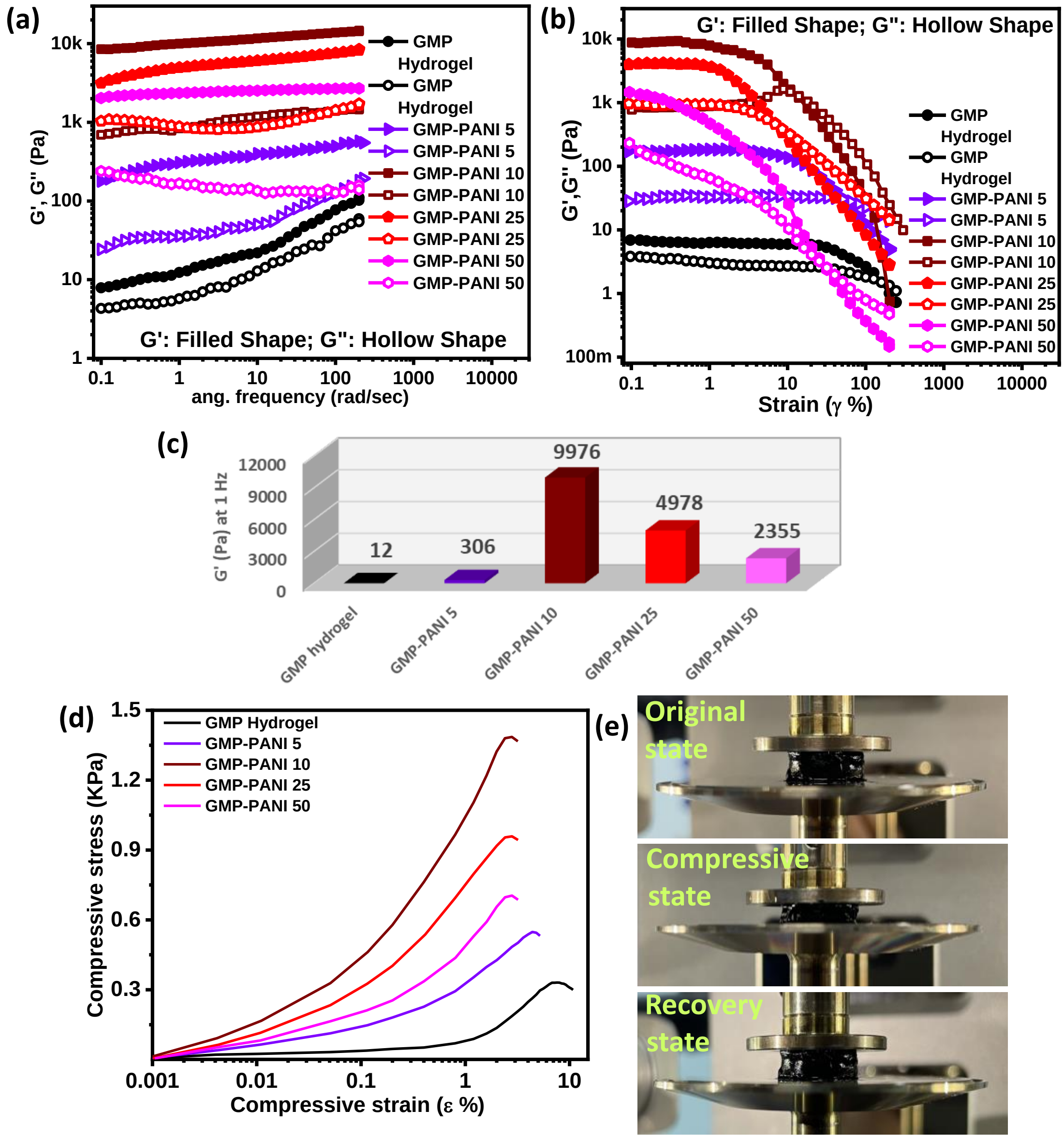

Figure 4.1. (a) Rheological angular frequency sweeping measurements, (b) Strain sweeping measurements, (c) storage moduli for GMP hydrogel network and GMP-PANI hybrid networks at a frequency of 1 Hz., (d) compressive stress - strain curves of GMP and its GMP-PANI hybrid gel networks at 25°C and (e) the representative photograph of cylindrical shape (diameter = 10.00 mm and length = 5.00 mm) of the GMP-PANI 10 hybrid networks.

As compared to GMP network only, GMP-PANI hybrid networks are revealing more compressive strength as well as relatively higher value of toughness because of a) the presence of PANI nanotubes within the hydrogel matrix, b) the large surface area for interactions and c) the substantial ionic interactions between phosphate group of GMP network and aminic / iminic nitrogen atoms present in PANI chains. Based on the above results, GMP PANI 10 hybrid network has been picked for the further studies.

Table 4.3. Comparison of the dynamic mechanical parameters of GMP, GMP-PANI 5, GMP-PANI 10, GMP-PANI 25 and GMP-PANI 50 networks (data taken at the maximum compressive stress)

Sample Name	**Compressive Strain (e %)**	**Compressive Strength (Pa)**	**% Increase in Strength**	**Compressive Storage Modulus (E′, Pa)**	**Compressive Loss Modulus (E″, Pa)**	**Compressive Complex Modulus (E*, Pa)**	**tan δ**
GMP	7.18	330	-	4020	1301	4225.3	0.32
GMP-PANI 5	4.79	546	66	9493.8	4335.5	10436.9	0.46
GMP-PANI 10	2.80	1385	320	38524	22348	44536.9	0.58
GMP-PANI 25	2.80	957	190	28424	13412	31429.4	0.47
GMP-PANI 50	2.80	656	99	23307	8781.9	24906.6	0.37

4.3.3 Absorption studies

In a well-dispersed aqueous solution, the absorption properties of GPM network and GMP-PANI 10 hybrid network have been conducted and it demonstrates the presence of three distinct absorption peaks at ~ 350, 435 and 900 nm, respectively shown in (**Figure 4.2a**) [49-52] for GMP-PANI network. The two peaks at 350 and 435 nm are due to π-π* and polaron-π* transitions of the benzenoid rings of PANI chains, respectively. Another peak at around 900 nm with a free tail that extends to the near infra-red region ascribes to the π-polaron transition. These findings suggest the formation of PANI chains within the GMP hydrogel matrix. Owing to the presence of absorption at the longer wavelength, PANI chains are in the emeraldine salt state, and these are conducting in nature.

4.3.4 FTIR studies

To know about the presence of GMP and PANI formation in GMP-PANI hybrid networks, FTIR studies have been carried out (Figure 2b). Typical stretching frequencies at 821, 1131, 1310, 1498, 1584, and 3385 cm^{-1} demonstrate the presence of PANI emeraldine salt into GMP-PANI networks. Stretching vibration bands at 821 and 1131 cm^{-1} are characteristic for n_{C-H} aromatic in the plane and deform 1,4-disubstituted benzene out of the plane, respectively. Stretching vibration bands at 1297 cm^{-1} are for n_{C-H} of secondary aromatic amines. There are another two extending vibration band at 1498 cm^{-1} (for $n_{C=C}$ for benzenoid rings) and 1584 cm^{-1} (for $n_{C=C}$ quinoid rings).[49, 50]

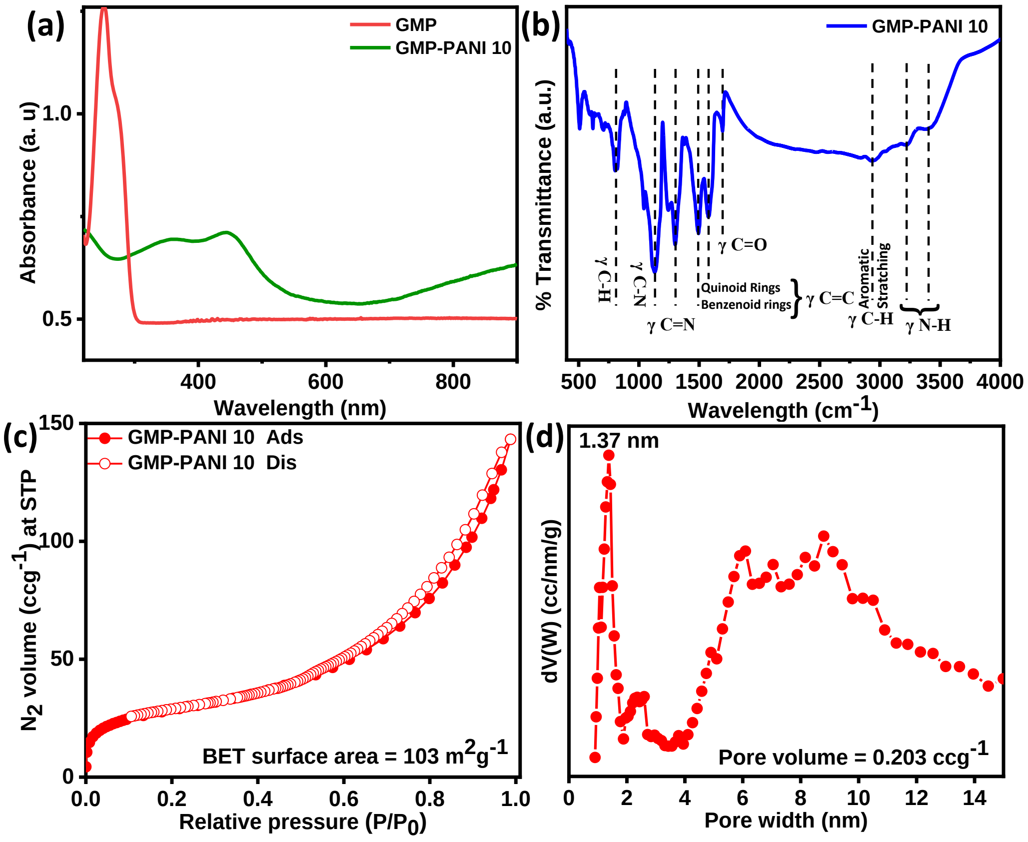

Figure 4.2. (a) UV-Vis Spectra of GMP hydrogel network (redline) and GMP-PANI 10 hybrid network (green line) after washing several times with ice-cold water, (b) Representative FTIR spectra of GMP-PANI hybrid network after washing several times with ice-cold water /methanol to remove excess GMP network, (c) N2 adsorption and desorption isotherm and (d) pore-size distribution curves of GMP-PANI 10 hybrid network after washing.

Even after several times washing, a small but significant stretching vibration of $n_{C=O}$ at 1690 cm^{-1} indicates the overwhelming presence of GMP moieties that interact with PANI chains of hybrid network. Apart from the formation of GMP network within the hybrid network, GMP moieties are also behaving as dopant acid during the polymerization of aniline in presence of APS. The n_{N-H} stretching vibrations (hydrogen bonded or non-bonded) originating either from GMP or PANI chains are at 3220 and 3385 cm^{-1}, respectively.

4.3.5 Surface area analysis

N_2 adsorption/desorption isotherms of **GMP-PANI 10** hybrid network reveal the sharp capillary uptake at low P/P_o, suggesting the microporous nature of the sample (**Figure 4.2c**). It is followed by large and steady increase of N_2 uptake at higher P/P_o region, resulting from the presence of a broad range of mesopores. [53,54] BET surface area of GMP-PANI material is 103 m^2/g with total pore volume 0.203 cc/g. Pore size distribution plot (**Figure 4.2d**) gives peak micropores of dimension 1.37 nm and a very broad distribution of large mesopores of dimension 5.0 - 11.0 nm. The presence of large mesopores may be attributed to the interparticle void space as observed other porous polymers. [53,54]

4.3.6 Morphological studies

FESEM, a sophisticated microscopy method, has been used to precisely study the surface of the GMP network and GMP-PANI hybrid network. In **Figure 4.5a**, it reveals that the GMP hydrogel networks are composed of fibres having diameter 40-50 nm as further confirmed by HRTEM and AFM results (**Figure 4.3**). Additionally, **figure 4.5b** offers a fascinating glimpse into the structural characteristics of unwashed hybrid network in which larger PANI fibres are wrapped as well as glued by the GMP network. It seems to be the cover of jelly like substance over PANI fibres, possibly owing to the GMP hydrogel network and APS. After washing several times with water and methanol, the **GMP-PANI** hybrid network reveals its fantastic tube-like morphology and clear surface in **Figure 4.5c**. A stunning high-resolution transmission electron microscopy (HRTEM) impression of the GMP-PANI hybrid network is also shown in **Figure 4.5d**. This incredibly excellent quality offers priceless details about length, diameter of the fibres, and unique fibrous arrangement, which is characterized by a hollow tube-like structure and results in a homogeneous morphology. Furthermore, we also investigate the tubular shaped structural morphology of other GMP-PANI composites shown in **Figure 4.4**. The captivating tube-like hollow pattern observed in the fibre signifies the

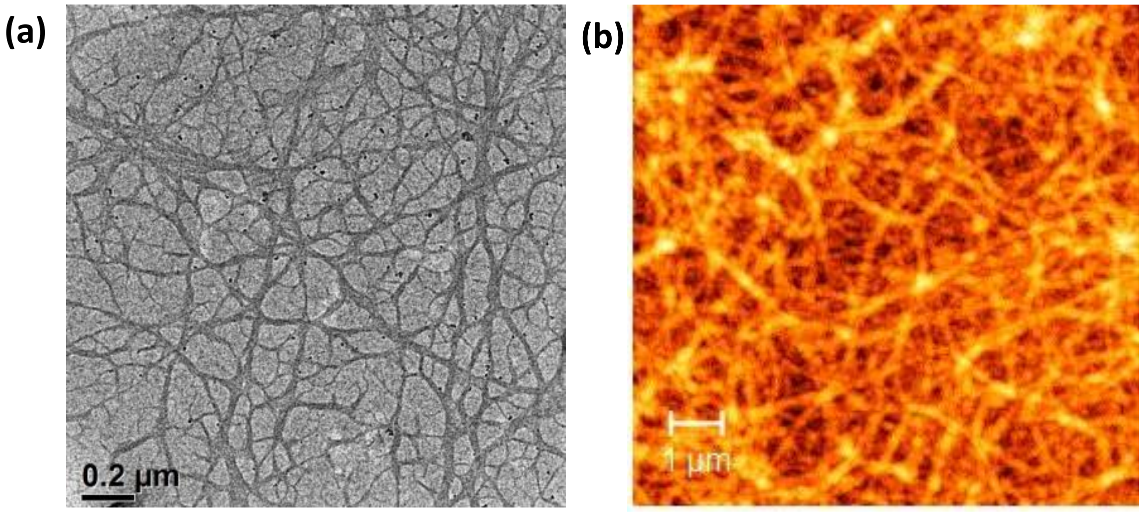

Figure 4.3. (a) HRTEM and (b) AFM Data of GMP-PANI 10 hybrid composite

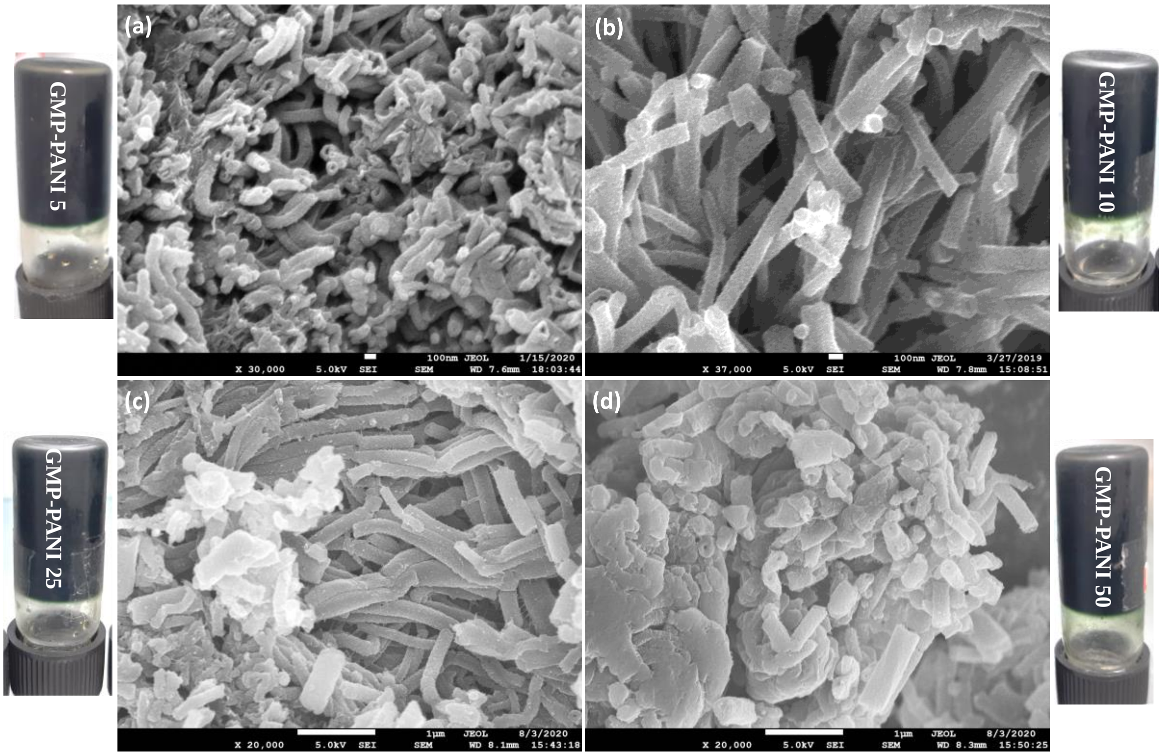

Figure 4.4. FESEM image of (a) GMP-PANI 5, (b) GMP-PANI 10, (c) GMP-PANI 25, (d) GMP-PANI 50

presence of nanotubes or nanofibers within the hybrid network, contributing to its exceptional characteristics and potential applications.

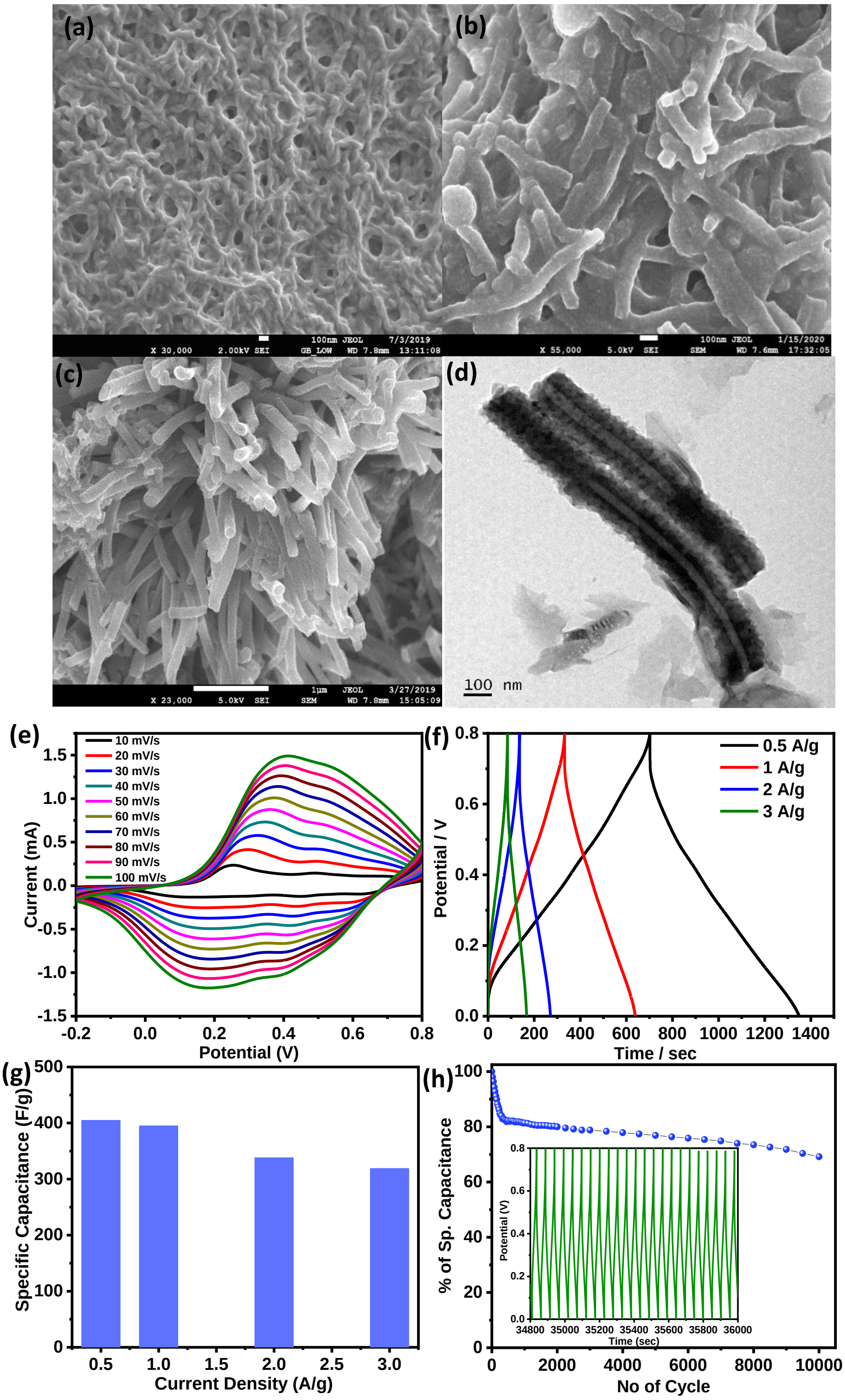

Figure 4.5. FESEM images of (a) GMP hydrogel network and **GMP-PANI 10** hybrid network, (b) before washing, (c) after washing and, (d) HRTEM image of **GMP-PANI 10** hybrid network after washing on carbon coated Cu grid, (e) Scan dependent CV plots, (f) Scan dependent galvanic charge discharge (GCD), (g) specific. Capacitance vs current density plot and (h) cycle stability of **GMP-PANI 10** hybrid network.

4.3.7 In vitro cytotoxicity study

To examine the biocompatibility of the hybrid network, the cytotoxicity of GMP-PANI 10 was evaluated using cancer cells such as osteosarcoma epithelial cells (U2OS) and colorectal carcinoma cells (HCT116), along with human fetal lung fibroblast cells (WI-38) as a normal cell line. When exposed to GMP-PANI 10 concentrations spanning from 0 to 90 µg/ml, the IC50 values were estimated to be around 7.68 µg/mL for U2OS cells and nearly 41.8 µg/mL for HCT116 cells (**Figure 4.6.**) The results revealed that while GMP-PANI 10 exhibited significant cytotoxic effects on U2OS cells, its impact on HCT116 cells was milder and benign. Remarkably, it had no observable effect on normal lung fibroblast cells. The lack of significant cytotoxicity on normal lung fibroblast cells suggests that GMP-PANI 10 is compatible with normal cell lines, indicating its potential for biological applications.

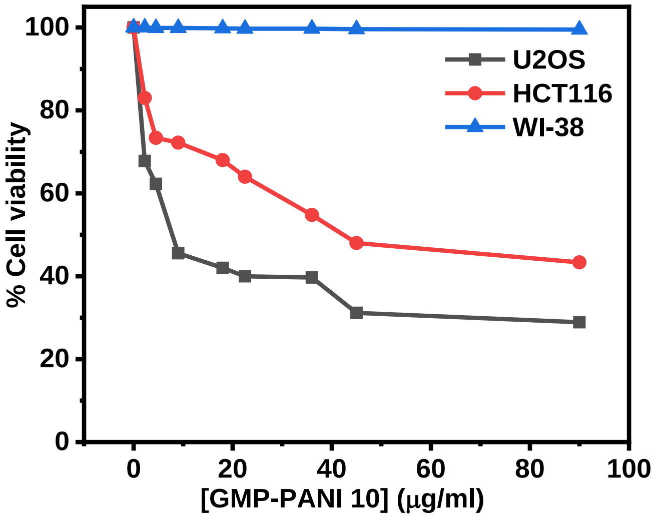

Figure 4.6 Cell viability results at various concentration of GMP-PANI 10.

4.3.8 Electrochemical studies

After removing the GMP network and other ions by washing successively with ice-cold water/methanol successively, the capacitive behaviour of **GMP-PANI 10** hybrid network has been assessed using cyclic voltammetry (CV) and galvanostatic charge-discharge (GCD) methods employing a three-electrode system using a glassy carbon electrode as the working electrode consisted of, while a Pt electrode served as the counter electrode and an Ag/AgCl electrode as the reference electrode. In **Figure 4.5e**, it can be observed that as the scan rate increases, the peak current also increases, accompanied by a broadening of the CV peaks. These observations indicate the presence of pseudo-capacitance characteristics in the **GMP-PANI 10** hybrid network. The electrochemical capacitance properties have been evaluated using the galvanostatic charge-discharge (GCD) method at various current densities ranging from 0.5 to 3 A/g (**Figure 4.5f**) and the specific capacitance values are 405, 395, 338, and 319 F/g at current densities of 0.5, 1, 2, and 3 A/g, respectively. Furthermore, in **Figure 4.5g**, the plot of specific capacitance (F/g) against current density (A/g) demonstrates a negligible decrease rate of specific capacitance values as the current density increases. Plot of specific. capacitance versus number of cycles is showing a steep decrease at the initial 300 cycles and it remains flat over 9000 cycles of charging/discharging. The stability of the hybrid network is revealing a remarkable ~ 70% retention of specific capacitance even after 10,000 cycles (**Figure 4.5h**). These results emphasize the favourable electrochemical capacitance properties of the **GMP-PANI 10** hybrid network, making it a promising candidate for various applications in energy storage systems.

4.3.9 Solid-state symmetric device study

The capacitive behaviours have been also checked by CV, GCD and electrochemical impedance spectroscopy (EIS) analysis using the classical two-electrode method by making a symmetric device (2 × 2 cm^2) on carbon cloth. The details fabrication procedure of the all-solid state flexible device has been demonstrated in **Scheme 4.2** and in the experimental section. The Polyvinyl alcohol (PVA)/H_2SO_4 gel electrolyte has been used as solid electrolyte, which also acts as a separator for the fabricated device. The CV curves of the all-solid-state flexible device fabricated using the **GMP-PANI 10** hybrid networks are depicted in **Figure 4.7a**. These curves are showing the typical pseudo-capacitive behaviours at different scan rates (10-500 mV/s), exhibiting a couple of redox peaks that indicate the redox behaviour of the polyaniline chains present in the flexible all-solid-state device. Furthermore, it is observed that the integrated area of the CV curves is noticeably better, implying an enhanced specific capacitance value (C_S). GCD curves of all-solid-state flexible supercapacitor device are quasi-triangular in nature in various current densities like 0.5 to 5 A/g in **Figure 4.7b** and 6 to 10 A/g in Fig. S6b. From the GCD curve, the device's C_S value has been calculated. A C_S of 118 ± 2 F/g is produced by the **GMP-PANI 10** hybrid network based all solid-state device at a current density of 1 A/g by using **equation 1**.[49, 55] In **Figure 4.7c**, at various current densities ranging from 0.5 to 10 A/g, the C_S values of the device are measured and found to be 127, 118, 113, 108, 106, 102, 98, 94, 91, 90, and 86 F/g respectively.

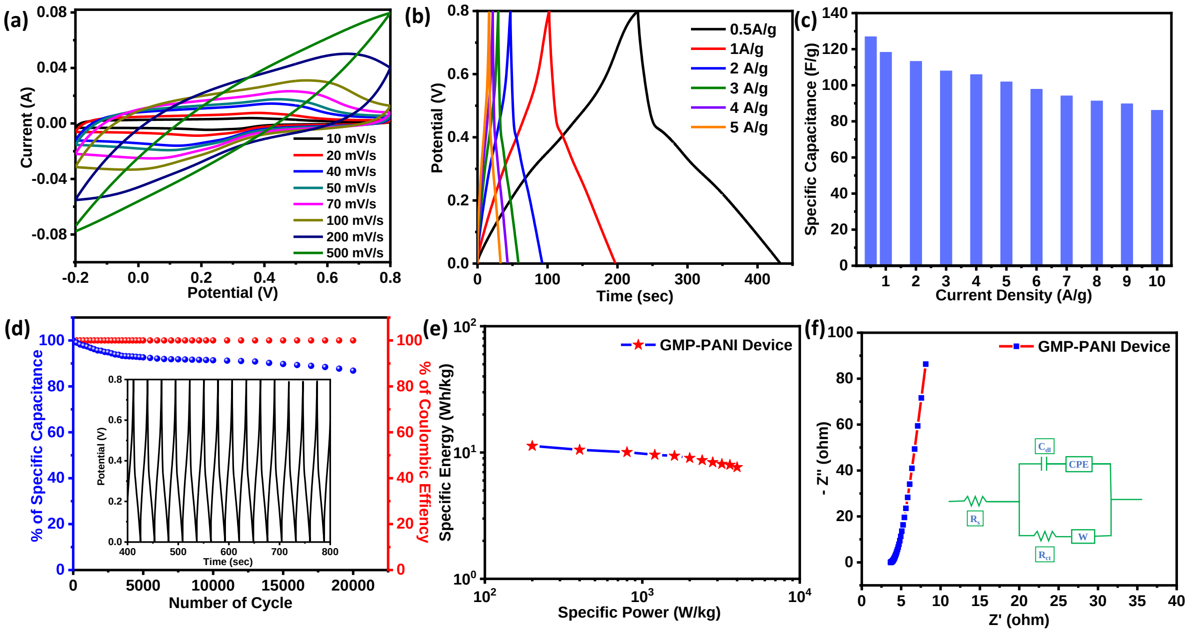

Figure 4.7. (a) Scan dependent Cyclic voltammetry, (b) Scan dependent galvanic charge - discharge at indicated current density, (c) sp. Capacitance vs current density plot, (d) cycle stability at 7 A/g current density, (e) Ragone plot, (f) electrochemical impedance studies of the all-solid-state flexible device made of the **GMP-PANI 10** hybrid network.

These results demonstrate the device's excellent performance in energy storage capabilities at different operating conditions. Moreover, the corresponding specific energy (E) values have been calculated and observed to be 11.3, 10.5, 10.1, 9.6, 9.4, 9, 8.7, 8.4, 8.11, 8, and 7.7 Wh/kg respectively, at the mentioned current densities. Additionally, the specific power (P) values are 200, 400, 800, 1200, 1600, 2000, 2400, 2800, 3200, 3600, and 4000 W/kg respectively at the mentioned current densities (**Figure 4.7e**). These values of specific energy and specific power showcase the device's ability to efficiently store and deliver electrical energy at different charge and discharge rates. The highest C_S value of 127 F/g is achieved at a current density of 0.5 A/g, indicating its outstanding energy storage capacity at lower current loads. Furthermore, even after subjecting the device to 20,000 cycles at a higher current density of 7 A/g (**Figure 4.7d**), the specific capacitance demonstrates the remarkable stability with around ~87% retention, signifying its excellent durability and cycle life. The coulombic efficiency of the device remains consistent throughout the extensive cycling tests, reaffirming its ability to maintain a high level of charge and discharge efficiency over multiple charge-discharge cycles. EIS measurements have been further performed at the frequency range of $0.1-10^5$ Hz and at an open-circuit potential for the all-solid-state flexible device (**Figure 4.7f**). A solution resistance value of ~3.7 Ω is obtained for the all-solid-state flexible device. From the Nyquist plot, it has been observed that the flexible device exhibits ideal supercapacitor behaviour. Overall, these results establish the device's robust electrochemical performance, making it a promising candidate for various energy storage applications that require high specific capacitance, specific energy, and specific power, along with superior cycling stability.

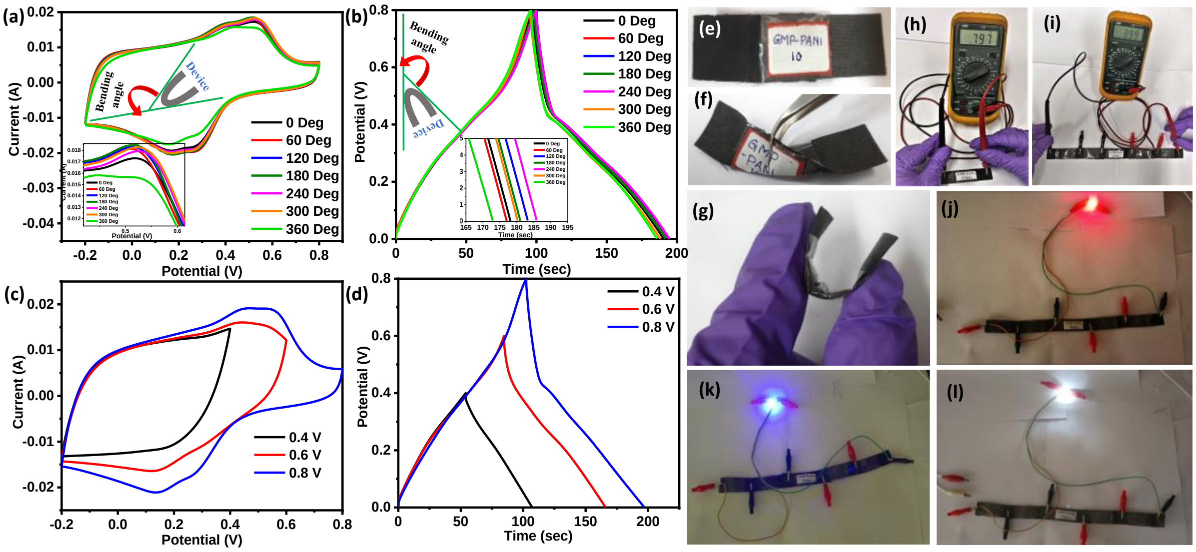

Figure 4.8. Flexibility test of all- solid-state device made of **GMP-PANI 10** hybrid network at different bending situation (a) CV plot at 50 mV/s scan rate, (b) GCD plot at 1 A/g scan rate, (c) CV plot in different voltage window at 50 mV/s scan rate and (d) GCD plot in different voltage window at 1 A/g scan rate. (e) Optical image of the flexible device in normal condition (f) in twisting condition (g) in bending conditions, (h, i) Photograph of single and 5 series supercapacitor devices showing output voltages of ~0.8 and ~4.0 V (approximately), respectively, (j) Red LED (k) Blue LED, and (l) White LED glowing via five flexible supercapacitor devices in series.

4.3.10 Flexibility study

For flexibility test, the electrochemical performances (CV and GCD) of the as-fabricated device have been thoroughly investigated at various bending angles: 0°, 60°, 120°, 180°, 240°, 300°, and 360°. CV plots performed at a scan rate of 100 mV/s for the all-solid-state device made of **GMP-PANI 10** hybrid network, are showing that there is no discernible effect on its electrochemical performance at various bending angles (**Figure 4.8a**). CV results reveal consistent behaviour and performance regardless of the bending angle, demonstrating the robustness and resilience of the device in various configurations. In addition to the CV studies, GCD analysis that have been performed at the same bending angles of 0°, 60°, 120°, 180°, 240°, 300°, and 360° at a constant current density of 1 A/g, is showing negligible differences at different bending angles (**Figure 4.8b**).

This further confirms that the as-fabricated device exhibits exceptional electrochemical characteristics even when subjected to bending, highlighting its superior performance in flexible states. For assessing the stability of the flexible device, Cyclic voltammetry study has been conducted at different potential windows such as -0.2 to 0.4 V, -0.2 to 0.6 V, and -0.2 to 0.8 V, all at a scan rate of 50 mV/s, as depicted in **Figure 4.8c**. Remarkably, all the CV curves exhibit a quasi-rectangular in shape within the range of -0.2 to 0.8 V indicating a highly reversible and stable electrochemical behaviour. Moreover, to further investigate the stability, galvanostatic charge-discharge (GCD) measurements have been performed in different potential windows while maintaining a constant current density of 1 A/g, (**Figure 4.8d**).

Interestingly, the GCD plots display constant and unalter characteristics, even when operate at a higher voltage of 0 to 0.8 V. It unequivocally establishes the robustness and stability of the all-solid-state flexible device. Furthermore, it is observed that widening the potential window leads to an enhancement in discharge time, resulting in improved capacitance value. This suggests that the all-solid-state flexible device can effectively operate within a broad range of potential windows, extending from 0 to 0.8 V, without compromising its stability and performance. To explore the practical applications of the flexible solid-state capacitors (SSCs) (**Figure 4.8e-g**) based on the **GMP-PANI 10** hybrid network, experiments of glowing of light emitting diode (LED) bulbs with varying operating voltage ranging from 2.2 to 3.5 V have been carried out by involving five supercapacitors connected in series. Notably, the tandem SSCs exhibit enhanced performance characteristics compared to the individual single SSCs. After charging the devices, the corresponding voltage using a multimeter has been monitored. The single SSC produces a voltage of approximately 0.8 V, while the series-connected SSCs exhibit an impressive voltage of approximately 4.0 V (**Figure 4.8h-i**). This significant increase in voltage highlights the capability of the series configuration to effectively enhance the overall output for practical applications. Furthermore, the real-world applicability of these SSC devices have been demonstrated by powering LED bulbs. The charged series of SSC devices have been successfully illuminated red, blue, and white LED bulbs, as shown in **Figure 4.8j-i**.

This practical application clearly demonstrates the capability of the **GMP-PANI 10** hybrid network-based SSCs to power LED bulbs effectively, showcasing their potential in various portable lighting applications. These findings emphasize the versatility and efficiency of the flexible SSCs in real-world scenarios, making them promising candidates for powering small-scale electronics, wearable devices, and energy-efficient lighting systems. The exceptional performance of the series-connected SSCs in powering LED bulbs opens novel possibilities for their utilization in diverse and energy-conscious applications.

4.4 Conclusions

A novel hybrid network, GMP-PANI, combining polyaniline with G-quadruplex (GMP), has been synthesized through *in-situ* polymerization of aniline in the presence of APS. The hybrid network has been investigated through rheological /dynamic mechanical studies, demonstrating its exceptional strength of hybrid gel network compared to GMP hydrogel network. Detailed investigations of the GMP network's morphology, both before and after polymerization, using FESEM and HRTEM, have revealed the formation of polyaniline fibres within the GMP network, without any macroscopic phase separation. Therefore, a unique GMP-PANI hybrid network is created, displaying exceptional electrochemical performance with biocompatible. In a three-electrode system, the GMP-PANI hybrid network demonstrates a high specific capacitance of 405 F/g at a current density of 0.5 A/g. This remarkable capacitance value is indicative of its excellent charge storage capacity, making it an ideal candidate for supercapacitor applications. Notably, when incorporated into a all-solid-state symmetric supercapacitor, the GMP-PANI hybrid network showcases a significantly enhanced specific capacitance, along with impressive cycle stability, retaining approximately 87% of its capacitance over multiple charge-discharge cycles. This excellent cycle stability is of paramount importance for real-world applications where longevity and consistent performance are critical factors. Moreover, in a tandem configuration, a series of five GMP-PANI hybrid network-based supercapacitors collectively powers red, blue, white, and multi-coloured LED bulbs, demonstrating its robust capability as a reliable and high-performing supercapacitor. The ability to power different types of LED bulbs exemplifies the versatility and suitability of the GMP-PANI hybrid network as a biocompatible material for practical energy storage solutions.

4.5 References

1. M. Yu, Y. Peng, X. Wang, F. Ran, *Adv. Funct. Mater*. 2023, **33**, 2301877.
2. Y. Yuan, X. Li, L. Jiang, M. Liang, X. Zhang, S. Wu, J. Wu, M. Tian, Y. Zhao, L. Qu, *Nat Commun.* 2023, **14**, 3967.
3. D. H. Kim, N. Lu, R. Ma, Y. S. Kim, R. H. Kim, S. Wang, J. Wu, S. M. Won, H. Tao, A. Islam, et al. *Science*. 2011, **333**, 838–843.
4. H. Nishide, K. Oyaizu, *Science*. 2008, **319**, 737–738.
5. P. Simon, Y. Gogotsi, *Nat. Mater*. 2008, **7**, 845–854.
6. Z. Zhu, T. Jiang, M. Ali, Y. Meng, Y. Jin, Y. Cui, W. Chen, *Chem. Rev*. 2022, **122**, 16610–16751.
7. G. P. Wang, L. Zhang, J. J. Zhang, *Chem. Soc. Rev*. 2012, **41**, 792–828.
8. S. Nathabumroong, C. Poochai, J. P. Mensing, C. Sriprachuabwong, J. Lohitkarn, T. Lomas, R. Yimnirun, A. Tuantranont, *ACS Appl. Nano Mater*. 2023, **6**, 34−43
9. C. Meng, C. Liu, L. Chen, C. Hu, S. Fan, *Nano Lett*. 2010, **10**, 4025–4031.
10. Y. J. Kang, S. J. Chun, S. S. Lee, B. Y. Kim, J. H. Kim, H. Chung, S. Y. Lee, W. Kim, *ACS Nano*. 2012, **6**, 6400–6406.
11. Y. J. Kang, H. Chung, C. H. Han, W. Kim, *Nanotechnology*., 2012, **23**, 065401.
12. S. Hu, R. Rajamani and X. Yu, *Appl. Phys. Lett.*, 2012, **100**, 104103.
13. M. F. El-Kady, V. Strong, S. Dubin and R. B. Kaner, *Science*, 2012, **335**, 1326–1330.
14. Z. Weng, Y. Su, D.-W. Wang, F. Li, J. Du and H.-M. Cheng, *Adv. Energ. Mater*., 2011, **1**, 917–922.
15. D. M. Reinoso, M. A. Frechero, *Energy Storage Mater*. 2022, **52**, 430-464.
16. B. G. Choi, S. J. Chang, H. W. Kang, C. P. Park, H. J. Kim, W. H. Hong, S. Lee and Y. S. Huh, *Nanoscale*, 2012, **4**, 4983–4988.
17. L. Yuan, X. H. Lu, X. Xiao, T. Zhai, J. Dai, F. Zhang, B. Hu, X. Wang, L. Gong and J. Chen, et al. *ACS Nano*, 2012, **6**, 656–661.
18. J. Kim, J. Lee, J. You, M. -S. Park, Md S. Al Hossain, Y. Yamauchi and J. H. Kim, *Mater. Horiz.*, 2016, **3**,517.
19. X. Chu, W. Yang and H. Li, *Mater. Horiz.*, 2023, **10**, 670.
20. H. M. Zhang, Q. Zhao, S. P. Zhou, N. J. Liu, X. H. Wang, J. Li and F. S. Wang, *J. Power Sources*, 2011, **196**, 10484–10489.
21. O. S. Kwon, S. J. Park, J. S. Lee, E. Park, T. Kim, H. -W. Park, S. A. You, H. Yoon and J. Jang, *Nano Lett.*, 2012, **12**, 2797–2802.

22. S. L. Liu, K. He, X. Wu, X. G. Luo and B. Li, *RSC Adv.*, 2015, **5**, 87266–87276.

23. R. Salimian and C. Nardin, *Biomacromolecules*, 2023, **24**, 3411−3437.

24. J. Luo, W. Zhong, Y. Zou, C. Xiong and W. Yang, *J. Power Sources*, 2016, **319**, 73–81.

25. H. Heydari and M. B. Gholivand, *New J. Chem.*, 2017, **41**, 237–244.

26. S. Zeng, H. Chen, F. Cai, Y. Kang, M. Chen and Q. Li, *J. Mater. Chem. A*, 2015, **3**, 23864–23870.

27. D. Caccavo, S. Cascone, G. Lamberti and A. A. Barba, *Chem. Soc. Rev.*, 2018, **47**, 2357–2373.

28. Y. Chen, H. Feng, L. Li, S. Shang and M. C. Yuen, *J. Macromol. Sci. Part A.*, 2013, **50**, 1225–1229.

29. R. Du, Y. Xu, Y. Luo, X. Zhang and J. Zhang, *Chem. Commun.*, 2011, **47**, 6287–6289.

30. Y. Wang, Y. Shi, L. Pan, Y. Ding, Y. Zhao, Y. Li, Y. Shi and G. Yu, *Nano Lett.*, 2015, **15**, 7736–7741.

31. M. M. El. Sayed, *J. Environ. Polym. Degrad.* 2023, **31**,2855–2879.

32. H. Huang, J. Wu, X. Lin, L. Li, S. Shang, M. C. Yuen and G. Yan, *Carbohydr. Polym.*, 2013, **95**, 72–76.

33. T. Dai, X. Qing, J. Wang, C. Shen and Y. Lu, *Compos. Sci. Technol.*, 2010, **70**, 498–503.

34. W. Zhao, L. Glavas, K. Odelius, U. Edlund and A. Albertsson, *Chem. Mater.*, 2014, **26**, 4265–4273.

35. J. Ji, X. Yu, P. Cheng, Q. Zhang, F. Du, L. Li and S. Shang, *J. Macromol. Sci., Part B: Phys.*, 2015, **54**, 1122–1131.

36. X. Wu and M. Lian, *J. Power Sources*, 2017, **362**, 184–191.

37. H. Guo, W. He, Y. Lu and X. Zhang, *Carbon*, 2015, **92**, 133–141.

38. L. Pan, G. Yu, D. Zhai, H. R. Lee, W. Zhao, N. Liu, H. Wang, B. C. K. Tee, Y. Shi, Y. Cui and Z. Bao, *Proc. Natl. Acad. Sci. U. S. A.*, 2012, **109**, 9287−9292.

39. P. Li, Z. Jin, L. Peng, F. Zhao, D. Xiao, Y. Jin and G. Yu, *Adv. Mater.*, 2018, **30**, 1800124.

40. F. Zhao, Y. Shi, L. Pan and G. Yu, *Acc. Chem. Res.*, 2017, **50**, 1734−1743.

41. S. Das, P. Chakraborty, S. Mondal, A. Shit and A. K. Nandi, *ACS Appl. Mater. Interfaces*, 2016, **8**, 28055−28067.

42. S. Das, R. Ghosh, P. Routh, A. Shit, S. Mondal, A. Panja and A. K. Nandi, *ACS Appl. Nano Mater.*, 2018, **1**, 2306−2316.

43. T. Bhattacharyya, P. Saha and J. Dash, *ACS Omega*, 2018, **3**, 2230-2241.

44. T. Bhattacharyya, Y. P. Kumar and J. Dash, *ACS Biomater. Sci. Eng.*, 2017, **3**, 2358–2365.

45. E. N. Zare, P. Makvandi, B. Ashtari, F. Rossi, A. Motahari, and G. Perale, *J. Med. Chem.*, 2020, **63**, 1−22.

46. C. Yang, P. Zhang, A. Nautiyal, S. Li, N. Liu, J. Yin, K. Deng, and X. Zhang, *ACS Appl. Mater. Interfaces*, 2019, **11**, 4258−4267.

47. R. Zhong, Q. Tang, S. Wang, H. Zhang, F. Zhang, M. Xiao, T. Man, X. Qu, L. Li, W. Zhang, and H. Pei, *Adv. Mater.*, 2018, **30**, 1706887

48. C. Yan and D. J. Pochan, *Chem. Soc. Rev.*, 2010, **39**, 3528–3540.

49. P. Das, S. Mondal and S. Malik, *J. Energy Storage*, 2021, **39**, 102662.

50. U. Rana, K. Chakrabarti and S. Malik, *J. Mater. Chem.*, 2012, **22**, 15665–15671.

51. U. Rana, S. Mondal, J. Sannigrahi, P. K. Sukul, M. A. Amin, S. Majumdar and S. Malik, *J. Mater. Chem. C*, 2014, **2**, 3382–3389.

52. S. Mondal, U. Rana and S. Malik, *ACS Appl. Mater. Interfaces*, 2015, **7**, 10457–10465.

53. S. K. Kundu and A. Bhaumik, *ACS Sustainable Chem. Eng.*, 2015, **3**, 1715–1723.

54. B. C. Patra, S. Khilari, L. Satyanarayana, D. Pradhan and A. Bhaumik, *Chem. Commun.*, 2016, **52**, 7592-7595.

55. M. S. Kumar, P. Das, K. Y. Yasoda, N. K. Kothurkara, S. Malik and S. K. Batabyal, *J. Energy Storage*, 2020, **31**, 101700.

CHAPTER 5

Charge transport in metal-nanoparticle embedded one-dimensional conducting polymer nanotubes: multiple resistive switching phenomena

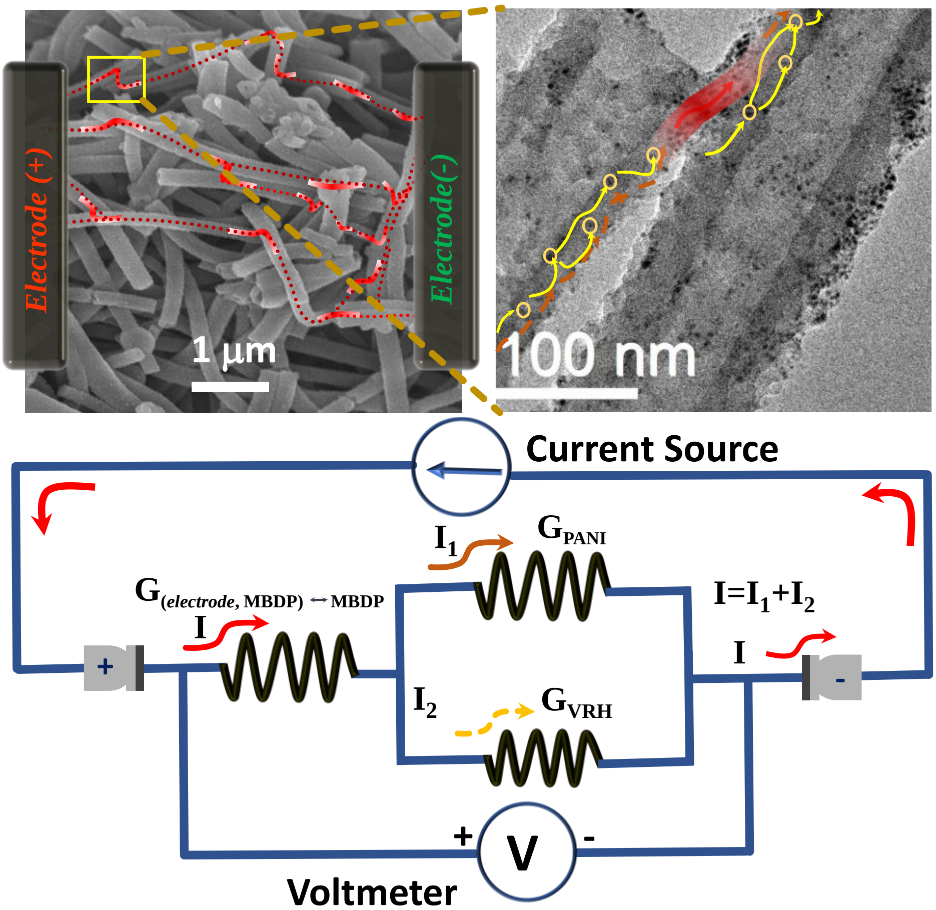

5.1. Introduction

Polymers are increasingly playing a significant role in a wide variety of applications in electronics and photonics [1-3]. From polymer resists for lithography, which is the backbone of the development of modern-day technology, to polymer-based optical data storage (optical disc) have played a crucial role in the social revolution in recent decades [4-7]. Now we are in the era of big data generated from media, social networks, archives, etc [8,9]. Unfortunately, processing and storage are increasingly becoming key challenges, primarily due to hardware issues [10]. Most popular memory technologies like SRAM, DRAM, and FLASH (based on conventional Von Neumann architecture) are based on complementary metal-oxide-semiconductor (CMOS) architectures with floating gates [11,12]. To achieve a high-density and fast data storage device, it needs to downscale the size of the electrical gate [12,13]. Due to gradual reaching towards the fundamental limits in scaling down, explorations of new device architecture with alternative materials and technologies for next-generation memory devices have been under active consideration for decades [14,15]. Recently, resistive switching (RS) based memory has appeared as the most promising candidate to overcome these challenges [16]. A considerable number of materials, for example, graphene, TMDs, topological insulators, h-BN, perovskites, polymer materials, and black phosphorus, have already been investigated for their excellent performances and characteristics for the next-generation resistive memory devices [17-22]. The nanodevice architectures based on one-dimensional (1D) materials, like CNT (carbon nanotube), are also explored for their unique electronic and structural properties [12,23,24]. However, the major drawback of CNT-based architecture is that it involves a complex fabrication process [12,23,24]. The economically cheap and easily processable synthetic/ organic p -conjugated conducting polymer (CP) having controlled nano-architectures like nanofibers, nanobelts, or nanotubes are promising 1D materials for next-generation electronics and device applications [21,22,25-28]. These CPs show finite electrical conductivity at room temperature due to their π-π interaction in the polymer chains [29,30]. Among these CPs, the polyaniline (PANI) nanotubes have drawn significant attention due to their ecofriendly processability, low cost, and excellent mechanical, optical, and electrical conducting properties [31,32]. The delocalized conjugated p electrons inside the CPs network facilitate the intrinsic low resistive state (high conducting) [33-36]. The high conductivities of CPs reduce RS ratio as well as retention performance which is a significant challenge for developing pure CP based RS devices. Therefore, the careful engineering of CP nanotubes is pursued through the development of active hybrid structure [37-39]. PANI nanotubes have active surface sites which may easily attach different materials [40]. Therefore, it can be functionalized or decorated with different types of nanoparticles (NPs) and materials for desired physical properties [41]. Here, the silver (Ag) NPs have been embedded on CP nanotubes to explore the effect on charge transport behaviours and subsequently on RS characteristics. The Ag NPs act as the sources, traps of free charge carriers and play a crucial role in electronic resistive states through electron-phonon and electron-electron interactions [41]. The nature of charge conduction mechanisms determines the resistive states of these materials [42-45]. Various transport mechanisms of charge conduction, for example, thermionic emission, Ohmic conduction, ionic conduction, hopping conduction, trap-assisted tunneling (TAT) methods, and carrier diffusion, can lead the active system to a particular resistive state [21,22,46-49]. However, there are hardly any report investigating the correlation of charge transport mechanism and RS phenomena in CP-based memory devices through charge transport study and conductance fluctuation measurements. In this work, metal nano-particle embedded one-dimensional conducting functional polymer nanotubes have been judiciously picked up for RS memory applications.

Pure benzene tetracarboxylic acid-doped polyaniline (BDP) and silver (Ag) metal-doped BDP (MBDP) have been synthesized by the chemical polymerization method [50]. Before investigating RS performances, all the samples have been thoroughly characterized by FTIR, UV-Vis, XRD, FESEM, TEM, etc. Electrical transport study reveals that pure BDP sample does not produce any RS, whereas MBDP samples with optimized Ag NPs reveal a distinct low resistive state (LRS) and high resistive state (HRS). The ON/OFF resistance ratio strongly depends on loading concentration of Ag NPs. Sample with 36.7 % loaded Ag concentration (MBDP 10) reaches the optimum RS characteristics and also exhibits a distinct second resistive transition at a high applied current. Significant improvement of RS characteristics, including retention time (104 s), endurance (250 cycles), and narrow distribution of RS, makes these materials very promising candidates for plastic-based RS device applications. Furthermore, multiple resistive states allow MBDP 10 to be used in logic operation (for example, OR gate). Detailed charge transport in pristine BDP and MBDP 10 (with an optimal concentration of Ag NPs) samples have been investigated through temperature-dependent transport measurement and low-frequency 1/f conductance noise spectroscopy to understand the underlying physics of the RS phenomena.

5.2. Experimental section

5.2.1. Preparation of materials

Silver nitrate (AgNO3), 1,2,4,5-benzenetetracarboxylic acid (BTCA), and ammonium persulphate [(NH4)2S2O8] (APS) were procured from Sigma-Aldrich, used without further purification. Aniline purchased from Merck Chemicals (India) was distilled at reduced pressure prior to use. Water (18 M U) obtained from a Millipore Milli-Q system was utilized to prepare all aqueous solutions.

5.2.2. Preparation of benzene tetracarboxylic acid-doped polyaniline (BDP) fibres

BDP fibres were prepared according to our published reports [51-55]. Initially, BTCA (70 mg) and freshly distilled aniline (0.1 mL) were dispersed and homogenized in an aqueous medium, and aniline was added to it with stirring at a low temperature. An aqueous solution of the oxidizing agent (APS, 248.7 mg) was slowly added to the mixture and stirred for 30 min. Subsequently, the colour of the mixture was changed to brown, indicating the formation of an oligomer. The mixture was kept at a low temperature overnight. The green products precipitated at the bottom of the flask were washed with double distilled water and methanol repeatedly to remove excess amount of APS and oligomers. The precipitate was dried in a pool of air for 6 h and finally in a vacuum to achieve BDP.

5.2.3. Preparation of MBDP

Typically, 100 mg of BDP fibre was taken in a cleaned glass tube, and it was dispersed in 10 mL of water with a magnetic stirrer at room temperature (25°C). Next, 10 mL of AgNO3 solutions with varying concentrations were slowly added to the mixture solution. The resulting mixture was stirred for 2.75 h (**Table-1**). Finally, MBDP composites were kept under 10,000 rpm and washed with water several times to remove excess AgNO3 from the surface of BDP fibres.

Table 5.1 The MBDP composites with increasing loading percentage of Ag NPs.

Composites name	Amount of BDP (mg)	Concentration of $AgNO_3$ (mmol)	Loading of Ag (%)	Distribution of AgNPs over BDP
MBDP 0.1	100	0.1	8.7	On/into
MBDP 1	100	1.0	21.7	On/into
MBDP 5	100	5.0	26.3	On/into
MBDP 7.5	100	7.5	28.4	On/into
MBDP 10	100	10.0	36.7	On/into
MBDP 11	100	11.0	38.3	On/into and outside
MBDP 12.5	100	12.5	40.5	On/into and outside

MBDP 15	100	15.0	48.7	On/into and outside
MBDP 20	100	20.0	58.4	On/into and outside

5.3. Results & discussion

5.3.1. XRD, UV-Vis and FTIR Analysis

Fig.1 shows detailed characterization (XRD, UV-Vis and FTIR) of BDP and MBDP samples (Table 1) with loading concentrations of Ag NPs and the distribution NPs inside/outside of BDP. The powder X-ray diffraction (XRD) spectra of BDP and MBDP samples display several diffraction peaks at 2θ ~ 15°, 20.3° and 25.6° for (011), (100) and (110) plane as shown in (1(a)), revealing semi-crystalline nature of BDP composites. Peaks appeared at 2θ ~ 20.3° and 25.6° are for regularity in the parallel and the perpendicular direction of the PANI chain, respectively [51, 56-58]. The diffraction peak at 25.6° corresponds to the d-spacing ~3.48 Å for the face-to-face interaction of phenyl rings of PANI chains [59]. Five sharp diffraction peaks at the range of 2θ ~ 38° - 81.5° indicate the presence of Ag nanoparticle in MBDP, and these peaks at 2θ ~ 38.1°, 44.3°, 64.5°, 77.4°, and 82.5° are attributed to the (111), (200), (220), (311), and (222) crystal planes of the face-cantered cubic structure of Ag NPs [60,61]. Distance between two similar crystal planes of Ag NPs has been calculated from Bragg's equations: $n\lambda = 2d \sin\theta$, where λ is the X-ray wavelength (0.154 nm), d is the separation between two similar crystal planes, and θ is the Bragg angle (in degree). Here, the estimated layer distance for the (111) crystal plane by using Bragg's equation is 0.235 nm ((111) plane). With increasing the amount of silver in MBDP, the peak intensities of crystal planes assigned to Ag NPs gradually increases [62]. Absorption spectra (**Figure-5.1b**) of BDP and MBDP in disperse aqueous solution reveal three absorption peaks at 350, 435, and 900 nm. Initial two peaks centered at around 350 and 435 nm are ascribed to π-π* transition, and polaron-π* transition of benzenoid rings [63]. A strong peak at 900 nm with a free tail extended to IR region is assigned to π-polaron transition, revealing the emeraldine salt of PANI chains [50,51,64]. With the increasing Ag NPs in MBDP, this π - polaron peak is shifted to a lower wavelength, and the formation of Ag NPs onto BDP may possibly enhance the bandgap of π-polaron state of PANI. Characteristic absorption of Ag NPs at ~ 410 nm is not resolved in these spectra owing to the overlap of the broad π-π* band and the polaron -π* band of PANI chains [50]. Characteristic stretching frequencies at 821, 1131, 1310, 1498, 1584 and 3431 cm^{-1} in **Figure-5.1c** are clearly visible in BDP and MBDP, revealing the presence of emeraldine salt of PANI composites, and these vibrations are little shifted to the higher wavenumber as compared to BDP only. The characteristic stretching vibration band

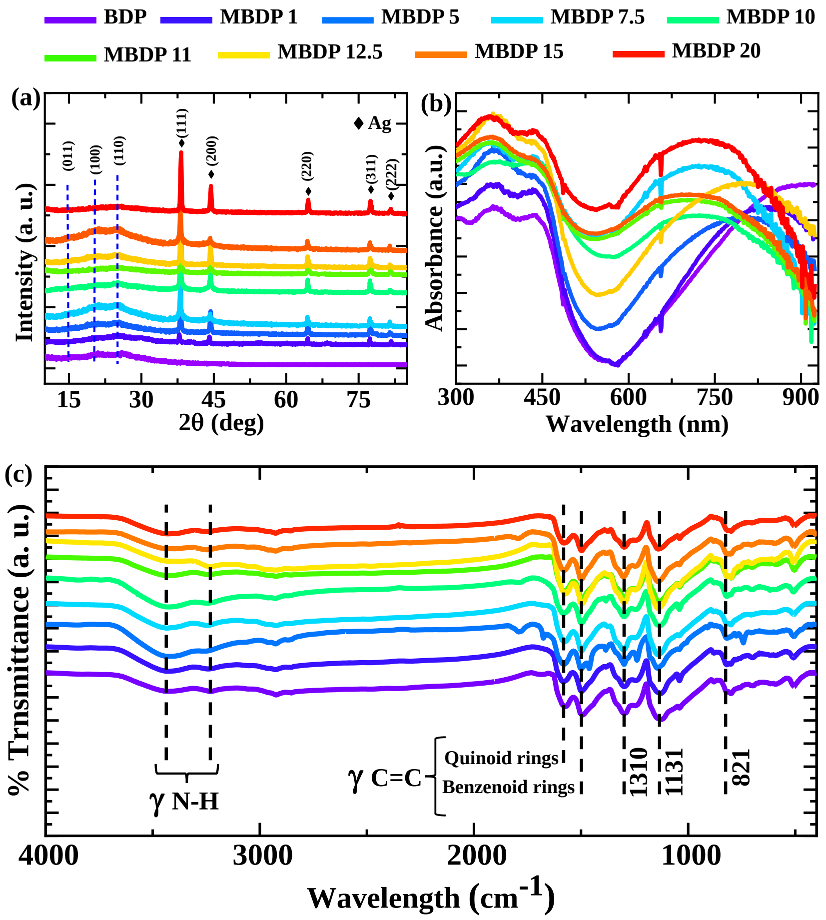

Figure- 5.1. Characterizations of metal Ag NPs embedded BDP prepared in-situ by dipping it into AgNO3 aqueous solution for 3 h (a) XRD spectra, (b) Absorption spectra, and (c) FTIR spectra of BDP and MBDP.

at 821 and 1131 cm^{-1} are for γ C-H aromatic in the plane, and the out of the plane deformation of 1,4-disubstituted benzene, stretching vibration band at 1310 cm^{-1} is for γ C-H for the secondary aromatic amine. Another two stretching vibration bands are at 1498 cm^{-1} (for γ C = C for benzenoid rings) and 1584 cm^{-1} (for g C = C quinoid rings). The band at ~3431 cm^{-1} is for γ N-H stretching vibration for PANI chains.

5.3.2. XPS Analysis

The survey spectra of X-ray photoelectron spectroscopy (XPS) of BDP and MBDP 10 composite (**Figure-5.2**), show four prominent peaks in the region of binding energy E_b = 50 - 700 eV coming from different elements. Strong XPS signals at 283.6, 398.7, and 530.5 eV correspond to C1s, N1s, and O1s, respectively, indicating the chemical environment of C, N, and O in BDP [65-67] and small but significant signal

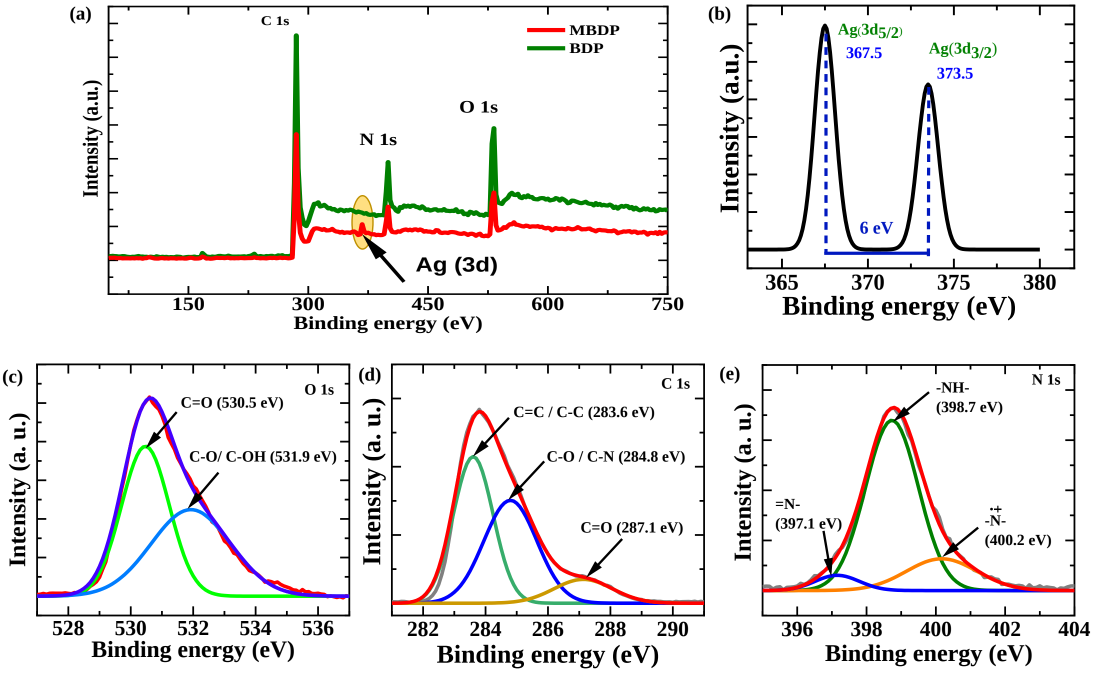

Figure- 5.2. XPS spectra of MBDP 10 sample. (a) Complete spectral scan and the enlarged spectra of (b) carbon, (c) oxygen, (d) nitrogen, and (e) silver, respectively.

centred at 370.0 eV reveals the presence of silver onto BDP nanotubes. XPS signals at ~366.8 and 372.8 eV correspond to the $Ag3d_{5/2}$ and $Ag3d_{3/2}$ energy levels respectively, are clearly

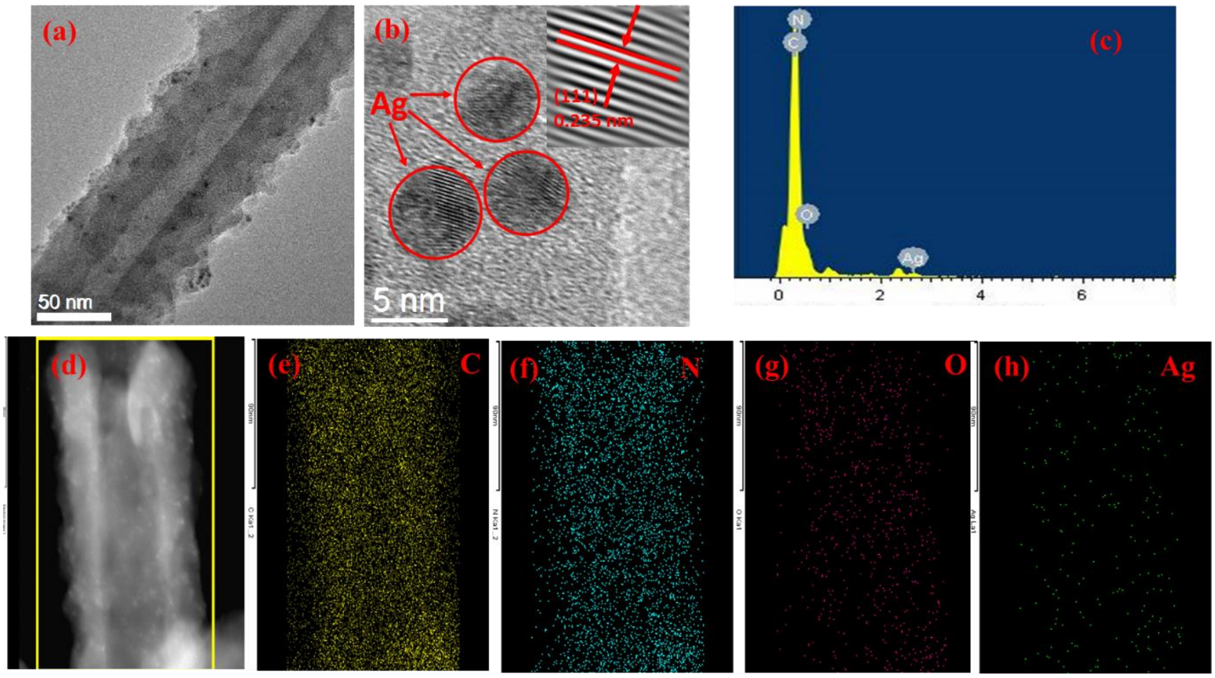

Figure-5.3. Composition analysis of MBDP 10 sample. (a) FEG-TEM image, and (b) high resolution image of Ag NPs attached on BDP and its FFT image in its inset. (c) EDX spectra. (d) TEM image and corresponding EDS-based elemental mapping from (e) C, (f) N, (g) O and (h) Ag.

visible as shown in **Figure-5.2e** and confirm the formation of Ag NPs into/on BDP surface [68]. Peak positions of Ag $3d_{5/2}$ and $3d_{3/2}$ are slightly different from reported values; however, the peak difference is same (~6 eV) [69].

5.3.3. Morphology Analysis

FEG-TEM images (**Figure-5.3**) exhibit the formation of nanotubes of BDP and the overwhelming presence of Ag NPs (without using the reducing agent) on the surface of BDP nanotubes after stirring BDP into an aqueous solution of AgNO3. The polaron form of PANI chain possibly reduces Ag ion to Ag (0) to BDP fibre, leading to the formation of Ag NPs. High-resolution HRTEM images (**Figure- 3a** and **b**) reveal the spherical shape of Ag NPs with an approximate diameter ~5 nm, and Ag NPs are distributed on/over the BDP nanotubes. With the increasing concentration of AgNO3, the shape and size of the Ag NPs almost remain the same. However, the growth of NPs is also observed outside of the MBDP fibre (see Table 1) at higher concentrations. The estimated lattice distance from the Fast Fourier Transform (FFT) of the TEM image (inset of 3(b)) is about 0.235 nm, which exactly matches with the (111) plane of Ag consistent with the XRD pattern (**Figure-5.1b**). Elemental mapping of the MBDP sample reveals the presence of C, N, and O in the BDP matrix and Ag in the NPs (distributed on/into BDP fibres). EDX patterns of the MBDP samples also support these observations.

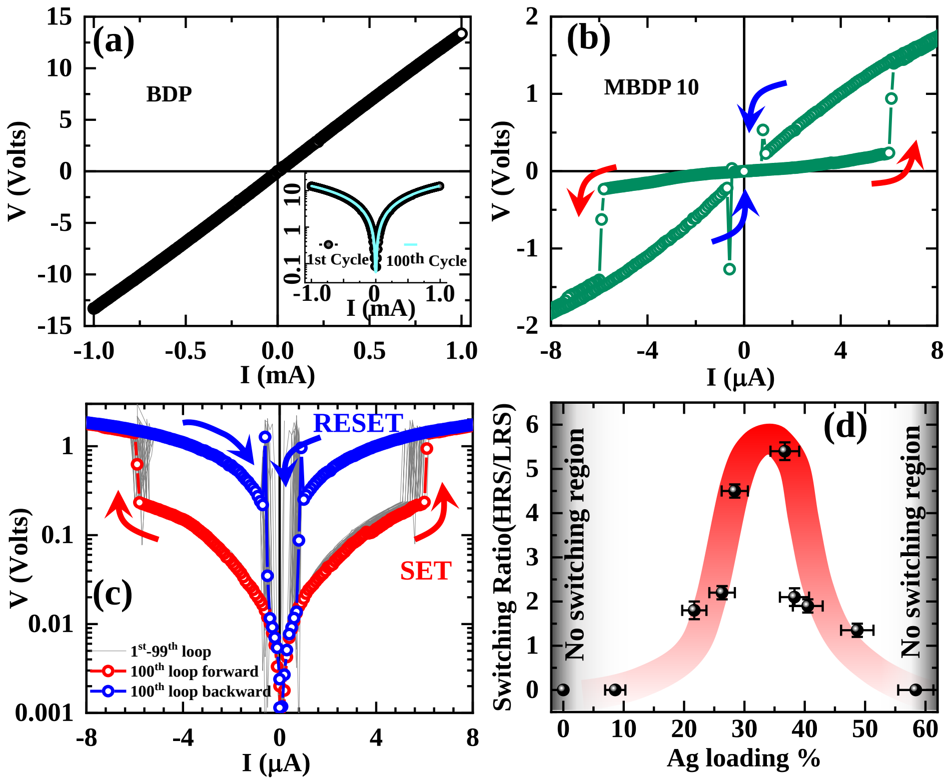

Figure- 5.4. The current-voltage (IV) characteristics of (a) BDP (semi-log IV plot in the inset) and (b) MBDP 10. (c) The semi-log IV presentation over 100 cycles measured at room temperature for MBDP 10. (d) The HRS/LRS switching ratio as a function of Ag loading percentage.

5.3.4. Charge-transport measurement

Charge-transport measurements have been carried out in a ’symmetric’ four-probe electrode configuration, and the resultant current-voltage (IV) graphs are presented in **Figure- 5.4**. For the BDP sample, the linear plot and semi-log presentation of the 100th cycle of repetitive IV plots are shown in **Figure- 5.4(a)**. The BDP sample doesn't produce any signs of hysteresis over the entire current range and follows the same trace perfectly. Interestingly, the IV graph of MBDP 10 exhibits significant hysteretic behaviour as evident in **Figure- 5.4(b)**. The semi-log plots of 100 repetitive IV graphs in **Figure- 5.4(c)** confirm two well-distinguished resistive states. The transport results manifest typical unipolar, non-volatile RS behaviour between its pristine low resistive state (LRS) and an induced high resistive state (HRS) **Figure- 5.4(c)**. The pristine MBDP sample is in LRS and indicates an Ohmic type of conduction. With the increasing current above a certain value i.e., I_{SET}, the sample switches to a high resistive state (HRS) called as ‘SET’ process. Furthermore, the sample does not trace the previous path after reducing the applied current. Instead, it holds the HRS until the applied current becomes smaller than a certain reset current (I_{RESET}). Below the I_{RESET}, the sample switches back to LRS, which is called the RESET process. This unipolar RS behaviour is obtained by applying a ‘SET’ or ‘write’ current (I_{SET} ~ 6 mA) for switching to HRS, whereas the ‘RESET’ or ‘erase’ current (I_{RESET} ~ 1 mA) is applied to reset to its pristine LRS in the same polarity. The resistance changes between the HRS and LRS is ~5.4 for the MBDP 10 sample at an applied current of 2 mA. The evolution of IV spectra with the loading concentration of Ag NPs reveals that Ag NPs strongly influence the charge conduction process and change the resistance values (for details, see Section 3 in supplementary). The HRS/LRS switching ratio has been used to quantify RS characteristics to find an optimal concentration. With increasing loading concentration of Ag NPs, the RS ratios, and area of hysteresis loop increase and become maximum for MBDP 10 (with 36.7 % Ag NPs loading concentration), and then the switching ratio starts to decrease (**Figure- 5.4d**). Interestingly, no switching has been observed either at very low (10 %) or very high (a 58 %) concentrations of Ag NPs. Therefore, the optimal presence of Ag NPs inside the CPs is needed for the emergence of RS in these functional materials. With the further increase in the forward current (beyond the first ‘HRS’), another transition appears at a current value of I_{SET2} ~ 14.5 mA, and the system switches to a second high resistive state, called HRS2 (see Fig. 5(a). To mention here that no other RS has been observed within our measurement limits (up to a voltage limit of 100 V). **Figure- 5.5(b)** shows semi-log plots of IV spectra with 100 repetitive cycles confirming the presence of two distinct SET and RESET processes in MBDP 10 sample. The second SET and RESET currents appear at $I_{SET\ 2}$ ~ 14.5 mA and @$I_{RESET\ 2}$ ~ 7.25 mA, respectively.

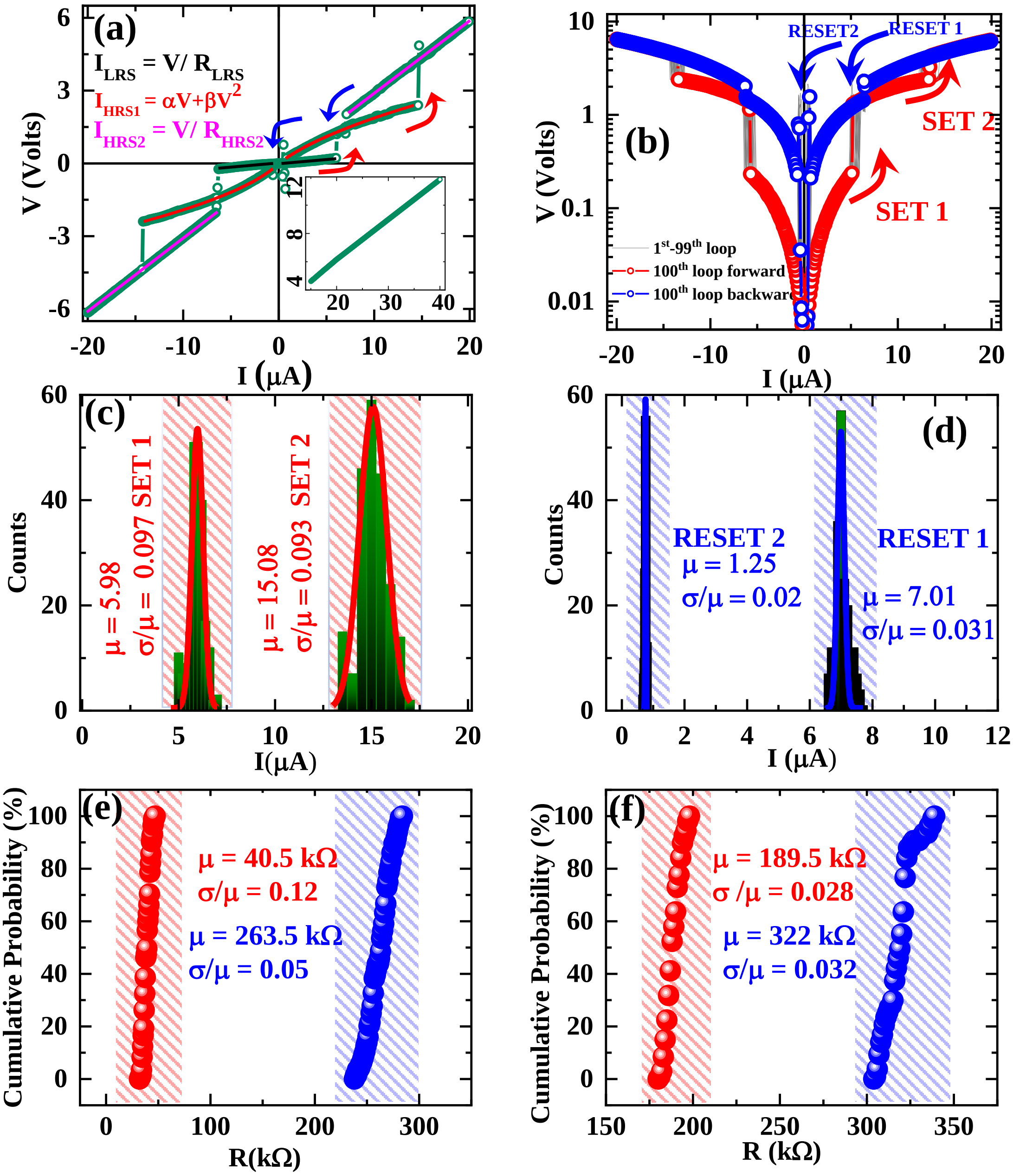

Figure. 5.5. Multiple resistive states and statistical analysis RS transitions of MBDP 10. (a) The current-voltage (IV) characteristics shows the double symmetric complementary RS behaviour and (b) The semi log presentation over 100 cycles. Statistical distribution of (c) I_{SET} and (d) I_{RESET} current distribution and their corresponding Gaussian fits. Cumulative probability of resistance is shown in (e) first switching and (f) second switching process.

Interestingly, three distinct resistive states (LRS, HRS1 & HRS2) have been observed convincingly over the hundreds of cycles of IV measurements without any sign of damage or breakdown. Distributions of switching currents which have been analysed critically to investigate the re-producibility and uniformity of resistive transitions for both the 'SET' and 'RESET' processes, provide well-separated Gaussian peaks as shown in **Figure-5.5(c, d)**. For the MBDP 10 sample, the mean switching current values for 'SET1', & 'SET2' have been found to be 5.98 mA, & 15.08 mA, respectively and for the 'RESET1', & 'RESET2' are 7.01 mA, & 1.25 mA, respectively.

Coefficients of variance for 'SET1' & 'SET2' currents are estimated to be 9.7 % & 9.3 % and for 'RESET1' & 'RESET2' are found to be 3.1 % & 2.0 %, respectively. The cumulative probability of the different resistance states for the MBDP sample has been presented in **Figure-5.5(e, f)**. The resistance distribution of the LRS and HRS1 for the MBDP sample has been presented in **Figure-5.5(e)**, where the ratio between these two states is more than five times the coefficient of variations is 5 % and 12 %, respectively. Similarly, the cumulative probability distributions for the other two states, HRS1 and HRS2, have been presented in **Figure-5.5(f)**. The ratio of the resistance state, HRS1, and HRS2, is two times, and the coefficient of variations are 2.8 % and 3.2 %, respectively. **Figure- 5.7(a-b)** show the positive cycles of IV data of BDP & MBDP samples plotted in log-log scales. As expected, the BDP sample follows the linear IV characteristics (Ohmic transport) and exponential temperature-dependent resistivity due to thermally generated charge carriers as expected for semiconducting materials (see Fig. 7(c and g)). However, the transport properties of the MBDP 10 sample strongly depend on its resistive states. In the LRS, the IV results follow the linear Ohmic behaviour, and the temperature-dependent resistivity reveals exponential activated behaviour as expected for a semiconducting material (**Figure-5.7(d and h)**). Whereas in HRS1, IV characteristics exhibit predominantly non-linear IV spectra, and the temperature dependence resistivity indicates variable range hopping (VRH) transport in **Figure-5.7**(**e** and **i**).

With further increase of current the MBDP switch to HRS2, IV characteristics again become linear at significantly higher resistance. In HRS2, the temperature-dependent resistivity surmises the activated behaviour like a semiconducting material.

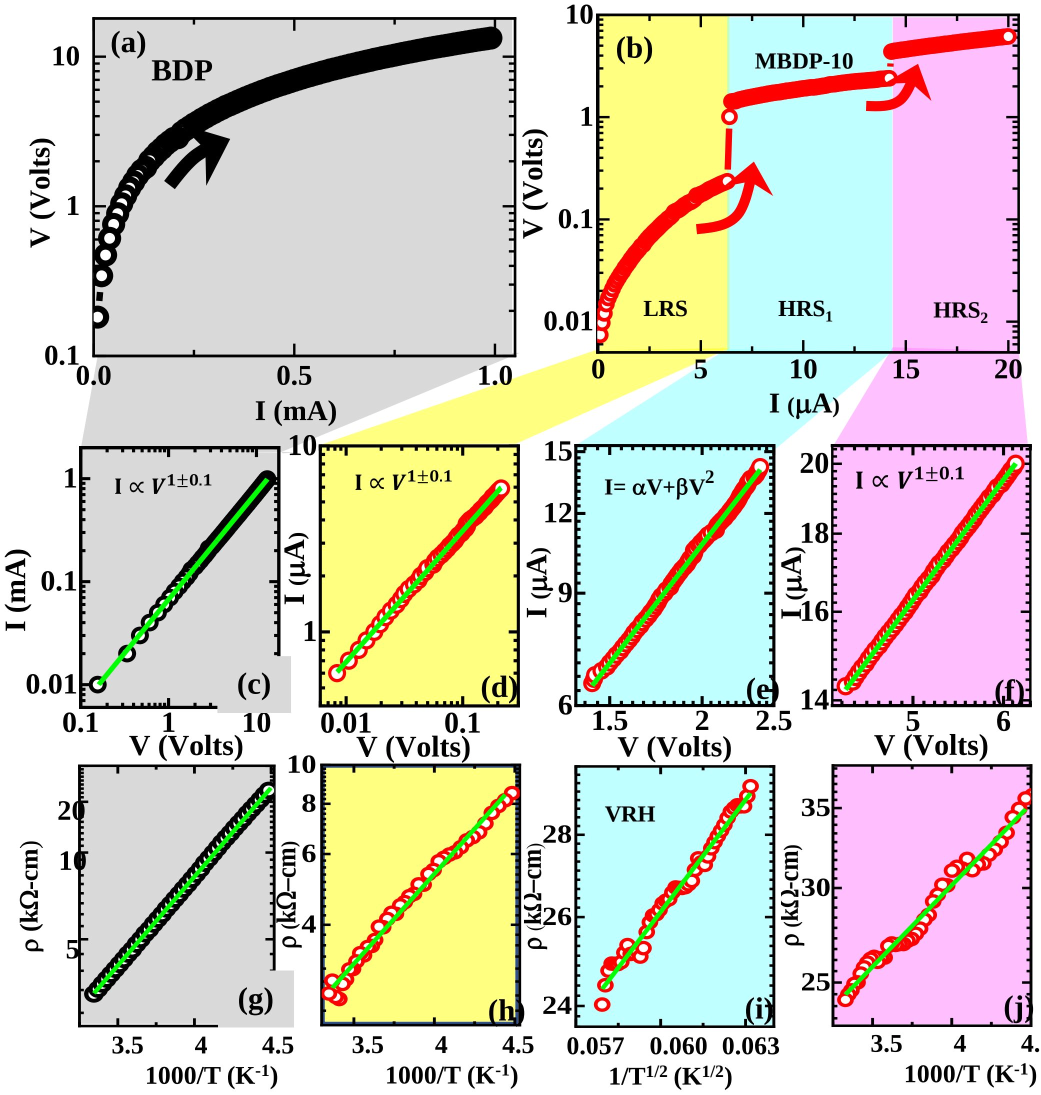

Figure- 5.7. Single cycle semi log current-voltage (IV) characteristics of the (a) BDP and (b) MBDP 10. The corresponding theoretical fittings with experimental data with different regimes for (c) BDP and (def) MBDP 10. (g-j) The temperature dependent resistivity along with the theoretical fits.

5.3.5. The IV measurements of the MBDP samples as a function of loading factor of Ag NPs and with time

Figure 5.8 represented the typical current-voltage (IV) characteristics of MBDP samples with increasing loading concentrations of Ag NPs. The measurements were carried out in the conventional four-point dc method at room temperature. The IV curve for MBDP samples showed the existence of hysteretic behaviour as the current was swept cycle (corresponding 0 → $+I_{max}$ → 0 → $-I_{max}$ → 0) as shown in **Figure 5.8 (b-h)**, except for sample MBDP 0.1 and MBDP 20 as shown in **Figure-5.8 (a and j)**.

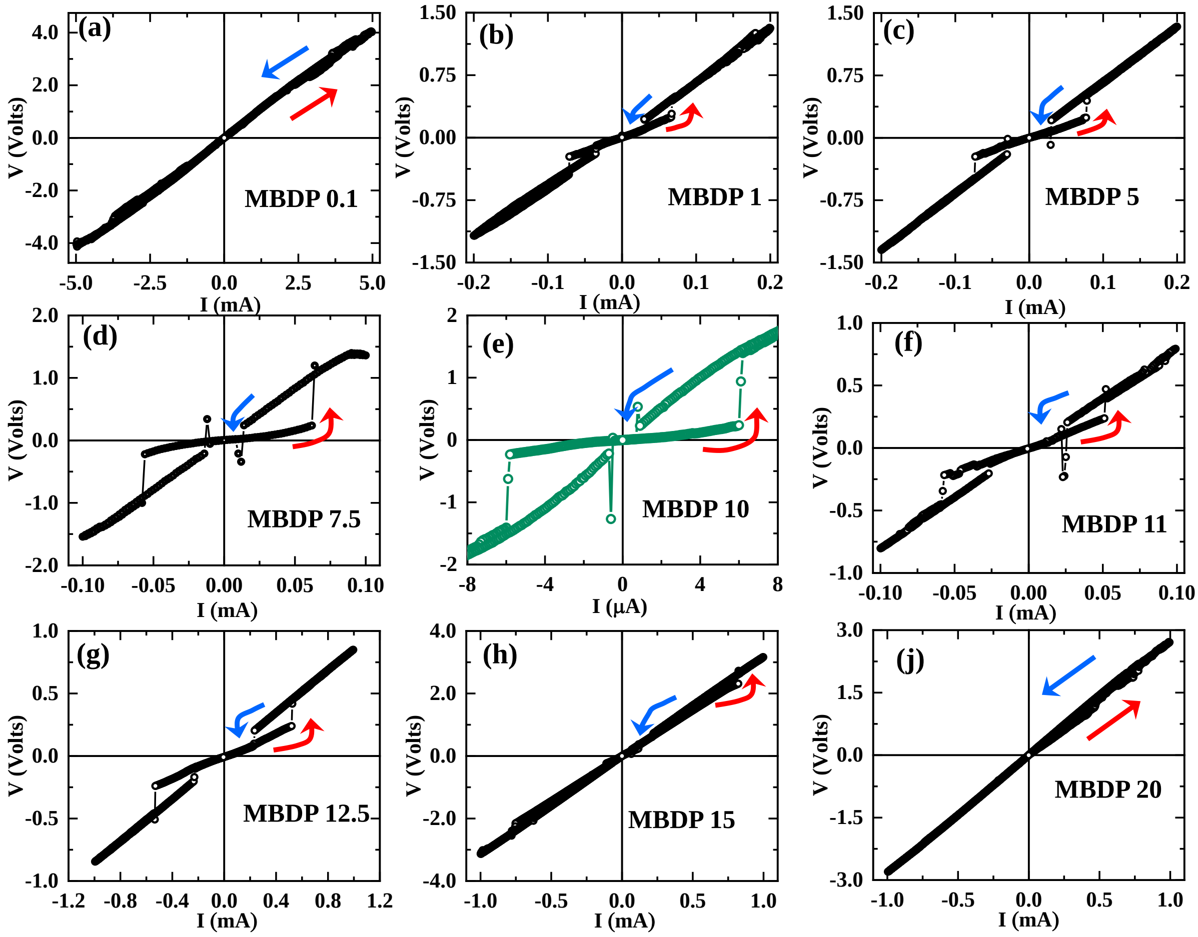

Figure-5.8 The current-voltage (IV) characteristics of MBDP samples with varying loading factors of Ag NPs

The nature of the IV curve suggested the unipolar, nonvolatile resistive switching (RS) behavior between its pristine low resistive state (LRS) and an induced high resistive state (HRS). With increasing Ag loading concentration, the RS ratios and area of the hysteresis loop were increased and reached a maximum value for MBDP 10 (with 36.7 % Ag NPs concentration), and after that, it started to decline, as evident from the plots. The MBDP 20 sample (with ≳ 58.4 % Ag NPs concentration) did not produce any RS phenomena. The presence of Ag NPs inside the CPs is critical for RS.

The stability of the samples against the aging effect is demonstrated by the time-dependent current-voltage (IV) characteristics of MBDP 10 sample, as shown in **Figure 5.9**. The nature of IV remained the same, with a slightly reduced switching ratio with time. The time dependent IV data suggested that Ag NPs embedded functional BDPs were stable enough over a long time.

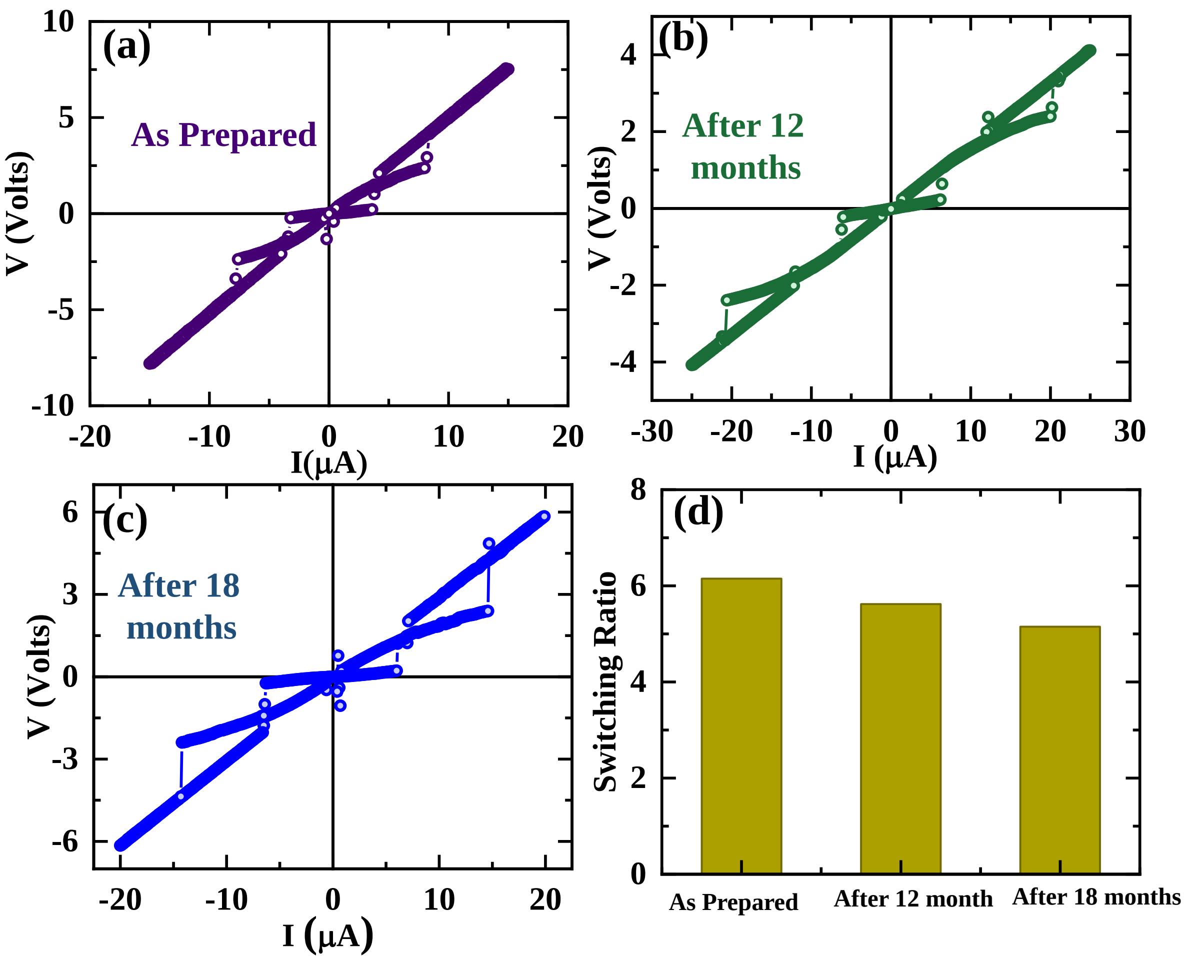

Figure-5.9 Effect of sample aging. The current-voltage (IV) characteristics of the MBDP 10 sample (a) As prepared (b) After 12 months, (c) After 18 months, and (d) Their HRS/LRS switching ratio as a function of time.

5.4. Conclusion

We demonstrate explicitly multilevel resistive switching phenomena of functionalized conducting polymer nanotube in presence of Ag NPs as compared to pristine nanotube. This study reveals that the loading percentage of Ag NPs in the polyaniline nanotubes plays a critical role in determining the multilevel RS phenomena in polymer composites. The MBDP 10 with 36 % Ag in BDP reveals the optimal RS characteristics with the considerable resistance OFF/ON ratio, appreciable retention capacity, and long-cycle endurance performances. The IV transport measurements over a large bias current vehemently support the multilevel RS behaviour of MBDP 10. The multilevel RS has been utilized as proof of principle to demonstrate a logic-gate (OR) operation. The charge conduction mechanism leading to multi-level RS phenomena has been investigated using temperature-dependent electrical transport. The present study on RS phenomena in functionalized conducting polymer embedded with metal NPs, may provide a significant new direction toward developing multilevel RS memory devices with outstanding performances.

5.5. References

1. C. Wong, Elsevier, 2013.
2. H. Schift, *J. Vac. Sci. Technol. B Microelectron. Nanometer Struct. Process. Meas. Phenom.*, 2008, **26** 458-480.
3. B.D. Gates, Q. Xu, M. Stewart, D. Ryan, C.G. Willson, G.M. Whitesides, *Chem. Rev.*, 2005, **105** 1171-1196.
4. R. Hagen, T. Bieringer, *Adv. Mater.*, 2001, **13** 1805-1810.
5. K. Bock, *Proc. IEEE*, 2005, **93** 1400-1406.
6. T.J. White, D.J. Broer, *Nat. Mater.*, 2015, **14** 1087-1098.
7. K. Fukukawa, M. Ueda, *Polym. J.*, 2008, **40** 281-296.
8. G.W. Burr, B.N. Kurdi, J.C. Scott, C.H. Lam, K. Gopalakrishnan, R.S. Shenoy, *IBM J. Res. Dev.*, 2008, **52** 449-464.
9. O. Mutlu, *in: 2013 5th IEEE international memory workshop*, 2013, pp. 21-25.
10. G. Molas, E. Nowak, *Appl. Sci*, 2021, **11** ISSN 2076-3417.
11. A. Chen, *Solid State Electron.*, 2016, **125** 25-38.
12. C. Du, Y. Ren, Z. Qu, L. Gao, Y. Zhai, S.-T. Han, Y. Zhou, *Nanoscale*, 2021, **13** 7498-7522.
13. L.V. Hai, M. Takahashi, W. Zhang, S. Sakai, *Jpn. J. Appl. Phys.*, 2015, **54**, 088004.
14. J.Y. Seok, S.J. Song, J.H. Yoon, K.J. Yoon, T.H. Park, D.E. Kwon, H. Lim, G.H. Kim, D.S. Jeong, C.S. Hwang, *Adv. Funct. Mater.*, 2014, **24** 5316-5339.
15. Y. Yang, J. Ouyang, L. Ma, R.J. Tseng, C. Chu, *Adv. Funct. Mater.*, 2006,**16**, 1001-1014.
16. J. Li, W. Sui, Y. Li, *J. Phys. Chem. C*, 2017, **121** 13723-13728.
17. M. Park, S. Park, K. Yoo, *ACS Appl. Mater. Interfaces*, 2016, **8** 14046-14052.
18. Y. Sun, J. Lu, C. Ai, D. Wen, X. Bai, *Org. Electron.*, 2016, **32**, 7-14.
19. J. Ouyang, *Nano Rev.*, 2010, **1**, 5118.
20. D.S. Jeong, R. Thomas, R.S. Katiyar, J.F. Scott, H. Kohlstedt, A. Petraru, C.S. Hwang, *Rep. Prog. Phys.*, 2012, **75**, 076502.
21. N. Raeis Hosseini, J.-S. Lee, *ACS Nano*, 2015, **9**, 419-426.
22. J. Xu, X. Zhao, Z. Wang, H. Xu, J. Hu, J. Ma, Y. Liu, *Small*, 2019, **15**, 1803970.

23. A. Venkataraman, E.V. Amadi, Y. Chen, C. Papadopoulos, *Nanoscale Res. Lett.*, 2019, **14**, 220.

24. K. Donaldson, R. Aitken, L. Tran, V. Stone, R. Duffin, G. Forrest, A. Alexander, *Toxicol. Sci.*, 2006, **9**,2 5-22.

25. M.H. Naveen, N.G. Gurudatt, Y. Shim, *Appl. Mater. Today*, 2017, **9**, 419-433.

26. W. Lin, S. Liu, T. Gong, Q. Zhao, W. Huang, *Adv. Mater.*, 2014, **26**, 570-606.

27. H. Yen, C. Shan, L. Wang, P. Xu, M. Zhou, H. Wang, *Polymers*, 2017, **9**.

28. A. Rahman, M. Sanyal, *Adv. Mater.*, 2007, **19**, 3956-3960.

29. W. Elsawy, M. Son, J. Jang, M.J. Kim, Y. Ji, T. Kim, H. Ko, A. Elbarbary, M. Ham, J. Lee, *ACS Macro Lett.*, 2015, **4**, 322-326.

30. Y. Yin, Z. Zhou, X. Wang, H. Mao, C. Ban, Y. Chen, J. Liu, Z. Liu, W. Huang, *ACS Appl. Mater. Interfaces.*, 2020, **12**, 1103-1109.

31. S. Mondal, S. Malik, *J. Power Sources*, 2016, **328**, 271-279.

32. S. Mondal, U. Rana, P. Das, S. Malik, *ACS Appl. Polym. Mater.*, 2019, **1**, 1624-1633.

33. Z. Xu, M. Gao, L. Yu, L. Lu, X. Xu, Y. Jiang, *ACS Appl. Mater. Interfaces*, 2014, **6**, 17823-17830.

34. G.U. Siddiqui, M.M. Rehman, Y. Yang, K.H. Choi, *J. Mater. Chem. C*, 2017, **5**, 862-871.

35. U.S. Bhansali, M. Khan, D. Cha, M.N. AlMadhoun, R. Li, L. Chen, A. Amassian, I.N. Odeh, H.N. Alshareef, *ACS Nano*,2013, **7**, 10518-10524.

36. D.A. Lapkin, A.V. Emelyanov, V.A. Demin, V.V. Erokhin, L.A. Feigin, P.K. Kashkarov, M.V. Kovalchuk, *Appl. Phys. Lett.*, 2018, **112**, 043302.

37. R.J. Tseng, J. Huang, J. Ouyang, R.B. Kaner, Yang, *Nano Lett.*, 2005, **5**, 1077-1080.

38. M. El Rhazi, S. Majid, M. Elbasri, F.E. Salih, L. Oularbi, K. Lafdi, *Int. Nano Lett.*, 2018, **8**, 79-99.

39. W. Zhang, Y. Kong, X. Jin, B. Yan, G. Diao, Y. Piao, *Electrochem. Acta*, 2020, **331**, 135345.

40. Y. Dou, W. Zhang, A. Kaiser, *Adv. Sci.*, 2020, **7**, 1902590,

41. S.I. White, P.M. Vora, J.M. Kikkawa, K.I. Winey, *Adv. Funct. Mater.*, 2011, **21**, 233-240.

42. Q. Liu, W. Guan, S. Long, R. Jia, M. Liu, J. Chen, *Appl. Phys. Lett.*, 2008, **92**.

43. S. Chakrabarti, S. Samanta, S. Maikap, S.Z. Rahaman, H. Cheng, *Nanoscale Res. Lett.*, 2016, **11**, 389.

44. E.W. Lim, R. Ismail, *Electronics*, 2015, **4**, 586-613.

45. Z. Wang, M. Rao, R. Midya, S. Joshi, H. Jiang, P. Lin, W. Song, S. Asapu, Y. Zhuo, C. Li, H. Wu, Q. Xia, J.J. Yang, *Adv. Funct. Mater.*, 2018, **28**, 1704862.

46. F. Pan, S. Gao, C. Chen, C. Song, F. Zeng, *Mater. Sci. Eng. R Rep.*, 2014, **83**, 1-59.

47. S. Yu, X. Guan, H.P. Wong, *Appl. Phys. Lett.*, 2011, **99**, 063507.

48. J. Lee, S. Jung, J. Park, S. Chung, J.S. Roh, S.-J. Hong, J. Lee, *Appl. Phys. Lett.*, 2012, **101**, 103506.

49. J.S. Lee, S. Lee, T.W. Noh, *Appl. Phys. Rev.*, 2015, **2**, 031303.

50. S. Mondal, U. Rana, S. Malik, *ACS Appl. Mater. Interfaces*, 2015, **7**, 10457-10465.

51. U. Rana, K. Chakrabarti, S. Malik, *J. Mater. Chem.*, 2012, **22**, 15665-15671.

52. U. Rana, S. Mondal, J. Sannigrahi, P.K. Sukul, M.A. Amin, S. Majumdar, S. Malik, *J. Mater. Chem. C*, 2014, **2**, 3382-3389.

53. A. Eftekhari, L. Li, Y. Yang, *J. Power Sources*, 2017, **347**, 86-107.

54. W. Chen, R.B. Rakhi, H.N. Alshareef, *J. Mater. Chem. A*, 2013, **1**, 3315-3324.

55. Y. Miao, W. Fan, D. Chen, T. Liu, *ACS Appl. Mater. Interfaces*, 2013, **5**, 4423-4428.

56. Y. Wang, H. Tran, L. Liao, X. Duan, R.B. Kaner, *J. Am. Chem. Soc.*, 2010, **132**, 10365-10373.

57. Y. Yan, R. Wang, X. Qiu, Z. Wei, *J. Am. Chem. Soc.*, 2010, **132**, 12006-12012.

58. Y. Ma, C. Hou, H. Zhang, M. Qiao, Y. Chen, H. Zhang, Q. Zhang, Z. Guo, *J. Mater. Chem. A*, 2017, **5**, 14041-14052.

59. K. Lee, S. Cho, S.H. Park, A.J. Heeger, C. Lee, S. Lee, *Nature*, 2006, **441**, 65-68.

60. A. Drury, S. Chaure, M. Kroll, V. Nicolosi, N. Chaure, W.J. Blau, *Chem. Mater.*, 2007, **19**, 4252-4258.

61. S.K. Pillalamarri, F.D. Blum, A.T. Tokuhiro, M.F. Bertino, *Chem. Mater.*, 2005, **17**, 5941-5944.

62. A.C. Patel, S. Li, C. Wang, W. Zhang, Y. Wei, *Chem. Mater.*, 2007, **19**, 1231-1238.

63. C. Wang, D. Niu, H. Xie, B. Liu, S. Wang, M. Zhu, Y. Gao, *J. Chem. Phys.*, 2017, **147**.

64. U. Rana, S. Mondal, J. Sannigrahi, P.K. Sukul, M.A. Amin, S. Majumdar, S. Malik, *J. Mater. Chem. C*, 2014, **2**, 3382-3389.

65. Y. Gao, D. Shan, F. Cao, J. Gong, X. Li, H. Ma, Z. Su, L. Qu, *J. Phys. Chem. C*, 2009, **113**, 15175-15181.

66. H. Tsunoyama, H. Sakurai, N. Ichikuni, Y. Negishi, T. Tsukuda, *Langmuir*, 2004, **20**, 11293-11296.

67. X.-R. Li, X.-L. Li, M.-C. Xu, J.-J. Xu, H.-Y. Chen, *J. Mater. Chem. A*, 2014, **2**, 1697-1703.

68. S.Y. Kang, K. Kim, *Langmuir*, 1998, **14**, 226-230.

69. D. Briggs, Handbook of x-ray photoelectron spectroscopy C.D. Wanger, W.M. Riggs, L.E. Davis, J.F. Moulder and G.E. Muilenberg Perkin-Elmer Corp., Physical Electronics Division, Eden Prairie, Minnesota, USA, 1979. 190 pp. 195, *Surf. Interface Anal.*, 1981, **3**.

70. S. Wu, T. Tsuruoka, K. Terabe, T. Hasegawa, J.P. Hill, K. Ariga, M. Aono, *Adv. Funct. Mater.*, 2011, **21**, 93-99.

CHAPTER 6

Summary and Conclusions

6.1 Summary & Conclusion

The present thesis mainly deals with conducting polymer, especially synthesis, properties, application of polyaniline and polyaniline/metal nanocomposite. Polyaniline is a widely popular conduction polymer, having promising electrochemical capacitive property suited for real application. Mild reducing cum stabilizing property of polyaniline towards Noble metal nanoparticles has been explored. Applications related to synthesis of polyaniline nanostructures and polyaniline/metal nanocomposites have been described. This thesis consists of total eight chapters. The summary of all eight chapters are present below:

6.1.1. Chapter 1

In Chapter 1, describes general introduction about conducting polymer and synthesis procedure, properties and different field of application regarding polyaniline nanostructures and polyaniline/metal nanocomposites. The chemical structures of PANI and its different form have been explained. Different synthesis procedure of PANI and morphology of PANI nanostructures depending upon template, dopant acid, molar ratio of aniline to dopant acid have been discussed. Some applications like supercapacitor, electronic memory device, catalysis, electro-catalysis, water purification etc. related to PANI and advantages of PANI have been explain. Finally, we have presented some literature surveys related to the direction of this thesis and our work motivation.

6.1.2. Chapter 2

The Chapter 2 contains the details information about the instrumentation techniques that were used during characterization, property measurement and application of synthesized polyaniline and polyaniline/metal nanocomposites. Basically, in the experiment we used these characterization techniques included Field-emission Scanning Electron Microscopy (FESEM), Transmission Electron Microscopy (TEM), Atomic Force Microscopy (AFM), X- Ray Diffraction (XRD), Electrochemical study, UV-Vis spectroscopy, X-Ray Photoelectron Spectroscopy (XPS), Fourier transform infrared (FTIR) spectroscopy, Raman spectroscopy, Thermal Gravimetric Analysis (TGA), Current (I)-Voltage (V) Measurement etc.

6.1.3. Chapter 3

In Chapter 3 we have successfully demonstrated the organic acid doped polyaniline nanotubes have been employed as an electrode material for the development of electrochemical capacitor.

Organic acids used as dopant in the chemical oxidation of aniline are benzene dicarboxylic acids (OA2), benzene tricarboxylic acids (OA3) and benzene tetracarboxylic acids (OA4) to make polyaniline nanostructures. Morphological studies with the help of FESEM and HRTEM reveal the formation of nanotubes with organic acids on contrary to HCl doped PAN. After characterization of OPAN with UV-Vis, XRD, XPS and FTIR, these OPAN are subjected to electrochemical studies and subsequently to galvanostatic charge-discharge studies to have the idea about the suitability of these as electrode materials. It has been noticed that OA4PAN is the optimum nanostructures among four OPAN having specific capacitance 394 F/g with 76.8% retention of total specific capacitance after 3000 cycles. The OA4PAN solid-state flexible device has showed the specific capacitance of 84 F/g at a 0.5 A/g, energy density of 7.42 Wh/kg at a 0.5 A/g, power density of 200 W/kg at a 0.5 A/g and also retains 90.9% of its specific capacitance after 5000 charge-discharge cycles. Albeit low as comparative to nanocomposites with carboneous analogue but significant electrochemical performances with simple organic acid doped polyaniline nanotube provides its potential for prospective application as electrode materials for flexible supercapacitor device.

6.1.4. Chapter 4

The Chapter 4 deals with a novel hybrid network, GMP-PANI, combining polyaniline with G-quadruplex (GMP), has been synthesized through *in-situ* polymerization of aniline in the presence of APS. The hybrid network has been investigated through rheological /dynamic mechanical studies, demonstrating its exceptional strength of hybrid gel network compared to GMP hydrogel network. Detailed investigations of the GMP network's morphology, both before and after polymerization, using FESEM and HRTEM, have revealed the formation of polyaniline fibres within the GMP network, without any macroscopic phase separation. Therefore, a unique GMP-PANI hybrid network is created, displaying exceptional electrochemical performance with biocompatible. In a three-electrode system, the GMP-PANI hybrid network demonstrates a high specific capacitance of 405 F/g at a current density of 0.5 A/g. This remarkable capacitance value is indicative of its excellent charge storage capacity, making it an ideal candidate for supercapacitor applications. Notably, when incorporated into an all-solid-state symmetric supercapacitor, the GMP-PANI hybrid network showcases a significantly enhanced specific capacitance, along with impressive cycle stability, retaining approximately 87% of its capacitance over multiple charge-discharge cycles. This excellent cycle stability is of paramount importance for real-world applications where longevity and consistent performance are critical factors. Moreover, in a tandem configuration, a series of five GMP-PANI hybrid network-based supercapacitors collectively powers red, blue, white, and multi-coloured LED bulbs, demonstrating its robust capability as a reliable and high-performing supercapacitor. The ability to power different types of LED bulbs exemplifies the versatility and suitability of the GMP-PANI hybrid network as a biocompatible material for practical energy storage solutions.

6.1.5. Chapter 5

In Chapter 5 we demonstrate explicitly multilevel resistive switching phenomena of functionalized conducting polymer nanotube in presence of Ag NPs as compared to pristine nanotube. This study reveals that the loading percentage of Ag NPs in the polyaniline nanotubes plays a critical role in determining the multilevel RS phenomena in polymer composites. The MBDP 10 with 36 % Ag in BDP reveals the optimal RS characteristics with the considerable resistance OFF/ON ratio, appreciable retention capacity, and long-cycle endurance performances. The IV transport measurements over a large bias current vehemently support the multilevel RS behaviour of MBDP 10. The charge conduction mechanism leading to multi-level RS phenomena has been investigated using temperature-dependent electrical transport. The present study on RS phenomena in functionalized conducting polymer embedded with metal NPs, may provide a significant new direction toward developing multilevel RS memory devices with outstanding performances.

6.2. Scope of future work

Polyaniline nanostructures are expected to exhibit superior performance in technological applications compared to bulk, because of the unique properties arising from their nanostructures. In accordance, my research interest is focuses on the potential application-based polyaniline nanostructures synthesis. These nanocomposite materials are highly applicable in energy storage device, sensors device, electro-optic, solar cell device, electro-chromic devices and many others. There are several scopes for advanced application based on polyaniline nanomaterial. To get prospective application for new generation further work is needed.

1. Utilizing Polyaniline/Metal Nanocomposites as Active Electrocatalysts for Energy Harvesting.
2. Facile Fabrication of Polyaniline/Au Composites for Future Electronic Memory Devices.
3. Exploring GMP-PANI 10 Composites for High-Performance Supercapacitors: Towards Flexible, Transparent, All Solid-State Devices.
4. Future Prospects of Highly Ordered Polyaniline Nanotubes for Integrated Energy Harvesting and Storage Devices.
5. Development of Sensor Devices for Toxic Gas Detection Using Polyaniline or Polyaniline/Metal Composites.
6. Industrial Applications of Polyaniline Nanostructures for Wastewater Purification.
7. Towards Macroscopic PANI Fiber Synthesis: Enabling Visible Observability for Future Applications.
8. Polyaniline Nanotubes for Future Electrochromic Device Fabrication.
9. Exploring Polyaniline as a Metal-Free Catalyst: Thermal Stability and Conductivity Perspectives for Industrial Applications.

LIST OF PUBLICATIONS

Book Chapter:

Conjugated Polymer Based Nanocomposites as Electrode Materials

S. Dhibar, **Puspendu Das**, S. Mondal, U. Rana, Sudip Malik, **WILEY-VCH GmbH**, *Conjugated Polymer Nanostructures for Energy Conversion and Storage Applications*, Pages 401-444

Journals:

1. G-quadruplex/Polyaniline hybrid networks as next-generation biocompatible electrode materials with unprecedented rheological performance.
   Puspendu Das, Sk M. Ahamed, G. L. Dhakar, B. Lala, R. Chatterjee, J. Dash, S. Malik, (Under review in *ACS Applied Energy Materials*)
2. Charge transport and low-frequency conductance noise in metal-nanoparticle embedded one-dimensional conducting polymer nanotubes: multiple resistive switching phenomena.
   S. Bera, **Puspendu Das**, B. Das, S. Mondal, P. K. Gupta, A. Bera, Sk Kalimuddin, Sk M. Ahamed, S. Gayen, M. Mondal, S Malik, *Materials Today Nano*, **2023**, 22, 100312
3. Urea-mediated synthesized carbon quantum dots to tune the electrochemical performance of polyaniline nanorods for supercapacitor device.
   M. S. Kumar, K. Y. Yasoda, **Puspendu Das**, S. Malik, N. K. Kothurkar, S. K. Batabyal, *Journal of Science: Advanced Materials and Devices*, **2022**, 7, 100403
4. Effect of tricarboxylic acids on the formation of hydrogels with melem or melamine: morphological, structural and rheological investigations
   P. K. Sukul, **Puspendu Das**, G. L. Dhakar, L. Das, S. Malik, *Gels*, **2022**, 8, 51
5. Fully organic polyaniline nanotubes as electrode material for durable supercapacitor
   Puspendu Das, S. Mondal, S. Malik, *Journal of Energy Storage*, **2021**, 39, 102662
6. Fabrication of organic nanocomposite of polyaniline for enhanced electrochemical performance
   M. S. Kumar, **Puspendu Das**, K. Y. Yasoda, N. K. Kothurkar, S. Malik, S. K. Batabyal, *Journal of Energy Storage*, **2020**, 31, 101700

7. Network of polyaniline nanotubes for wastewater treatment and oil/water separation
S. Mondal, U. Rana, **Puspendu Das**, S. Malik, *ACS Applied Polymer Materials*, **2019**, 1, 1624-1633.

Under Preparation / Communication:

1. Oxygen tolerant electrocatalytic hydrogen generation by a bio-inspired [FeFe]-hydrogenase mimic in a polymeric matrix.
   Md E. Ahmed, **Puspendu Das**, Sk. M. Ahamed, S. Chattopadhyay, A. Nayek, M. Mondal, S. Malik, and A. Dey. **(Communicated)**
2. Tailoring Polyaniline Nanotubes with Pt Nanoparticles for Efficient Hydrogen Evolution Reaction
   Puspendu Das, Sk. M. Ahamed, P. K. Gupta and S. Malik. **(Communicated)**
3. Surface modified MoS_2 doped Polyaniline nanotube for durable supercapacitor.
   Puspendu Das, Sk. M. Ahamed, P. K. Gupta and S. Malik. **(Communicated)**

SAIS SYMPOSIUM 2024

CERTIFICATE OF PARTICIPATION

This certificate is awarded to

Puspendu Das

Who has delivered Key Note Address / Invited Talk / presented Poster / participated in this symposium held at the Indian Association for the Cultivation of Science (IACS), Kolkata, India on March 1st-2nd, 2024.

Organized by
School of Applied and Interdisciplinary Sciences (SAIS), IACS, Kolkata

Dr. Sudip Malik
Professor and Chairman
School of Applied & Interdisciplinary Sciences (SAIS)
I.A.C.S, Jadavpur, Kolkata-700 032

Malik
Prof. Sudip Malik
Convener

SAIS SYMPOSIUM 2023

CERTIFICATE FOR PARTICIPATION

This certificate is awarded to

Puspendu Das

Who has participated/presented poster in this symposium held at the Indian Association for the Cultivation of Science (IACS), Kolkata, India on February 27–28, 2023

Organized by
School of Applied and Interdisciplinary Sciences (SAIS), IACS, Kolkata

Dr. Sudip Malik
Professor and Chairman
School of Applied & Interdisciplinary Sciences (SAIS)
I.A.C.S, Jadavpur, Kolkata-700 032

Malik
28/02/23
Prof. Sudip Malik
Convener

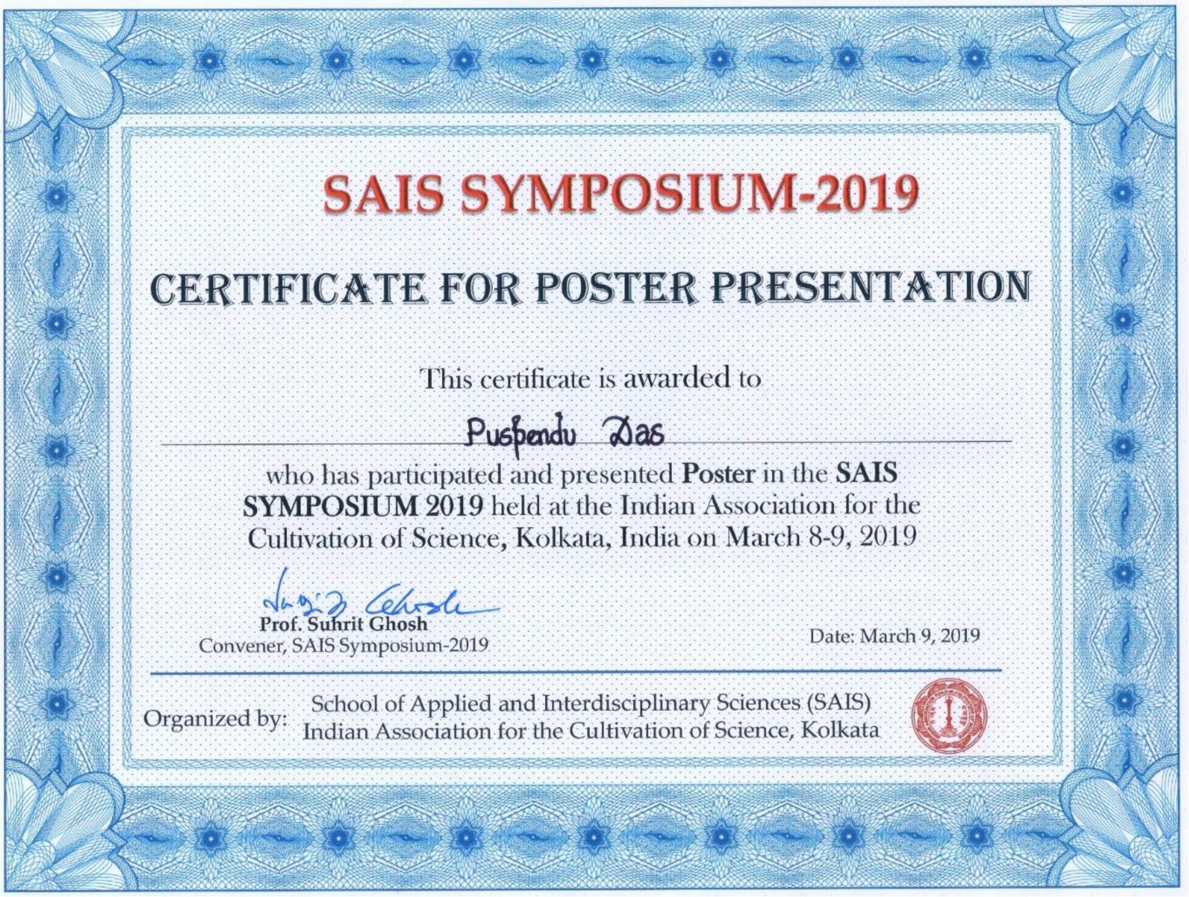

SAIS SYMPOSIUM-2019

CERTIFICATE FOR POSTER PRESENTATION

This certificate is awarded to

Puspendu Das

who has participated and presented **Poster** in the **SAIS SYMPOSIUM 2019** held at the Indian Association for the Cultivation of Science, **Kolkata**, India on March 8-9, 2019

Prof. Suhrit Ghosh
Convener, SAIS Symposium-2019

Date: March 9, 2019

Organized by: School of Applied and Interdisciplinary Sciences (SAIS)
Indian Association for the Cultivation of Science, Kolkata

SPS THE SOCIETY FOR POLYMER SCIENCE (INDIA)

SPSI MACRO 2018

15th International Conference on
Polymer Science and Technology

Certificate for Poster Presentation

This certificate is awarded to

Puspendu Das

who has presented Poster
in the SPSI MACRO-2018 Conference in IISER-Pune and CSIR-NCL Pune in Maharashtra, India from December 19 to 22, 2018

Dr. Prakash P. Wadgaonkar
Co-convener, SPSI-MACRO-2018

Professor M. Jayakannan
Convener, SPSI-MACRO-2018

Professor S. Ramakrishnan
President, SPSI

Organized by

IISER PUNE
CSIR - NCL

Date: December 22, 2018

Preparation of Polyaniline Nanostructures for Energy and Charge-Transport Application

<u>Puspendu Das</u> and Sudip Malik
School of Applied & Interdisciplinary Sciences,
Indian Association for the Cultivation of Science,
2A & 2B Raja S. C. Mullick Rd., Jadavpur, Kolkata-32, India.
E-mail: psusm2@iacs.res.in

Polyaniline nanotubes for durable supercapacitor

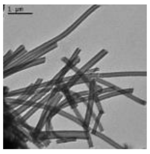

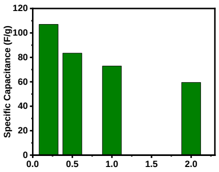

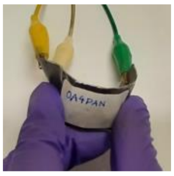

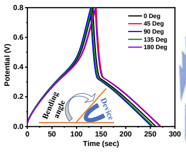

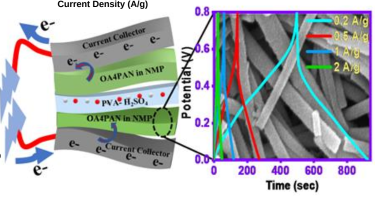

Polyaniline/G-Quadruplex Hybrid Networks as Electrode Materials

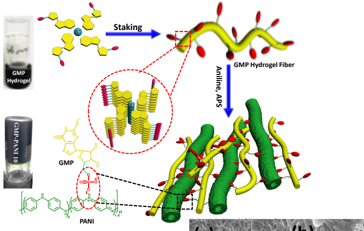

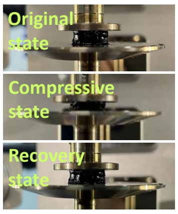

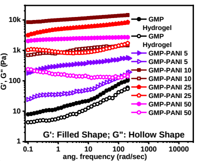

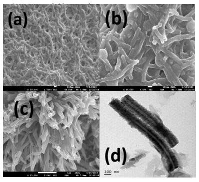

PANI/Ag composite for Memory Application

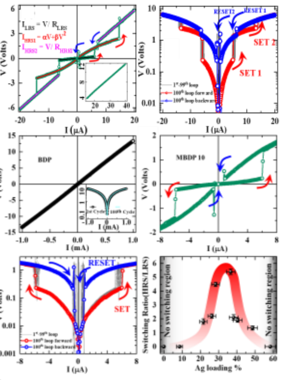

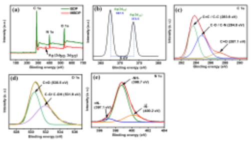

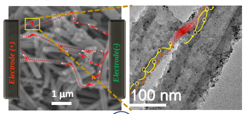

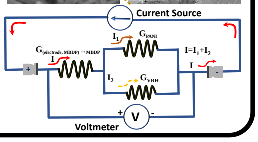

Conclusion:

1. Fully organic polyaniline nanotubes as electrode material for durable supercapacitor
2. Polyaniline/G-Quadruplex Hybrid Networks as Next-Generation Electrode Materials with Unprecedented Rheological Performance
3. Charge transport in metal-nanoparticle embedded one-dimensional conducting polymer nanotubes: multiple resistive switching phenomena

References:

1. Journal of Energy Storage, 2021, **39**, 102662.
2. Materials Today Nano, 2023, 22, 100312

CURRICULUM VITAE

Mr. Puspendu Das was born on 1st March, 1992 at Purba Medinipur, West Bengal, India. He attended Rangadih S. B. H. S. School for secondary education and Purulia Zilla School for higher secondary education. After schooling, he started his bachelor degree (B.Sc) study in chemistry honours from Presidency University, Kolkata where he received his B.Sc degree in 2014. Afterwards he started his Master degree in Physical Chemistry at University of Calcutta and received M. Sc degree in 2016. He qualified GATE – 2017 organized by IIT Roorkee. In June 2017 he started his Ph.D career on the topic of "**Preparation of Polyaniline Nanostructures for Energy and Charge-Transport Application**" under the supervision of Prof. Sudip Malik in the School of Applied and Interdisciplinary Sciences of Indian Association for the Cultivation of Science under Jadavpur University at Jadavpur, India. He has published seven article and one book chapter in high impact international journals. Apart from lab work he was also engaged in various outdoor games and cooking